NNT : 79433

THÈSE DE DOCTORAT DE L'ÉTABLISSEMENT UNIVERSITÉ BOURGOGNE FRANCHE-COMTÉ (France)

PRÉPARÉE À L'EMPA (Suisse)

Ecole doctorale n°553

ED Carnot Pasteur

Doctorat de Chimie et Physique

Par

Madame Ellina Bernard

Magnesium silicate hydrate (M-S-H) characterization: temperature, calcium, aluminum and alkali

Thèse présentée et soutenue à Dübendorf, Suisse, le 30 novembre 2017

Composition du Jury :

Pr. Sandrine Gauffinet,	Enseignante-chercheure, Université de Bourgogne Franche-Comté,	Présidente
Dr. Jean-Baptiste d'ESPINOSE de LACAILLERIE,	Enseignant-chercheur, ESPCI,	Rapporteur
Pr. Urs Mäder,	Professor, Université de Berne,	Rapporteur
Dr. Isabelle Pochard,	Enseignante-chercheure, Université de Bourgogne Franche-Comté,	Directrice de thèse
Dr. Alexandre Dauzères,	Chercheur, IRSN,	Codirecteur de thèse
Dr. Barbara Lothenbach,	Chercheure, Empa,	Codirectrice de thèse
Dr. Céline Cau-Dit-Coumes,	Chercheure, CEA,	Invitée

ECOLE DOCTORALE
CARNOT - PASTEUR

Titre : Caractérisation de phases silico-magnésiennes (M-S-H et M-A-S-H) en fonction de la température, de la présence de calcium et en condition alcalines

Mots clés : Stockage en couches profondes, argiles, pâtes de ciment bas-pH ; silicate de calcium hydraté (C-S-H) ; silicate de magnésium hydraté (M-S-H) ; alumino-silicate de magnésium hydraté (M-A-S-H) ; adsorption d'alcalins et de calcium ; composition chimique ; modélisations thermodynamiques

Résumé : Les différentes options envisagées par la France et la Suisse pour le stockage de déchets radioactifs en couches géologiques profondes argileuses prévoient l'utilisation d'importants volumes de matériaux cimentaires. Les liants dits bas-pH ont été développés afin de limiter la perturbation de la roche encaissante par le panache alcalin. Les études expérimentales menées sur les interfaces béton bas-pH-argile mettent systématiquement en évidence la formation de phases silico-magnésiennes, potentiellement de silicate de magnésium hydraté (M-S-H), mal modélisées à cause de données thermodynamiques limitées. Cette étude a pour objectif de caractériser ces phases en température, en présence d'aluminium, calcium et d'alcalins pour alimenter les bases de données thermodynamiques et améliorer les calculs sur les évolutions physico-chimiques des bétons bas pH et éventuellement des bétons de Portland.

Des suspensions de M-S-H ont été synthétisées à partir d'oxyde de magnésium et de fumée de silice à différentes températures, à différents temps de réaction et différents rapports Mg/Si. Un panel de techniques d'analyses de chimie du solide et des mesures en suspensions couplées à des analyses des phases liquides a été utilisé pour caractériser les phases synthétisées. Initialement, et quel que soit le Mg/Si total choisi pour la synthèse, un M-S-H avec un rapport Mg/Si ~1 précipite en présence de brucite et de silice amorphe. Lorsque l'équilibre du système est atteint, 2 à 3 ans à 20 °C ou 1 an à 50 et 70 °C, le Mg/Si varie de ~0,8 à ~1,4. La température a peu d'influence sur le M-S-H formé même si le M-S-H se forme plus rapidement et qu'il est légèrement moins stable thermodynamiquement lorsque la température augmente. A l'équilibre, sa structure mal définie est comparable à des nano-cristallites de phyllosilicates hydratés avec une surface spécifique supérieure à 200 m^2/g.

Un modèle de solution solide pour le M-S-H a été calculé et ajouté aux bases de données.

Dans un second temps, les travaux ont été focalisés sur la formation de M-S-H à partir de silicate de calcium hydraté (C-S-H) avec un faible Ca/Si (= 0,8) et de magnésium. Le C-S-H n'est pas stable à des pH avoisinant un pH = 10, ce qui favorise la précipitation de M-S-H. Des recherches détaillées montrent que du calcium peut être faiblement incorporé dans le M-S-H (Ca/Si ≤ 0,10), et des solutions solides contenant du calcium ont été ajoutés à la base de données. Pour des pH supérieurs à 10-10,5, les C-S-H et M-S-H coexistent. L'observation par MEB-EDS d'une interface en cellule de diffusion entre C-S-H (Ca/Si=0,8 représentant un liant bas pH) et M-S-H (Mg/Si=0,8), couplée à la modélisation de celle-ci en transport réactif, sur la base des nouvelles données thermodynamiques dérivées des expériences précédentes, montrent la détérioration rapide du C-S-H et la précipitation de M-S-H dans le disque C-S-H, ainsi qu'une absorption homogène du calcium dans le disque de M-S-H.

L'augmentation du pH en solution favorise la sorption de cations. Des M-S-H présentant une sorption de sodium jusqu'à Na/Si ~ 0,20 en absence de brucite ont été observés à des pH avoisinants 12,5. La sorption sur le M-S-H est favorisée dans l'ordre $Na^+ < Mg^{2+} < Ca^{2+}$.

Enfin, l'aluminium s'incorpore dans le M-S-H pour former du M-A-S-H. Un rapport Al/Si jusqu'à 0,2 est observé dans des suspensions synthétisées en présence d'aluminate de sodium ou de métakaolin. Les données de RMN de l'aluminium ont montré que celui-ci est présent dans les sites tétraédriques et octaédriques du M-A-S-H. La phase formée a une structure similaire à celle du M-S-H avec un degré de polymérisation des silicates et une charge effective de surface comparables.

Title: Magnesium silicate hydrate (M-S-H) characterization: temperature, calcium, aluminum and alkali

Keywords: Geological disposal, clays, low-pH cement, calcium silicate hydrate (C-S-H), magnesium silicate hydrate (M-S-H), magnesium (alumino-) silicate hydrate (M-(A-)S-H), alkali and calcium binding, chemical composition, thermodynamic modelling

Abstract: The various options to store radioactive wastes in deep geological strata considered in France or Switzerland include the use of large volumes of cementitious materials for infrastructure in contact with argillaceous rocks. So-called low-pH binders were developed to minimize disruption to the surrounding rock by the alkaline plume. Studies conducted on the interaction zone between concrete and clay systematically highlighted the formation of magnesium silicate phases including magnesium silicate hydrate (M-S-H) at the interfaces, which can presently be modeled only partially due to incomplete thermodynamic data. The purpose of this study was to characterize these phases in temperature, aluminum, calcium, and alkali conditions in order to provide the thermos-dynamic data and improve the calculations on physicochemical evolutions of low-pH concretes and possibly Portland concretes.

M-S-H phases were synthesized from magnesium oxide and silica fume in batch experiments at different temperatures, for various times and varying Mg/Si. A large number of different techniques such as chemical solid characterizations coupled with suspension investigations and liquid analyses were used to characterize the phases synthesized. Initially a M-S-H phase with Mg/Si equal to 1 was precipitated in addition to amorphous silica and brucite whatever the total Mg/Si used for the synthesis. After long equilibration times, 2 to 3 years at 20°C or 1 year at 50 and 70°C, the Mg/Si in M-S-H ranged from ~0.8 to ~1.4. The temperature had little influence on the M-S-H formed even if the M-S-H formation occurred faster and M-S-H was thermodynamically slightly less stable when the temperature was increased. At or near to equilibrium, M-S-H phases were characterized with ill-defined structure comparable to nano-crystalline, hydrated phyllosilicates with a surface area greater than 200 m^2/g. A M-S-H solid-solution model was calculated and implemented in a thermodynamic database.

It was observed that M-S-H also form from calcium silicate hydrate (C-S-H) with a Ca/Si = 0.8 in the presence of additional magnesium. In batch experiments, a low pH of the suspensions (pH ≤ 10) destabilized C-S-H or prevented its formation and favored the precipitation of M-S-H. Detailed investigations showed that small amounts of calcium could be incorporated in M-S-H (Ca/Si ≤0.10), such that also calcium containing end-members were added to the M-S-H solid-solution. At pH ≥ 10-10.5, two separate silicate phases coexist: C-S-H and M-S-H. The interface between a simplified "low-pH" binder mimicked by C-S-H with Ca/Si = 0.8 and a magnesium-rich environment mimicked by M-S-H with Mg/Si = 0.8 confirmed these phenomena. SEM-EDS observations and reactive transport modelling using the thermodynamic data derived in the batch experiments showed the fast deterioration of the C-S-H and the precipitation of M-S-H in the C-S-H disk at the interface and a homogeneous uptake of calcium in the M-S-H disk.

The increase of pH favors the sorption of cations. M-S-H with a sodium uptake up to Na/Si ~ 0.20 and without brucite formation were observed at high pH (12.5). The sorption on M-S-H was favored in the order $Na^+ < Mg^{2+} < Ca^{2+}$.

Finally, aluminum was incorporated into M-S-H to form magnesium alumino-silicate hydrate (M-A-S-H). An Al/Si ratio up to 0.2 was observed in presence of sodium aluminate or metakaolin. 27Al MAS NMR data showed that aluminum was present in both tetrahedral and octahedral sites of M-(A-)S-H. The M-(A-)S-H formed had a similar structure as M-S-H with a comparable polymerization degree of the tetrahedral silicates and a similar surface charge.

Université Bourgogne Franche-Comté
32, avenue de l'Observatoire
25000 Besançon

Preface

This thesis presents the results obtained during my PhD project from December 2013 to September 2017 at Empa, Swiss Federal Laboratories for Materials Science and Technology in the Laboratory for Concrete & Construction Chemistry. The project was funded by IRSN, the French Institute of Radiation Protection and Nuclear Safety and Empa in collaboration with the University of Bourgogne and the CEA in Marcoule. The experiments were carried out in the laboratories at Empa, in the LUTECE lab at IRSN, at the University of Bourgogne and at the CEA in Marcoule. The NMR hardware was partially granted by the Swiss National Science Foundation (SNFS, grant no. 150638).

The manuscript is organized with an introduction of the context as first chapter and a description of the materials and methods as the second chapter. The following chapters are based on published, submitted or in preparation journal papers. The last chapter contains the conclusions and outlooks.

The formation of magnesium silicate hydrate, M-S-H, has been observed at the interface between hydrated cement and clay rocks and/or at the surface of cement exposed to seawater. The present dissertation investigates the properties of M-S-H and whether foreign ions (calcium, aluminum, and alkali) may be incorporated and the stability of those phases. The investigations focus on conditions relevant at the interface of hydrated cement pastes and bentonite or natural clay rocks in the context of the envisaged disposal sites for radioactive waste.

Acknowledgements

The first acknowledgments go to my Ph.D. supervisors, *Barbara Lothenbach*, *Isabelle Pochard*, and *Alexandre Dauzères*.

Barbara, you encouraged my curiosity and gave me the opportunity to do my Ph.D. at EMPA. Thank you for all the support and for sharing with me the knowledge about cement and particularly the thermodynamics. Your enthusiasm and passion for research always helped me to go through. It was very inspiring to work with you, and a special thank you for the support at the end of the thesis for correcting and commenting my thesis or the paper drafts. Thank you for everything!

Thank you for the financial support of IRSN and especially to Alexandre who has initiated this project. Thank you very much for the explanations on the safety issues of the context, the experiments at IRSN, and the general support.

A particular acknowledgment goes to Isabelle, always available for sharing knowledge and for the valuable discussions during these 4 years and the thorough re-reading at the end.

I am lucky and grateful to have been advised by such nice persons and to have had this environment to achieve my Ph.D. work.

I am extremely grateful to *Jean-Baptiste d'Espinose de Lacaillerie* and *Urs Mäder* for accepting and taking the time to report my thesis, *Sandrine Gauffinet* and *Céline Cau-Dit-Coumes* for accepting to be part of my committee, thank you all for coming to Dübendorf for the defense.
A special gratitude goes out to Céline who was always present for the great scientific discussions during these 4 years and took the time to read and give me comments on the journal papers.

Specific thankyous go to the lab 308 at Empa and particularly, Andreas, Emilie, Frank, Josef and more specifically to Mateusz for the helpful discussions and to always find time to answer my questions; Boris, Fabien, and Luigi for the help in the lab. I do not want to forget the other Ph.D. students for the great atmosphere. Lab 308, it was a pleasure to share these 4 years with you.

Furthermore, I would like to thank the following people for their collaboration and help in the completion of this work, in particular:

- *Daniel Rentsch* especially for teaching and guiding me with the solid state MAS NMR. Thank you also, to the Swiss National Science Foundation (grant no. 150638) for the partial granting of the NMR hardware.
- *Andreas Jenni*, and *Catherine Lerouge* for the nice discussions and for providing the mineral samples. A collective thank you to the scientists that I met in the CI meetings.
- *Karen Scrivener* for letting me join the ski seminar and use the H-relaxometry device at the LMC lab. Thank you to the welcoming LMC group and special thanks to François and Lily.
- *Rémi Chassagnon* for the TEM analysis, *Christophe Chlique* for the PDF analysis, *Dimitrii Kulik* and *Gwenn Le Saout* for the helpful discussions.

Lastly, I would like to thank my family and my friends for all their love, encouragement and support.

Contents

Chapter 1:

Introduction

Contents

1.1. Magnesium silicate hydrate (M-S-H) precipitation in cementitious materials in deep geological formations

1.1.1. General concepts of radioactive waste storage example with the Cigéo project

The creation of a disposal facility for radioactive waste in geological environment is a key issue addressed in the countries dealing with nuclear power industry. The long-term safety of such a geological repository is based on a multi-barrier system where the wastes are embedded in suitable packages ("inert" matrix as glass, concrete, etc.), the disposal, i.e. the underground facility and the geological environment. Together they should ensure a very long term containment of long-lived radionuclides and prevent its release to the biosphere.

Research on the long-term stability of such disposals is carried out in a number of countries, e.g. in Belgium, Finland, France, Sweden, Switzerland, the United Kingdom, Canada, China, and the United States depending on the host rock available. In France, Belgium, and Switzerland the concept of storage in a natural clayey environment is explored for several decades. Clay-based geological barriers have a low permeability which limits the ingress of groundwater and are thus favorable to contain radionuclides (NAGRA, 2002; ANDRA, 2005).

The Cigéo project of ANDRA, the French agency for radioactive waste management, envisages an underground facility with a high volume of cementitious materials used for the linear of gallery and disposal cell, and also for confinement plug used in the sealing areas (to contain the bentonite swelling during the water natural re-saturation). Only the intermediate long-lived nuclear wastes (ILLW) are envisaged to be stored in such storage cells. Cement will also be used to stabilize the wastes. The low permeability and the high pH of the cement paste favor the incorporation of radionuclides in the hydrated phases and limit their mobility into the far-field (Wieland et al., 2004; Tits et al., 2006; Evans, 2008). The Cigéo concept foresees two temporary sites on the ground level: the zone of waste package receipt and preparation and the base of the underground excavation and construction work. These two sites will be linked to the underground facility by two temporary accesses: one for the radioactive wastes and the other one for access to the personnel and material during the storage process (Appendix A).

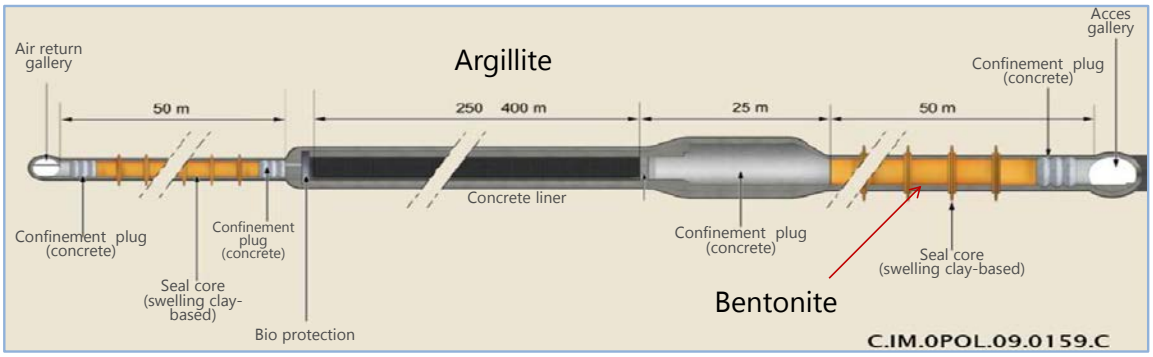

Figure 1: Design of the intermediate long lived waste (ILLW) cell (Cigéo project, ANDRA, adapted from (ANDRA, 2005)).

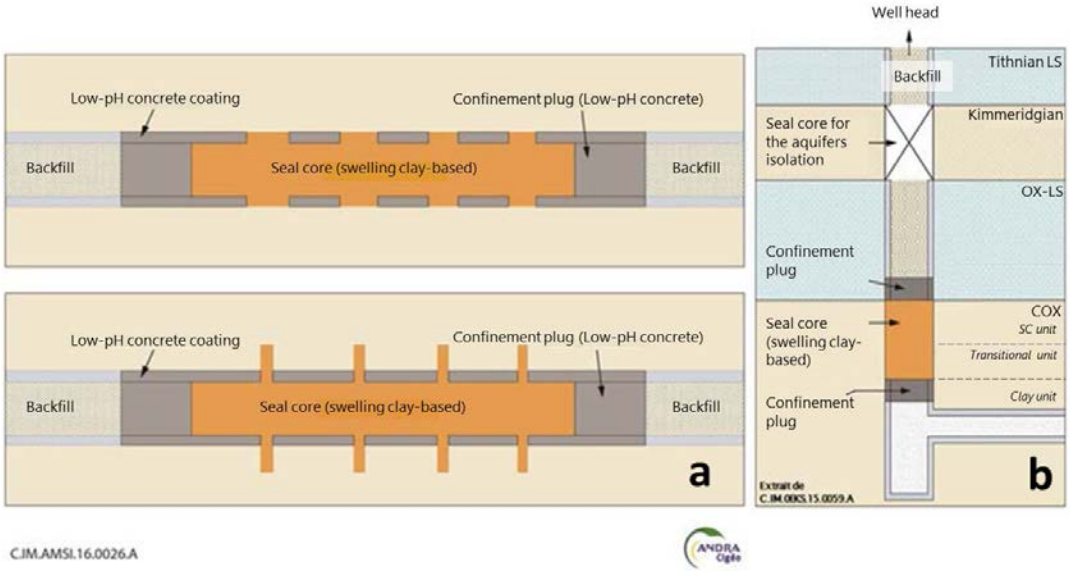

Figure 2: Sealing zones with concrete in Cigéo: a) two options for ILLW alveoli and galleries; b) well (Cigéo project, ANDRA, adapted from ANDRA (2016)).

Different types of sealing zones are envisaged. The intermediate long lived waste disposal cells are planned to be sealed by swelling clays as detailed in Figure 1 and Figure 2 deep below the ground level, to obtain a high degree of impermeability. The swelling of the clayey-seal core will be restrained by two concrete confinement plugs. Also, the access galleries will be backfilled and sealed. The cementitious materials will thus be in direct contact with the clayey host-rocks and with the swelling clay used for the sealing.

1.1.2. The cement pastes/clays interactions

In freshly hydrated Portland cement, the pH values in the porewater can reach 13.5 due to the high alkali content in such solutions (Lothenbach and Winnefeld, 2006; Vollpracht et al., 2015). This is likely to impact claystone and swelling clays at the contact zone as summarized e.g. in (Gaucher and Blanc, 2006; Savage et al., 2007; Dauzères et al., 2010). The combination of high pH values and alkali concentrations leads to the partial dissolution of clayey-rocks (Adler et al., 1999; Claret et al., 2002) or clays (Bauer and Berger, 1998; Ramírez et al., 2002) with the formation of calcium aluminate silicate hydrate phases and zeolites; zeolite formation is favored at increased temperature (Lalan et al., 2016; Lothenbach et al., 2017). Additionally, the heat generated during the early hydration of the Portland cement accelerates the destabilization of the clayey aluminosilicates at early age.

To reduce the early heat of hydration of Portland cement and lower the alkaline plume, so called "low-pH" binders have been developed, which contain in addition to Portland cement, pozzolanic materials such as silica fume, fly ash or slag (Cau Dit Coumes et al., 2006; Codina, 2007; Codina et al., 2008; Lothenbach et al., 2012a; Lothenbach et al., 2014). Such low pH-cements are mainly composed of calcium silicate hydrate (C-S-H) and ettringite, while portlandite is generally absent. The presence of pozzolanic materials which react with the portlandite, lowers the pH values of the pore solution; pH values in the range from 10.5 to 12 (Cau Dit Coumes et al., 2006; Codina, 2007; Codina et al., 2008; Lothenbach et al., 2012a; Bach et al., 2013; Lothenbach et al., 2014; Poyet et al., 2014) have been observed for "low-pH" cement pastes after 3 months of hydration. The presence of silica-rich materials lowers as well as the Ca/Si ratio in C-S-H to 0.7-1.2.

As shown in Figure 1 and Figure 2, different interfaces between cementitious and clayey materials occur in geological repositories of radioactive waste, where alteration of the clay due to the high pH of the pore solution solutions from the cement can be expected. The main interfaces include:

1- Portland concrete / natural clayey host rock interface at the external wall of the storage structure (storage cell and access galleries, and backfilling of the access galleries);

2- bentonite / potentially Low-pH concrete (regarding the current option) / natural argillite in the sealing interface in the sealing area

1.1.3. Magnesium disturbance at the low-pH binder-clay interface

Although "low pH" cement pastes have significantly lower pH values than Portland cement pastes, mineralogical changes still occurred at the interface with the host rock (Garcia Calvo et al., 2010; Jenni et al., 2014; Dauzères et al., 2016; Lerouge et al., 2017; Mäder et al., 2017). The pore water from the clay has lower pH values and higher carbonate concentration (Table 1) which leaches, decalcifies the C-S-H and can result in the presence of amorphous silica. Carbonates and sulfates (Table 1) from the ground water precipitate with calcium and aluminum in calcite and ettringite.

Table 1: Composition of the pore water of different host rocks.

	K	Na	Ca	Mg	Al	Si	SO_4	Cl	HCO_3	pH	Ref.
	mmol/l										
COX argillite	1	45.6	7.4	6.7	n.d.	0.2	15.6	41	3.3	7.1	(Gaucher and Lerouge, 2007)
Tournemire argilite	0.8	23.5	1.5	0.7	n.d.	0.03	9.5	4.5	4.6	7.4	(Tremosa et al., 2012)
Opalinus clay	1.8	248.7	23.1	39.1	n.d.	n.d.	17.7	338.5	1.6	7.2	(Pearson et al., 2003)

COX argillite: Bure, France, Cigéo project, ANDRA; Tournemire argilite, IRSN's in-situ laboratory; Opalinus clay: St-Ursanne, Switzerland, Mont-terri project, NAGRA.

In addition, magnesium from the interstitial solutions of the host rocks, from the clay minerals exchanges, or from the dissolution of the host rocks was observed precipitated at the interface (Garcia Calvo et al., 2010; Dauzères et al., 2014; Jenni et al., 2014; Dauzères et al., 2016; Fernández et al., 2017; Lerouge et al., 2017; Mäder et al., 2017).

Whether this magnesium enrichment at the interface between clay and Portland cement was associated with the formation of brucite, hydrotalcite or other magnesium containing solids was under debate. Garcia Calvo et al. (Garcia Calvo et al., 2010) observed on a low pH cement paste exposed to ground water a magnesium enrichment but exclude the formation of brucite. In laboratory experiments where the interface of cement with clay was investigated, the presence of Mg-containing calcite layer together with an amorphous phase containing magnesium and silica was observed (Dauzères et al., 2014). Similarly, magnesium silicate hydrate (M-S-H) and possibly hydrotalcite were tentatively observed in field experiments at the Mont Terri rock laboratory (Jenni et al., 2014; Dauzères et al., 2016; Mäder et al., 2017). While SEM/EDS data suggested the presence of a magnesium and silica phase, its clear identification is hampered by the structural similarities between clay minerals and such M-S-H phases. Based on TEM/EDS data, it has been recently suggested that this M-S-H phase at the interface contains not only magnesium and silicate, but also some aluminum, calcium and iron, comparable to a (Ca, Mg) smectite (Lerouge et al., 2017).

The experimental evidence suggested that although the magnesium concentrations in the clay interstitial solutions are moderate with 3 to 40 mmol/l, a magnesium silicate phase formed at the interface between clays and "low pH" cement pastes after 2 and 5 years. In the long-term, the carbonation and the leaching decrease the pH of the Portland cement paste. Hence, M-S-H could be expected to form also at the interface with Portland cement and clays.

In addition, the release of some heat from the radioactive waste packages may increase the temperature at the interfaces up 70°C. At this temperature, ettringite, a main component of Portland and low-pH cement pastes, might be destabilized and different types of zeolite might precipitate as observed by diffusion or batch experiments by (Lalan et al., 2016; Lothenbach et al., 2017). The effect of increased temperature on the formation of magnesium silicate hydrate has not yet been investigated.

1.2. M-S-H formation on cement pastes in the presence of magnesium sulfate or sea water

On the surface of Portland cement exposed to sulfate solutions, expansion and/or spalling was observed due to the formation of additional ettringite, often together with gypsum and at a lower temperature also with thaumasite. If in addition, magnesium was present in the solutions, surface erosion is dominant and the precipitation of brucite was reported. The presence of magnesium led to a destabilization of C-S-H gels at the surface. In few studies, also the formation of M-S-H phases was reported (Bonen and Cohen, 1992; Gollop and Taylor, 1992; Santhanam et al., 2002). M-S-H as a secondary product was observed more clearly for low Ca/Si C-S-H samples and in CEM III/B cement pastes than in CEM I cements, as the presence of slag reduces the amount of portlandite and lowers the Ca/Si in C-S-H (Kunther et al., 2013; Kunther et al., 2015). The formation of M-S-H was also reported at the surface of cement pastes and mortars exposed to groundwater or seawater (De Weerdt and Justnes, 2015; Jakobsen et al., 2016).

Thus, M-S-H was observed to form generally at the surface of both Portland and "low-pH" cements exposed to leaching by magnesium containing solution as e.g. magnesium sulfate test solutions, seawater or groundwater in contact with clay rocks. The leaching decreases the pH, destabilizes portlandite and decalcifies C-S-H at the surface of the cement sample while magnesium reacts with silica to form M-S-H.

1.3. Magnesia-based binders as an alternative to Portland cements

The manufacture of Portland clinker is an energy intensive process and causes 5 to 8% of the anthropogenic CO_2 emissions. The production of reactive magnesium instead of Portland cement would reduce CO_2 emissions. Firstly, reactive magnesium can be obtained from magnesium silicate minerals at temperatures below 1000°C (Gartner et al., 2014). Secondly, the temperature needed to produce a reactive magnesium oxide from magnesite (750-900°C) is much lower than the temperature required to produce Portland clinker from limestone (1450°C). Magnesium oxide can also be present as a non-minor element in blast furnace slags used as a supplementary cementitious material (SCMs).

During the hydration of magnesia and silica based cement pastes magnesium silicate hydrates (M-S-H) form as primary reaction products. The pH values of the pore solution of such cement are lower than 12 (Zhang et al., 2011; Zhang et al., 2012; Walling et al., 2015). Hence, such magnesia and silica based cement pastes could also be a good alternative to Portland cement for waste immobilizations as lower pH values are present and the formation of calcite and additional M-S-H due to the interaction with the groundwater would be minimized. However, research on the strength or the engineering properties of magnesia and silica based cement pastes will need to be required as only few studies gave insight on compressive strength resistance.

1.4. Stability of magnesium silicate hydrate

The stability of the disposal of radioactive wastes in underground repositories needs to be predicted up to millions of years. For this purpose, models to predict the physicochemical changes, including the phase composition, porosity, diffusion, and evolution of the mechanical properties, at the interface between cement and clay based materials are needed. While the composition and the long-term behavior of cements and of clay minerals can be predicted based on available thermodynamic databases (Helgeson, 1978; Holland and Powell, 1998; Hummel et al., 2002; Matschei et al., 2007; Lothenbach et al., 2008; Blanc et al., 2012; Thoenen et al., 2014), such data for magnesium silicates hydrate (M-S-H) are missing.

Although synthetic M-S-H was described and characterized in several papers (Kalousek and Mui, 1954; d'Espinose de Lacaillerie et al., 1995; Brew and Glasser, 2005b; Zhang et al., 2011; Jin and Al-Tabbaa, 2013; Szczerba et al., 2013; Li et al., 2014; Roosz et al., 2015; Walling et al., 2015; Nied et al., 2016), solubility data were generally

not reported and no thermodynamic data were available. Modelling of M-S-H formation became possible only after the first set of solubility measurements at 20°C and after thermodynamic data (Nied et al., 2016) has been published. Based on these data, the precipitation of M-S-H at the interface low-pH concrete - OPA could recently be predicted (Dauzères et al., 2016), in agreement with the experimental observations.

1.5. Objectives of the thesis

The main aim of this Ph.D. was to determine experimentally the solubility of M-S-H and the conditions under which it forms. Additionally, no or very little work has been available on the possible incorporation of aluminum and calcium and alkalis in M-S-H and its effect on M-S-H stability. In order to be able to understand where foreign ions such as Na^{+}, Ca^{2+}, and Al^{3+} could be taken up and to assess their upper limit, the presence of only one phase, M-(A-)S-H without brucite or amorphous silica, was desired. Therefore, most experiments were done in batch experiments, mixing the raw materials in a large amount of water which enabled a relatively fast reaction and a homogeneous composition of the solid phase. This batch approach allowed also to adapt the pH of the solution, where needed.

These studies were carried out at room temperature but also in a wider temperature range from 20 up to 70°C to cover the possible temperature range expected in the cementitious near-field of radioactive waste disposal sites.

The main topics investigated in this work were:

1) To understand under which conditions M-S-H may form and its compositional variations:

- How M-S-H formed in pure MgO-SiO_2 mixes? In which compositional range and at which pH range?
- Can M-S-H be formed from C-S-H and magnesium from ground water or from solid magnesium phases? What is the effect of magnesium on the stability of C-S-H?

2) To describe the structure and stability of M-S-H, based on a detailed investigation of the solid and liquid phases:

- Is there ordering in the ill-defined M-S-H structure? How much water is present and does M-S-H have a charged surface?
- Does the temperature affect the stability and structure M-S-H?
- Can aluminum, alkali or calcium be incorporated in M-S-H?

- How will the uptake of aluminum, alkali or calcium influence the structure and stability of M-S-H?

Based on these questions the thesis is structured as follows:

Chapter 2 summarizes the syntheses methods and the main analytical techniques used. Chapter 3 studies the effect of Mg/Si and temperature on the kinetic of M-S-H formation from MgO and SiO_2 and its stability. It also focuses on M-S-H samples equilibrated for 2 years and longer to elucidate their possible structure by comparison with phyllosilicates, to get their distribution of the water and their surface properties. Chapter 4 investigates the formation of M-S-H from pre-synthesized C-S-H and the effect of Ca on M-S-H stability and Mg on C-S-H stability in a pH range from 7 to 12. Chapter 4 also studies in details co-precipitated samples (MgO-CaO-SiO_2-H_2O) on a smaller pH range (8.5-10.5) and shows an incorporation of calcium in M-S-H. The chemical changes at an interface between calcium silicate hydrate (C-S-H) with a low Ca/Si ratio and magnesium silicate hydrate (M-S-H) are also presented. Chapter 5 is dedicated to the binding of alkalis at low and high pH and studies the incorporation of aluminum in M-S-H.

Chapter 2:

Syntheses and analytical techniques

Contents

2.1. Synthesis

2.1.1. Pure M-S-H in batch experiments

Magnesium oxide (Merck, pro analysis, 0.18±0.02wt.% Na_2O) and silica fume (SiO_2, Aerosil 200, 0.9wt.% HCl) were chosen as starting materials. The total Mg/Si varied between 0.7 and 1.6 and synthesis were optimized to obtain ~ 5 g of M-S-H (Table 2). The impurities in the starting SiO_2 and MgO resulted in approximately 0.03 mmol/l [Cl] and 0.7 mmol/l [Na] in the solution of the Mg/Si=0.8 sample. The specific surface area (BET) of the magnesium oxide equals to 24 m^2/g which corresponds to a good MgO reactivity (Jin and Al-Tabbaa, 2013). M-S-H samples were prepared in PE-HD containers using Milli-Q water (ultra-pure water) and a water/solid (W/S) ratio of 45 to ensure a homogeneous suspension and sufficient solution for analysis. All sample handling was done in a glove box under N_2 to avoid CO_2 contamination. The samples equilibrated at 20°C were placed on a horizontal shaker, the samples at 50°C and 70°C were manually shaken once a week.

Table 2: Starting materials for the different Mg/Si of M-S-H samples (g=grams; Mg/Si = molar magnesium to silica ratio).

Mg/Si	0.7	0.8	0.9	1	1.1	1.2	1.3	1.4	1.5	1.6
MgO [g]	1.60	1.75	1.88	2.01	2.12	2.23	2.33	2.42	2.51	2.59
SiO_2 [g]	3.40	3.25	3.12	2.99	2.88	2.77	2.67	2.58	2.49	2.41

For comparison, also crystalline magnesium silicate hydrates such as synthetic talc (Mg/Si=0.75) (Alfa Aesar), natural antigorite (Mg/Si=1.5) (from the location Geisspfad, Binntal) and natural sepiolite (Mg/Si=0.67) (from the location Kaffa, Crimea) were studied. Small amounts of the synthetic talc and natural antigorite samples were ground, mixed with Milli-Q-water at a W/S of 20 and after an equilibration time of ~1 year, their solution composition was analyzed to determine their solubility at 20°C.

2.1.2. C-S-H in batch and magnesium additions; co-precipitated samples in batch experiments

Calcium oxide and silica fume (SiO_2, Aerosil 200, 0.9 wt.% HCl) have been chosen as starting materials for the C-S-H synthesis. CaO has been obtained by burning calcium carbonate ($CaCO_3$, Merck, pro analysis) for 12 hours at 1000 °C as detailed in (L'Hôpital et al., 2015). 4.27 g of CaO and 5.73 g of SiO_2 were mixed with 225 ml of Milli-Q water in 250 ml PE-HD containers to obtain C-S-H with a Ca/Si of 0.8. The containers were sealed and stored at 20°C on a horizontal shaker (100 rpm) for one month. After one

month, the C-S-H suspensions were separated by vacuum filtration using nylon filters (0.45 µm) in a glove box under nitrogen. Directly following the filtration, the wet C-S-H (2 g of C-S-H with additional pure water of approx. 20 ml) was put in 100 ml PE-HD containers.

$MgCl_2$ (Anhydrous ≥ 98 %, Sigma Aldrich) was dissolved in Milli-Q water and added to the C-S-H in the containers, resulting a water/solid (W/S) ratio equal to 54 and Mg/Si ratios of 0.05, 0.11, 0.15, 0.26, 0.87 and 1.34. MgO (Merk, pro analysis, containing 0.18 ± 0.02 wt.% Na_2O) was added directly to C-S-H, as the solubility of MgO in water is low, and 90 ml Milli-Q water in the containers to reach W/S equal to 54 and Mg/Si of 0.04, 0.23, 0.59 and 0.86 (details given in Table 3).

After the addition of MgO or $MgCl_2$ to C-S-H, the samples were again equilibrated for 3 and 12 months at 20 and 50°C. Also, pure C-S-H suspension samples have been prepared and analyzed. The suspensions equilibrated at 20°C were placed on a horizontal shaker (100 rpm) while the suspensions at 50°C were shaken weekly by hand. The analysis of the solids in this part is focused on three samples of each set at 20°C after 12 months only as detailed in bold in Table 3.

Table 3: Starting materials for the theoretical 2 g of wet C-S-H with Ca/Si=0.80 and the different additions of $MgCl_2$ to reach the theoretical Mg/Si of 0.05; 0.26; 0.87; 1.34 and the different additions of MgO to reach the theoretical Mg/Si of 0.04; 0.23; 0.59; 0.86 (g = grams; Mg/Si = molar ratio).

		g				mmol/l			mmol		
	Mg/Si	Sample name	CaO[a]	SiO_2[a]	$MgCl_2$[b]	Ca[a]	Si[a]	Mg[b]	Ca[a]	Si[a]	Mg[b]
$MgCl_2$	**0.05**	**0.05$MgCl_2$**	0.85	1.15	0.09	138.5	173.3	9.0	15.2	19.1	1.0
	0.26	**0.26$MgCl_2$**	0.85	1.15	0.48	138.5	173.3	45.4	15.2	19.1	5.0
	0.87	**0.87$MgCl_2$**	0.85	1.15	1.57	138.5	173.3	149.7	15.2	19.1	16.5
	1.34	1.34$MgCl_2$	0.85	1.15	2.42	138.5	173.3	231.5	15.2	19.1	25.5
					MgO[b]						
MgO	**0.04**	**0.04MgO**	0.85	1.15	0.03	138.5	173.3	6.8	15.2	19.1	0.7
	0.23	**0.23MgO**	0.85	1.15	0.18	138.5	173.3	40.6	15.2	19.1	4.5
	0.59	**0.59MgO**	0.85	1.15	0.45	138.5	173.3	101.5	15.2	19.1	11.2
	0.86	0.86MgO	0.85	1.15	1.38	138.5	173.3	149.0	15.2	19.1	16.4

Samples in bold=samples fully analysed

[a] theoretical values

[b] measured values.

The MgO-CaO-SiO_2-H_2O co-precipitated samples were obtained by mixing MgO, CaO and SiO_2 directly with ultrapure water as detailed in (Lothenbach et al., 2015) to obtain M-S-H or C-S-H with small amounts of calcium or magnesium. The synthesized products are summarized in Table 4. The syntheses were carried out to obtain ~ 5 g of solid and the water-to-solid (W/S) ratio was set to 45.

Pure C-S-H (Ca/Si=0.8) and pure M-S-H (Mg/Si=0.8) were analyzed for comparison. In addition, powdered mixtures labelled Mix-0.05, Mix-0.10, Mix-0.70 and Mix-0.75 were prepared by mechanical mixing in a grinder of pure C-S-H and M-S-H with the same molar ratios as the co-precipitated samples.

Table 4: Labelling and initial composition of mixes of the plain M-S-H and C-S-H samples and of the co-precipitated samples. Bold co-precipitated samples correspond to the fully analyzed samples while the Co-0.40 and the Co-0.50 samples are presented to supplement the analytical data of the aqueous phase.

M-S-H	0.8							
Coprecipitated samples		**Co-0.05**	**Co-0.10**	Co-0.40	Co-0.50	**Co-0.70**	**Co-0.75**	
C-S-H								0.8
Total Mg/Si	0.8	**0.75**	**0.70**	0.40	0.30	**0.10**	**0.05**	
Total Ca/Si		**0.05**	**0.10**	0.40	0.50	**0.70**	**0.75**	0.80
Total (Mg+Ca)/Si	0.80	**0.80**	**0.80**	0.80	0.80	**0.80**	**0.80**	0.80

2.1.3. M-S-H in presence of alkalis in batch experiments

To study the alkali uptake, $NaNO_3$, NaOH, KOH and LiOH solutions replaced Milli-Q water for specific M-S-H syntheses: 0.8, 1.0 and 1.2.

M-S-H phases with Mg/Si=0.8 were equilibrated in sodium nitrate or sodium hydroxide solutions with a concentration between 10 and 500 mmol/l. Sodium nitrate (AnalaR Normapure, VWR chemical) was dissolved in Milli-Q while sodium hydroxide solution (1 molar, titrisol, Merck) was diluted to reach the different concentrations wanted. Additional M-S-H 1.2 samples were synthetized in the presence of sodium nitrate, M-S-H 0.8 & 1.0 in the presence of lithium hydroxide and potassium hydroxide.

2.1.4. M-A-S-H in batch experiments

Metakaolin ($Al_2O_3.2SiO_2$, ARGICAL-M 1200S, purity 93.8%, surface area of 19 m^2/g) was added to SiO_2 and MgO to synthesize the first series of M-A-S-H samples. The XRD pattern of the metakaolin is shown in Figure 3, and traces of anatase, quartz, muscovite and kaolinite were found. The starting mixes of the so-called M-A-S-H samples were prepared with Mg/Si=1.1 and Mg/Si=1.7 and the Al/Si=0.05, 0.10, 0.15 and 0.20.

In a second series, sodium aluminate ($NaAlO_2$, anhydrous, technical from Sigma Aldrich, which contains 6.9 wt.% of water as quantified by TGA) was used to synthetize M-A-S-H N. Additional nitric acid (HNO_3, Merck, suprapur, 65%) was used to decrease the pH and sodium nitrate (AnalaR Normapure, VWR chemical) to regulate the sodium

concentration to 100 mmol/l in the samples. Two Mg/Si were studied: 0.8 and 1.2 and the studied Al/Si in the mixes was set at 0.10 and 0.20 as detailed in Table 5.

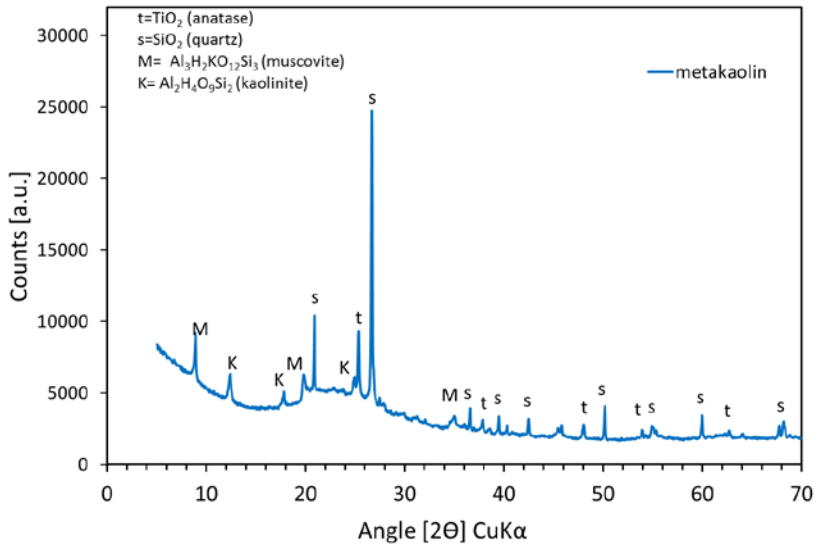

Figure 3 : XRD pattern of the metakaolin ARGICAL-M 1200S.

Table 5: Starting materials used in the M-A-S-H=MgO + SiO_2 + metakaolin, M-A-S-H N= MgO + SiO_2 +$NaAlO_2$ + $NaNO_3$ + HNO_3.

theoretical	M-A-S-H								M-A-S-H N			
Mg/Si	1.1				1.7				0.8		1.2	
Al/Si	0.05	0.1	0.15	0.2	0.05	0.1	0.15	0.2	0.1	0.2	0.1	0.2
MgO (g)	2.09	2.04	1.99	1.95	2.59	2.54	2.49	2.45				
SiO_2 (g)	2.65	2.46	2.27	2.09	2.20	2.04	1.89	1.75				
$Al_2O_3.2SiO_2$ (g)	0.26	0.50	0.74	0.96	0.21	0.42	0.62	0.81				
MgO (g)									1.60	1.48	2.07	1.94
SiO_2 (g)									2.99	2.76	2.58	2.41
$NaAlO_2$ (g)									0.44	0.81	0.38	0.70
$NaNO_3$ (g)									1.56	1.26	1.61	1.35
HNO_3 (mol/l)									0.02	0.035	0.028	0.048

2.1.5. Filtrations and preparation of the solid samples

After different curing times (1, 3, 6 months, 1, 2 or 3.3 years) the suspensions were separated by filtration using pressure (4-5 bars N_2) filtration and nylon filters (0.45µm). The solids were washed with a 50/50 (volume) water-ethanol mix and a second time with ethanol (94wt% alcohol) to eliminate dissolved ions and to prevent the precipitation of salts during drying which could perturb the analyses. The samples were dried by freezing with liquid nitrogen (around 20 min at -195°C) and kept at -40°C under 0.280 mbar pressure (vacuum) for further 7 days in a freeze dryer. The

freeze drying minimizes carbonation as it removes free water efficiently. The solid characterizations were performed after further equilibration in N_2 filled desiccators over saturated $CaCl_2$ solution for a period of 14 days or longer to ensure ~30% RH in all the samples. After drying the samples were gently ground by hand.

2.1.6. Cell experiments

After drying of pure M-S-H (Mg/Si=0.8) and pure C-S-H (Ca/Si=0.8), the samples were gently ground by hand and the M-S-H and C-S-H powders were compacted and shaped into disks (32mm by diameter, 2.0 ± 0.2 cm by height, and 2.2 g and 1.6g for C-S-H and M-S-H respectively) using a mechanical press (Specac). Comparing to the apparent density measured by helium pycnometry (2.3 and 2 for C-S-H and M-S-H respectively) the porosity was evaluated to 50-60%. The applied force depended on the materials (10kN for C-S-H and 5kN for M-S-H). C-S-H powder was easy to compact, while preparing M-S-H disks was very challenging. The disks were mounted and fixed together using a resin (a mix 50:50 mix of Resoltech 3037 and 3030) in the cell as shown in Figure 4. Finally, the reservoirs on each side were filled with 125 mL of solution at equilibrium with the respective material which has been collected during the filtration of the synthesized C-S-H and M-S-H.

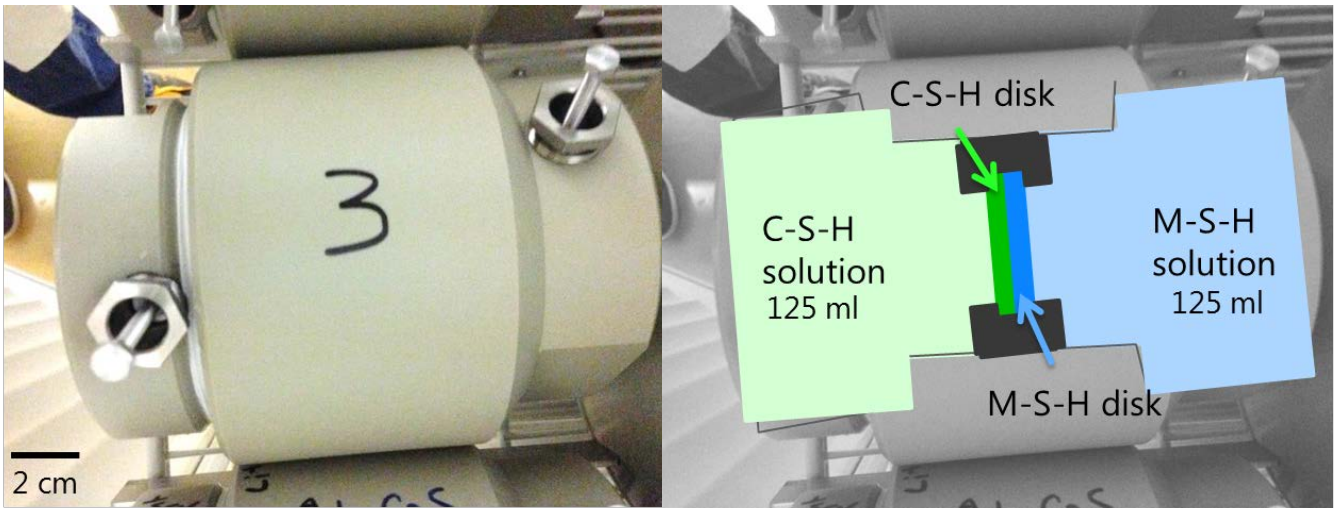

Figure 4: Cell experiment, picture and schematic sketches.

2.2. Main analytical techniques

The main analytical techniques described in the following part were used to get the chemical compositions and to characterize the hydrated magnesium silicate phases of the batch experiments in each chapter.

The composition of the liquid phase was analyzed by ion chromatography (IC) immediately after filtration. The dissolved concentrations of Mg, Si, Na, and Cl in undiluted solutions or in solutions diluted by factors 10 were quantified using a Dionex DP serie ICS-3000 ion chromatography system. Independent measurements of solutions with known compositions indicated a measurement error ≤ 10%. All concentrations were determined in duplicates and hence, the mean values are given. The pH value measured in filtrated solution can be lower than the pH values measured directly in the suspension as charge balancing anions, such as hydroxides, can be removed during the filtration (Plusquellec, 2014; Nied et al., 2016). Therefore, the pH (±0.1) was measured in the supernatant at ambient temperature (23±2°C) in an aliquot of the unfiltered suspension where the solid particles had been allowed to settle. The measured pH values were corrected to 20, 50 or 70°C. No significant changes in the aqueous phase composition is expected within the 30 minutes used to cool down the solutions from 50 and 70°C to ambient temperature, as M-S-H precipitation occurs only very slowly and as no significant differences in the measured concentrations between diluted and not-diluted solutions were observed. Additionally in high alkali hydroxide concentration systems (chapter 5.2), in order to minimize the alkali error, fresh alkali hydroxide solutions with known conductivity were measured (10 mmol/l to 500 mmol/l).

Thermogravimetric analyses (TGA) were carried out on ground powder (~30 mg) with a Mettler Toledo TGA/SDTA 8513 instrument using a heating rate of 20°C/min from 30 to 980 °C. The amount of $Mg(OH)_2$ (brucite) was quantified from the water weight loss at around 400-420°C using the tangential method (Lothenbach et al., 2016) and calculated according to the equation (1):

$$wt.\,\%\,brucite_{dry} = \frac{water\ loss\ (brucite)}{100 - water\ loss_{(30-550°C)}} \times \frac{M_{brucite}}{M_{H2O}} \times 100 \qquad (1)$$

where wt. % brucite $_{dry}$ corresponds to the wt.% of brucite for 100g of dry mass, the water loss is expressed in wt. %, the M $_{brucite}$ is taken equal to 58.32 g/mol, while the M_{H2O} is taken equal to 18.02 g/mol.

The relative error on the brucite content is ± 5-10% (Deschner et al., 2012; Lothenbach et al., 2016). The total water bound in M-S-H was quantified from the total water loss between 30 and 980°C and the water associated to hydroxyl groups in M-S-H was quantified from the water loss between 270 and 800°C. Both results were normalized to the dry weight and corrected for the amount of brucite; the results are given per silicon.

X-ray diffraction (XRD) data were collected using a PANalytical X'Pert Pro MPD diffractometer equipped with a rotating sample stage in a θ-2θ configuration applying CuKα radiation (λ=1.54 Å) at 45 mV voltage and 40 mA intensity with a fixed divergence slit size and an anti-scattering slit on the incident beam of 0.5° and 1°. The samples were scanned between 5° and 75° 2θ with a X'Celerator detector.

Attenuated total reflectance (ATR) Fourier Transformation-Infrared (FT-IR) spectra were recorded in the mid-region on a Bruker Tensor 27 FT-IR spectrometer between 600 and 4000 cm^{-1} with a resolution of 4 cm^{-1} by transmittance on small amounts of powder. Spectra were background corrected and scaled to the maximum of Si-O bonds to ease comparison. In chapter 3.2, to separate the wavenumbers corresponding to the different Si bounds from 600 to 1200 cm^{-1}, the second derivative of FT-IR spectra was used to identify the different bands as previously reported by (Gionis et al., 2006). "Hydrated" silica fume (silica fume stored in water and freeze dried under the same conditions as M-S-H), synthetic talc, natural antigorite and sepiolite as detailed above were used as references.

The ^{29}Si MAS NMR experiments were recorded on a Bruker Avance III NMR spectrometer using a 7 mm CP/MAS probe at 79.5 MHz applying the following parameters for the single pulse experiments: 4500 Hz sample rotation rate, minimum of 3072 scans, 30° ^{29}Si pulse of 2.5 µs, 20 s relaxation delays, RF field strength of 33.3 kHz during SPINAL64 proton decoupling.

The ^{29}Si NMR chemical shifts of the spectra were referenced to the most intense resonance at -2.3 ppm of an external sample of an octamethylsilsesquioxane (Aldrich No. 52,683-5) which was referenced to tetramethylsilane (TMS, $\delta^{29}Si$ = 0.0 ppm). The observed ^{29}Si resonances were analyzed using the Q^n classification, where a Si tetrahedron is connected to n Si tetrahedra with n varying from 0 to 4. The quantification was performed by nonlinear least-square fits using the software ''DMFIT'' developed by (Massiot et al., 2002) with a linear combination of Gaussian and Lorentzian functions where η was fixed ($\eta G + (1-\eta)L$ with G=Gaussian, L=Lorentzian). The Q^1 and Q^2 environments were deconvoluted using mainly Lorentzian ($\eta = 0 - 0.1$) while the Q^3 environment was deconvoluted with Gaussian ($\eta = 0.8 - 1.0$).

Silica fume was quantified taking into account the shift at -100.9 ppm (silanol from the surface of the amorphous silica (d'Espinose de Lacaillerie et al., 1995; Nied et al., 2016)) and the Q^4 resonance at -110 ppm. However, the relaxation time T_1 of silica fume can be very long and it could be that the amount of silica fume was slightly underestimated.

The ^{27}Al NMR measurements were recorded with a 2.5 mm CP/MAS probe on the same equipment. The ^{27}Al MAS NMR single pulse experiments were register at 104.26 MHz applying the following parameters: 20 000 Hz sample rotation rate, between 2000 and 4000 scans depending on the content of aluminum in the samples, π/12 pulses of 1.5 μs, 0.5 s relaxation delays, without ^{1}H decoupling. The chemical shifts of the ^{27}Al MAS NMR spectra were referenced to an external sample of Al(acac)3.

After quantification of brucite by TGA, and amorphous silica by ^{29}Si MAS NMR, the experimental molar Mg/Si ratios in M-S-H were calculated by mass balance including the IC results following the equation (2):

$$\frac{\mathrm{Mg}}{\mathrm{Si}} = \frac{n_{init}(MgO) - n_{tga}(brucite) - n_{IC}([Mg])}{n_{init}(SiO_2) - n_{nmr}(unreact.\ silica) - n_{IC}([Si])} \qquad (2)$$

where n_{init} (MgO) and n_{init} (SiO_2) denotes to the moles of magnesium oxide and silica fume initially added, n_{tga} (brucite) to the moles of magnesium hydroxide in the sample quantified by thermogravimetric analysis, n_{nmr} (unreact. silica) to the moles of amorphous silica in the sample quantified by ^{29}Si MAS NMR, n_{IC} ([Mg]) and n_{IC} ([Si]) to the moles of dissolved magnesium and dissolved silicon in solution quantified by ion chromatography.

For those samples not analyzed by ^{29}Si MAS NMR, the absence of unreacted silica in the samples was assessed by the nonexistence of FT-IR bands at 1090 and 1035 cm^{-1} characteristic for amorphous silica and based on the low silicon concentration (<0.3 mmol/l) in the aqueous solution.

The zeta potential measurements were carried out directly in suspension before filtration with 20 g of solid per liter. The samples were stirred in a beaker at 500 rpm during 10 minutes to reach a stable value before the measurement. During the measurements, they were stirred at 400 rpm and each measurement was repeated 10 times. Zeta potential data were recorded with a ZetaProbe from Colloidal Dynamics Inc., which is based on the frequency-dependent electroacoustic effect. Shortly, an alternating voltage is applied to the suspension which causes charged particles to move

back and forth at a mobility that depends on their zeta potential. The software calculates the zeta potential from the frequency-dependent mobility using the O'Brien equation (James et al., 1992). Finally, the values obtained were background corrected with a measurement of the filtrated aqueous phase. The zeta potential is measured close to the interface between the stern layer and the diffusive layer (Kaya and Yukselen, 2005; Plusquellec and Nonat, 2016) and give the effective charge of the particle in suspension.

Cation exchange capacity (CEC) in the samples was measured on 100 mg of powder. The cations on the surface and/or from the interlayer were exchanged with cobalt hexamine trichloride during 30 min at room temperature (Jenni et al., 2014) using a solution/solid mass ratio of 30. The suspensions were filtered and the concentrations of Na, K, Ca, Mg, Al in solution were determined by ion chromatography (IC) as detailed above. The sum of measured cations was compared to the total CEC which was obtained from the difference in the cobalt hexamine concentration from the original solution and from the leachate. Such concentrations were determined by colorimetry (absorption band at 473 nm) using a UNI-CAM UV visible spectrometer. The good agreement between the total CEC and the CEC calculated from the measured cations showed that dissolution of solids was negligible.

2.3. Details of the additional methods used in each chapter

2.3.1. Chapter 3.2: saturation indices and thermodynamic data methods

Thermodynamic modelling of the experiments was carried out using the Gibbs free energy minimization program GEMS (Kulik et al., 2013a). GEMS is a broad-purpose geochemical modelling code which computes equilibrium phase assemblage and speciation in a complex chemical system from its total bulk elemental composition. From the measured concentrations in solution and the pH values, the activities of dissolved species were calculated using the geochemical software GEMS v3.3 (Kulik et al., 2013b) together with the PSI database (Thoenen et al., 2014).

The activity of a species i, {i}, is calculated from the measured concentrations considering the formation of different aqueous complexes; $\{i\} = \gamma_i \cdot m_i$, where γ_i is the activity coefficient and m_i is the concentration in mol/kg H_2O. The activity coefficients of the aqueous species γ_i were computed with the built-in extended Debye-Hückel equation with common ion-size parameter a_i = 3.67 Å for KOH solutions and common third parameter b_y according to the equation (3):

$$\log \gamma_i = \frac{-A_y z_i^2 \sqrt{I}}{1 + B_y a_i \sqrt{I}} + b_y I \qquad (3)$$

where z_i denotes the charge of species *i*, I the effective molal ionic strength, b_y is a semi-empirical parameter (~0.123 for KOH electrolyte at 25°C), and A_y and B_y are P, T-dependent coefficients. This activity correction is applicable up to ~ 1 M ionic strength (Merkel and Planer-Friedrich, 2008).

The saturation indices (SI) of the different solids were calculated from the ion activity product (IAP) based on the measured concentrations in the solution according to the equation (4):

$$SI = \log \frac{\mathrm{IAP}}{\mathrm{Kso}} \qquad (4)$$

where IAP is the ion activity product and Kso the theoretical solubility product of the solid.

A saturation index (SI) inferior to 0 indicates that the solution is undersaturated and the respective solid should not form or will dissolve if present, SI superior to 0 means that the solution is oversaturated and the formation of the respective solid is possible. In our case, knowledge of the SI of the solution with respect to brucite or amorphous silica was used to follow their kinetics of dissolution during the formation of M-S-H. The solubility product of amorphous silica used equals to $10^{-2.90}$ for the reaction of $SiO_{2,solid}$ to $Si(OH)_{4,aq}$ corresponding to the measured silicon concentrations at 20°C. Similarly, solubility products of $10^{-2.63}$ and $10^{-2.57}$ were calculated for 50 and 70°C from the experimental data.

The solubility products of M-S-H were calculated with respect to two end members with compositions of $M_{0.78}S_1H_{1.48}$ (M=MgO, S=SiO_2, H=H_2O) and $M_{1.30}S_1H_{1.80}$. The composition from $0.78 < Mg/Si < 1.30$ were obtained by assuming an ideal solid solution between the two end members with Mg/Si=0.78 and Mg/Si=1.30 as suggested by (Nied et al., 2016).

From the solubility products calculated at different temperatures, the Gibbs free energy of reaction, $\Delta_r G°$, and the Gibbs free energy of formation, $\Delta_f G°$, at 25°C can be obtained according to equations (5) and (6):

$$\Delta_r G° = -\mathrm{RT}\ln K = \sum_i \nu_i \Delta_f G°_T \qquad (5)$$

$$\Delta_a G°_T = \Delta_f G°_{T_0} - S°_{T_0}(T - T_0) - \int_{T_0}^{T}\int_{T_0}^{T} \frac{C°_p}{T} dT dT \cong \Delta_f G°_{T_0} - S°_{T_0}(T - T_0) -$$

$$a\left(T ln \frac{T}{T_0} - T - T_0\right) - b\frac{(T-T_0)^2}{2} - c\frac{(T-T_0)^2}{2T\cdot {T_0}^2} - d\frac{2\left(\sqrt{T}-\sqrt{T_0}\right)^2}{\sqrt{T_0}} \qquad (6)$$

where ν_i correspond to the stoichiometric reaction coefficients, R = 8.31451 J/mol/K and T is the temperature in K. The apparent Gibbs free energy of formation, $\Delta_a G°_T$, refers to the free energies of the elements at 298 K. A more detailed description of the derivation of the dependence of the Gibbs free energy on temperature is given in (Anderson and Crerar, 1993; Kulik, 2002). In the present paper the empirical coefficients a, b, c, and d of the heat capacity, $C°_p$ ($C^0_p = a + bT + cT^{-2} + dT^{-1/2}$) were calculated from the coefficients of talc, chrysotile and antigorite given in (Holland and Powell, 1998) and adjusted for the water content of the M-S-H phases. The entropy, S°, was calculated in the same way from talc, chrysotile and antigorite and water.

2.3.2. Chapter 3.3: additional methods for M-S-H characterization

In addition to typical XRD measurements, X-ray Pair Distribution Function (PDF) analyses were performed. This analysis focusses on the entire signals including Bragg peaks and diffuse scattering. PDF represents the distribution of interatomic distances in a compound, regardless of its crystalline state, determined experimentally by a Fourier transform of the powder pattern. PDF is thus an efficient technique for studying of short coherence lengths materials such as cement (Meral et al., 2011) or geopolymers (White et al., 2013). The reduced PDF, G(r), was obtained by taking a sine Fourier transform of the measured total scattering function S(Q), as shown in equation (7), where Q is the momentum transfer given in equation (8) with θ as the scattering angle and λ as the wavelength of the incident radiation (Egami and Billinge, 2003; White et al., 2013).

$$G(r) = \frac{2}{\pi}\int_{Q_{min}}^{Q_{max}} Q[S(Q) - 1]\sin(Q_r)\, dQ \qquad (7)$$

$$Q = \frac{4\pi sin\theta}{\lambda} \qquad (8)$$

It is important to obtain diffraction data with a high momentum transfer (Q) in order to maximize the resolution after the Fourier transform. We, therefore, used an X'Celerator Panalytical diffractometer equipped with a Mo source ($\lambda_{k_\alpha} = 0.70926$Å). The powder diffraction pattern was scanned over the 6.004-153.932° angular range with a step size of 0.0083°. The total acquisition was the average of 2 runs recorded over 24 hours. The PDF and standard corrections (Egami and Billinge, 2003) were calculated with PDFGetX2 (Qiu et al., 2004). The density number of atoms ρ_0 used to calculate the PDF was 0.10 atoms Å^{-3}. The use of a finite value of Q (17Å) for the PDF analysis led to the addition of spurious oscillations to G(r) depending on the distance r. These oscillations were smoothed by the use of a Lorch (1969) function. On the other hand, calculated PDF from a given structure was obtained with PDFGui (Farrow et al., 2007). Due to limited Q resolution, a value of 0.05 Gaussian dampening (Q_{damp}) envelope was introduced in the refinement.

Nitrogen sorption isotherms were measured at 77.35 K using a Coulter SA3100 equipment. The specific surface area (SSA) was obtained by using Brunauer-Emmett-Teller (BET) equation (Brunauer et al., 1938), in the pressure range from 0.01 to 0.2 P/P_0. The t-plot method (Lippens and De Boer, 1965) is used to find the non-micro-pore surface area (so-called "external area") subtracting the micro-pore surface area. The calculation of those SSA and the micropore volume were made with the Beckman Coulter Sorption Analysis software. The IUPAC classification (Everett, 1972; Sing et al., 1985) gave the definition: micro-pore ≤ 2 nm ≤ meso-pores ≤ 50 nm ≤ macro-pores.

The measurements were performed on the samples kept in N_2-desiccators equilibrated at 30% relative humidity. Just before analysis the samples were freeze dried for 2 hours to remove any adsorbed water molecules. The apparent density was measured by helium pycnometry with a PMI Hg-porosimeter.

Additionally to the ^{29}Si MAS NMR spectroscopy, ^{1}H-^{29}Si cross polarization MAS NMR spectra were recorded on the same equipment applying the following parameters: 4500 Hz sample rotation rate; minimum of 1536 scans, 3 s relaxation delays, RF field strengths of 33 kHz during the polarisation transfer (ramp from 100-50%) with contact times varying from 0.5 to 5 ms using the above mentioned proton decoupling conditions.

The water adsorption and desorption was determined with a VTI-SA Dynamic Vapour Sorption Apparatus (DVS) manufactured by TA Inc. The DVS device allows continuous monitoring of the mass loss of samples exposed to changing relative humidity (RH) by means of a high-precision micro balance with an accuracy of 10 μg. The RH in the chamber was varied from 35 to 50, 70, 80, 85, 90, 92, 94, 90, 80, 70, 50, 35 by a controlled flow of a mixture of dry gas (N_2) and wet gas (saturated H_2O vapor) with accuracy ±1%; the RH was measured and adjusted based on the readings of a dew point analyzer. The ad- and desorption isotherms were determined at 20.0±0.2°C; as controlled by means of Peltier elements. Approximately 15 mg of M-S-H, pre-dried at a relative humidity of 35%, was placed in a sample holder in the measuring chamber of the DVS. Changes in mass were monitored continuously and logged at 1-min intervals at different RH steps. Equilibrium criterion to be reached before proceeding to each next RH step was set as 0.001% of a sample mass in 5 min. At the end of the sequence of RH steps, the sample was dried in the DVS to constant mass at 105°C and 0% RH in order to obtain the reference mass for water content and at 980 °C in the TGA to obtain the ignited mass. The water content is expressed relative to its ignited weight (i.e. the mass after heating to 980°C and not the mass after drying at 105°C and 0% RH, which is slightly different).

The total water bound in M-S-H was quantified from the total water loss between 30 and 980°C and the water associated with hydroxyl groups in M-S-H was quantified from the water loss between 250 and 800°C. Both results were normalized to the dry weight and corrected for the amount of brucite; the results are given per silica.

^{1}H NMR relaxometry measurements were performed on a Bruker Minispec NMR spectrometer operating at 7.5 MHz. The 90° pulse length was 2.9 μs. The Carr–Purcell–Meiboom–Gill CPMG (spin) echo and the quadrature (solid) echo were measured. The quadrature echo signals were recorded as a function of pulse gap in the range τ = 15–45 μs. ^{1}H NMR relaxometry probes the protons in hydroxyl groups, so-called *solid* or

structural water, and the protons in *mobile* water and allows distinguishing different sites for water as a function of the mobility of the protons. The samples previously conditioned at different RH were measured while sealed in miniature PCTFE containers. Mass measurements before and after the NMR tests were carried out to confirm no mass lost from the samples.

The Carr-Purcell-Meiboom-Gill (CPMG) pulse sequence, gives access to the transverse relaxation time T_2 of the proton, which is related to interactions of the proton with solid surfaces, with faster relaxation time for higher interactions; this enables estimating the pore sizes and thus can be used to characterize the pore structure and physically bound water content of hydrates, e.g. calcium silicate hydrate (C-S-H) (Valori et al., 2013; Muller et al., 2016). Three types of water confined in microstructure had been described in C-S-H: the interlayer/adsorbed water, gel water, and bulk water (comprising water in interhydrate spaces and bulk water in larger pores). The relation between the transverse relaxation time and the size of the pore can be estimated, e.g., using the fast exchange model of relaxation (9):

$$\frac{1}{T_2} \sim \frac{\lambda S}{V} \qquad (9)$$

where λ is the surface relaxivity, S the surface area and V the pore volume (Halperin et al., 1994).

For C-S-H, short T_2 of approximately 0.1 ms has been assigned to interlayer and/or surface water, a T_2 of 0.3 ms to gel water and T_2 of 1-3 ms to bulk water based on NMR measurements on samples conditioned at different RH (Muller et al., 2016). Similarly, in swelling clays such as montmorillonite, $T_2 \leq 0.05$ ms have been assigned to hydroxyl groups in the clays, while signals at ~ 0.05-0.5 ms have been related to water in the interlayer and/or adsorbed water; the T_2 time varies depending on the interlayer distance. Longer relaxation times have been assigned to water present in interparticle (external) pore space (Fleury et al., 2013).

The CPMG sequence can be deconvoluted into the different exponential components using numerical inversion. The results of the inverse Laplace transformation (ILT), most commonly used for cement hydrates, depends on the α-parameter, which influences the width and hence possibly also separation of the peaks due to different water populations. In any case, applying the ILT requires relatively high signal-to-noise ratio (S/N), usually in excess of 300-400/1; for the lower S/N the algorithm may often result in erroneous deconvoluted data with artificial peaks at low T_2. Typical CPMG recorded for M-S-H (Mg/Si=0.9) equilibrated at 84% relative humidity are shown in Figure 5, and three populations of water can be found the first at

~ 0.05 ms, a 2nd at ~ 0.8 ms and the 3rd above 6 ms. The structure of M-S-H and the distribution of the water in M-S-H are less well known than for C-S-H or clays. Based on the assignments made for clays and C-S-H, the three different populations of water were assigned to sorbed water (interlayer and surface), water in the micropores so called gel water and water in the space between the M-S-H agglomerates, i.e., bulk water. The ILT was used to find the position of the T_2 peaks corresponding to the different populations of water. However, the amounts of different water populations found with the ILT was prone to a high scatter due to the aforementioned lows S/N. Hence, a simple multi-exponential fitting with the constrained number and positions of the T_2 peaks (as revealed by the ILT) was applied here to get the repartition of the amounts of the different types of waters. The multi-exponential fitting was carried out by minimizing the sum of squared errors.

Additionally, the "structural water" corresponding to the hydroxyl group signal can be accessed using the quadrature-echo (QE) pulse sequence. Those were deconvoluted into a Gaussian and an exponential decay part. The exponential fraction was attributed to mobile water. The Gaussian with a very short time constant, of the order of 10 µs, was assigned to the structural water, i.e., to the hydroxyl groups (Valori et al., 2013; Muller et al., 2016). The combination of the QE and CPMG signal is used to describe the different type water in the samples. A good correlation between the results obtained by QE and TGA on the repartition between solid/liquid water indicates a good reliability of the measurements. Similarly, the total liquid water quantified by CPMG needs to be comparable to the one quantified by QE.

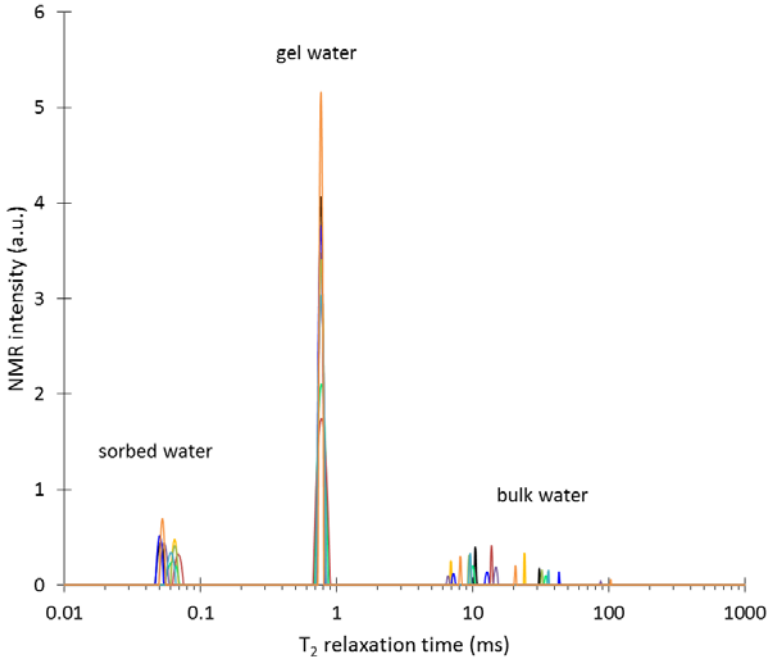

Figure 5: 10 examples of CPMG T_2 results for the M-S-H 0.9 (84 %RH).

2.3.3. Chapters 4.2 and 4.3: additional methods and thermodynamic modelling

2.3.3.1. Methods

The ^{29}Si MAS NMR experiments were recorded and the signals attributed to M-S-H deconvoluted as detailed in 2.2. The deconvolutions of the signals attributed to C-S-H were done following the procedure outlined in (Myers et al., 2015a), with a constant Lorentzian/Gaussian ratio equal to 0.5 and by keeping constant the ratio between bridging and pairing silicate tetrahedra following the Equation (10):

$$\frac{Q^2{}_b + Q^2{}_u}{Q^2{}_p} = 0.5 \qquad (10)$$

where Q^2_b is the bridging silicate tetrahedra with one calcium neighbor in the interlayer, Q^2_u is the bridging tetrahedra with one H^+ neighbor in the interlayer and finally Q^2_p is the pairing tetrahedra. The mean chain length (MCL) of the silicate chains in C-S-H was calculated following the Equation (11):

$$MCL = \frac{2(Q^1 + Q^2{}_b + Q^2{}_u + Q^2{}_p)}{Q^1} \qquad (11)$$

Based on the available M-S-H deconvolutions in literature (Roosz et al., 2015; Walling et al., 2015; Nied et al., 2016), the Q^2/Q^3 ratio was kept between 0.4 (Walling et al., 2015) and 1 (observed in chapter 3.2.).

The Raman spectra, shown in chapter 4.2, were measured with a Bruker Senterra instrument of 5 cm^{-1} spectral resolution, using a 532 nm laser (20 mW) at room temperature and with ×50 objective lens. The spectral acquisition time was 40 s and 5 spectra were accumulated for each sample in the frequency ranges of 110–1560 cm^{-1}.

After quantification of brucite by TGA, and amorphous silica by 29Si MAS NMR, the composition of the solids in chapter 4.2, was calculated by mass balance including the solution composition based on the IC results. The composition of some solids has been also determined directly by dissolving 20 mg of the solid sample in 10 ml of 100 mmol/l hydrochloric acid. This was repeated 3 times and the mean values are given.

The TEM characterizations, from chapter 4.3, were carried out on a JEOL JEM 2100F microscope operating at 200 kV and fitted out with a Bruker XFlash 5030 for EDS analysis. A few milligrams of powder was vigorously mixed with a few milliliters of pure ethanol in a mortar with a pestle for less than one minute. A TEM carbon-covered cupper grid held with tweezers was then dipped just below the ethanol surface to

collect suspended particles on it. The grid was then inserted in the TEM chamber and the vacuum was recovered after about 15 min.

Additionally to the CEC measurements performed in chapter 4.3, the solids were washed after the CEC and dissolved in 100 mmol/l HCl to investigate whether any calcium remained in the M-S-H. The solutions were analyzed by ICP-MS with Agilent triplequad MS (Agilent 8900 QQQ ICP-MS). Sodium and magnesium concentrations have been measured in the "NoGas" mode while the calcium concentration has been measured in the "Helium" mode. It might be that calcium was slightly overestimated due the presence of residual calcium from the exchange.

2.3.3.2. Thermodynamic modelling

The thermodynamic data for aqueous species as well as for brucite and portlandite were taken from the PSI-GEMS thermodynamic database (Thoenen et al., 2014). Solid solution models were used for C-S-H (Kulik, 2011) and M-S-H (chapter 3.2). The amorphous SiO_2 data were taken from (chapter 3.2 but detailed in 2.3.1). The data used are summarized in Table 6. Note that the $M_{0.68}C_{0.1}SH_{1.48}$ and $M_{1.2}C_{0.1}SH_{1.80}$ end-members (detailed below) are not taking into account in the thermodynamic modelling shown chapter 4.2.

In chapter 4.3 only, solubility products were calculated for all the samples of with respect to $M_{0.78}SH_{1.48}$ and $C_{0.80}SH_{1.94}$. Based on the experimental observations, M-S-H phases containing small amounts of calcium were defined. The solubility products of two possible end-members, $M_{0.68}C_{0.1}SH_{1.48}$ and $M_{1.2}C_{0.1}SH_{1.80,}$ were fitted using the measured concentrations and implemented in the solid solution model of M-S-H as detailed in Table 6. The formation of an ideal solid solution between the 4 end members ($M_{0.78}SH_{1.48}$, $M_{1.2}SH_{1.80}$, $M_{0.68}C_{0.1}SH_{1.48}$ and $M_{1.2}C_{0.1}SH_{1.80}$) was assumed.

Table 6: Standard thermodynamic properties in the system MgO-CaO-SiO_2-H_2O at 25 °C and P = 1 atm.

	*	$LogK_{S0}$[a]	$\Delta_fG°$ [kJ/mol]	V° [cm^3/mol]	density [g/cm^3]	Ref.
Brucite	MH	-11.16	−832.23	24.6	2.37	(Thoenen et al., 2014)
Portlandite	CH	-5.2	−897.01	33.1	2.24	(Thoenen et al., 2014)
SiO_2,am	S	-2.9	-849.9	29	2.07	Chapter 3.2 (detailed in 2.3.1)
M-S-H						
Mg/Si = 0.78	$M_{0.78}SH_{1.48}$	-14.59	-1682.2	56	2 [b]	Chapter 3.2
Mg/Si=1.30	$M_{1.30}SH_{1.80}$	-21.44	-2073.5	72	2 [b]	Chapter 3.2
Mg/Si = 0.68 Ca/Si = 0.10	**$M_{0.68}C_{0.1}SH_{1.48}$**	**-14.42**[c]	-1689.7	57	2 [b]	[d]
Mg/Si = 1.20 Ca/Si = 0.10	**$M_{01.20}C_{0.1}SH_{1.80}$**	**-21.57**[c]	-2082.0	73	2 [b]	[d]
C-S-H						
Ca/Si = 0.67	$C_{0.67}SH_{1.67}$	-10.24	-1707.3	56.6	2.25	(Kulik, 2011)
Ca/Si = 1.0	$C_{1.00}SH_{2.00}$	-13.41	-2014.5	63.4	2.4	(Kulik, 2011)
Ca/Si = 1.5	$C_{1.5}SH_{2.50}$	-16.61	-2466	80.6	2.35	(Kulik, 2011)

*cement shorthand notations: C= CaO; H =H_2O; M = MgO; S = SiO_2
[a] all solubility products refer to the solubility with respect to the species Mg^{2+}, Ca^{2+}, SiO_2^0, OH^-, or H_2O
[b] experimental data from chapter 3.3.
[c] values at 20°C
[d] values calculated in chapter 4.3.

2.3.4. Chapter 4.4: SEM/EDS and reactive transport modelling

The scanning electron microscopy (SEM) characterizations performed in chapter 4.4 were carried out on a SEM Hitachi in high vacuum mode under a 15 kV working voltage. The semi-quantification of Mg, Si, Ca, C by energy dispersive spectrometry (EDS) was determined with two Bruker SDD EDS detectors. The working distance used for elementary mappings is 16 mm and the duration of map acquisition was about 25 minutes. Observations were performed on a polished section coated with carbon for chemical analyses. The EDS measurements were calibrated by measuring the Cu. The composition of 300 to 500 points after 3 months and 1000 measurement after 12 months was determined by EDS for the M-S-H and C-S-H disks. Note that initially the M-S-H disk and C-S-H disk are completely free of calcium or magnesium respectively.

The HYTEC reactive transport code (Van der Lee, 1998; Van Der Lee et al., 2003) was used to reproduce the chemical changes and model the interactions between the C-S-H and the M-S-H disks and in the surrounding solutions.

HYTEC takes into account geochemistry and physical parameters variations due to mineralogical changes in the solid. The HYTEC code solves the chemical-transport problem by coupling CHESS chemical equilibrium code with a R2D2 transport module.

The transport equation of a chemical species in water saturated media can be written following (12):

$$\frac{\partial \omega C_i^{sol}}{\partial t} = div\left(D * \overrightarrow{grad}.C_i^{sol}\right) - \frac{\partial \omega C_i^{p}}{\partial t} \qquad (12)$$

where ω is the porosity, C_i^{sol} the mobile fraction in the chemical component C_i, C_i^p the immobile fraction incorporating component C_i (precipitate), and D the effective diffusion coefficient.

In the present case all calculations were performed at thermodynamic equilibrium with the Newton-Raphson iterative method, taking into account: minerals, solutions, aqueous and gaseous species. In the present modelling, the effect of precipitation and dissolution on porosity and the effect of diffusion coefficient were not used for the sake of simplicity.

A one-dimension system was used for the present simulation. The reservoirs, the C-S-H and the M-S-H disks were represented by successive rectangles. The volume of each zone was representative of the experimental conditions. A zero flux condition was imposed on the right and the left border. The mesh-size was equal to 20 µm in the disks and a progressive meshing was imposed in the reservoir (between 100 and 500 µm). The modelling aimed rather at assessing whether the formation of Mg-phases was possible in the C-S-H disk and not at reproducing perfectly the extension of the disturbance front, only the places of the chemical changes were of interest. Thus, the transport properties of the disks were of minor interest and an effective diffusion coefficient of 2.10^{-11} m^2/s was assumed for both the C-S-H and M-S-H disks.

The thermodynamic data used for modelling are given in Table 7. The equilibrium constants were recalculated to the master species used in CHESS i.e. SiO_2, Mg^{2+}, Ca^{2+}, H_2O, and H^+. As the available solid-solution models for C-S-H (Kulik, 2011), M-S-H (chapter 3.2) and M-(C)-S-H (chapter 4.3) cannot be directly implemented in CHESS, 4 different C-S-H phases (Ca/Si=0.67, 0.80, 1.00 and 1.50) and 5 M-S-H phases (without calcium: Mg/Si=0.78, 0.83, 1.00 and 1.30; with calcium: Mg/Si=0.78 and Ca/Si=0.05) were defined instead and introduced in the database. The use of several solubility products instead of a continuous solid solution allows reproducing the general trends of the solid and the liquid phase compositions, although stepwise instead of continues changes occur (Kulik, 2011; Lothenbach et al., 2015; Nied et al., 2016; Walker et al., 2016).

Table 7: Standard thermodynamic properties, singles phases adapted from Table 6, at 25 °C.

			Log Kf	Réf.
Brucite		$Mg^{2+} + 2H_2O \rightarrow Mg(OH)_2 + 2H^+$	-17.12	(Hummel et al., 2002)
M-S-H	Mg/Si = 0.78	$0.78Mg^{2+} + SiO_2 + 2.26\ H_2O \rightarrow (MgO)_{0.78}.SiO_2.(H_2O)_{1.48} + 1.56H^+$	-7.25	Chapter 3.2
M-S-H	Mg/Si = 0.83[a]	$0.83Mg^{2+} + SiO_2 + 2.33\ H_2O \rightarrow (MgO)_{0.83}.SiO_2.(H_2O)_{1.50} + 1.66H^+$	-7.90	Adp. Chapter 3.2
M-S-H	Mg/Si = 1.00[a]	$Mg^{2+} + SiO_2 + 2.60\ H_2O \rightarrow MgO.SiO_2.(H_2O)_{1.60} + 2H^+$	-10.43	Adp. Chapter 3.2
M-S-H	Mg/Si = 1.30	$1.3Mg^{2+} + SiO_2 + 3.1\ H_2O \rightarrow (MgO)_{1.30}.SiO_2.(H_2O)_{1.8} + 2.6H^+$	-14.96	Chapter 3.2
M-(C)-S-H	Mg/Si = 0.78 Ca/Si = 0.05[b]	$0.78Mg^{2+} + 0.05Ca^{2+} + SiO_2 + 2.33\ H_2O \rightarrow (MgO)_{0.78}(CaO)_{0.05}.SiO_2.(H_2O)_{1.5} + 1.66H^+$	-7.92	Adp. Chapter 3.2 and Chapter 4.3
C-S-H	Ca/Si = 0.67[c]	$0.67Ca^{2+} + SiO_2 + 2.34\ H_2O \rightarrow (CaO)_{0.67}.SiO_2.(H_2O)_{1.67} + 1.34H^+$	-8.29	Adp.(Kulik, 2011)
C-S-H	Ca/Si = 0.80[c]	$0.8Ca^{2+} + SiO_2 + 2.74\ H_2O \rightarrow (CaO)_{0.8}.SiO_2.(H_2O)_{1.94} + 1.6H^+$	-10.60	Adp.(Kulik, 2011)
C-S-H	Ca/Si = 1.00	$Ca^{2+} + SiO_2 + 3\ H_2O \rightarrow (CaO).SiO_2.(H_2O)_2 + 2H^+$	-12.15	(Kulik, 2011)
C-S-H	Ca/Si = 1.50	$1.5Ca^{2+} + SiO_2 + 4\ H_2O \rightarrow (CaO)_{1.5}.SiO_2.(H_2O)_{2.5} + 3H^+$	-25.39	(Kulik, 2011)
SiO_2	amorphous	$SiO_2\ (aq) \rightarrow SiO_2\ (am)$	2.71	(Hummel et al., 2002)

[a] single phases adapted from chapter 3.2

[b] single phase adapted from chapter 3.2: the Ca/Si has been set lower than the end-members proposed in chapter 4.3 as Ca/Si of 0.10 has never been observed experimentally nor in the modelling

[c] single phase adapted from (Kulik, 2011)

2.3.5. Chapter 5.3: saturation indices of M-A-S-H samples

The thermodynamic data for aqueous species as well as for brucite and portlandite were taken from the PSI-GEMS thermodynamic database (Thoenen et al., 2014). The data for the M-S-H solid solution and for amorphous SiO_2 data were taken from chapter 3.2, for microcrystalline aluminum hydroxide from (Lothenbach et al., 2012b), for hydrotalcite from (Myers et al., 2015b) and for Mg-saponite from (Vidal et al., 2012) as summarized in Table 8.

The saturation indices (SI) of the different solids as, M-S-H solid solution, amorphous SiO_2, microcrystalline $Al(OH)_3$, $Mg(OH)_2$, and hydrotalcite ($Mg_4Al_2(OH)_{14}(H_2O)_3$) and saponite were calculated from the ion activity product (IAP) (cf. chapter 2.3.1).

Based on the experimental observations, M-S-H phases containing up to 0.2 Al/Si were defined and the ion activity product of two possible end-members, $M_{0.76}A_{0.20}SH$ and $M_{1.50}A_{0.20}SH$, were calculated from the measured concentrations as detailed in the results part.

Table 8: Standard thermodynamic properties of the system $MgO-Al_2O_3-SiO_2-H_2O$ at 25 °C.

	*	$LogK_{S0}$[a]	$\Delta_f G°$ [kJ/mol]	V° [cm^3/mol]	density [g/cm^3]	Ref.
Brucite	MH	-11.16	−832.23	24.6	2.37	(Thoenen et al., 2014)
M-S-H (solid-solution)						
Mg/Si = 0.78	$M_{0.78}SH_{1.48}$	-14.59	-1682.2	57	2.1[b]	Chapter 3.2
Mg/Si=1.30	$M_{1.3}SH_{1.80}$	-21.44	-2073.5	71	2.0[b]	Chapter 3.2
OH-hydrotalcite 2:1	$M_4A_2(OH)_{14}H_3$	-49.7	-6358.49	21.9		(Myers et al., 2015b)
OH-hydrotalcite 3:1	$M_6A_2(OH)_{18}H_3$	-72.02	-8022.94	30.54		(Myers et al., 2015b)
Microcrys. $Al(OH)_3$	AH_3	-0.67	-1265.28	31.95		(Lothenbach et al., 2012b)
Mg-saponite	$M_{3.15}A_{0.3}S_{3.7}O_{10}(OH)_2 \cdot 4H$		-6571.27	220		(Vidal et al., 2012)
SiO_2,am	S	-2.9	-849.96	29	2.07	Chapter 3.2

[a] All solubility products refer to the solubility with respect to the species Mg^{2+}, AlO_2^-, SiO_2^0, OH^-, or H_2O
[b] Experimental data from chapter 3.3.

Chapter 3:

Pure magnesium silicate hydrate

Contents

3.1. Introduction

M-S-H phases have been synthesized in the laboratory in order to be able to study their properties and solubility (Brew and Glasser, 2005b; Roosz et al., 2015; Walling et al., 2015; Nied et al., 2016). M-S-H is a non-well crystalline phase with characteristic broad peaks observed by XRD at 19.7 (110), 26.7, 35.0 (201) and 59.9 (060) °2θ (λ=1.54Å) (Roosz et al., 2015).

Investigations of the structure of M-S-H gels (d'Espinose de Lacaillerie et al., 1995; Brew and Glasser, 2005b; Roosz et al., 2015; Walling et al., 2015; Nied et al., 2016) by FT-IR and/or ^{29}Si MAS NMR show a high polymerization degree of the Si-network in M-S-H.

^{29}Si MAS NMR studies showed that the silicates are arranged in tetrahedral layers and magnesium in octahedral layers comparable to 2:1 or 1:1 phyllosilicate as shown schematically in Figure 6. The structure of M-S-H is poorly ordered and has been related to sepiolite (Brew and Glasser, 2005b), hydrated nanoparticles of talc (Roosz et al., 2015), hydrated talc or hydrated antigorite (Nied et al., 2016), lizardite (Walling et al., 2015; Pedone et al., 2017), stevensite (Nied et al., 2016) or saponite (Roosz et al., 2015; Lerouge et al., 2017).

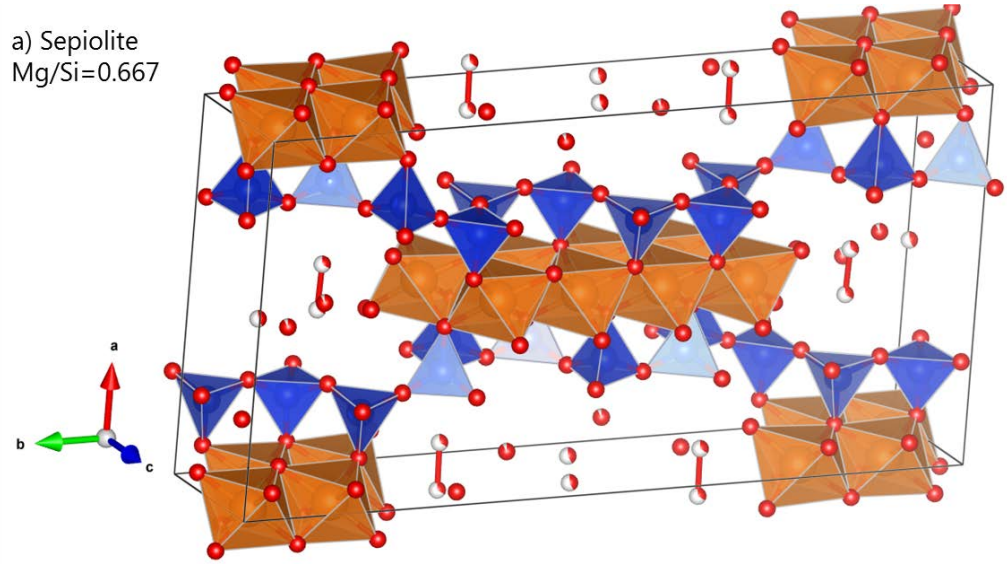

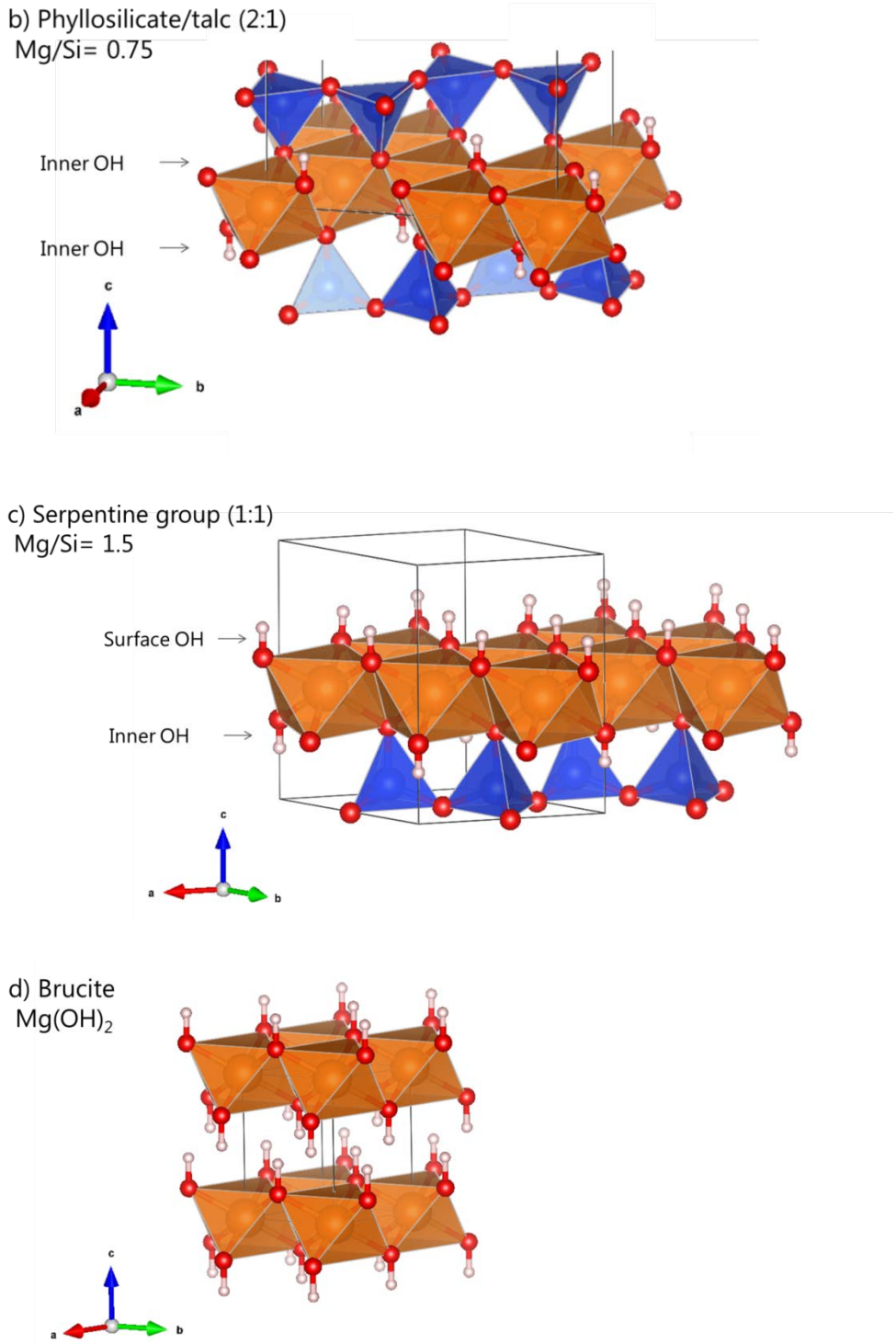

Figure 6: Schematic sketches of the structure of a) sepiolite, T:O:T structure, b) 2:1 phyllosilicates with a T:O:T structure such as talc, c) 1:1 phyllosilicate (T:O structure) such as the serpentine group, and c) brucite (orange: octahedral magnesium site, blue: tetrahedral silicate site). The structures are from (Gruner, 1934; Zigan and Rothbauer, 1967; Mellini and Zanazzi, 1987; Sánchez del Río et al., 2011) using the VESTA software (Momma and Izumi, 2011).

The ^{29}Si MAS NMR spectra of M-S-H showed approximately $^{2}/_{3}$ Q^3 signals indicating silica sheets and $^{1}/_{3}$ of Q^2 signals indicating either very small coherent areas of silica sheets and/or defects in the silicate sheets or even double chain silicate layers

(Roosz et al., 2015; Nied et al., 2016). The Q^2 resonance occurs at a chemical shift of -85.5 ppm, while the broad signal at -92 to -97 has been attributed to 2 or 3 different Q^3 silicate sites depending on the deconvolution (Walling et al., 2015; Nied et al., 2016; Tonelli et al., 2016). Deconvolutions taking into account the presence of 3 different sites indicated chemical shifts at -92.7, -94.7 and -96.8 ppm: Q^{3a}, Q^{3b}, and Q^{3c} (Nied et al., 2016). The "poorly-organized" character of M-S-H leads to significantly broader signals than those observed in crystalline phyllosilicates. The chemical shift at -92.7 ppm is characteristic for serpentine group minerals (MacKenzie and Meinhold, 1994b; Nied et al., 2016) such as antigorite, chrysotile or lizardite with a T:O structure (see Figure 6), while the chemical shift of -96.8 ppm is characteristic for talc (Rhouta et al., 2008; Chabrol et al., 2010; Dumas et al., 2013; Roosz et al., 2015; Nied et al., 2016) with a T:O:T structure. Both classes of minerals exhibit a potentially infinite layer of silicate. The presence of a second silicate tetrahedral layer on the other side of the octahedral magnesium layer doubles the sheets of silicate (T:O:T) and results in a more negative chemical shift for silica in talc than in serpentine group minerals with a T:O structure. The intermediate ^{29}Si MAS NMR resonance at -94.7 ppm in the M-S-H spectra could not be attributed (Chabrol et al., 2010; Dumas et al., 2013; Roosz et al., 2015; Nied et al., 2016). This intermediate chemical shift could be related i) to the presence of an empty neighboring magnesium site as in stevensite, which has as talc a T:O:T structure, but is deficient in magnesium: ($\square$O)-Si-(O-Si)$_3$) where $\square$ is a vacant site (Rhouta et al., 2008; Chabrol et al., 2010), ii) to a high content of surrounding water in M-S-H structure (Pedone et al., 2017), which would result in a resonance at -95 ppm as in the case of saponite or hectorite and/or iii) to the variability of the Si-O-Si angles in M-S-H (Pedone et al., 2017).

M-S-H as a precursor of sepiolite has been suggested by (Brew and Glasser, 2005b). The ^{29}Si MAS NMR spectra of M-S-H shows similarities with sepiolite ($Si_6O_{15}Mg_4(OH)_2(OH_2)_2{\cdot}4H_2O$) spectrum. Sepiolite has a phyllosilicate chain-structure derived from talc T:O:T ribbons with alternate silica and magnesium layers (Figure 6a) for which, similar silicate signals as for M-S-H have been reported: one Q^2 (at -85.2 to -85.5 ppm) and three Q^3 signals (first at -92.3 to -92.7 ppm, second at -94.3 to -94.5 ppm and last at -98.2 ppm) as shown in Appendix D. The $Q^3{}_a$ signal was attributed to the near edge of the silicate sheet in the blocks while the $Q^3{}_b$ and $Q^3{}_c$ signals were attributed to the center or the edge of the silicate sheet (Barron et al., 1985; d'Espinose de la caillerie and Fripiat, 1994; Aramendía et al., 1997; Weir et al., 2002). Sepiolite is needle-like clay with a low charge density, low cation exchange capacity, and a non-swelling clay. The Mg/Si ratio of sepiolite is equal to 0.667, lower than observed in pure M-S-H (Nied et al., 2016) synthesized from MgO and silica fume, although some studies, with other raw materials, have reported such a low ratio (Brew and Glasser, 2005b; Zhang et al., 2011). In fact, Wollast and al. (Wollast et al., 1968) have observed a very poorly crystalline sepiolite-like phase from the reaction of aqueous silica with seawater

comparable to M-S-H. Sepiolite contains different types of water, i) zeolitic water which can be removed by thermal treatment below 150°C, ii) coordinated water which is lost above 150°C and probably below 450°C and is bound to the terminal magnesium cations of the octahedral sheet and iii) structural water which corresponds to the hydroxyl group linked either to tetrahedral or octahedral layers (Nagata et al., 1974; Weir et al., 2002; Frost and Ding, 2003).

Roosz et al. (Roosz et al., 2015) suggested based on the X-rays diffraction (XRD) patterns of M-S-H and the presence of the Q^2 signal in the ^{29}Si MAS NMR spectra that the M-S-H had only nanometer-sized coherent scattering domains which also caused the broad reflections in the XRD pattern. The size of a coherent region of M-S-H was estimated as 1.5 nm in the ab plane, and 2.4 nm along c. Similarly, Chiang et al. (Chiang et al., 2014) suggested based on SAXS measurement a spherical structure for M-S-H with an average radius of 1.7±1 nm.

Under laboratory conditions, M-S-H formation has been observed to be very slow (Zhang et al., 2011; Szczerba et al., 2013; Li et al., 2014). Studies on the formation of synthetic M-S-H from MgO and silica fume (Zhang et al., 2011; Szczerba et al., 2013; Li et al., 2014) indicate that initially magnesium hydroxide, i.e. brucite, is formed, which subsequently reacts to form M-S-H phases. The magnesium hydroxide dissolves slowly in the presence of M-S-H; it takes up to 6 months for initially precipitated magnesium hydroxide to completely react to M-S-H with Mg/Si=1 (Szczerba et al., 2013).

A number of factors seem to influence the kinetics: i) a higher temperature leads to faster formation of M-S-H and the destabilization of brucite (Kalousek and Mui, 1954; Brew and Glasser, 2005b; Golubeva et al., 2005; Szczerba et al., 2013), ii) the magnesium to silica ratio of the magnesium silicate phases is increased at higher temperature (Kalousek and Mui, 1954), iii) the properties of the starting materials have a strong impact on the kinetics. Magnesium oxide reacts faster than brucite (Yang, 1960) and MgO calcined at lower temperature or with a higher specific surface area reacts even faster (Yang, 1960; Jin and Al-Tabbaa, 2013). Not only the temperature or the initial raw materials but also the water to solid ratio (W/S) and the Mg/Si ratio seem to influence the kinetics of M-S-H formation (Kalousek and Mui, 1954; d'Espinose de Lacaillerie et al., 1995; Brew and Glasser, 2005b; Wei et al., 2011; Zhang et al., 2011; Jin and Al-Tabbaa, 2013; Nied et al., 2016). In addition, it can be expected that also the pH value could have an influence, as higher pH values increase dissolution kinetics of silica (Brantley et al., 2008) but slow down brucite dissolution (Pokrovsky and Schott, 2004). Most studies on M-S-H were carried out on samples equilibrated up to 1 year (Roosz et al., 2015; Nied et al., 2016) or even less (d'Espinose de Lacaillerie et al., 1995; Brew and Glasser, 2005a; Brew and Glasser, 2005b; Zhang et al., 2011; Szczerba et al., 2013; Li et al., 2014) under ambient conditions, i.e. under conditions where M-S-H has

not yet reached equilibrium. Longer equilibration times and/or higher temperatures are needed to investigate the effect of Mg/Si on the M-S-H properties.

This chapter studies the effect of the initial Mg/Si (ranging from 0.7 to 1.4) on the formation of M-S-H and its structure and solubility up to 3.3 years at 20°C and up to 1 year at 50 and 70°C. Solubility products of two end members were calculated based on the measured concentrations and pH values. The distribution of the water and the particle properties, were investigated by ^{29}Si MAS-NMR, ^{1}H-^{29}Si CP MAS-NMR and FT-IR spectroscopy and with X-rays diffraction and X-ray pair distribution function analysis, the water and hydroxyl contents and their distribution by DVS, TGA and ^{1}H-NMR relaxometry, the particle size and the porosity by N_2 physisorption measurements and the surface properties by CEC and zeta potential measurements. This study aims to contribute to better understand the formation and ill-structure of M-S-H, the repartition of the different types of water in it and its surface properties.

3.2. Formation of magnesium silicate hydrate

This part is shortened version of the publication: Ellina Bernard, Barbara Lothenbach, Daniel Rentsch, Isabelle Pochard, Alexandre Dauzères, Formation of magnesium silicate hydrates (M-S-H), **Physics and Chemistry of the Earth**, Parts A/B/C, 99 (2017) 142-157 (Bernard et al., 2017b).

It studies the effect of the initial Mg/Si on the formation of M-S-H and its structure and solubility up to 2 years at 20°C and up to 1 year at 50 and 70°C. Solubility products of two end members were calculated based on the measured concentrations and pH values.

Ion chromatography, pH measurements, thermogravimetry analysis, X-ray diffraction, attenuated total reflectance Fourier Transformation-Infrared (FT-IR), ^{29}Si MAS NMR spectroscopy, Zeta potential and CEC measurements were carried out as detailed in chapter 2.2. Part 2.3.1 contains the details of the calculations of the saturation indices and the thermodynamic data.

3.2.1. Results and Discussions

3.2.1.1. Kinetics of M-S-H formation at 20°C

3.2.1.1.1. Up to 3 months

To understand the M-S-H formation process, the reaction of samples with initial Mg/Si=0.8 and 1.2 ratio was followed from 1 day to 3 months. The MgO reacted completely within the first day (absence of reflections at 36.9, 42.9, 62.3 °2θ (Li et al., 2014)) to $Mg(OH)_2$ (brucite) and M-S-H, leaving some unreacted silica as shown in Figure 7.

The dissolved concentrations and pH values measured for the two samples are displayed in Figure 8a and b. The magnesium concentrations decreased between 1 and 3 days to ~0.1 mmol/l. Saturation indices (SI) with respect to brucite (Figure 8d) showed values close to saturation (SI ≈ 0) during the first day, consistent with the observed precipitation of brucite. However, after 3 days the solution became undersaturated with respect to brucite (Figure 8d) although brucite was observed. The silicon concentrations increased slowly and reached ~1.3 mmol/l (Figure 8a and b), i.e. saturation with respect to silica, within 3 days (Figure 8c).

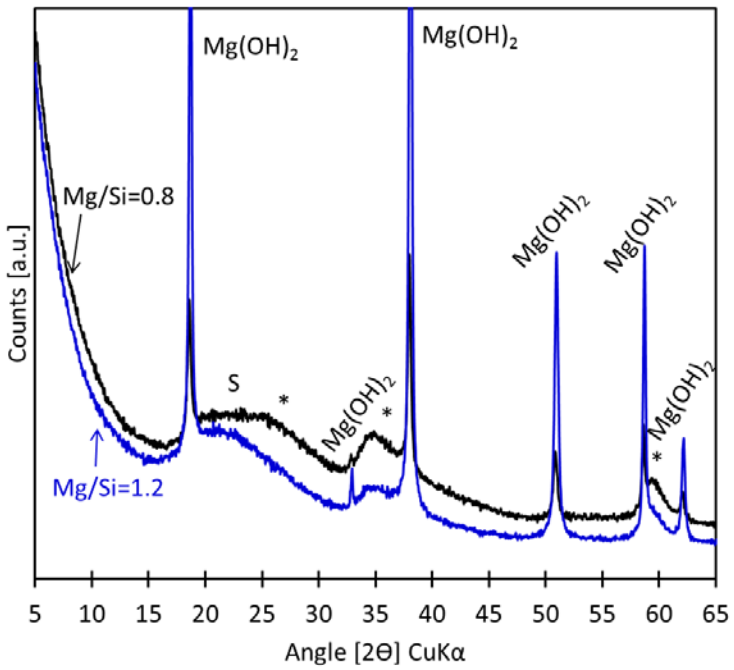

Figure 7: XRD patterns of M-S-H 0.8 and 1.2 after 1 day of curing at 20°C (*=M-S-H, S= silica fume).

From 3 to 91 days little change was observed in the solutions. At Mg/Si = 0.8 and 1.2, representing low and high ratios, similar concentrations were measured: a relatively high concentration of silicon in equilibrium with amorphous silica (Gunnarsson and Arnórsson, 2000) (Figure 8a and b). Low concentrations of magnesium (Figure 8a and b) and pH values between 9.3-9.6 were observed (Figure 9) while M-S-H phases formed slowly. The magnesium concentration increased slightly from 2 to 3 months. Up to day 91, the solutions were still undersaturated with respect to brucite (as detailed in Figure 8d) although XRD and TGA data indicate that brucite was present in the solid phase (as detailed further below in section 3.1.2.3). This persistence of brucite indicates a kinetic hindrance of brucite dissolution which is discussed in section *reaction of brucite* and probably limits the rate of M-S-H formation.

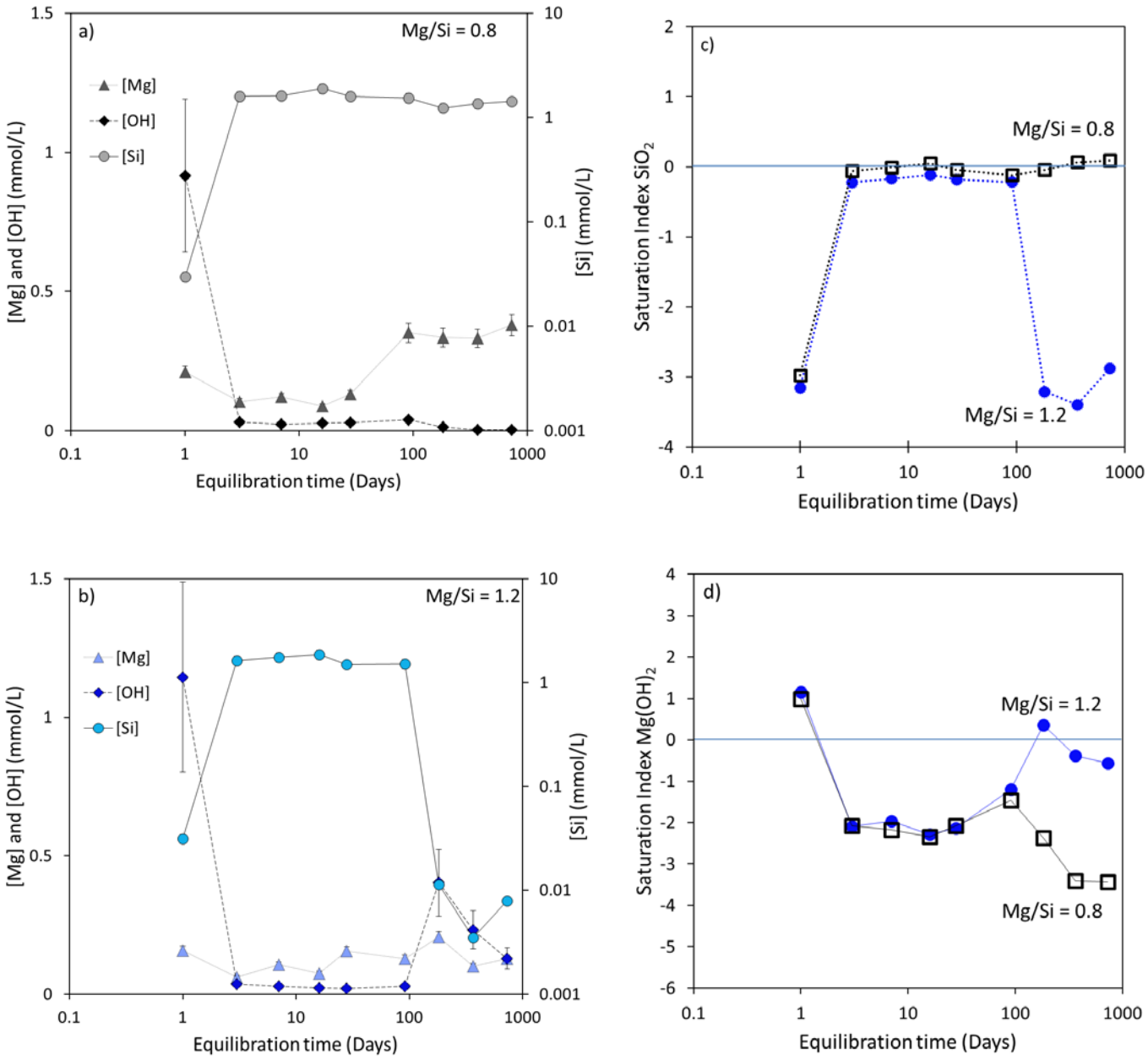

Figure 8: Dissolved ions in the aqueous phase at equilibrium with MgO and SiO_2 during the formation of M-S-H a) Mg/Si=0.8 and b) Mg/Si=1.2. c) Calculated saturation indices (SI) of silica fume and d) calculated SI of brucite for samples Mg/Si = 0.8 and 1.2.

3.2.1.1.2. 3 months to 2 years

Aqueous phase

Only after 91 days, the pore solutions of the samples Mg/Si=0.8 and Mg/Si=1.2 started to differentiate. The equilibrium for Mg/Si = 0.8 seems to be approximately reached within 91 days and the silicon and magnesium concentrations remained stable

thereafter (Figure 8a) while pH decreased somewhat from 9.6 to 8.4 after 730 days (Figure 9). In contrast, in the sample with Mg/Si = 1.2 the silicon concentration dropped as the silica initially present had reacted (see section below section *unreacted silica*) and the pH values increased from 9.4 to 10.3 (Figure 9). The solution became undersaturated with respect to silica fume and saturated with respect to brucite (Figure 8c and d).

After the first 91 days (3 months), all pH values were within a narrow range of 9.3-9.6 independently of the total Mg/Si ratio which varied from 0.8 to 1.6 (Figure 9). Also, the concentrations of magnesium and silicon were similar as they were determined by the presence of brucite and amorphous silica independently of the initial Mg/Si ratio (see Appendix B). Only after 182 days (6 months) and longer, clear differences in the pH values were observed. The samples with higher initial Mg/Si ratio (Mg/Si ≥ 1) showed an increase of the pH values, while pH decreased at lower Mg/Si ratio. After 365 days and longer, the pH increased with the initial Mg/Si ratio ranging between 0.8 and 1.2 and was constant at Mg/Si ratio higher than 1.3 with pH values from 10.3 to 10.5. The pH of the solution in equilibrium with sample M-S-H 1.0 was at all times between ~9.5 to 9.2 indicating little change at Mg/Si=1.0.

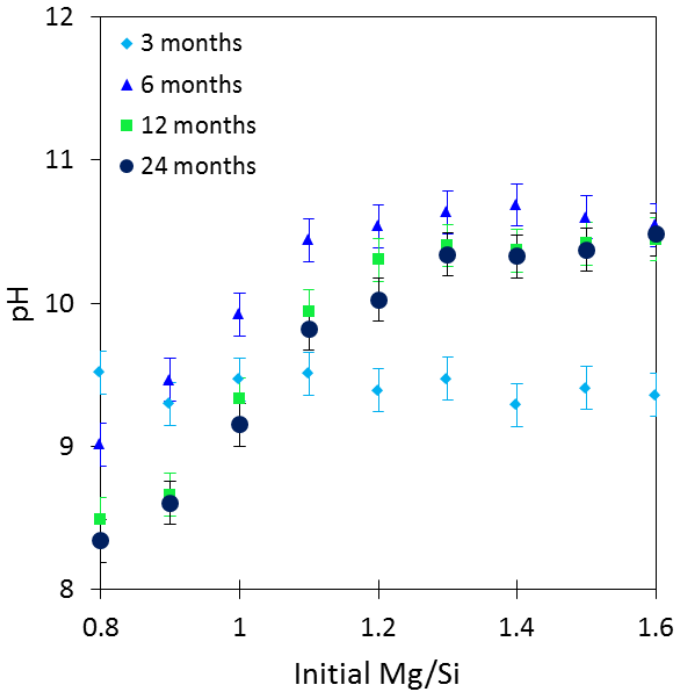

Figure 9: Evolution of pH values at 20°C over time as function of initial Mg/Si ratio (0.8-1.6).

Unreacted silica

The silicon concentrations are plotted versus pH in Figure 10. The dissolved silicon concentrations measured after 3 months were close to the solubility of the amorphous silica which indicates that unreacted silica could be present in the samples. The presence of unreacted silica fume is confirmed by ^{29}Si MAS NMR (Figure 11) and FT-IR (Figure 12). Silica was observed after 3 months in all samples, independently of the initial Mg/Si ratio.

In ^{29}Si MAS NMR spectra unreacted silica was observed by a main resonance at -110 ppm (Q^4) (Figure 11), and by a minor resonance at -100.9 ppm related to hydrated silanol groups Q^3(-OH) (d'Espinose de Lacaillerie et al., 1995; Nied et al., 2016). The amount of unreacted silica was quantified based on the intensity of the resonances Q^4 at -110 and Q^3(-OH) at -100.9 ppm as shown in Figure 11 following the procedure outlined by Nied et al. (Nied et al., 2016). In the samples with initial Mg/Si ratio of 0.8 and 1.4 approximately 16% and 6% of unreacted silica was detected after 3 months. After 1 year $\simeq$ 4% of unreacted silica was observed in the sample with initial Mg/Si = 0.8 and none for Mg/Si = 1.4 (Table 9 and Figure 14), indicating that most of amorphous silica reacted within 12 months to form more M-S-H.

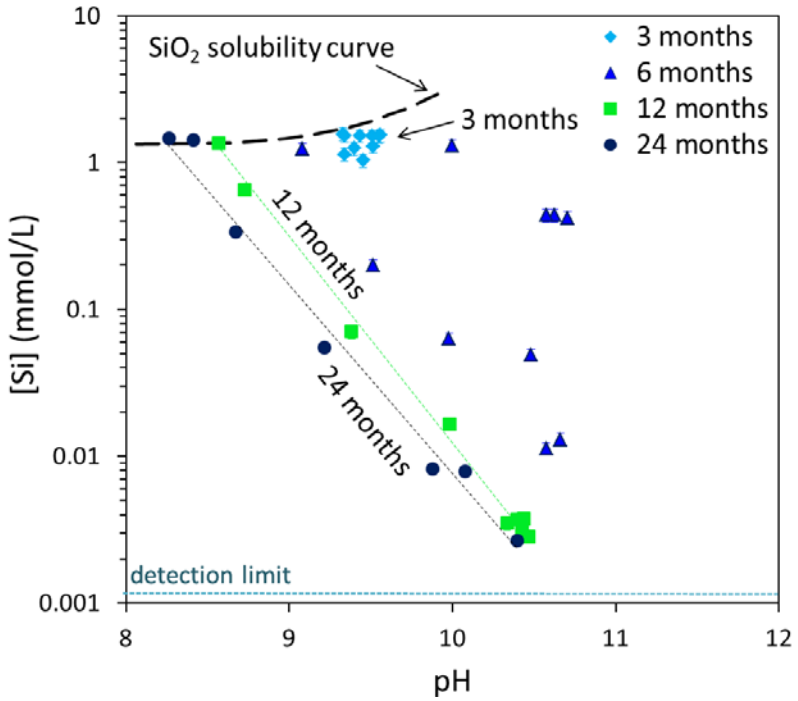

Figure 10: Changes of silicon concentrations with pH (pH at 20°C) and time. Dotted lines have been added as guide line.

Unreacted silica can also be identified by FT-IR based on the bands at ~ 1090 cm^{-1}, 1035 cm^{-1} and 803 cm^{-1} as shown in Figure 12. As already detailed by Nied et al. (Nied et al., 2016), Q^2 and Q^3 silica species present in M-S-H show vibrations at 870-920 cm^{-1}

and 950-1150 cm^{-1} as indicated in Figure 12 by the gray shaded regions. The second derivative can be used to identify the characteristic peak positions at 985-1095 cm^{-1} more clearly. The FT-IR data confirm the presence of unreacted silica by the shoulder at 1035 cm^{-1} in all samples after 3 months and to a lower extent also after 6 months. After 1 year the presence of residual silica was only observed for Mg/Si ≤ 0.8, in agreement with the ^{29}Si MAS NMR data. Although FT-IR can indicate only qualitatively the presence of amorphous silica, in combination with high silicon concentrations, which signpost saturation with respect to amorphous silica (see values in Appendix B), the presence of amorphous silica can be shown for those samples where no ^{29}Si MAS NMR data could be measured.

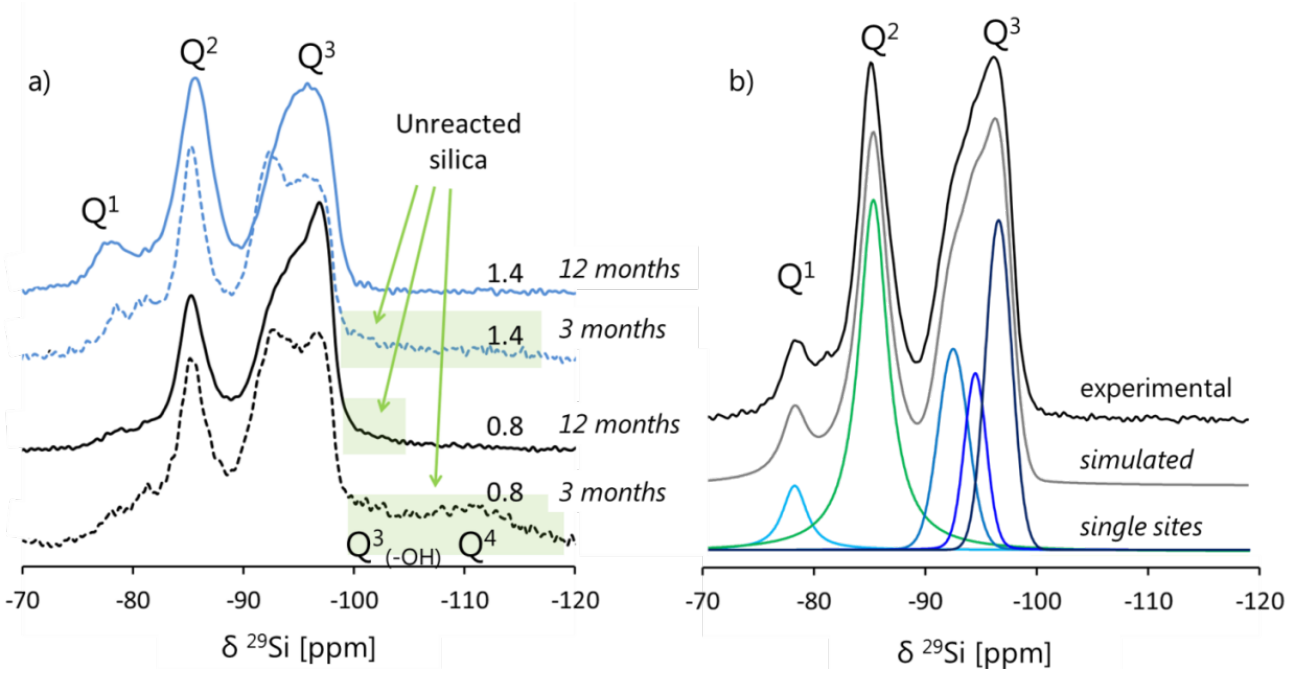

Figure 11: a) ^{29}Si MAS NMR spectra with assignments of single sites of M-S-H samples (Mg/Si=0.8 and 1.4) after 3 and 12 months, the shaded regions assign unreacted silica species, b) example of the deconvolution (sample Mg/Si=1.0, after 12 months) of the indicated single sites listed in Table 9.

Table 9 : Relative intensities of different silicon sites obtained from the deconvolution of the ^{29}Si MAS NMR spectra (δ ^{29}Si in ppm ± 0.3 ppm).

		δ ^{29}Si (ppm) and relative intensities (%Si)							
		M-S-H					Unreacted Silica		Q^2/Q^3
		Q^1	Q^2	Q^3_a	Q^3_b	Q^3_c	Q^3 (-OH)	Q^4	in
Mg/Si	time	-78.3	-85.4	-92.7	-94.7	-96.8	-100.9	-110	M-S-H
0.8	3 months	4	32	29	3	15	7	9	0.7
1.4		8	36	32	2	16	4	2	0.7
0.8	12 months	3	34	25	8	26	4	0	0.6
1.0		6	42	17	11	23	0	0	0.8
1.2		7	46	14	12	21	0	0	1.0
1.4		7	46	14	11	22	0	0	1.0

Quantification error ≃ ± 10% of absolute amount of (%Si) +2.5%.

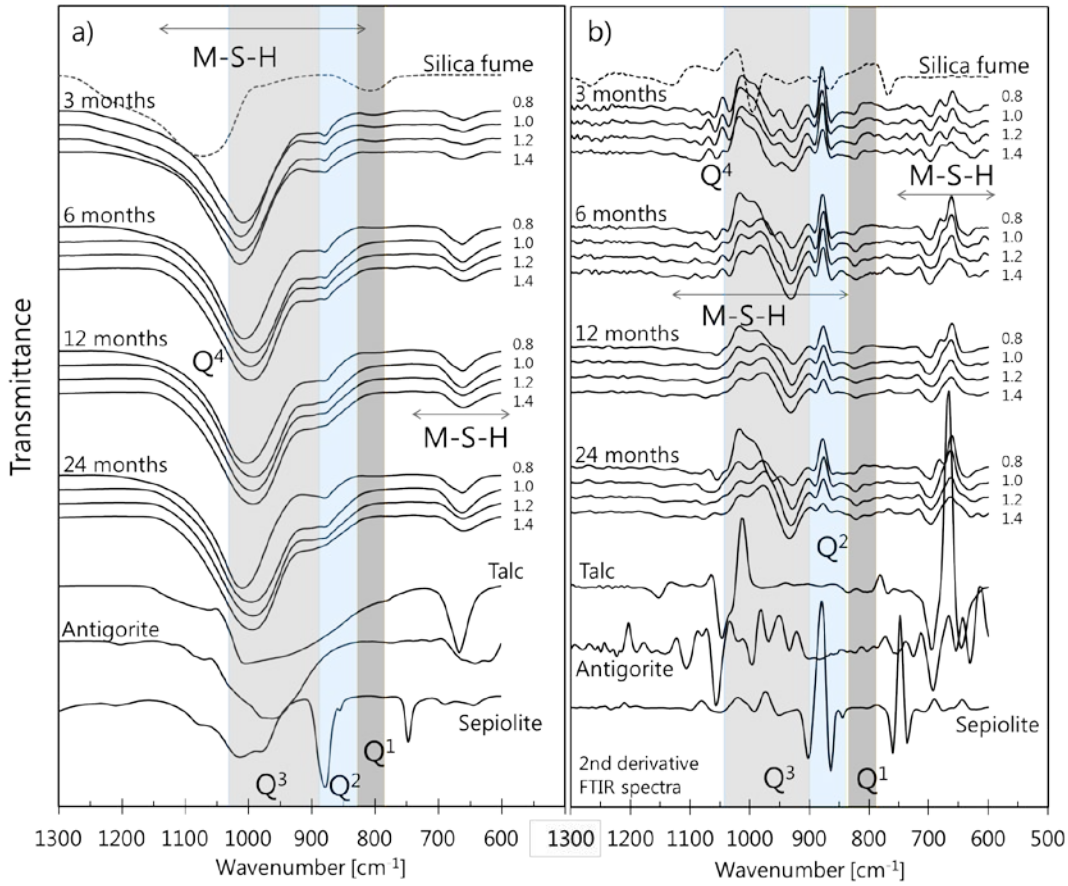

Figure 12: a) FT-IR spectra and b) second derivatives of the FT-IR spectra of M-S-H samples (20°C) with Mg/Si of 0.8, 1.0, 1.2, 1.4. Only the regions characteristic for silica are shown. The shaded areas show characteristic regions for Q^1, Q^2, Q^3, and Q^4. Measured spectra of silica fume, talc, antigorite, and sepiolite are shown for comparison.

Reaction of brucite

The thermogravimetric analyses of the solid phases confirm that brucite dissolution and M-S-H formation occurred only slowly as shown in Figure 13a. After 3

months of equilibration thermogravimetric analysis indicates that brucite was still present in all samples, as visible by a well-defined weight loss in the shaded temperature range centered at 410°C. XRD measurements (Figure 13b) confirm the presence of brucite (reflections peaks at 18.6, 32.7, 38.0, 50.9, 58.7, 62.0 °2θ (Brew and Glasser, 2005b; Zhang et al., 2011) in the XRD patterns (Figure 13b)) together with unreacted silica (broad hump at 21-24 °2θ) as previously observed by FT-IR and ^{29}Si MAS NMR.

The thermogravimetric data (Figure 13a) show already after 3 months the two water loss regions typical for M-S-H (Mitsuda and Taguchi, 1977; Zhang et al., 2011; Nied et al., 2016). The first weight loss between 30°C and 250°C is due to poorly bound water in the interlayer or on the surface. The second weight loss between 250°C and 800°C, overlapping with the "brucite weight loss", is attributed to the dehydroxylation of magnesium or silanol hydroxyl groups (Szczerba et al., 2013; Nied et al., 2016).

After 2 years the characteristic XRD humps of M-S-H are better defined than after 1 day (Figure 7) or 3 months (Figure 13b) of reaction, while much less (Mg/Si = 1.4) or no brucite (Mg/Si = 0.8) was present.

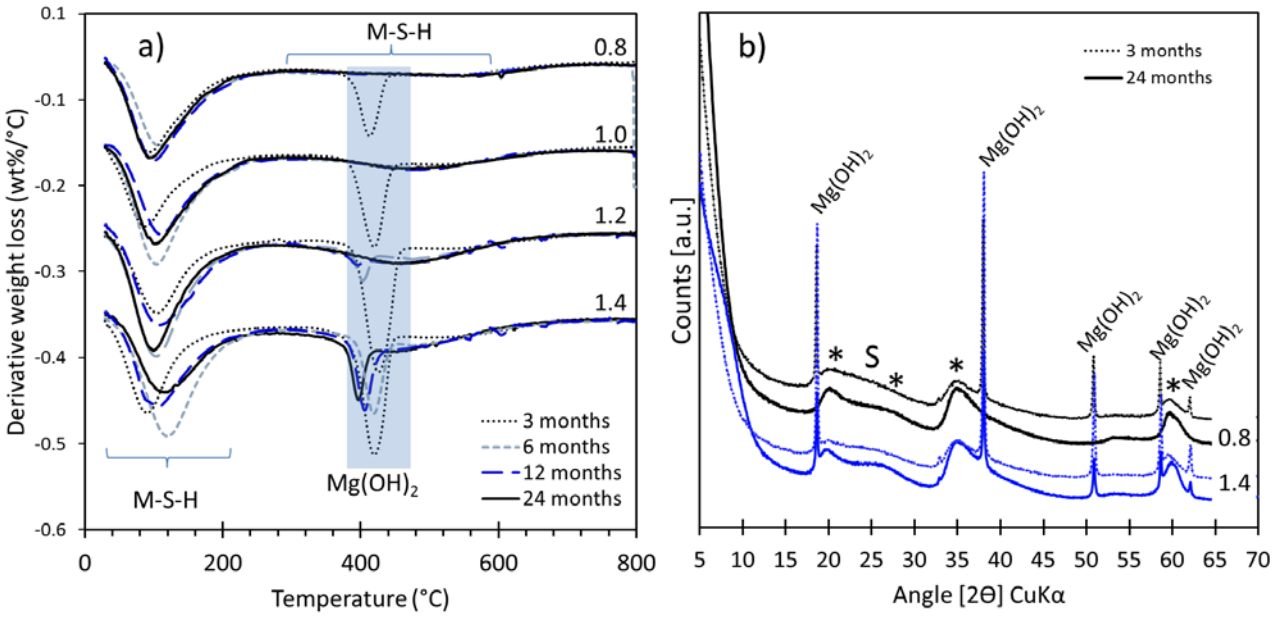

Figure 13: a) Derivative of thermogravimetric analyses of M-S-H samples synthesized at 20°C, Mg/Si = 0.8, 1.0, 1.2, 1.4 aged of 3 months (dotted lines) 6 months (grey dashed lines), 1 year (blue large dashed lines) and 2 years (solid lines),grey shaded region= water loss of brucite. b)XRD patterns of M-S-H samples synthesized at 20°C, Mg/Si = 0.8, 1.4 aged of 3 months (dotted lines) and 2 years (solid lines) (*=M-S-H, S= silica fume).

Figure 14a summarizes the amount of brucite contained in the samples as a function of time. The presence of brucite after 3 months in all samples is consistent with the similar magnesium concentrations in all solutions. The amount of brucite increased with the initial MgO content. While after 3 months brucite was observed in all

samples, brucite was only present for Mg/Si > 1 after 6 months and for Mg/Si > 1.2 after 2 years, indicating that all the magnesium is in M-S-H phases after long reaction times and that a maximum Mg/Si of ≈ 1.3 can be reached at room temperature.

If brucite was present, its amount increased nearly linearly with the total Mg/Si (Figure 14a). Even though some brucite was still present, the amount was very low compared to the initial amount of magnesium as indicated in Table 10 confirming the dissolution of brucite and the presence of mainly M-S-H after 1 year and longer.

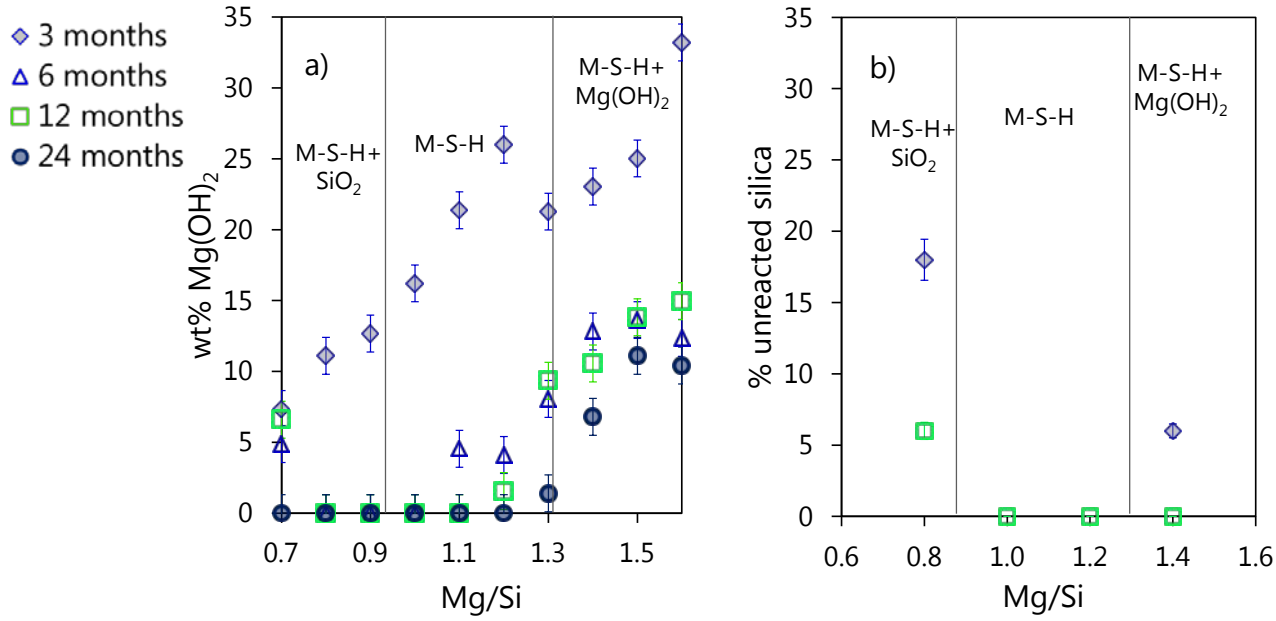

Figure 14 : Amount of a) brucite (from TGA) (wt.% of brucite normalized to 100g dry mass) and b) unreacted silica (from ^{29}Si MAS NMR) per total of silica in samples cured at 20°C as a function of the initial Mg/Si and time. Vertical lines separate the area where i) silica + M-S-H, ii) M-S-H only and iii) M-S-H + brucite are present after long reaction times.

Table 10: Theoretical and experimental measured brucite content in wt.%.

total Mg/Si	0.8	1	1.2	1.4
theoretical maximum brucite content*	51	58	65	70
experimental brucite				
1 year at 20°C	<0.1	<0.1	1.5 ± 1	10.6 ± 1
2 years at 20°C	<0.1	<0.1	<0.1	6.8 ± 1
1 year at 50°C	<0.1	<0.1	0.2 ± 0.2	7.2 ± 1
1 year at 70°C	<0.1	<0.1	<0.1	6.2 ± 1

* Theoretical maximum brucite content: amount of brucite which could form from MgO considering the total mass of the solids (brucite + amorphous silica)

<0.1: not detected by TGA

It has been reported that the reaction of MgO to brucite is strongly retarded by the presence of dissolved silicon (Salomão and Pandolfelli, 2008). Based on that it may be tentatively concluded that also the dissolution of brucite is retarded by the presence of silicon in solution. In the absence of silica, the solutions equilibrated fast with brucite and measured magnesium concentrations and pH values were in the range of the calculated brucite solubility as shown in Figure 15a. In contrast, samples with 1 or 1.5 mmol/l silicon in solution had lower pH values and remained clearly under saturated with respect to brucite. A plot of saturation indices of brucite versus the measured silica concentrations (Figure 15b) shows a strong undersaturation with respect to brucite at silicon concentrations of 1 mmol/l or higher. This dependence confirms a kinetic hindrance of brucite dissolution at high silicon concentrations (>1mmol/l).

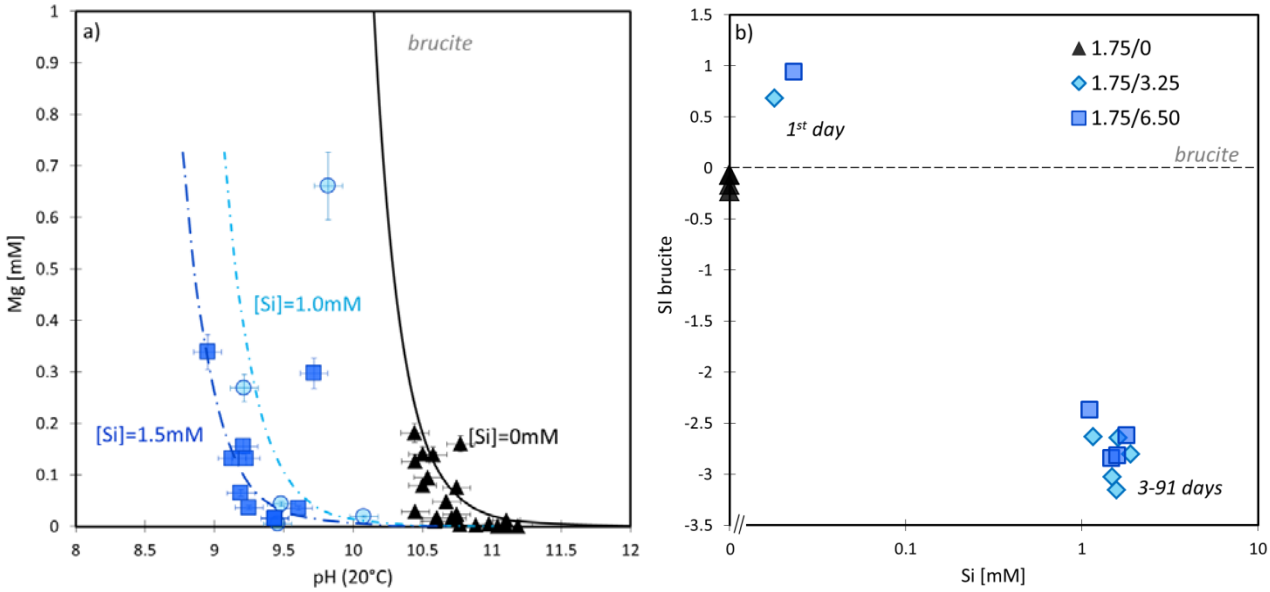

Figure 15: a) Concentration of magnesium measured for MgO only and for MgO/SiO_2 with weight ratio = 1.75g/0g, 1.75g/3.25g and 1.75g/6.50g between 1 and 28 days plotted as a function of pH and compared to solubility of brucite as calculated with GEMS; b)Calculated saturation indices of brucite as a function of the silicon concentrations.

At later ages when the amorphous silica is dissolved, silicon concentrations are lowered, such that the dissolution of brucite is no longer hindered and saturation with respect to brucite is reached again as shown in Figure 8. However, even under these conditions, the dissolution of brucite is expected to be slow due to the high pH values and low magnesium concentrations which limits magnesium uptake in M-S-H.

3.2.1.2. Rearrangement of M-S-H structure with time

3.2.1.2.1. Structure of the transitional product

^{29}Si MAS NMR spectra in Figure 11 show the presence of a small quantity of Q^1, some Q^2 and mainly Q^3 silicate sites indicating the predominance of sheets of silica in the M-S-H phases. The deconvolution of the Q^3 silicates resonance exhibits 3 different ^{29}Si chemical shifts indicating 3 slightly differing chemical environments, as previously discussed in (Roosz et al., 2015; Nied et al., 2016). The ^{29}Si NMR chemical shifts of the Q^3_a, Q^3_b, and Q^3_c signals at -93, -95, and -97 ppm (Figure 11b and Table 9) correspond to the shifts observed for serpentine group minerals (MacKenzie and Meinhold, 1994b; Nied et al., 2016) and for talc (Rhouta et al., 2008; Chabrol et al., 2010; Dumas et al., 2013; Roosz et al., 2015; Nied et al., 2016), respectively. Neglecting the unreacted silica (Table 9), the distribution of silica species in M-S-H 0.8 and M-S-H 1.4 was similar after 3 months, except that the sample with the higher Mg/Si ratio contained slightly more Q^1 (Table 9). The samples have also a similar Q^2/Q^3 ratio of ~ 0.7 (details in Table 9 and Figure 16) as well as similar FT-IR spectra (Figure 12), independently of the Mg/Si ratio. Also, the FT-IR data indicate the presence of a small quantity of Q^1 sites, two different Q^2 and three different Q^3 sites corresponding to the maxima of the second derivatives in Figure 12b between 950 and 1020 cm^{-1}. The position of the Q^3_c peak at 1016 cm^{-1} corresponds to the Q^3 site of talc. In addition, shoulders at 985 cm^{-1} and at 957 cm^{-1} are visible, which could correspond to the Q^3_a and Q^3_b sites observed by ^{29}Si MAS NMR. This indicates the presence of a "transitional" M-S-H phase after 3 months with a structure independently of the total Mg/Si ratio as the transitional M-S-H was formed due to simultaneous presence of unreacted silica (Table 9) and brucite (Figure 14) and was present as long as silica and/or brucite were fully consumed. The initial formation of such a transitional M-S-H and its persistence up to 3 months is consistent with the constant composition of the pore solution during this time shown in Figure 8a and b.

After ≃ 6 months, these "transitional" Q^3a and Q^3b peaks in the second derivative of FT-IR spectra are replaced by better-defined peaks at 1000 and 985 cm^{-1} corresponding to the bands observed for antigorite. More intense bands of these Q^3_a and Q^3_b are present at high Mg/Si, as previously observed by Nied et al. (Nied et al., 2016).

The position of the Si-O-Si bending band at ~660 cm^{-1} is influenced by the Si-O-Si angles and by the occupancy of neighboring sites. Well defined, narrow bands as in the case of talc indicate a high degree of symmetry and ordering (Cong and Kirkpatrick, 1996; Yu et al., 1999). The broadness of the M-S-H bands between 600 and 710 cm^{-1} indicates a low symmetry of the structure which became more ordered with time as narrower bands can be observed in Figure 12a after 12 and 24 months. Similar

observations by XRD with better-defined humps indicate as well a better crystallinity after 12 and 24 months.

In summary, after 3 months at 20°C, all samples contained brucite, unreacted silica fume and a "transitional" M-S-H with a low degree of organization and a Mg/Si ratio in the range of 0.9 - 1.1 (Table 11). This transitional M-S-H is in equilibrium with ~0.2 mmol/l magnesium and ~1.5 mmol/l silicon in all samples (Figure 8) as the presence of amorphous silica buffered the silicon concentrations to ~1.5 mmol/l and the pH values to ~ 9.4. This solution is in equilibrium with M-S-H with Mg/Si ≃ 1.0 (Figure 9).

Only after 12 and 24 months, M-S-H phases with different Mg/Si and thus different structures were identified with Mg/Si ratios in the range between 0.8 and 1.3 at 20°C as detailed in Table 11.

Table 11: Experimentally determined composition of M-S-H phases synthesized at 20, 50 and 70°C by mass balance following the equation (2) (corrected for the amount of brucite quantified by TGA and amorphous silica by ^{29}Si MAS NMR). Total water determined from TGA.

initial Mg/Si	0.8	1.0	1.2	1.4
3 months - 20°C	$M_{0.89}SH_{1.46}$	n.d.	n.d.	$M_{1.07}SH_{1.58}$
1 year - 20°C	$M_{0.84}SH_{1.52}$	$M_{1.00}SH_{1.58}$	$M_{1.19}SH_{1.75}$	$M_{1.24}SH_{1.67}$
2 years - 20°C	$M_{0.83}SH_{1.63}$	$M_{1.00}SH_{1.70}$	$M_{1.20}SH_{1.89}$	$M_{1.29}SH_{1.64}$
1 month - 50°C	$M_{0.84}SH_{1.63}$	n.d.	n.d.	n.d.
1 year - 50°C	$M_{0.85}SH_{1.49}$	$M_{1.00}SH_{1.46}$	$M_{1.20}SH_{1.59}$	$M_{1.28}SH_{1.62}$
1 year - 70°C	$M_{0.86}SH_{1.56}$	$M_{1.00}SH_{1.70}$	$M_{1.20}SH_{1.81}$	$M_{1.30}SH_{1.66}$

n.d.= not determined
Error ±0.1

3.2.1.2.2. Effect of Mg/Si on M-S-H structure (this part corresponds to the publication, but more details are given in the chapter 3.3)

For the samples aged for 1 year, clear differences were visible in the ^{29}Si MAS NMR data as the increase of the Q^2/Q^3 ratio at higher Mg/Si in the M-S-H (Table 9).

The Q^2/Q^3 ratios (total $Q^3 = Q^3_a+Q^3_b+Q^3_c$) of different samples are shown in Figure 16a as a function of the experimentally determined Mg/Si ratio in M-S-H as detailed in Table 11. A strong increase of the relative fraction of Q^2 was observed at high Mg/Si (Table 9) indicating a change in the arrangement of the silicate in M-S-H.

The total amount of water calculated to be present in M-S-H equilibrated at 30% relative humidity is detailed in Table 11. The amount of total water bound increased with the Mg/Si of the M-S-H as reported previously (Nied et al., 2016). It can be

expected that the amount of water present in M-S-H depends on the drying conditions as previously observed for C-S-H gels (Lothenbach and Nonat, 2015; Roosz et al., 2016). TGA analysis allows differentiating between loosely bound water in several layers at the surface and in the interlayer (< 250 °C) and structurally bound water (monolayer on the surface) or hydroxyl groups (weight loss between 250 to 800 °C). Both, the total amount of surface, interlayer and structural water, and the structurally bound water obtained by TGA analysis for the different samples are plotted in Figure 16b. The amount of structurally bound water identified from the weight loss by TGA is higher than the quantity of water in hydroxyl groups quantified by ^{1}H-NMR (Nied et al., 2016) as the TGA results include also the water present as a monolayer on the M-S-H surface (for a more detailed discussion see e.g. (Roosz et al., 2016) and the following chapter. However, this increase of hydroxyl groups at higher Mg/Si ratio could be related to the presence of more Q^2 sites as Nied et al. (Nied et al., 2016) found that hydroxyl groups are associated with Q^1 and Q^2 sites and possibly also to magnesium.

The amount of Q^3_a slightly decreased with aging time while Q^3_b and Q^3_c both increased. These changes could not be fully resolved, but the increase of Q^3_c sites could be related to the better ordering of the silica sheet of longer aged samples, as also observed in the XRD data given in Figure 13b. Although the silica arrangement varies with the Mg/Si ratio in M-S-H, above Mg/Si =1.2 no further increase of OH/Si was observed and a plateau seems to be reached with Q^2/Q^3 = 1. The ^{29}Si MAS NMR spectrum at Mg/Si= 1.4 is similar to the one at Mg/Si=1.2 consistent with the comparable magnesium concentrations due to the presence of brucite which buffers pH values and magnesium concentrations and limits the Mg/Si ratio in M-S-H at 1.2 to 1.3.

A Q^2/Q^3 equal to 1 would be characteristic for double chain silica (amphibole) (Welch et al., 1992), such as anthophyllite $(Mg,Fe)_7Si_8O_{22}(OH)_2$ or hornblende $(K,Ca,Na,Fe,Mg)_2(Mg,Fe,Al)_5$ $(Al,Si)_8O_{22}(OH)_2$, while phyllosilicates such as talc or antigorite possess only Q^3 sites. Thus the presence of a significant fraction of Q^2 could be explained either by very small coherent silica regions in M-S-H (Roosz et al., 2015) or alternatively by the presence of double chain silica such as in anthophyllite or triple chain silica such as in jimthompsonite $(Mg,Fe^{2+})_5Si_6O_{16}(OH)_2$ or chesterite $(Mg,Fe)_{17}Si_{20}O_{54}(OH)_6$ (Welch et al., 1992; Nied et al., 2016).

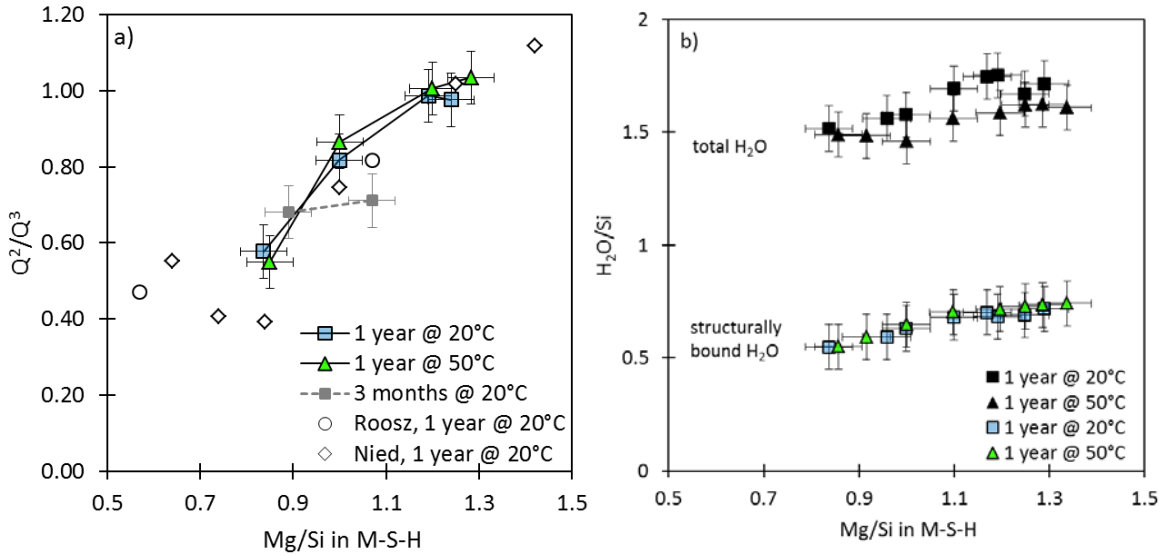

Figure 16: a) Q^2/Q^3 total from ^{29}Si MAS NMR as a function of the experimentally determined Mg/Si in M-S-H phases, after 3 and 12 months at 20°C and after 12 months at 50°C compared to literature data (Roosz et al., 2015; Nied et al., 2016), b) H_2O/Si structurally bound water plus hydroxyl groups of M-S-H, determined from the weight loss between 270-800°C by TGA, and total H_2O, determined from the entire weight loss by TGA, per silica as a function of the Mg/Si in M-S-H phases.

3.2.1.3. Effect of temperature

3.2.1.3.1. Solution

Temperature has a significant influence on the kinetics of M-S-H formation and its solubility. The reaction was faster at higher temperatures and the magnesium and silicon concentrations at 50 and 70°C were at equilibrium with M-S-H faster than at 20°C as visible from the silicon concentrations at 20, 50 and 70°C shown in Figure 17 (and detailed in Appendix B). At low Mg/Si ratios in M-S-H, where unreacted silica persists, the higher silicon concentrations (from 1.2 to 1.5, to 2.5 and to 3.8 mmol/l at 7°C, 20°C, 50°C and 70°C, respectively) simply relate to the increase of silica solubility with temperature (Gunnarsson and Arnórsson, 2000). In the presence of M-S-H without amorphous silica, lower silicon concentrations were observed at higher temperatures (Figure 17, Appendix B).

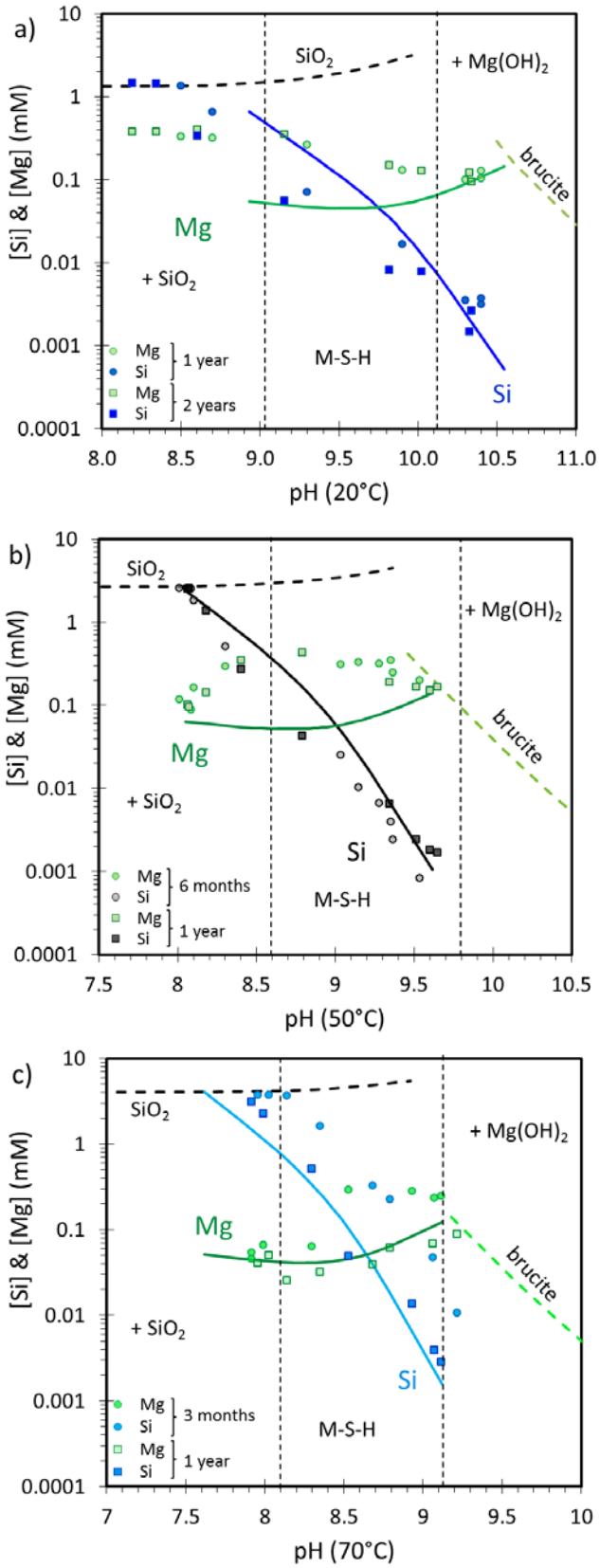

Figure 17: Magnesium (light green symbols) and silicon (dark blue, black or red symbols) concentrations as a function of pH a) at 20°C after 1 year (circles) and 2 years (squares) b) at 50°C after 6 months (circles) and 1 year (squares) c) at 70°C after 3 months (circles) and 1 year (squares). Lines indicate calculated solubility of amorphous SiO2, M-S-H and brucite (details in the text in section 3.3). Vertical lines separate the area where i) silica + M-S-H, ii) M-S-H only and iii) M-S-H + brucite are present.

At high Mg/Si ratio the magnesium concentrations at all temperatures are limited by brucite solubility as shown in Figure 17. The magnesium concentrations in equilibrium with brucite are similar at 20°C as at 50°C and 70°C although they are shifted on the pH scale. In the absence of brucite, however, magnesium concentrations are lower at 70°C than at 50 and 20°C (Figure 17) and highest at 7°C (Appendix B).

A strong influence of temperature was also visible in the relative changes of the magnesium concentrations as a function of pH and Mg/Si ratio. At 20°C, the magnesium concentrations decreased with increasing Mg/Si ratio after 6 months and 1 year (Appendix B), after 2 years no trend in the magnesium concentrations was observed for the low Mg/Si samples (Mg/Si= 0.7-1.0). At 50°C up to 3 months such a decrease was observed, while after 6 and 12 months at 50°C (and after 3 and 12 months at 70°C) a clear increase of magnesium concentrations with Mg/Si ratio was observed. In fact, one would expect, in the absence of brucite, an increase of the magnesium concentration with increasing Mg/Si ratio as observed at higher temperatures and longer equilibration times (Figure 17b) and as reported for C-S-H gels (Haas and Nonat, 2015; L'Hôpital et al., 2015). The reason for such a strongly different behavior is not yet fully understood, but it seems that the samples were near to equilibrium after 1 year at 70 °C. It can be speculated that the higher measured magnesium concentrations at 20°C and at 50°C than the calculated concentrations (see Figure 17a and b) indicate that equilibrium has not yet been completely reached even after 1 year at 50°C or 2 years at 20°C.

3.2.1.3.2. Solid phases

Higher temperatures lead to a faster consumption of brucite and amorphous silica as visualized in Figure 14 and Figure 18. After one month, the samples cured at 50°C still contained brucite, but significantly less than the samples cured for 3 months at 20°C (Figure 14).

After 3 months at 50°C and 70°C, no brucite was observed at Mg/Si < 1.0 indicating a faster formation of M-S-H at higher temperatures. However, at Mg/Si ≥ 1.2 at 50°C and 70°C, some brucite remained even after 1 year and no or very little decrease of the amount of brucite with time was observed. The Mg/Si ratio of 1.2 to 1.3 seems to be the higher limit, due to the presence of brucite.

Figure 18b and Figure 14 indicate that similar amounts of unreacted silica were observed by ^{29}Si MAS NMR at 20, 50 and 70°C for an initial Mg/Si ratio equal to 0.80 resulting at all temperatures in a similar minimum Mg/Si ratio of 0.84 ± 0.02 (Table 11).

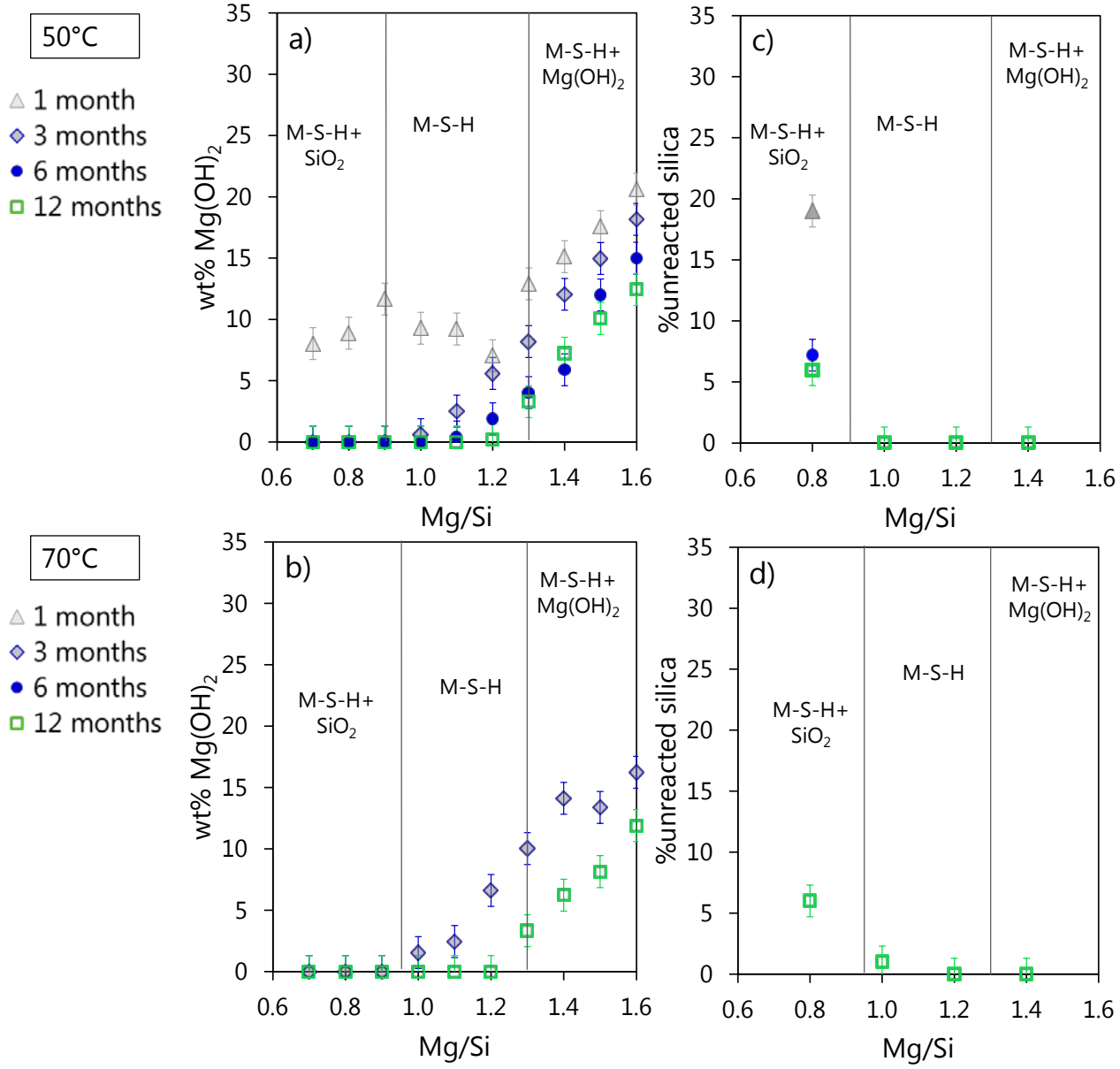

Figure 18: Amount of brucite (from TGA) (wt% of brucite for 100g dry mass) and b) unreacted silica (from 29Si MAS NMR) per total of silica in samples cured a) at 50°C and b) 70°C as a function of the initial Mg/Si and amount of unreacted silica (from the 29Si MAS NMR) in samples cured c) at 50°C and d) 70°C as a function of the initial Mg/Si. Vertical lines separate the area where i) silica + M-S-H, ii) M-S-H only and iii) M-S-H + brucite are present after long reaction times.

3.2.1.4. Solubility

3.2.1.4.1. Ion activity products of M-S-H as a function of time

Initially, a transitional M-S-H was formed with an experimentally determined Mg/Si ratio in the range of 0.9 - 1.1 independently of the total Mg/Si ratio. Ion activity products ($\{Mg^{2+}\}\{SiO_2^0\}\{OH^-\}^2\{H_2O\}^{0.6}$) corresponding to $MgSiO_{4.6}H_{3.2}$ were calculated with GEMS (Kulik et al., 2013b) for samples with Mg/Si= 0.9, 1.0, 1.1 (bold values in the Appendix B) for all investigated equilibration times. A decrease of ion activity products with time was clearly observed indicating the formation of a more stable M-S-H. Between 6 months and 1 year at 50°C, no further decrease in the calculated solubility products with time was found. The values obtained at 50 and 70°C after 1 year are slightly higher than the ion activity product obtained at 20°C after 2 years.

3.2.1.4.2. Solubility products of M-S-H

At later ages (2 years at 20°C, 1 year at 50 and 70°C) where better defined and distinct M-S-H compositions were present, two separate solubility products for high and low Mg/Si in M-S-H were calculated. Nied et al. (Nied et al., 2016) developed a solid solution model for M-S-H using two end members $M_3S_4H_5$ and $M_3S_2H_5$ representing Mg/Si ratios of 0.75 and 1.5. The present more detailed investigations show a minimum Mg/Si ratio of ~ 0.8 and a maximum Mg/Si ratio of 1.3, thus Mg/Si ratios of 0.78 and of 1.30 were selected as end-members. The solubility products of these end-members are summarized in Table 12. For low Mg/Si ratio (0.7-1.0), the solubility products of M-S-H phases ($Mg_{0.78}Si_1O_{4.26}H_{2.96} \Leftrightarrow 0.78Mg^{2+} + SiO_2^0 + 1.56OH^- + 0.7H_2O$) were calculated based only on samples where both M-S-H and silica were present. The averages of these solubility products are listed in Table 12, and the resulting solubility products show a clear decrease with time and slight increase with temperature as shown in Figure 19. Similarly, for samples where M-S-H and brucite were both presents (see the Appendix B), the solubility products for M-S-H phases with Mg/Si=1.30 were calculated accordingly: $Mg_{1.3}Si_1O_{5.1}H_{3.6} \Leftrightarrow 1.3Mg^{2+} + SiO_2^0 + 2.6OH^- + 0.5H_2O$ and their average values are given in Table 12. As at lower Mg/Si, the solubility products decrease with time and increase slightly with temperature. The calculated ion activities for the dissolution of crystalline talc and antigorite (Appendix B) are lower than the calculated solubility products of M-S-H samples.

Finally, the heat capacity of the two end-members presented in Table 13 was estimated from the heat capacities of talc, antigorite, and chrysotile as given in (Holland and Powell, 1998) and water content, assuming $\Delta_r C_p \approx 0$. The entropy given in Table 13 was adapted to fit the increase in the solubility with the temperature as shown in Figure 19.

Table 12: Calculated solubility products of $M_{0.78}SH_{1.48}$ ($\{Mg^{2+}\}^{0.78}\{SiO_2^0\}\{OH^-\}^{1.56}\{H_2O\}^{0.7}$) and of $Mg_{1.30}SiH_{1.80}$ ($\{Mg^{2+}\}^{1.3}\{SiO_2^0\}\{OH^-\}^{2.6}\{H_2O\}^{0.5}$), data averaged from bold values in Appendix B.

$M_{0.78}SH_{1.48}$	Log K_{S0} ± 0.5				
	1 month	3 months	6 months	1 year	2 years
7°C				**-14.8***	
20°C		-13.0	-14.1	-14.5	**-14.8**
50°C	-13.4	-13.5	-13.9	**-13.9**	
70°C		-13.4		**-13.6**	

$M_{1.30}SH_{1.60}$	Log K_{S0} ± 0.5				
	1 month	3 months	6 months	1 year	2 years
7°C				**-22.6***	
20°C		-18.2	-18.3	-21.2	**-21.6**
50°C	-19.6	-19.1	-20.4	**-20.6**	
70°C		-19.8		**-20.2**	

* Approximate value after 18 months from undersaturation, equilibrium might not yet have been reached.

Table 13: Tentative thermodynamic properties of the end-members $M_{0.78}SH_{1.48}$ and $M_{1.30}SH_{1.60}$ at the standard conditions (25°C and 1atm). Log K_{s0} designates the solubility product with respect to Mg^{2+}, SiO_2, OH^- and H_2O, Δ_fG^0 Gibbs free energy of formation, Δ_fH^0 enthalpy of formation; S^0 entropy; C^0p heat capacity ($C^0p=a+bT+cT^{-2}+dT^{-1/2}$).

	Log K_{s0}	$\Delta_fG°$	$\Delta_fH°$	$S°^a$	$C°_p{}^b$
		KJ/mol		J/K/mol	J/K/mol
$M_{0.78}SH_{1.48}$	-14.59 ± 0.50	-1682.2 ± 2.9	-1846.7 ± 12.4	123[a]± 30	176 ± 30
$M_{1.30}SH_{1.80}$	-21.44 ± 0.50	-2073.5 ± 2.9	-2270.4 ± 11.8	119[a]± 30	218 ± 30

[a] entropy values fitted to describe the solubility as a function of the temperature. For $\Delta_rS^0 = 0$, 153 and 189 J/K/mol would be obtained from the thermodynamic data of talc, chrysotile and antigorite (Holland and Powell, 1998).

[b] $C°p(M_{0.78}SH_{1.48})$ calculated from 96% talc, 2% chrysotile and 2% antigorite given in (Holland and Powell, 1998) and adjusted for the water content; $C°p(M_{1.30}SH_{1.60})$ calculated from 40% talc, 30% chrysotile and 30% antigorite given in (Holland and Powell, 1998) and adjusted for the water content

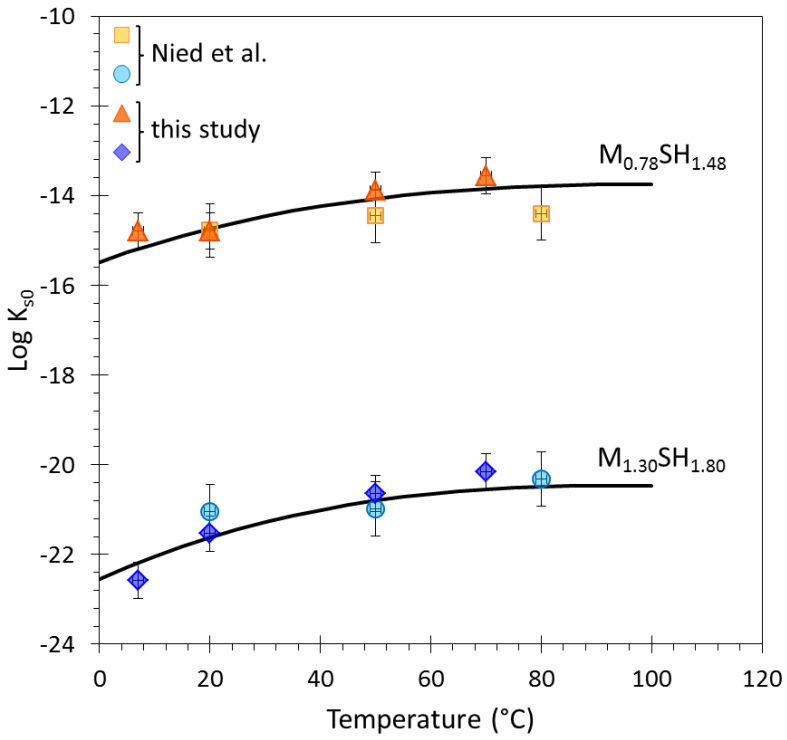

Figure 19: Changes of the solubility product as a function of temperature. Triangle and diamonds indicate the average of the experimental data given in Table 12, squares and circles the data from (Nied et al., 2016) after 1 year and from (Nied et al., 2011) after 3 months. The lines indicate the solubility calculated from the thermodynamic data in Table 13.

3.2.2. Conclusions

The formation of M-S-H from MgO and SiO_2 is a slow process which continues at least up to 2 years at 20°C and possibly longer. During the first day, the fast dissolution of MgO and the precipitation of brucite and of a small amount of M-S-H was observed. Silica fume dissolved more slowly. However, after one week and longer the solutions were equilibrated with respect to amorphous silica. Although brucite presence persisted at all Mg/Si ratio up to 3 months, the solutions were undersaturated with respect to brucite after 2 days indicating that the dissolution of brucite is the rate limiting step for the formation of M-S-H. It can be speculated that the presence of silicon in solution is responsible for the observed slow brucite dissolution.

In presence of both, silica and brucite, initially, a transitional M-S-H phase with a Mg/Si ratio of 0.9-1.1 is formed, independently of the total Mg/Si ratio in the sample. The formation of such an initial M-S-H with Mg/Si ≈1 in presence of amorphous silica and brucite is consistent with literature data on the properties of M-S-H after short equilibration times where generally only the formation of M-S-H with a Mg/Si ratio of approximately 1 is reported (d'Espinose de Lacaillerie et al., 1995; Brew and Glasser, 2005a; Brew and Glasser, 2005b; Zhang et al., 2011; Szczerba et al., 2013; Li et al., 2014). Only in a few studies where longer equilibration times had been monitored, a

wider range of Mg/Si ratio was observed (Kalousek and Mui, 1954; Roosz et al., 2015; Nied et al., 2016), consistent with the present study where a broader range of Mg/Si ratio from 0.8 to 1.3 in the solid was observed after longer storage and slightly different structures started to evolve depending on the initial Mg/Si ratio.

The M-S-H phases formed undergo a slow ripening process resulting in less soluble M-S-H after longer equilibration times. At 50 and 70°C the M-S-H formation occurred faster, but a similar gel-like structure of M-S-H and a comparable range of Mg/Si ratio were observed at 20°C. The calculated solubilities of M-S-H are similar in range to those reported in a previous study (Nied et al., 2016) and comparable to the solubility of crystalline magnesium silicate hydrates such as talc or antigorite investigated in this study or to talc and antigorite/chrysotile as reported in the literature (Helgeson, 1978; Tardy and Duplay, 1992; Holland and Powell, 1998; Melekhova et al., 2006) and as shown in Figure 20.

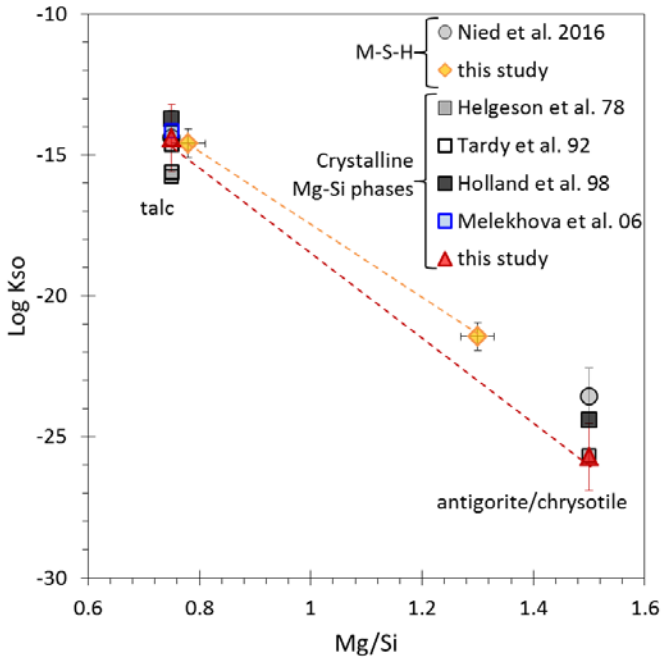

Figure 20: Evolution of the solubility product at 25°C as a function of the initial Mg/Si (with Si = 1), triangles and diamonds correspond to the experimental data presented in the Appendix and the Table 13, others are adapted from literature (Helgeson, 1978; Tardy and Duplay, 1992; Holland and Powell, 1998; Melekhova et al., 2006; Nied et al., 2016) for comparison.

3.3. Characterization of magnesium silicate hydrate

This part corresponds to the future publication in preparation: Ellina Bernard, Barbara Lothenbach, Christophe Chlique, Mateusz Wyrzykowski, Alexandre Dauzères, Isabelle Pochard, Céline Cau-Dit-Coumes, Characterization of magnesium silicate hydrate (M-S-H).

In the previous part, M-S-H phases were observed very slow to form and the range of compositions of pure M-S-H was described with Mg/Si from 0.8 to 1.3.

In this part, the effect of the Mg/Si ratio (ranging from 0.7 to 1.4) on the M-S-H structure (samples aged of 1, 2, or 3.3 years at 20°C), including the distribution of the water and the particle properties, were investigated by ^{29}Si MAS-NMR, ^{1}H-^{29}Si CP MAS-NMR and FT-IR spectroscopy and with X-rays diffraction and X-ray pair distribution function analysis, the water and hydroxyl contents and their distribution by DVS, TGA and ^{1}H-NMR relaxometry, the particle size and the porosity by N_2 physio-sorption measurements and the surface properties by CEC and zeta potential measurements. This study aimed to contribute to better understand the ill-structure of M-S-H, the repartition of the different types of water in it and its surface properties. Analytical techniques are detailed in chapter 2.2 and the specific techniques (X-ray pair distribution function analysis, N_2 physio-sorption measurements, ^{1}H-^{29}Si CP MAS-NMR, DVS, and ^{1}H-NMR relaxometry) are described in the Part 2.3.2.

In addition, two M-S-H (Mg/Si = 0.8 and 1.2) suspensions, which had been previously equilibrated at 20°C, were treated hydrothermally. The two suspensions were heated in a stainless steel autoclave at 180 °C for 4 days, followed by a slow cooling to room temperature during approximately 12-24 hours. The filtration process and freeze drying process was similar as M-S-H samples.

3.3.1. Results and discussions

3.3.1.1. Insights on the M-S-H particles

3.3.1.1.1. Ageing of M-S-H

The formation of M-S-H proceeds in batch experiments very slowly such that after 1 year at room temperature thermodynamic equilibrium is generally not yet reached while after 2 years M-S-H seemed to have been near to equilibrium conditions

as detailed in the previous chapter. Thus, in addition, also well-aged samples with an equilibration time of 3.3 years were investigated. To verify that (near) equilibrium conditions have been reached, the composition of the aqueous and solid phase after 3.3 years were compared to M-S-H equilibrated for 1 and 2 years from the previous chapter and to M-S-H which has been prepared at 180°C (hydrothermally prepared: "M-S-H HT"). Dissolved concentration and pH values measured in the aged samples (3.3 years) are presented in Table 14. The concentrations and pH measured after 3.3 years were comparable to the 2-year old samples which indicated that 3.3 years samples, as well as the 2 years ones, were close to thermodynamic equilibrium.

Table 14: Measured dissolved concentrations in the solutions and measured pH values in equilibrium with the synthesized M-S-H samples after 3.3 years of curing at 20°C and with the hydrothermally prepared M-S-H (0.8 and 1.2).

mmol/L	Mg	Si	Na	pH (20°C)
room temperature				
0.7	0.39	1.49	0.34	8.3
0.8	0.38	1.26	0.37	8.3
0.9	0.41	0.46	0.42	8.5
1.0	0.43	0.05	0.45	9.1
1.1	0.25	0.009	0.47	9.7
1.2	0.23	0.005	0.51	9.9
1.3	0.18	<0.002	0.52	10.3
1.4	0.15	<0.002	0.53	10.4
M-S-H HT				
0.8	0.24	1.821	0.38	8.1
1.2	0.35	0.024	0.53	9.2

Also, the ^{29}Si MAS NMR spectra of M-S-H samples cured 3.3 years at room temperature were compared to the spectra of the 1 year-old samples and to the hydrothermally prepared M-S-H in Figure 21. The overall shapes of the spectra were similar between the 1 year and 3.3 years samples.

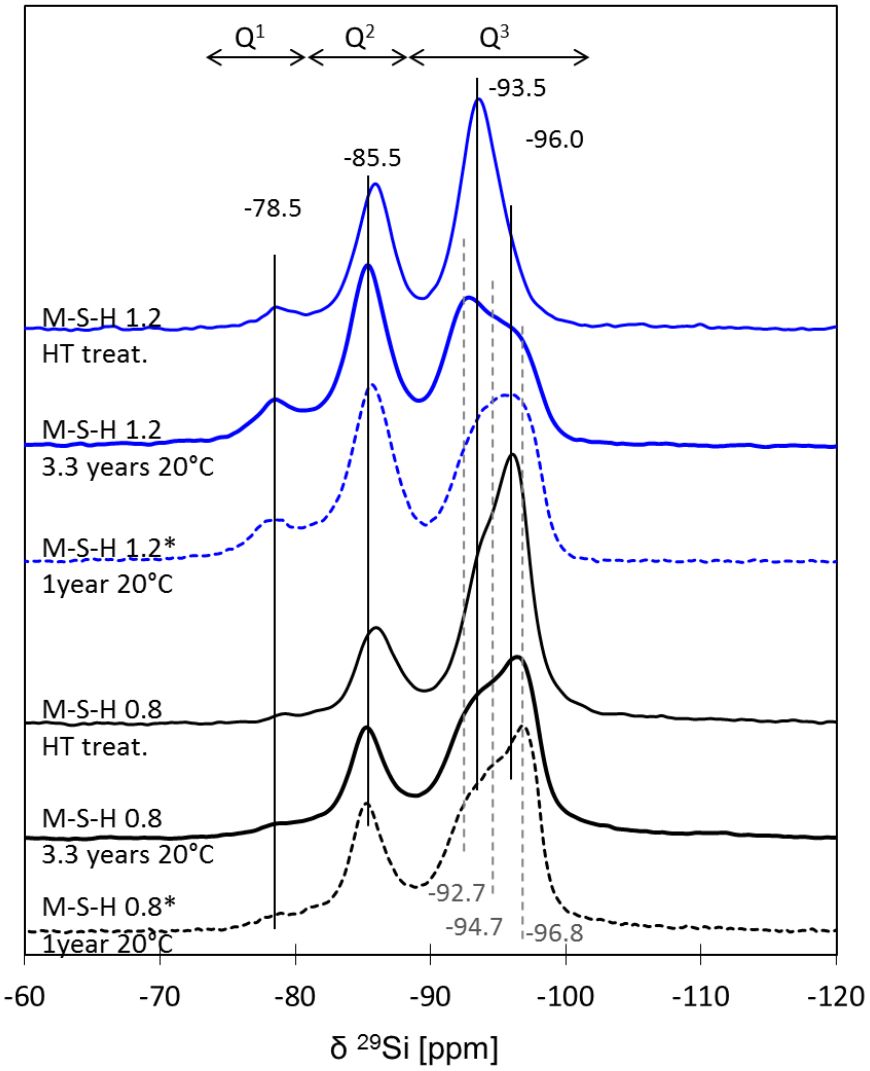

Figure 21: ^{29}Si MAS NMR spectra of the M-S-H hydrothermally prepared (0.8 and 1.2) compared to ^{29}Si MAS NMR spectra of M-S-H samples synthesized at 20°C after 1 year (*=from chapter 3.2) or 3.3 years of curing.

The deconvolutions of the spectra are detailed in Table 15. The M-S-H 0.8 aged for 3.3 years samples showed a lower content of Q^2 and higher content of Q^3_{tot} resulting in a reduced Q^2/Q^3 than the sample aged for 1 year. This greater degree of polymerization in the aged sample indicates that with time the structure of low Mg/Si M-S-H becomes more similar to talc, which shows a single, rather narrow Q^3 band at -97 ppm (Rhouta et al., 2008; Chabrol et al., 2010; Dumas et al., 2013). Also, the hydrothermally prepared M-S-H showed a higher degree of ordering and a more distinct but still rather broad band -96.5 ppm. This trend of higher ordering at higher temperature agrees with other findings (Yang, 1960; Mitsuda and Taguchi, 1977), who observed a progressive better ordered structure for M-S-H formed at higher temperatures and the formation of talc at 600°C.

For the M-S-H 1.2 sample which contains more magnesium, the amount of Q^1, Q^2 and Q^3_{tot} did not change significantly between 1 to 3.3 years. However, a higher

intensity of the signal at -92.7 ppm (Q^3_a) after 3.3 years indicated a somewhat greater degree of organization and a structure related to serpentine group minerals such as lizardite or antigorite (Mg/Si=1.5, T:O structure, see Figure 6). The hydrothermally prepared M-S-H 1.2 showed one only Q^3 band at -93 ppm which would be consistent with a 1:1 T:O well-ordered structure.

Table 15: Chemical shifts and relative intensities of different silicon sites obtained from the deconvolution of the ^{29}Si MAS NMR spectra of M-S-H synthesized at room temperature and prepared hydrothermally (HT) presented in Figure 21.

		M-S-H (room temperature)					
		Q^1 -78.3 ±0.3 ppm	Q^2 -85.5 ±0.3 ppm	Q^3a -92.7 ±0.3 ppm	Q^3b -94.7 ±0.3 ppm	Q^3c -96.7 ±0.3 ppm	Q^2/Q^3
0.8	1 year	3	34	25	8	26	0.6
0.8	3.3 years	2	28	26	17	23	0.4
1.2	1 year	7	46	14	12	21	1.0
1.2	3.3 years	8	47	25	6	14	1.0
		M-S-H (HT. prepared)					
		Q^1 -79.0 ±0.5 ppm	Q^2 -85.8 ±0.5 ppm	Q^3a -93.7 ±0.5 ppm		Q^3c -96.2 ±0.5 ppm	Q^2/Q^3
0.8	HT	0	22	30		48	0.3
1.2	HT	5	32	63		0	0.5

Quantification error ≃ ± 10% of absolute amount of (%Si) +2.5%.

In summary, M-S-H synthesized at room temperature were similar after 1 or 3.3 years although the longer reaction time resulted in slightly better-ordered structures. The M-S-H 0.8 HT structure is comparable to a poorly ordered 2:1 phyllosilicate such as talc or stevensite while M-S-H with a higher Mg/Si showed rather a structure similar to a 1:1 phyllosilicate such as antigorite. In all cases, a significant amount of Q^2 was still present, also in the hydrothermally prepared samples.

3.3.1.1.2. X-rays diffraction

X-ray diffraction patterns

The XRD patterns of the M-S-H phases with different Mg/Si ratios together with the hydrothermally prepared M-S-H are shown in Figure 22a. XRD patterns showed only large humps. The patterns were very similar with equal relative intensity and positions of the broad reflections independent of the Mg/Si ratio. The humps have been indexed, in Figure 22a, following the indexing of M-S-H based of talc, $Mg_3Si_4O_{10}(OH)_2$, from (Roosz et al., 2015) and also based on the structure of kerolite, $Mg_3Si_4O_{10}(OH)_2.H_2O$, a hydrated variety of talc from (Brindley et al., 1977; Brindley et al., 1979) and of deweylite from (Bish and Brindley, 1978), a naturally occurring hydrous amorphous magnesium silicate with a composition between $Mg_3Si_4O_{10}(OH)_2$ 0.3-0.7H_2O and $Mg_3Si_2O_5(OH)_4$0.3-0.7H_2O. Kerolite or deweylite had been described by (Brindley et al., 1977; Bish and Brindley, 1978; Brindley et al., 1979) as extremely fine-grained or disordered talc or stevensite minerals possibly mixed with minerals from the serpentine group such as lizardite or antigorite. Similar to the reflection profiles of M-S-H, the XRD patterns of these materials are broad indicating extremely small crystallite size, disorder or both. (Lin et al., 2017) compared M-S-H-like phase to hectorite, swelling clay, and indexed the broads reflections as detailed in Figure 22b.

The reflections at 59.9 °2θ are shifted to slightly lower angles at higher Mg/Si (both for preparations at ambient and hydrothermal temperatures). These reflections are characteristic for the main layer of trioctahedral phyllosilicates. This difference from M-S-H 0.8 to M-S-H 1.2 is consistent with the slight increase of the 060 distance from 1.528 Å (60.5 °2θ) in 2:1 phyllosilicates (talc) to 1.54 Å (60.05 °2θ) in 1:1 phyllosilicates (serpentine). This indicates only small changes in the large scale of the sheets arrangement.

The reflection at 27.2°2θ corresponds to the (003) distance of talc and is better defined in the M-S-H 0.8HT sample. A reflection at 24.9°2θ can be observed in M-S-H 1.2HT, which could be attributed to the (002) of the serpentine mineral. Those observations confirmed a high resemblance of the hydrothermally prepared M-S-H with the two end-members talc (2:1) in the case of M-S-H 0.8HT and serpentine (1:1) minerals in the case of M-S-H 1.2HT.

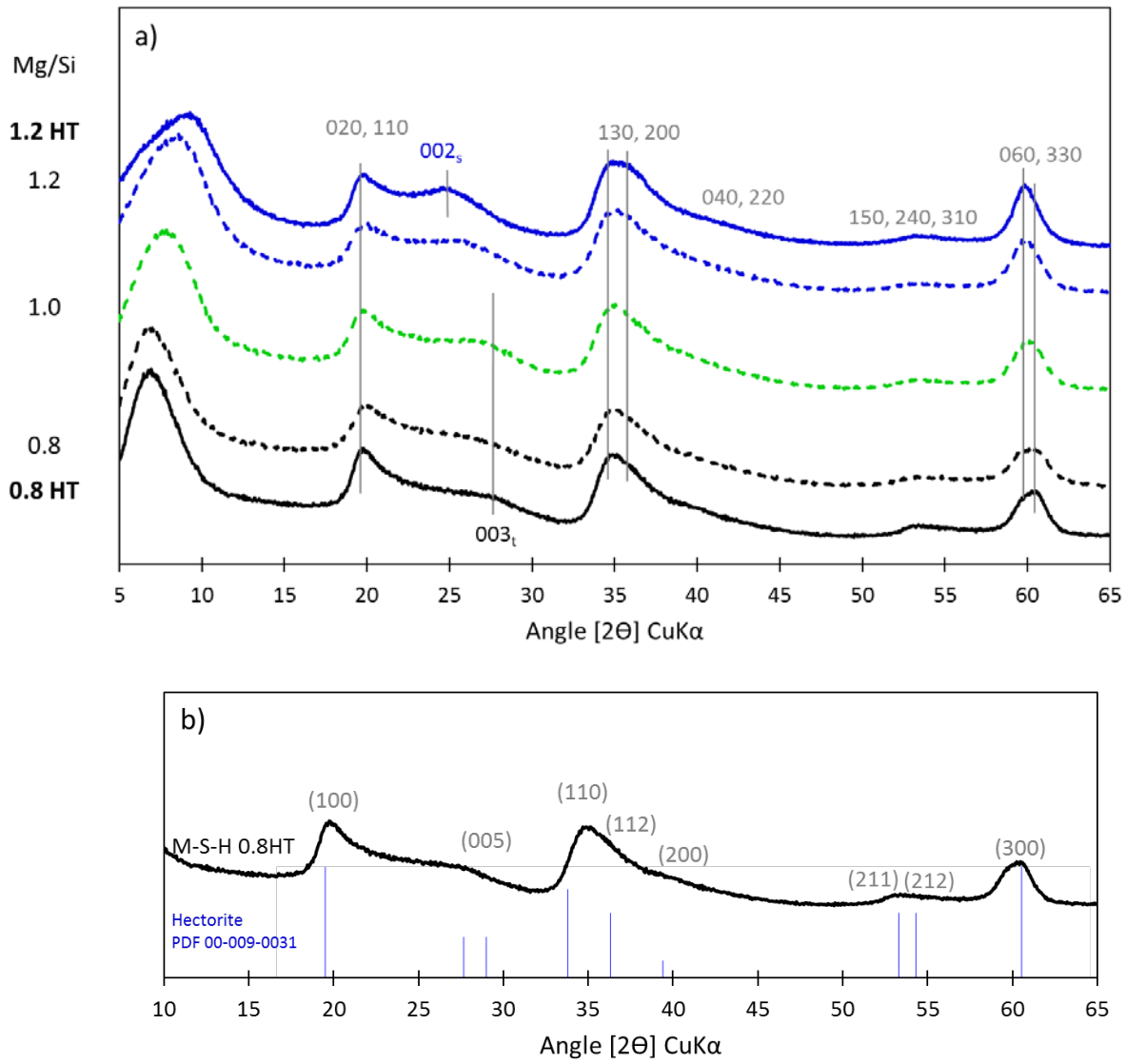

Figure 22: a) XRD patterns of M-S-H samples (3.3 years, 20°C) and of hydrothermally treated M-S-H indexed following kerolite, $Mg_3Si_4O_{10}(OH)_2.H_2O$ (0.8: $(003)_t$ for talc and 1.2$(002)_s$ for serpentine); b) XRD patterns of M-S-H 0.8 HT indexed following hectorite.

Basal spacing drying and swelling

The main difference between the patterns of M-S-H (Figure 22) was in the reflection at 7-9 °2θ which corresponds to layer-to-layer (001) distance as detailed in (Roosz et al., 2015). As discussed in (Roosz et al., 2015), the minimal coherent regions in M-S-H phases can lead to shifts of the signals related to the 001 distance which can result in an overestimation of this distance. The 001 distance of the M-S-H 0.8 was at the detection limit and could be larger than the 12.7 Å indicated in Figure 23. The measured layer-to-layer distances of the M-S-H synthetized at room temperature and hydrothermally prepared are plotted in Figure 23 as a function of the Mg/Si.

An increase of Mg/Si ratio from 0.8 to 1.2 resulted in a shift of the first reflection from 7.0 to 8.6° 2θ indicating a decrease of the mean basal spacing from at least 12.7 Å to 10.3 Å.

The drying procedure affected the measured (001) distance, as visible at high Mg/Si. The freeze dried samples re-equilibrated to 30 % RH always showed a lower layer-to-layer distance than samples which were dried directly to 30 % RH, without initial freeze drying as shown in Figure 23, indicating that freeze drying resulted in a collapse of the interlayer which was not or only partially restored during rehydration.

The addition of ethylene glycol to the freeze-dried samples resulted in an increase of their layer-to-layer distances indicating a swelling of the M-S-H as also characteristic for hydrated 2:1 phyllosilicates with layer charge. At low Mg/Si, the (001) the distance was either too large to be measured (>12.7) or non-existing while at high Mg/Si the distance increased 10.3 to 11.6 Å.

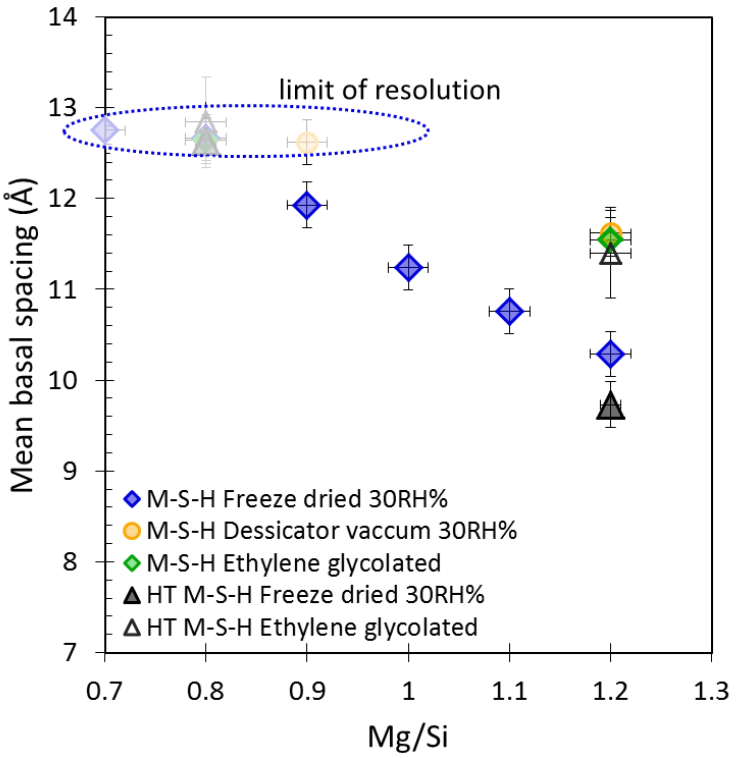

Figure 23: Mean basal spacing (layer-to-layer distance) measured from XRD patterns of the M-S-H samples (diamonds and circles) and for hydrothermal prepared M-S-H (triangles) as a function of Mg/Si in M-S-H. Freeze dried = freeze dried samples and re-equilibrated to 30RH% over $CaCl_2$, desiccator vacuum= directly dried over $CaCl_2$ 30RH% (*might be not completely equilibrated) in a vacuumed desiccator.

X-ray pair distribution function (PDF)

Additional characterizations of the M-S-H samples were performed using X-ray pair distribution function (PDF) analysis (Figure 24).

The X-ray PDF analyses of the M-S-H samples were very similar regardless the Mg/Si ratio (Figure 24a). Figure 24b compares the pair distribution functions of M-S-H, sepiolite (Sánchez del Río et al., 2011), talc (Gruner, 1934), antigorite T (Dódony et al., 2002) and brucite (Zigan and Rothbauer, 1967). The structures of these minerals are schematically represented in Figure 6 and Figure 25. Antigorite (Figure 25) corresponds to a 1:1 phyllosilicate (serpentine group) and differs from lizardite (Figure 6c) by a wave structure with alternated T:O blocks.

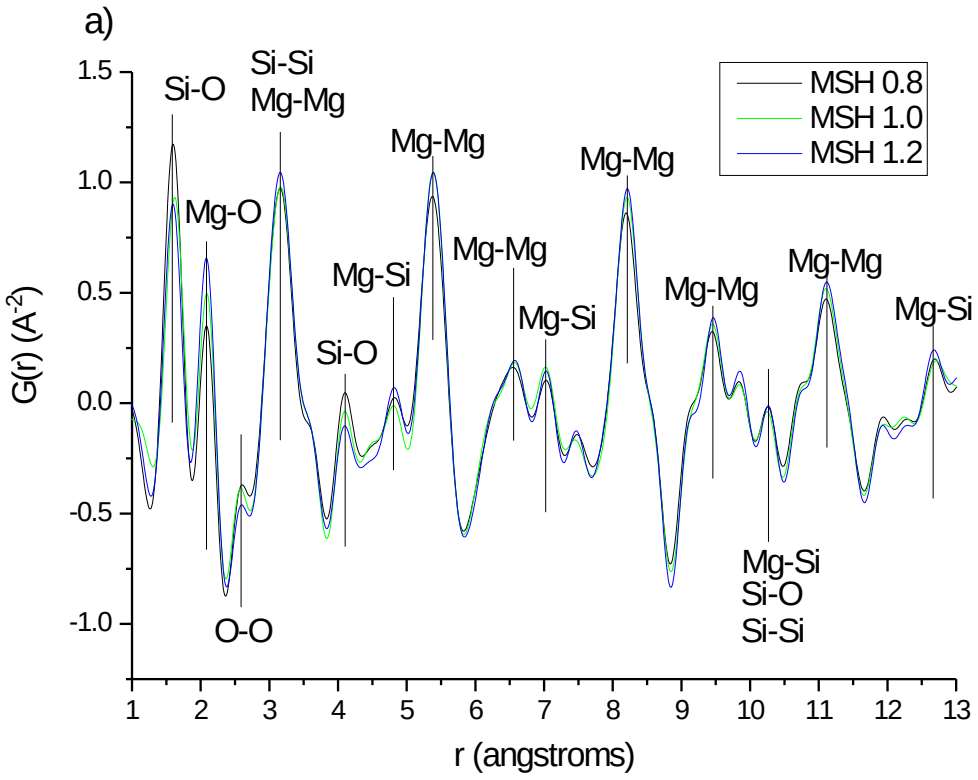

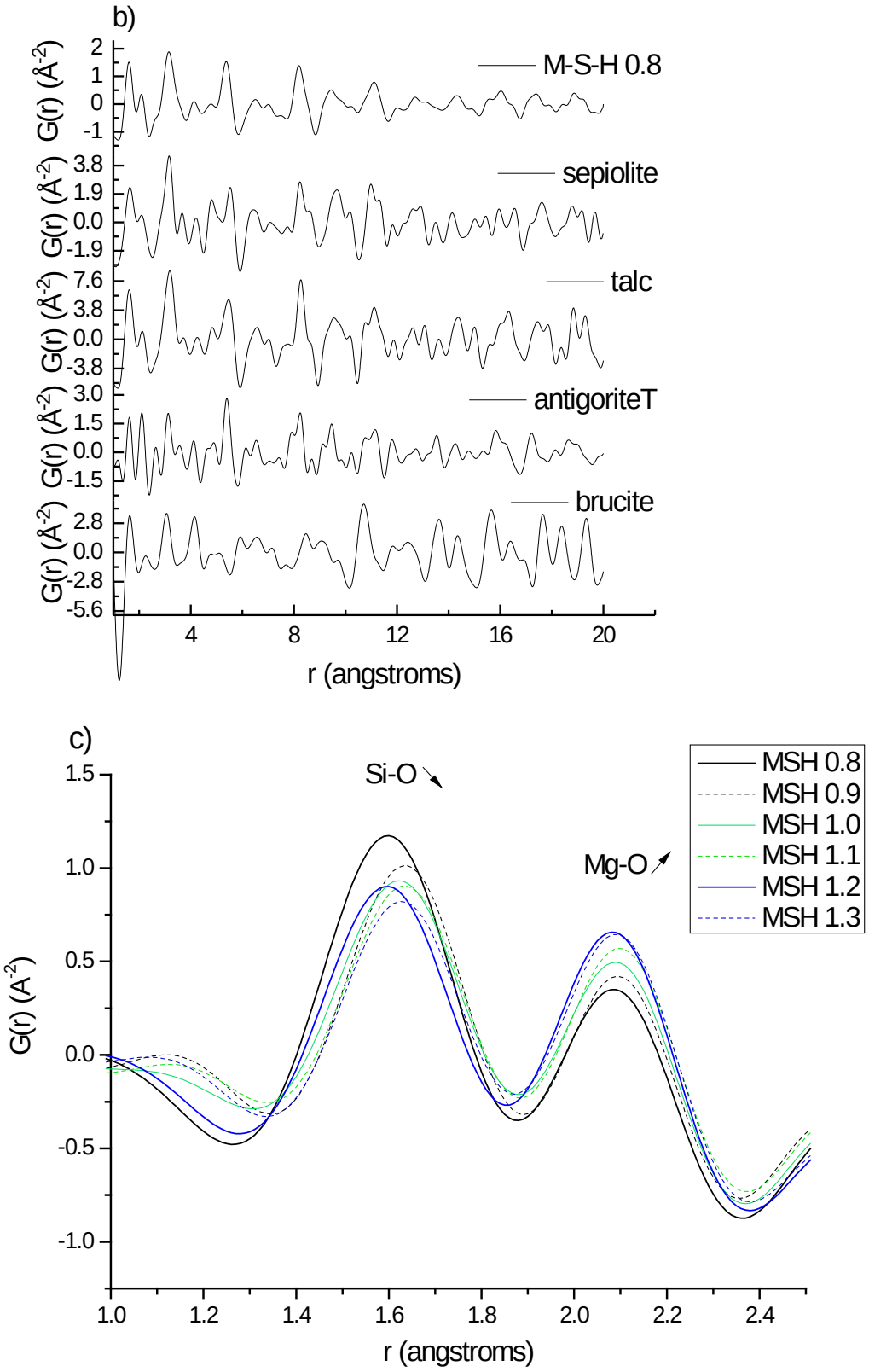

Figure 24: a) X-ray pair distribution function of M-S-H 0.8, 1.0 and 1.2, b) X-ray pair distribution function of M-S-H 0.8 compared to X-ray pair distribution functions of sepiolite, talc, antigorite T and brucite, c) Zoom on X-ray pair distribution functions of M-S-H 0.8 to 1.3.

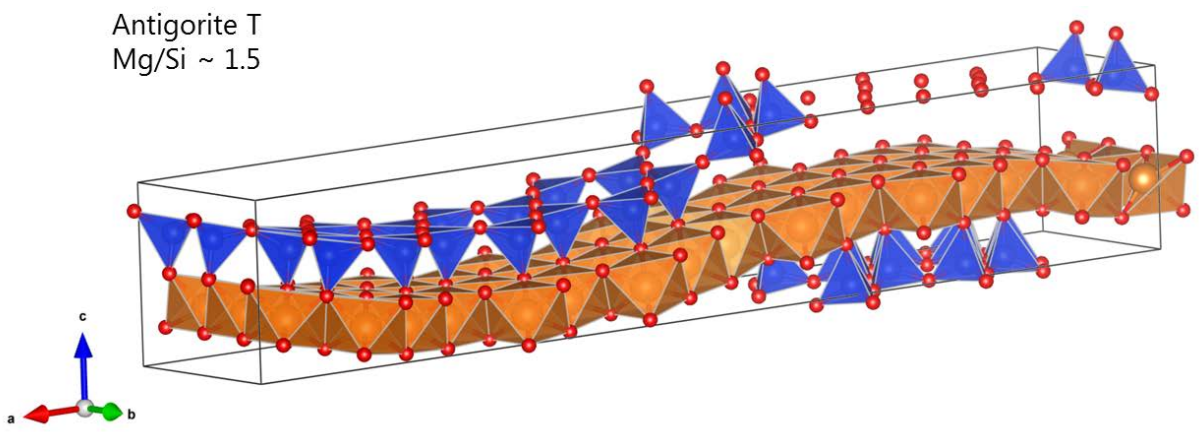

Figure 25: Schematic sketch of the structure of antigorite T (T:O structure phyllosilicate) from (Dódony et al., 2002).

Compared to the crystalline minerals which showed a coherence length higher than 20 Å (Figure 24b), M-S-H exhibited a rather short coherence length, close to 12 Å (Figure 24b) whatever the Mg/Si ratio, which is consistent with their poorly crystalline nature and the nano-sized particles as previously discussed.

The peaks were tentatively assigned using the structures of talc and antigorite as references (Gruner, 1934; Dódony et al., 2002): they mainly corresponded to Mg-Mg (r = 3.13 Å, 5.36 Å, 8.21 Å, 9.42 Å, 11.06 Å) and Mg-O (2.09 Å) distances within the same layer as well as Si-Si (3.20 Å) and Si-O distances in tetrahedral silicate layer (r =1.61 Å). The X-ray PDF analysis of M-S-H confirmed a structure where magnesium is bound to oxygen in the surrounding of silicon and hydroxyl groups. The intensity of the Si-O peak at r = 1.6 Å decreased whereas that of the Mg-O peak at r = 2.1 Å increased at high Mg/Si ratio, which was consistent with the depletion of SiO_2 and the enrichment in MgO (Figure 24c). The slight variations in the positions of the peak maxima were due to experimental uncertainties.

In a second stage; we tried to fit the pair distribution functions of M-S-H by refining the structures of the different phyllosilicate minerals using the PDFgui software (Farrow et al., 2007). The refined parameters included the scale factor, the lattice parameters (a, b and c, the angles being kept constant), the isotropic displacement parameters of Mg, Si and O, and δ_1, a coefficient for (1/r) contribution to the peak sharpening (for small distances, the motion of two contributing atoms can be correlated). The instrumental resolution parameter was determined by refinement of a nickel reference sample as Q_{damp} = 0.05. The calculations were performed over the 1-20 Å range. Figure 26 compares the pdf function of M-S-H 1.3 with those resulting from the refinement of sepiolite (Sánchez del Río et al., 2011), talc (Gruner, 1934), chrysotile

(Falini et al., 2004), lizardite (Mellini and Zanazzi, 1987), antigorite M (monoclinic) and antigorite T (triclinic) (Dódony et al., 2002). The fit parameters are detailed in the Appendix C. The best fit, corresponding to the lowest residuum r_w (quality weighted parameter characterizing the difference between observed and simulated pdfs) was obtained for triclinic antigorite Tb (Dódony et al., 2002). Antigorite has an alternating-wave structure slightly deficient in magnesium and hydroxyl groups. Antigorite Tb, described by (Dódony et al., 2002), shows one or more offsets in the octahedral sheet at the change of T:O. At this offset, the coordination number of the magnesium atoms decreases to six, and oxygen atoms in the vicinity form a tetragonal pyramid around it. Chrysotile was the second best fit. This mineral is composed of tubular fibers due to the rolls up of the sheets. The pdf results are consistent with the ^{29}Si MAS NMR data showing a silicate structure of M-S-H 1.3 similar to that of the phyllosilicates of the serpentine group. The better fits with chrysotile and antigorite T rather than with lizardite and antigorite M would indicate that the stacking of sheets is wavy and the T:O-like blocs are randomly repeated. The chemical composition and the nano-crystallinity of the M-S-H 1.3 sample would suggest a structure close to that of antigorite rather than chrysotile which has the almost ideal chemical composition $Mg_3Si_2O_5(OH)_4$ (Mg/Si = 1.5), causing the fibrous shape (octahedral sheet larger than the tetrahedral one).

Similarly, the X-ray pair distribution function of M-S-H 0.8 was fitted by refining the structures of lizardite, chrysotile, antigorite (monoclinic or triclinic) talc and sepiolite as shown in Figure 27. The best fit was surprisingly achieved with triclinic antigorite Tb, followed by talc and sepiolite. A structure close to that of triclinic antigorite, as for M-S-H 1.3, would be consistent with the fact that these two samples exhibit similar XRD patterns and pair distribution functions. It would also suggest a wavy structure at low Mg/Si ratio. However, the results obtained by other characterization techniques rather indicate a talc-like structure:

- the Mg/Si ratio of M-S-H 0.8 is close to that of a 2:1 phyllosilicate;
- M-S-H 0.8 HT and talc exhibit strong resemblance, as shown by X-ray diffraction and ^{29}Si MAS-NMR.

Looking more closely at the fit obtained with the refined structure of talc, it can be seen that the quality of the fit decreased for r distances above the coherence length of the M-S-H particles (12 Å). Restricting the fit calculations to the 1-12 Å range provided vey good results (Figure 28), both with talc and antigorite (r_w = 0.42 in both cases). Complementary techniques and/or a better resolution (provided by a high energy synchrotron source) are thus necessary to discriminate between the two structures.

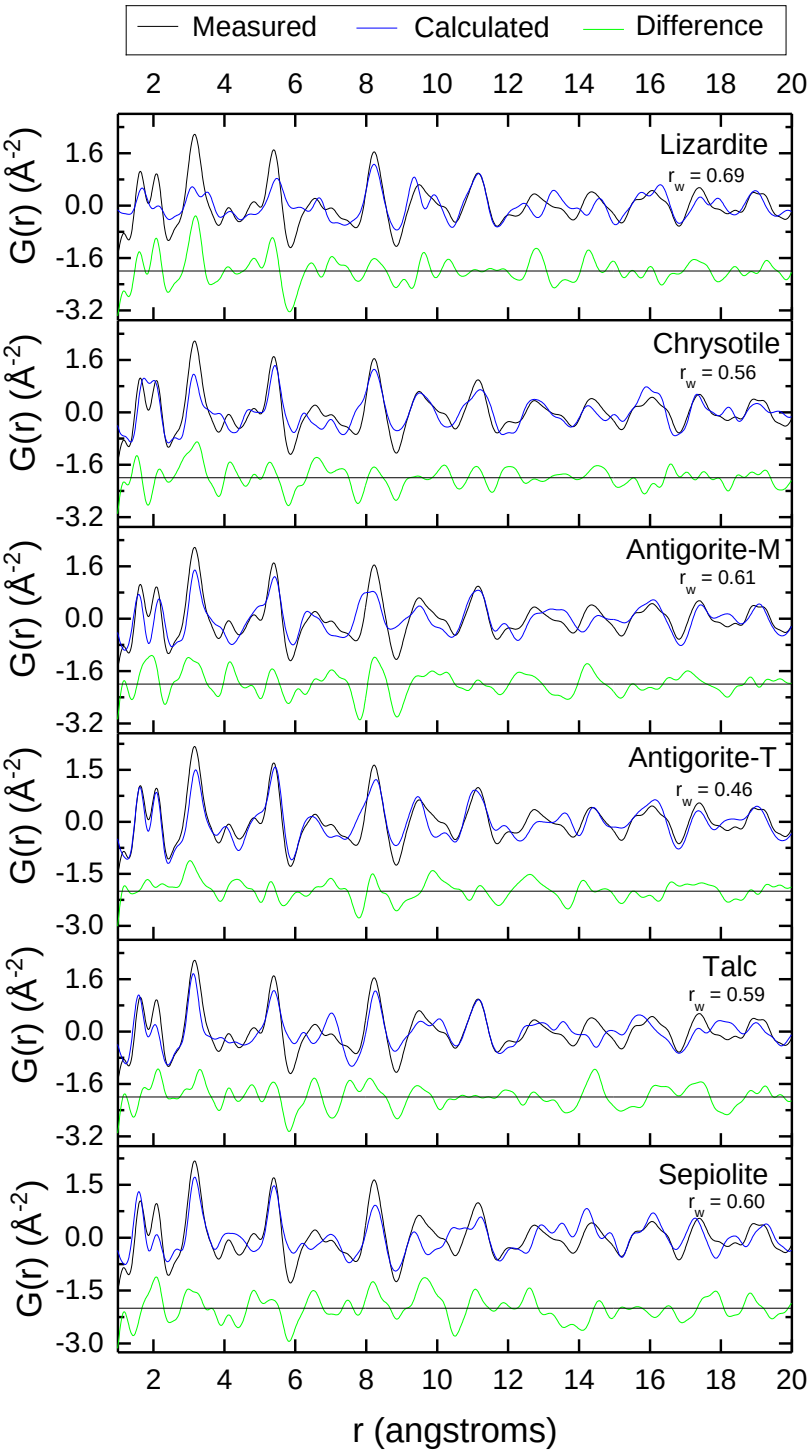

Figure 26: Comparison of M-S-H 1.3 X-ray distribution function with those of the refined structures of lizardite, chrysotile, antigorite, talc and sepiolite over the range 1-20 Å (details of the fits in the Appendix C).

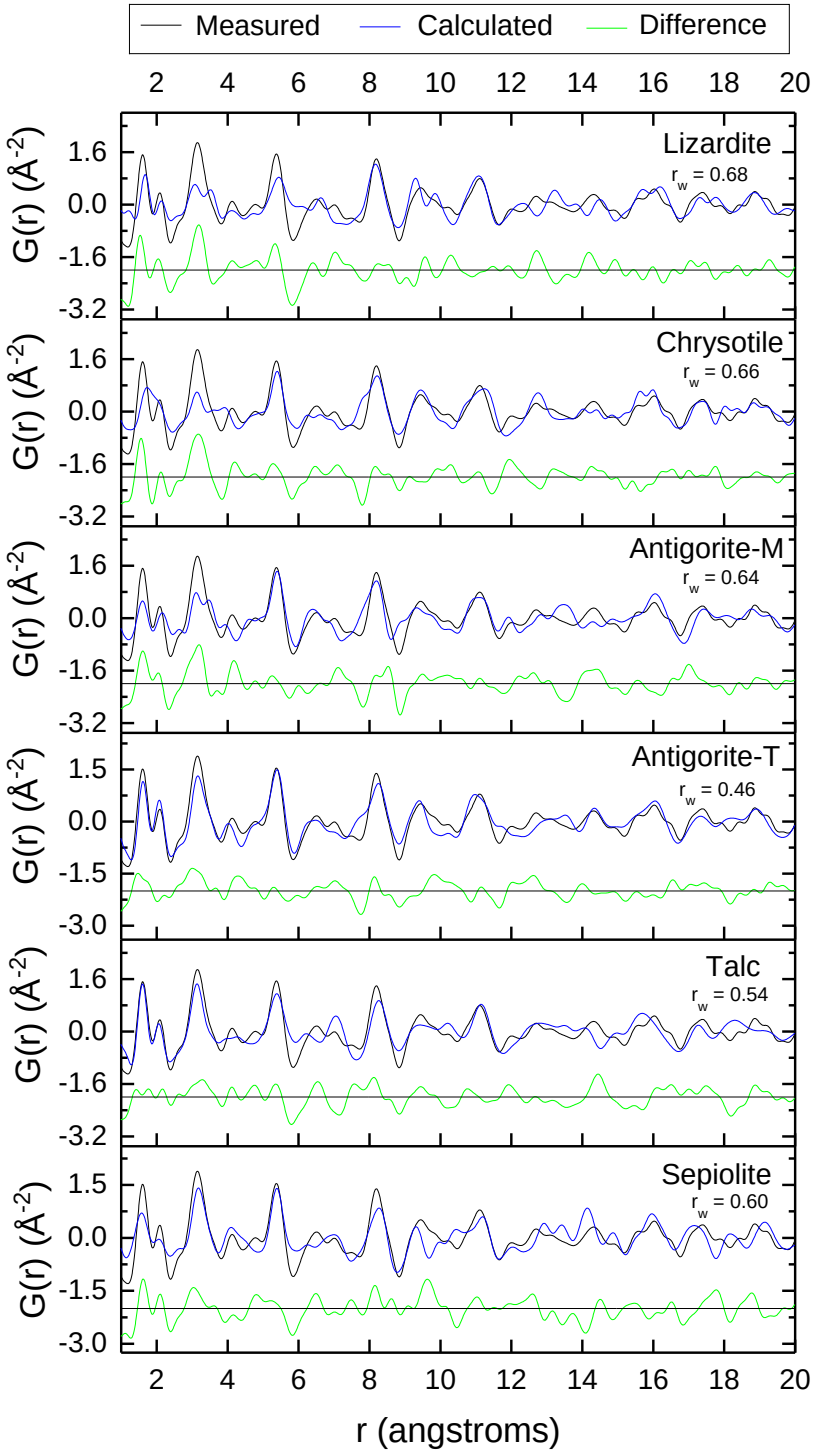

Figure 27: Comparison of M-S-H 0.8 X-ray distribution function with those of the refined structures of lizardite, chrysotile, antigorite, talc and sepiolite over the range 1-20 Å (details of the fits in the Appendix C).

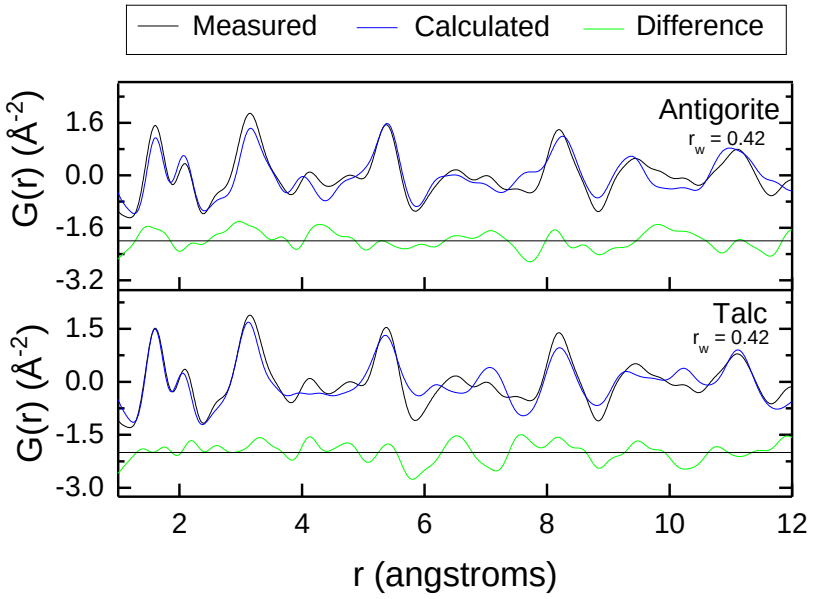

Figure 28: Comparison of M-S-H 0.8 X-ray distribution function with those of the refined structure of triclinic antigorite (Tb) and talc over the range 1-12 Å (details of the fits in the appendix Appendix C).

The X-ray PDF analyses of M-S-H showed similar atoms distances in M-S-H as in phyllosilicate minerals and thus agree with the ^{29}Si MAS NMR data: M-S-H phases are composed of silicate sheets with small coherent regions.

3.3.1.1.3. Particle size, porosity, and density

M-S-H samples aged of 3.3 years were characterized by N_2 physio-sorption measurements. The isotherms with the presence of hysteresis loops (Figure 29) were of the IV type according to the IUPAC classification (Sing et al., 1985). This hysteresis had been associated to capillary condensation taking place in mesopores (diameter between 2 nm and 50 nm). The initial part of the Type IV isotherm can be attributed to monolayer-multilayer adsorption. The general features of the N_2-isotherm were similar to those observed for phyllosilicates synthesized at room temperature such as reported for synthetic clay-like hydrated hetorite, stevensite or saponite (Vogels et al., 2005; Bisio et al., 2008; Chabrol et al., 2010) or talc (Michot et al., 1994).

The M-S-H samples synthesized at room temperature exhibited an H2 or H4 hysteresis characteristic of plate-like materials with mesopores (Sing et al., 1985). The H2 hysteresis is characteristic of less ordered material than H4. The micro-porosity (< 2 nm) in clay usually corresponds to the inter lamellar gallery (interlayer?), and the

meso- porosity corresponds to meso- pores formed between the particles (particularly during acid treatment) (Chevalier et al., 1994).

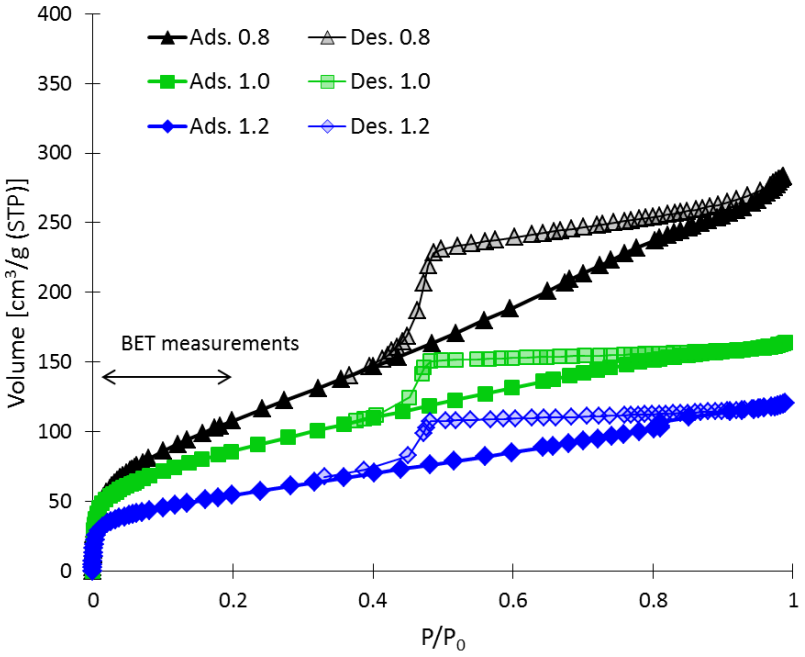

Figure 29: N_2 adsorption-desorption isotherms of the M-S-H samples 0.8, 1.0 and 1.2 (synthetized at room temperature during 3.3 years).

The specific surface areas (SSA) were calculated from the N_2 physio-sorption measurements by applying the BET equation (Brunauer et al., 1938). The SSA calculated by BET method is expected underestimated for this type of material due to a large fraction of the surface in the micropores. However, the relative comparison between SSA_{BET} of the different samples is possible. A SSA_{BET} of 400, 315 and 194 m^2/g, respectively, was calculated for M-S-H 0.8, 1.0 and 1.2 after 3.3 years (Figure 30). The relatively high measured SSA_{BET} for M-S-H were similar to the large surface area reported for synthetic clay-like (Vogels et al., 2005; Bisio et al., 2008; Chabrol et al., 2010), where macro and mesopores are present together with micropores, while the SSA of talc is much smaller, usually around 20 m^2/g (Michot et al., 1994). The SSA_{BET} of synthetic clay has been observed to increase with the water to solid ratio used during the synthesis (Bisio et al., 2008). Thus M-S-H formed in non-diluted systems or in field experiments might exhibit a smaller SSA.

Figure 30 shows the SSA_{BET} as a function of the Mg/Si in M-S-H and different curing time and temperature. The SSA_{BET} decreased with the Mg/Si in M-S-H. The curing temperature, 20 or 50°C, did not influence the SSA_{BET}. The SSA_{BET} was lower for the older samples indicating the formation of slightly bigger particles with time. The SSA_{BET} for M-S-H 0.8 (~ 400 m^2/g) was 2 times higher than for M-S-H 1.2 (~ 200 m^2/g).

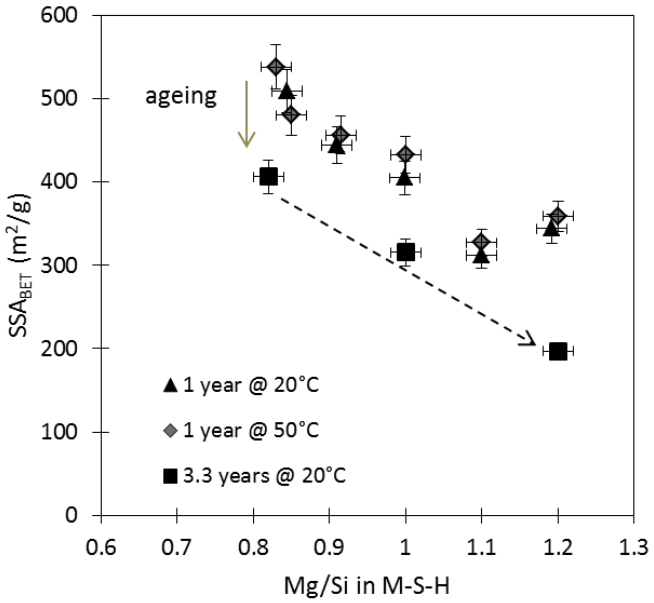

Figure 30: Specific surface area (SSA_{BET}) found in M-S-H as a function of the Mg/Si in M-S-H and of the curing time.

The t-plot method (which is detailed in the methods 2.3.2) quantifies the micropores in M-S-H. The volume of micropores decreased with the increase of the Mg/Si in M-S-H and the reduction of the specific surface area measured. New total $SSA_{t\text{-}plot}$ were calculated based on the $SSA_{t\text{-}plot}$ measured from the meso- and macro-pores and the volume of micro pores. The grain density of M-S-H measured by helium pycnometry was relatively constant between 2 and 2.1 g/cm^3 (Table 16) in M-S-H independently of the Mg/Si.

Table 16: Specific surface area (SSA) for M-S-H equilibrated for 3 years and hydrothermally prepared (HT) calculated by BET and t-plot methods from nitrogen isotherms.

	BET				t-plot			
	SSA[a]	C value[b]	Vads[c]	Pore volume[d]	SSA (meso and macro)	V (micro pore)	SSA total	Grain density[e]
	m^2/g		cm^3/g STP	cm^3/g	m^2/g	cm^3/g	m^2/g	
0.8	**400**	46	91	0.15	488	0.047	621	2.1
1	**315**	74	73	0.12	320	0.007	340	2.0
1.2	**194**	112	45	0.07	197	0.002	203	2.1
0.8HT	**378**	62	87	0.13	494	0.055	649	
1.2HT	**340**	105	78	0.12	377	0.017	425	

[a] Calculated directly with the software
[b] BET C constant value
[c] the volume adsorbed in one complete unimolecular layer
[d] Vads/647 (gas/liquid volume ratio ~ 647 for N_2 at 77 K)
[e] averaged values of the measurements on the samples synthetized 1 year at 20°C and 3 months at 50°C (standard deviation ± 0.05).

N_2 physio-sorption measurements on the hydrothermally treated M-S-H indicated also type IV isotherms according to the IUPAC classification, but an H3 hysteresis (Figure 31). The H3 hysteresis is related to aggregated materials with plate-

like structure creating slit-shaped pores. This confirms a better organization of the structure the hydrothermal treatment of the M-S-H and indicates the presence of a second porosity, which may be due to different packing.

A SSA_{BET} of 378 and 340 m^2/g have been measured in the M-S-H 0.8HT and M-S-H 1.2HT respectively. These values are relatively high and in the same range or even greater than the SSA_{BET} measured for M-S-H synthesized at room temperature. The upper surface area and higher volume adsorbed of M-S-H1.2HT compared to M-S-H 1.2 prepared at room temperature from BET might be related to this observed 2nd porosity difference in packing. The M-S-H 0.8 equilibrated at room temperature and the hydrothermally prepared HT show a strong similarity in N_2 sorption (size and volume of the micropores) and in ^{29}Si-NMR indicating no or little structural difference except the increased ordering in the sample treated at higher temperature. The different micro porosity and silicate structure defined in the M-S-H 1.2HT compared to M-S-H 1.2 seems to indicate a structural rearrangement during the hydrothermal treatment.

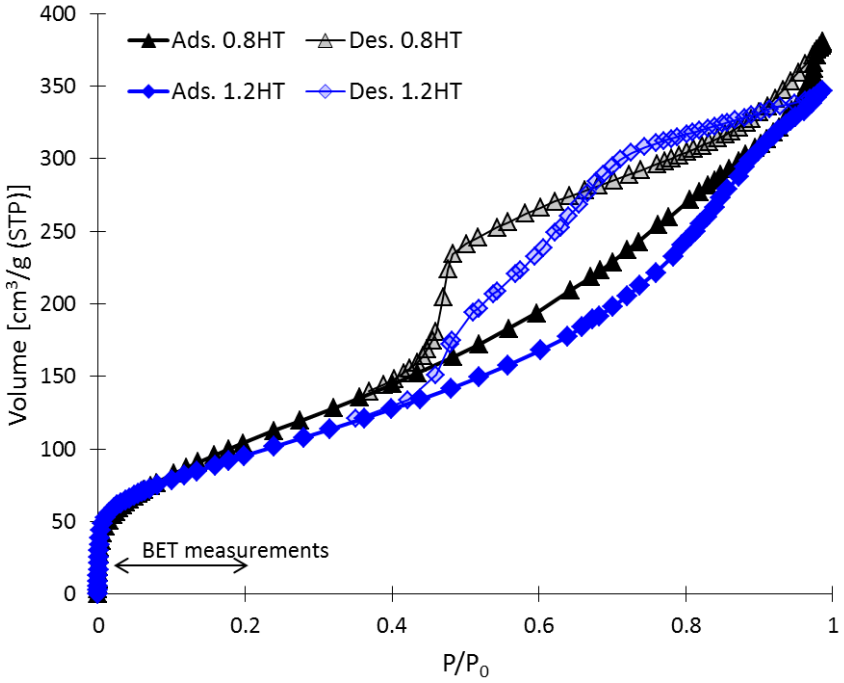

Figure 31: N_2 absorption-desorption isotherms of the hydrothermally treated M-S-H.

3.3.1.2. Water in M-S-H

Crystalline phyllosilicates, such as talc, which represents 2:1 structure, and serpentines (1:1 structure) are composed of theoretically infinite silicate layers and hydroxyl groups are only linked to the magnesium, the so-called inner OH, and surface OH groups as detailed in Figure 6. Some phyllosilicate such as sepiolite or amphibole contains zeolitic water and water coordinated to cations charge balancing cations, which is more confined than zeolitic water, while the smectite contains water confined in the interlayer and at the surface. M-S-H contains between 1 and 2.5 H_2O per silicon based on TGA measurements (see previous chapter and (Roosz et al., 2015; Nied et al., 2016)), thus significantly more water than talc, antigorite or clay minerals. Water in M-S-H was found to be present both as adsorbed water and within the structure as H_2O and hydroxyl groups ((Jin and Al-Tabbaa, 2013; Nied et al., 2016) and chapter 3.2).

In this part, the distribution of the water in the structure of M-S-H is investigated.

3.3.1.2.1. ^{1}H-^{29}Si CP MAS-NMR spectroscopy

The variation of the contact time in ^{1}H-^{29}Si CP MAS-NMR (cross polarization magic angle spinning NMR) experiments allows investigating whether protons (from the hydroxide groups or water) are in the vicinity of silicate sites. The shorter the contact time, the closer is a proton. Therefore, a water adsorbed on the surface results in higher contact time than hydroxyl groups directly bound to silicon.

The ^{1}H-^{29}Si CP MAS-NMR spectra of M-S-H synthesized at room temperature, and hydrothermally prepared M-S-H recorded with varying contact times between 0 and 5 ms and the associated absolute intensities are shown in Figure 32 and Figure 33. For the 4 samples, the intensities of Q^1 and Q^2 site reached a maximum at a contact time between 2 and 4 ms, which indicated the presence of protons in the second or third coordination shell. From the geometry, the Q^1 and Q^2 silicate sites are present at the surface as Si-OH confirming the hydroxyl groups are linked to the Q^1 and Q^2 silicate sites as already observed by Nied et al. (Nied et al., 2016).

The Q^3 sites showed a higher contact time of > 5 ms, which indicated that the Q^3 silicate sites were not directly linked to hydroxyl groups but that the protons were in further distant coordination spheres such as hydroxyl groups bound to magnesium or sorbed water.

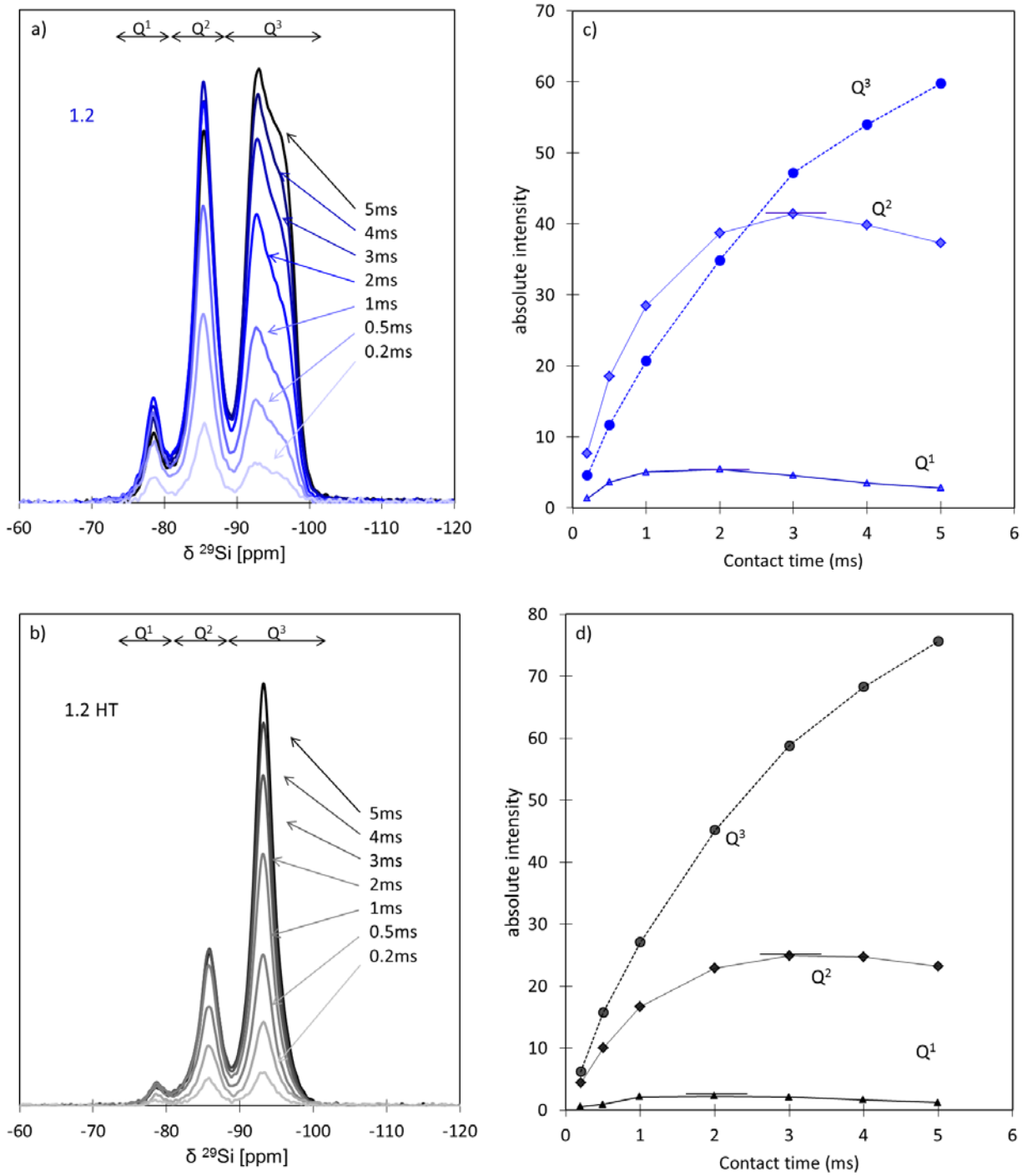

Figure 32: ^{1}H-^{29}Si CP MAS-NMR spectra at different contact time for a) the M-S-H 1.2 sample (3.3 years 20°C), b) the hydrothermally treated M-S-H 1.2 sample c) and d) absolute intensities associated as a function of the different contact times.

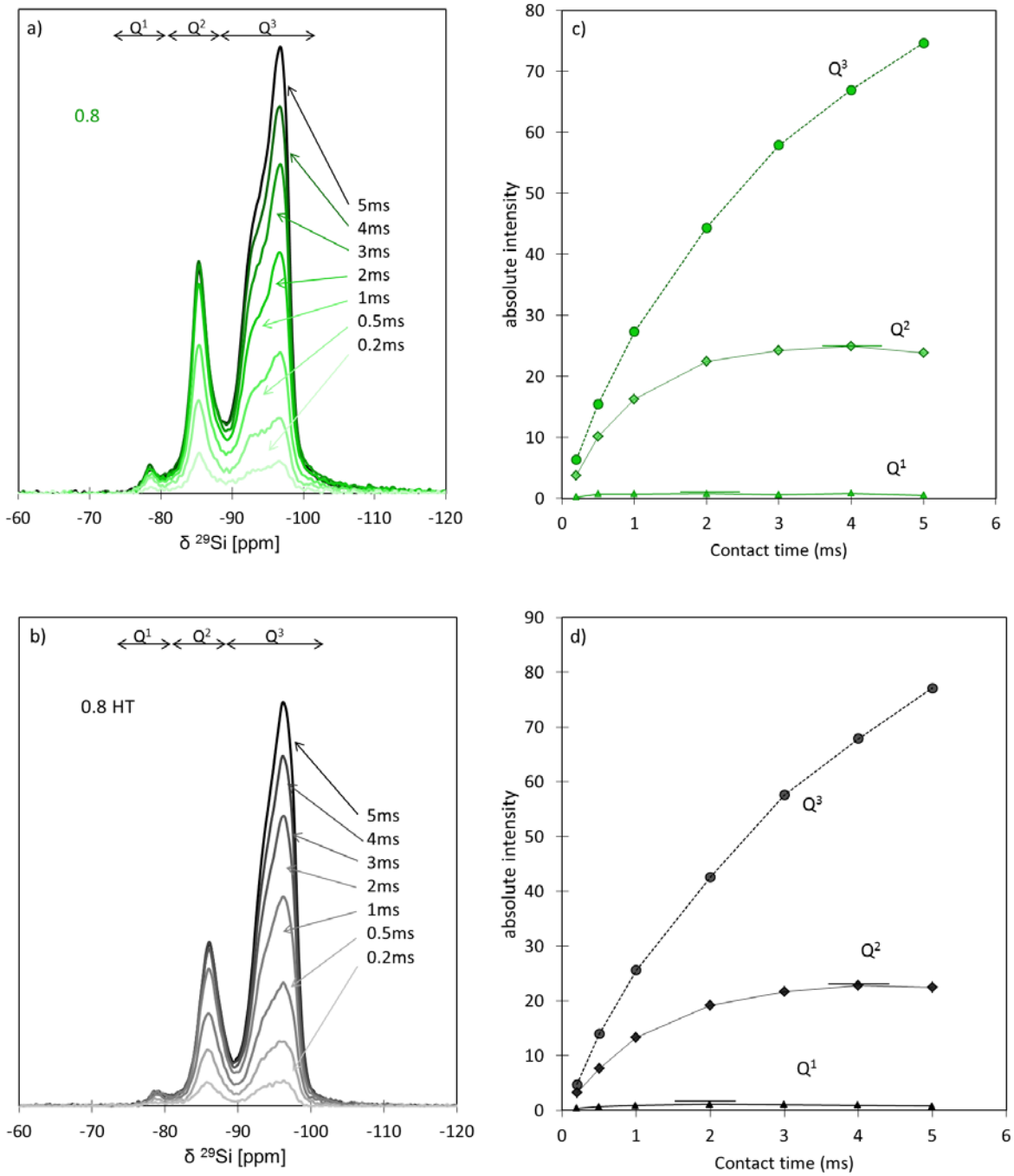

Figure 33: ^{1}H-^{29}Si CP MAS-NMR spectra at different contact time for a) the M-S-H 0.8 sample (3.3 years 20°C), b) the hydrothermally treated M-S-H 0.8 sample c) and d) absolute intensities associated as a function of the different contact times.

3.3.1.2.2. Infrared (FTIR) of hydroxyl vibrations

The FT-IR spectra recorded between 2600 and 3800 cm^{-1} on M-S-H with varying Mg/Si are presented in Figure 34a and compared with spectra of 2:1, 1:1

phyllosilicates, amorphous silica, and brucite in Figure 34b. The M-S-H 1.3 contained some residual brucite (~ 2 wt.% of brucite normalized to 100 g dry mass, quantified by TGA), which can be seen by the presence of the band at 3698 cm^{-1} (Frost and Kloprogge, 1999) and comparison with the spectra in Figure 34b. The band (shoulder) at 3680 cm^{-1} has been assigned to Mg-OH stretching vibrations in M-S-H (Nied et al., 2016; Lin et al., 2017). Else, little difference between the spectra recorded at different Mg/Si could be observed.

At lower wavenumbers, an overlapping of large bands corresponding to OH stretching vibrations of water molecules is found. The first band at ~3550-3600 cm^{-1} is attributed in sepiolite to water coordinated to magnesium, i.e., to water at the edges of the channels (Frost et al., 2001); this water is also observed in antigorite (Figure 34b). The presence of coordinated water is typical for well-crystalline minerals. Its observation in the poorly ordered M-S-H may be explained by the presence of very confined water molecules close to the octahedral layer in M-S-H. Indeed, Lin et al. (Lin et al., 2017) observed two types of water coordinated to magnesium in a M-S-H-like phase, the first one is described as adsorbed water on magnesium located at the edge of the layer (with a water loss at 90°C in TGA) and the second one adsorbed water on magnesium located in the silicates defects (with a water loss at 140°C). Furthermore, the similarities between M-S-H and antigorite observed by PDF analysis tend to confirm the presence of coordinated water in the samples M-S-H.

Hair (Hair, 1975) detailed that OH stretching of dried silanol groups at 3747 cm^{-1} cannot be seen in presence of adsorbed water and “wet” silanol groups band is observed at 3660 cm^{-1} and water sorbed on those hydroxyls at 3450 cm^{-1} (see Figure 35). The spectrum of the hydrated amorphous silica freeze dried and kept at 30% RH showed only the band at 3450 cm^{-1} and maybe the band at 3660 cm^{-1} (Figure 34b). Finally, the FT-IR spectra showed the trace of ethanol from the washing process.

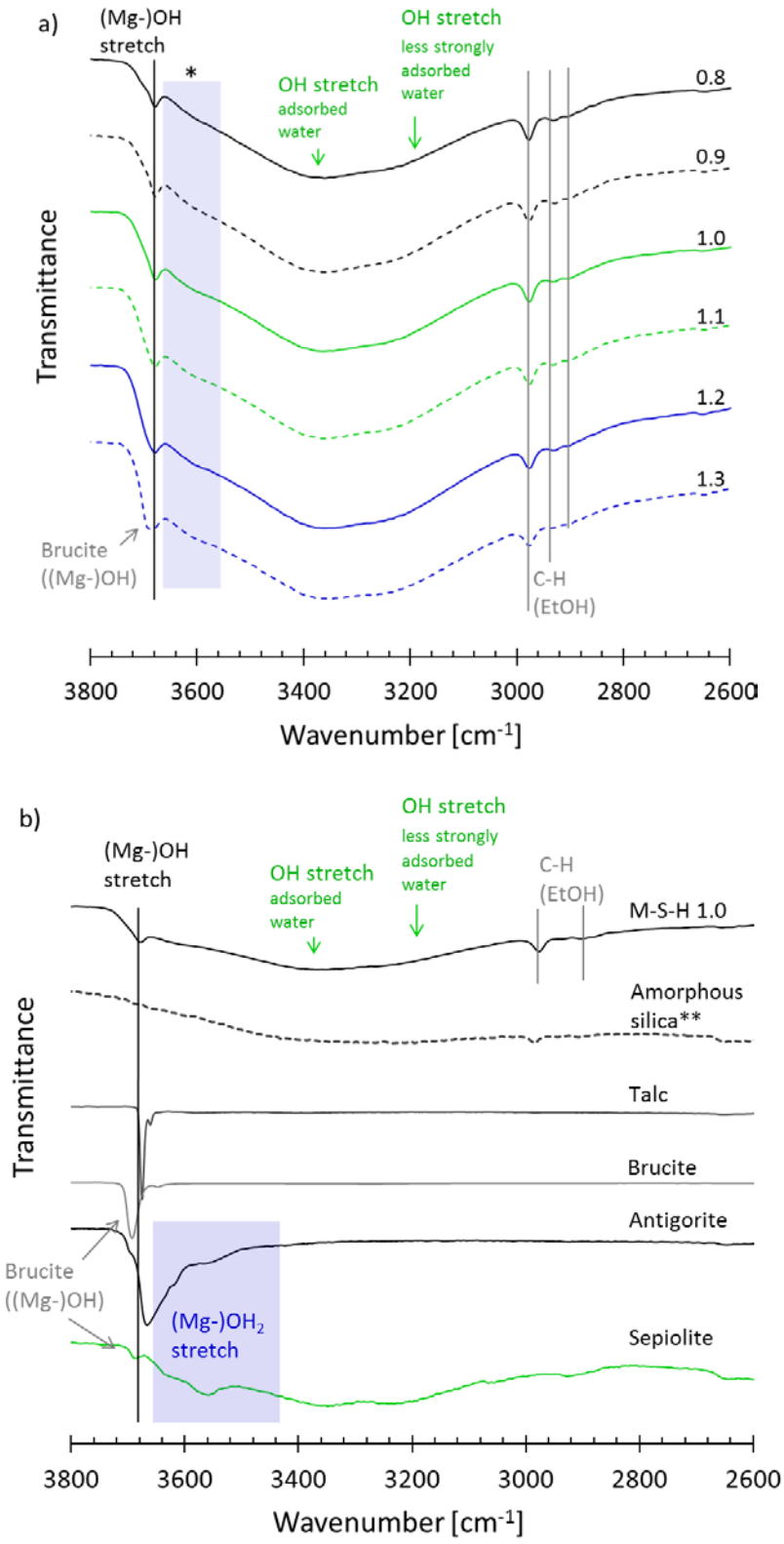

Figure 34: a) FT-IR spectra of the M-S-H samples (3.3 years, 20°C); b) FT-IR spectra of minerals from chapter 3.2 (the intensities of the spectra have been modified to fit the figure); both are zoomed between 2600 and 3800 cm^{-1} and the assignments of the stretching bands according to minerals comparison (Frost and Kloprogge, 1999; Frost and Mendelovici, 2006); *vibrations between 3600 and 3700 cm^{-1} (Si-)OH · · OH_2 stretch [Amorphous silica (Hair, 1975)] or (Mg-)OH_2 stretch [Sepiolite (Frost et al., 2001)or M-S-H (Lin et al., 2017)]; **amorphous silica, hydrated, washed and freeze dried and kept at 30% RH..

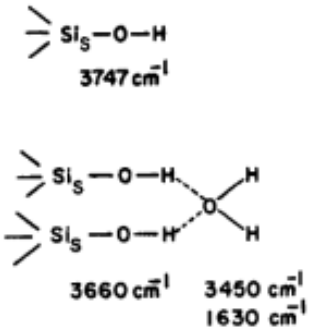

Figure 35: Re-hydration of silica surface (reproduced from (Hair, 1975)).

The FTIR data indicated that M-S-H phases contain hydroxyl groups bound directly to the silicon and magnesium, but also a significant amount of physically bound and adsorbed water, in agreement with ^{1}H MAS NMR (40kHz) data from literature (Nied et al., 2016) and our observations by ^{1}H-^{29}Si CP MAS NMR spectroscopy. The presence of coordinated water bound to magnesium might be possible. The dependence of the amount of water molecules to the relative humidity (RH) is further probed by dynamic vapor sorption (DVS) experiments and the different nature of the physically bound water by ^{1}H NMR relaxometry measurements coupled to TGA.

3.3.1.2.3. Dynamic vapor sorption (DVS)

The results of the dynamic vapor sorption (DVS) measurements for M-S-H 0.9 and M-S-H 1.2 are shown in Figure 36. Both curves show a hysteresis, as characteristic of microporous materials such as C-S-H (Roosz et al., 2016) or clay minerals (Cases et al., 1992) and confirming the micropores observed by the N_2 physio-sorption measurements.

Compared to C-S-H, where the content of water is relatively constant between 20 and 70% relative humidity (Roosz et al., 2016), the curve of M-S-H shows a gradual increase from 35 to 90% relative humidity. This gradual increase of water in M-S-H would be consistent with the dependence of the interlayer distances (and hence water absorbed in them) on the relative humidity as observed by XRD and with the behavior of swelling clays such as saponite or montmorillonite.

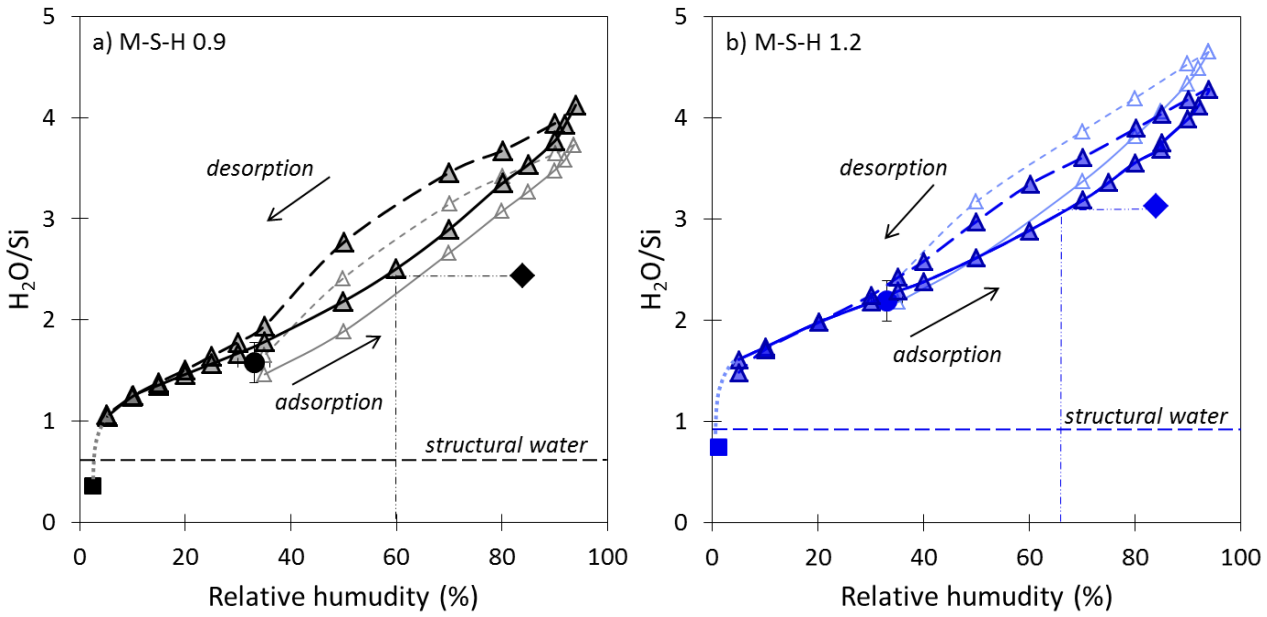

Figure 36: Water vapor isotherms (adsorption and desorption) of the a) M-S-H 0.9 and b) M-S-H 1.2 (20°C, 2 years: light and empty symbols; 3.3 years: dark symbols). The squares correspond to H_2O/Si in the sample at < 2.5 %RH measured by DVS (structural water), the horizontal dashed lines to the H_2O_{OH}/Si structural water in M-S-H measured by TGA (see Table 19) and the full circles to the H_2O_{tot}/Si measured by TGA (see Table 19); the diamonds to water measured by TGA in the sample at higher relative humidity humidity, the dashed-dot lines have been added as eye-guides to indicate the possible range of the effective relative humidity (≈60-80%RH).

3.3.1.2.4. Thermogravimetric analysis (TGA)

The TGA curves and the derivative weight losses of M-S-H prepared at room temperature aged for 3.3 years with Mg/Si = 0.8 and 1.2, and hydrothermally prepared M-S-H are shown in Figure 37. Three water loss regions characteristic of M-S-H can be seen.

The first water loss region between 30 °C and 250 °C observed for M-S-H synthesized at room temperature had been related to poorly (=physically) bound water sorbed on the surface (monolayer, multilayers and and/or in the interlayer) of the M-S-H (Jin and Al-Tabbaa, 2013; Nied et al., 2016). This water loss may also include the bulk water at high relative humidity and TGA cannot distinguish between the different types of physically bound water and the bulk water. The intensity of these low-temperature losses depends on the drying and the relative humidity of the samples (Table 17) as also observed for C-S-H (L'Hôpital et al., 2016a; Roosz et al., 2016). Two samples M-S-H 0.9 and 1.2 were freeze dried and re-equilibrated in a desiccator at ~ 84 % RH for 4 months. The comparison with the DVS measurements indicates that the samples might only equilibrated to ~ 60-80% RH (see Figure 36) during the experiments.

Table 17: Total bound water and hydroxyl content (molar) per silica from TGA in M-S-H equilibrated at 30% RH and 84% RH (250-980°C: *OH/Si* hydroxyl groups, 30-980°C: H_2O_{total}/Si total bound water).

Samples equilibrated at		30% RH				60-80% RH (84% RH) *	
	Mg/Si	0.9	1.0	1.1	1.2	0.9	1.2
TGA	H_2O_{total}/Si	1.58	1.84	2.01	2.19	2.44	3.12
	OH/Si	1.29	1.52	1.69	1.88	1.31	1.85

* In DVS measurement, the samples might be only equilibrated to 60-80% RH.

The second and third water losses (>250°C) have been attributed to silanol and/or magnesium hydroxyl groups in M-S-H (Jin and Al-Tabbaa, 2013; Roosz et al., 2015; Nied et al., 2016), but may comprise also water present as a monolayer on the M-S-H surface (Nied et al., 2016). The second water loss in M-S-H 0.8 is centered at 390°C and relates mainly to the dehydroxylation of silanol (Si-OH) groups (Zhuravlev, 2000), while the third weight loss at 500°C is related to the dehydroxylation of magnesium hydroxyl groups (Mg-OH). The M-S-H 1.2 seems to show only one bigger water loss centered at 450°C which is due to the higher content of both Mg-OH and Si-OH. Zhuravlev (Zhuravlev, 2000) reported the dehydroxylation of bridged hydroxyl groups at the surface of amorphous silica between 180 to 400°C, while the internal hydroxyl groups of the silica condensed only at around 900°C. The dehydroxylation of the minerals of the serpentine group (hydroxyl groups linked to the magnesium: inner OH and surface OH as detailed in Figure 6) has been observed by TGA at 670-900°C (Ivanova et al., 1974), while the inner OH groups linked to the magnesium in the talc structure dehydroxylates at 750-1000°C (Dumas et al., 2013), in agreement with the weight loss observed for M-S-H at 850 to 900°C.

The M-S-H synthesized at room temperature contained thus hydroxyl groups bound to silicon and magnesium, in inner and surface position. The gradual and almost continuous water loss compared to brucite with a sharp water loss of its hydroxyl groups at 410°C confirms the nano-crystalline character of M-S-H. Finally, the loss of the hydroxyl bound to magnesium at 450°C rather than at 700°C indicates that the hydroxyl groups are less bound to magnesium as usually observed in serpentines.

The TGA curves of the hydrothermally prepared M-S-H showed the same three water loss regions. The content of the physically bound water in the hydrothermally treated M-S-H seems more structured with a shoulder at 160°C. It is unclear whether this shoulder is associated to highly physically bound water, i.e., the most confined water or whether this is already related to dehydroxylation of silanol groups. This shoulder might also be related to the loss of coordinated water as described in the M-S-H-like (Lin et al., 2017) or in sepiolite. The water loss corresponding to the

dehydroxylation of the magnesium is centered at 570°C for the hydrothermally prepared M-S-H instead of the 500°C indicating a better structuring.

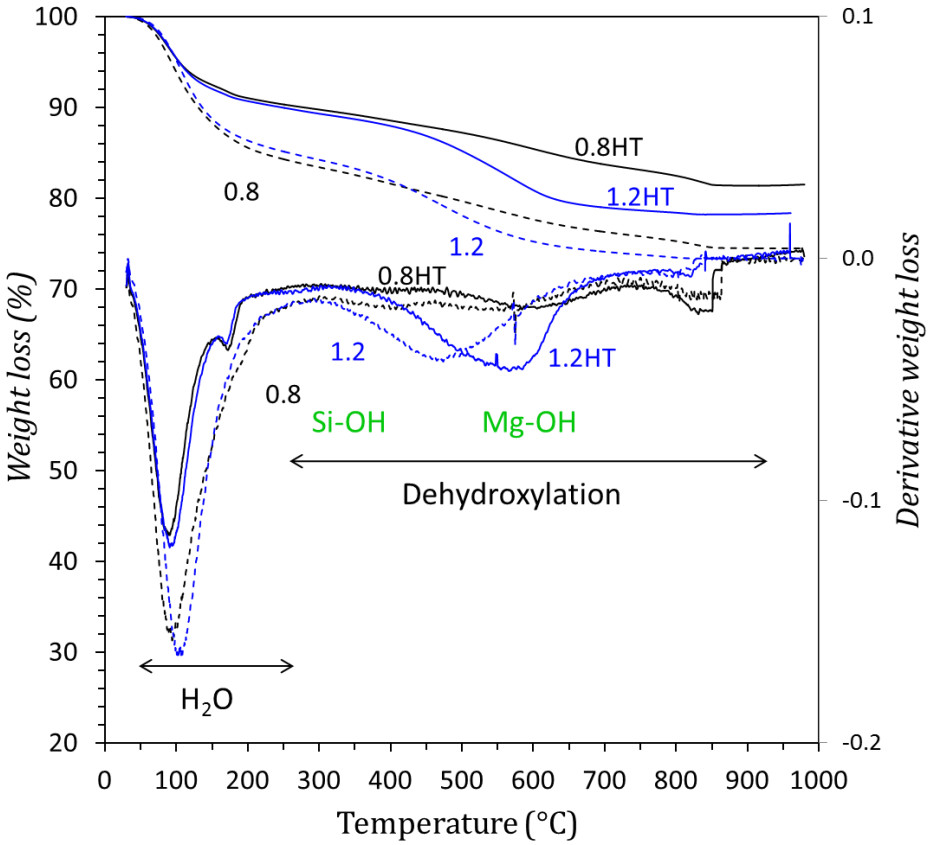

Figure 37: Thermogravimetric analysis (TGA) of hydrothermally prepared M-S-H samples compared to M-S-H samples with similar Mg/Si.

The repartition between physically bound water (30-250°C) and hydroxyl groups (250-900°C) quantified by TGA is shown in Figure 38 as a function of the H_2O/Si molar ratios. The samples equilibrated at higher relative humidity showed a comparable amount of hydroxyl groups but much more physically bound water. Table 17 summarizes the content of the total water and hydroxyl per silicon. The total bound water and of hydroxyl groups increases with Mg/Si in M-S-H as previously reported (Roosz et al., 2015; Nied et al., 2016).

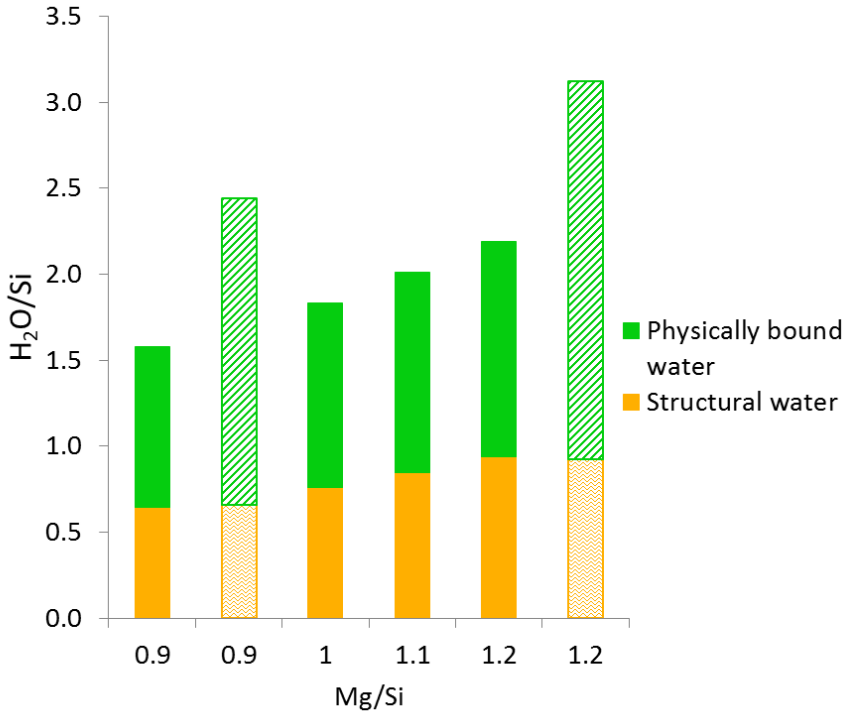

Figure 38: Repartition between water and hydroxyl groups in M-S-H as function of the Mg/Si quantified by TGA, physically bound water (30-250°C) and hydroxyl groups (250-900°C) (samples equilibrated at 30% RH (plain columns) and ~60-80% RH (patterned columns)).

3.3.1.2.5. ^{1}H NMR relaxometry

^{1}H NMR relaxometry measurements were performed on the two M-S-H samples Mg/Si=0.9 and 1.2 re-equilibrated at ~60-80% RH.

The content of structural water and physically bound water obtained by QE is compared to TGA results in Figure 39. The sum of QE (solid+mobile) has been normalized to the total bound water quantified by TGA. The results were in good agreements and showed that the QE can as well differentiate the structural water from the physically bound water.

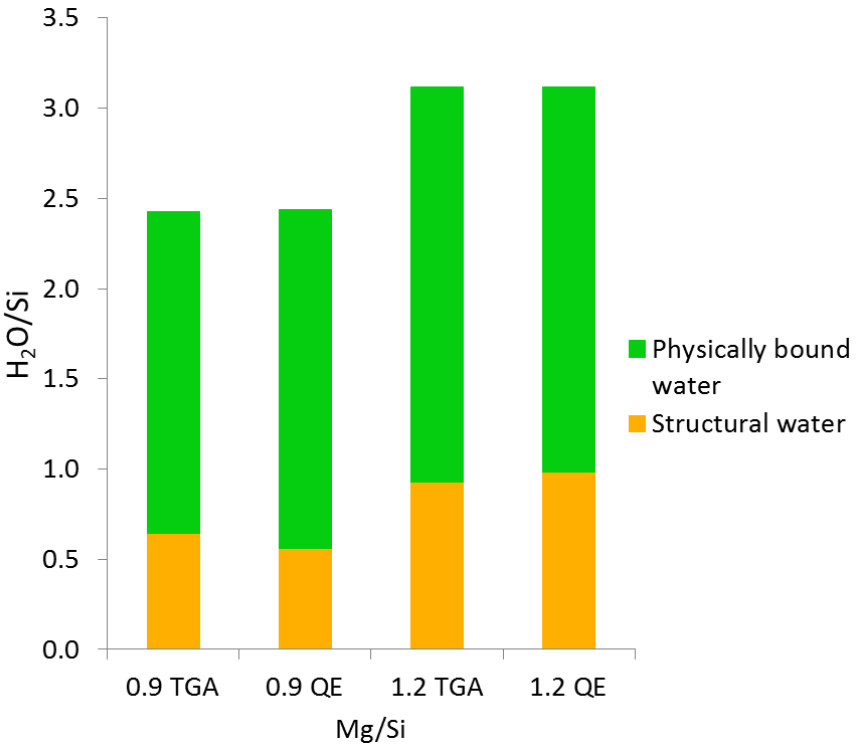

Figure 39: Comparison of the repartition between water and hydroxyl groups in M-S-H as function of the Mg/Si quantified by TGA, physically bound water (30-250°C) and hydroxyl groups (250-900°C) and the deconvolutions of the QE recordings (samples equilibrated at ~60-80% RH).

The mobile water quantified by the QE and the total mobile water quantified by CPMG with comparable intensities indicate good reliability of the results. The one quantified by the QE was slightly lower than the one quantified by the CPMG (2 and 9% lower in the M-S-H 0.9 and 1.2 respectively), which is in the order of the error of the technique.

As shown in Figure 5, different T_2 relaxation times (~0.05 ms, ~0.8 ms, and >6 ms) were observed which are assigned to sorbed water, gel water and bulk water. The specific T_2 relaxation times obtained by ILT are given in Table 18.

Table 18: Specific T_2 relaxation times obtained by ILT for the M-S-H samples equilibrated at 60-80% RH.

	sorbed water	gel water	bulk water
M-S-H	ms		
0.9	0.056	0.769	12.652
1.2	0.049	0.821	6.803

Figure 40 shows the repartition of water quantified by the QE (structural water) and multi-exponential fitting of the CPMG (physically bound water and bulk water) normalized to the mobile water found by the QE and the total bound water determined by TGA.

The calculations gave similar results as the TGA (see Figure 38, patterned columns) in the repartition between physically bound and structural water (hydroxyl groups). However, unlike TGA or QE, CPMG can differentiate between the different populations comprising physically bound and bulk water populations while the signals are overlapping in TGA. The ^{1}H NMR relaxometry showed that the content of bulk water is low (<3% of the total water) and is in fact at the level of the noise. The content of gel water is about 65 and 56 % of the total water for the 0.9 and 1.2 samples. At higher Mg/Si the content of sorbed water ($T_2 \sim 0.05$ ms) per silica increased (Table 19), but if the water content is expressed per magnesium (Table 20) the content of water is relatively constant.

The sorbed water could include water in the interlayers (internal water) and water adsorbed on the surface of the particle (external water). It cannot be excluded than this sorbed water contains the possible coordinated water discussed previously. At both Mg/Si ratios investigated, the sorbed water corresponded to approximately 10% of the signal, indicating the presence of more sorbed water per Si at higher Mg/Si ratios. It should be however noted that for the short T_2 of the first peak (here found at ~ 0.05 ms) the CPMG may have not resolved all possible water, or artificially overestimate the position of the first peak. This is because the first echo was at 0.05 ms and consequently only part of the decay from the lowest peak could be resolved in the range of echoes of 0.05 -12 ms applied here.

It might be postulated that the slightly increasing sorbed water content at higher Mg/Si is due to: a) higher water content adorbed on the surfaces of silicates, b) coordinated water and/or, c) more densified water in the smaller interlayer space.

In addition, the QE signals indicated the presence of hydroxyl groups (structural water) in M-S-H (Table 19 and Table 20). The amount of structural water was comparable to the TGA results as well as its increase with the Mg/Si in M-S-H.

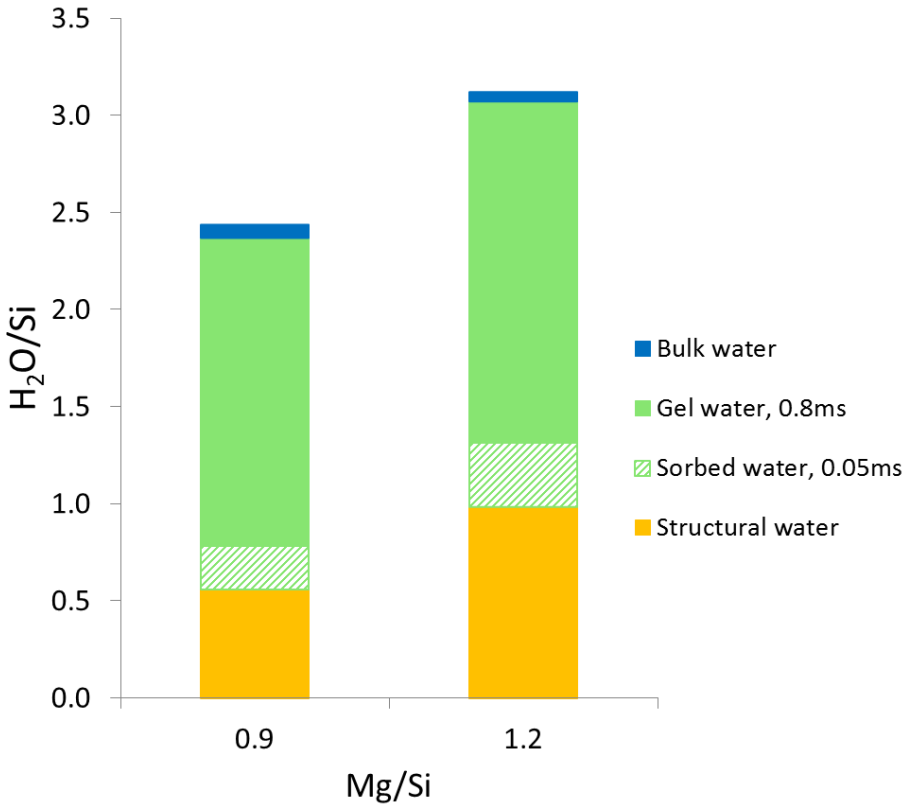

Figure 40: Repartition of the water in M-S-H expressed by the total bound water quantified by TGA as a function of the Mg/Si (structural water from the QE, sorbed+gel+bulk water from the deconvolution of CPMG decay by multi-exponential fitting with three constrained T_2 peak positions).

3.3.1.2.6. Discussion

The DVS measurements indicated that the amount of total water in M-S-H increased clearly with the relative humidity and showed a hysteresis between ad- and desorption, which is consistent with the observations for swelling clays or materials with microporosity. TGA and DVS indicated the presence of more physically bound water at higher relative humidity. This physically bound water was mainly present as *confined* water in the micro-pores even at ≈ 60-80% RH, while hardly any bulk water was quantified by ^{1}H-NMR relaxometry. DVS, TGA and ^{1}H-NMR relaxometry measurements indicated a relatively similar amount of physically bound water per magnesium in M-S-H independent of Mg/Si, which translated into a higher H_2O/Si at higher Mg/Si in M-S-H (Table 19 and Table 20). ^{1}H-NMR relaxometry allows differentiating the bound water in *very confined* water (including the few first layers of water adsorbed), *confined* water (gel water), and bulk water. The amount of bulk water was negligible while both the *confined* and *very confined* water content increased at higher Mg/Si.

A significant amount of hydroxyl groups (structural water) is also present in M-S-H, and the number of hydroxyl groups quantified by DVS, TGA and ^{1}H-NMR relaxometry increased with the Mg/Si in M-S-H (Table 19 and Table 20). ^{1}H-NMR

relaxometry data indicated that the amount of OH/Si nearly duplicated from Mg/Si = 0.8 to 1.2 (Table 19), while the difference in the amount quantified by TGA was less distinct, due to the substantial overlap of the different signals. Also, the ^{29}Si MAS NMR data indicated the presence of more Q^1 and Q^2 silicates which exhibit Si-OH groups (predominantly protonated, details in section 3.3) at higher Mg/Si (Table 19). As also the content of hydroxyl groups per magnesium increased with the Mg/Si (Table 20), not only more hydroxyl groups are bound to the silicate at high Mg/Si but also more Mg-OH groups are present.

Table 19: Total bound water and hydroxyl content (molar) per silica in M-S-H from DVS measurement, from TGA and quantification from the ^{1}H NMR relaxometry. The results are normalized to the total bound water quantified by TGA (errors in TGA ± 12%; DVS ± 10 %; H NMR ± 17%).

		0.9			1	1.1	1.2		
samples equilibrated at		30%	84%	94%	30%	30%	30%	84%	94%
DVS	H_2O/Si (ads)	1.46	3.26[b]	3.73			2.28	3.75[b]	4.28
	H_2O/Si (des)	1.65	3.53[b]				2.42	4.04[b]	
	OH/Si (structural) [c]	0.72					1.48		
TGA	H_2O/Si	1.58	2.44[a]		1.84	2.01	2.19	3.12[a]	
	OH/Si (structural) [d]	1.29	1.31		1.52	1.69	1.88	1.85	
H NMR	bulk water/Si	---	0.07				---	0.05	
	gel water/Si		1.58					1.75	
	sorbed water/Si		0.23					0.33	
	OH/Si (structural)		1.12					1.97	
CEC	Mg^{2+}/Si	0.022			0.025	0.028	0.030		

[a] Comparison with DVS measurement, the samples might be only equilibrated to ~ 60-80% RH; [b]From the DVS measurements of the M-S-H equilibrated at 30% RH; [c] two times the H_2O/Si quantified in the sample at <2.5 RH%; [d] structural water plus possibly sorbed water.

Table 20: Total bound water and hydroxyl content (molar) per magnesium in M-S-H from DVS measurement, from TGA and quantification from the ^{1}H NMR relaxometry. The results are normalized to the total bound water quantified by TGA (errors in TGA ± 13%; DVS ± 11 %; H NMR ± 19%) (calculated from (Table 19).

		0.9			1	1.1	1.2		
samples equilibrated at		30%	84%	94%	30%	30%	30%	84%	94%
DVS	H_2O/Mg (ads)	1.62	3.62 [b]	4.14			1.90	3.13 [b]	3.57
	H_2O/Mg (des)	1.83	3.92 [b]				2.02	3.37 [b]	
	OH/Mg (structural) [c]	0.80					1.23		
TGA	H_2O/Mg	1.76	2.71 [a]		1.84	1.83	1.83	2.60 [a]	
	OH/Mg (structural) [d]	1.43	1.46		1.52	1.54	1.57	1.54	
H NMR	bulk water/Mg	---	0.08				---	0.04	
	gel water/Mg		1.76					1.46	
	sorbed water/Mg		0.26					0.28	
	OH/Mg (structural)		1.24					1.64	
CEC	Mg^{2+}/Mg	0.025			0.025	0.025	0.025		

[a] Comparison with DVS measurement, the samples might be only equilibrated to ~ 60-80% RH; [b] From the DVS measurements of the M-S-H equilibrated at 30% RH; [c] two times the H_2O/Si quantified in the sample at <2.5 RH%; [d] structural water plus possibly sorbed water.

3.3.1.3. Surface properties

Swelling phyllosilicates such as montmorillonite or saponite exhibit a negatively charged surface due to the partial replacement of silicate by aluminate in the tetrahedral silicate layers. Cations are present in the interlayers and/or external surface to compensate these negative charges. The basal spacing depends on the nature of the counterion and its wettability.

Amorphous silica shows a negative zeta potential at pH values from 3 to 10 (Miller et al., 2007), due to the deprotonation of surface silanol groups, while brucite exhibits positive zeta potential of approximately 20 mV in the pH range 3-10 (Miller et al., 2007). Pokrovsky and Schott (Pokrovsky and Schott, 2004) found, by studying zeta potential of brucite as a function of the pH, a PZC (point of zero surface charge) of around 11, confirming that below this value, brucite has a positive effective surface charge (Figure 41).

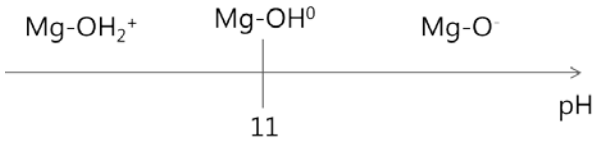

Figure 41: Schematic brucite surface charge in function of the pH (adapted from (Pokrovsky and Schott, 2004)).

Antigorite exhibits an intermediate only slightly negative zeta potential, indicating a contribution of both the positive magnesia-hydroxyl octahedral layers and the negative silica tetrahedral layers (Miller et al., 2007). In contrast, chrysotile with a comparable chemical composition exhibits a positive zeta potential as its needle like structure exposes magnesium hydroxide on the exterior surface (Giese et al., 1996; Miller et al., 2007).

3.3.1.3.1. CEC

The cation exchange capacity (CEC) is a measure of the amount of exchangeable cations present either at the surface (in the Stern and diffuse layer) or interlayer of the solid particle. The CEC quantifies the cations filtrated with the solid which charge-balance the surface charge of the solid and corresponds thus to the surface charge density.

A positive CEC has been measured for M-S-H, as shown in Figure 42, which indicates the presence of exchangeable cations in its structure and thus a negative surface charge of M-S-H as in phyllosilicates. The measured CEC increased from ≈ 35 meq/100g at pH from 8.3 (Mg/Si = 0.8) to ≈ 40 meq/100g at pH 10 and Mg/Si = 1.2. This observation confirmed the presence of hydroxyl surface groups like in amorphous

silica and brucite that experience deprotonation upon pH increase. As CEC measures the overall amount of exchangeable cations, it is well possible that in addition to the negatively charged SiO^- also some Mg-OH_2^+ surface sites were present, although less than the negatively charged silanol groups.

The kind and amount of cations present on the CEC sites were also measured; mainly magnesium was present plus 1 to 2 % sodium, which was present as an impurity in the starting materials. The presence of only 1 to 2% of Na^+ on the CEC sites, although similar magnesium and sodium concentrations in solution were measured (Table 14), showed that the sorption of the bivalent Mg^{2+} is favored compared to the monovalent Na^+, which is commonly observed on silica (see e.g. (Skluzacek et al., 2006; Bruzzoniti et al., 2009; de Lara et al., 2015)). The CEC measured by the total of the cations released by the cobalt(III) replacement agreed well with the total CEC measured by colorimetry, indicating that the M-S-H phases did not dissolve significantly.

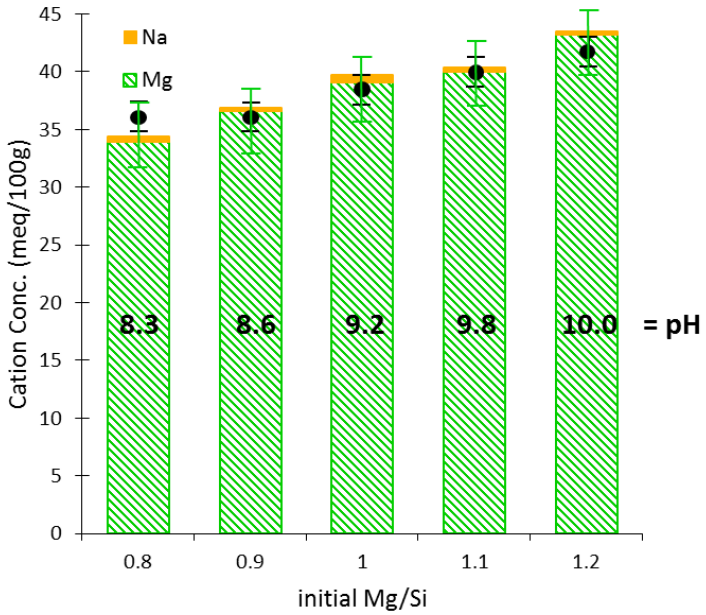

Figure 42: Cation exchange capacity (CEC) measured by colorimetry (black circles) and concentrations of cations sorbed on M-S-H samples (2 years- at 20°C) measured by cobalt hexamine method as a function of the initial Mg/Si.

The amount of magnesium at the cation exchange sites was related to the total amount of magnesium present in Table 19. Only 2 to 3% of the total magnesium was present on the cation exchange sites of M-S-H.

The total of exchangeable cations in M-S-H was higher than the CEC of sepiolite (≈ 10 meq/100g) (Shariatmadari et al., 1999) but lower than the CEC of e.g. saponite (≈ 70-150 meq/100g) (e.g., (Costenaro et al., 2012; Gailhanou et al., 2013)), where Al and Fe replace a fraction of Mg and Si in the structure.

3.3.1.3.2. Zeta potential

The zeta potential measures the charge of a particle not directly at the surface but in some distance, such that (cat)ions near the surface in the Stern and even some in the diffuse layer, appear as part of the solid (James et al., 1992; Giese et al., 1996; Kaya and Yukselen, 2005). Thus the presence of more magnesium in the cation exchange sites of M-S-H can result in less negative zeta potential measurement. The zeta potential measurements on M-S-H particles, as shown in Figure 43, indicate a decrease from -19 mV at pH 8.6 to -28 mV at pH 10.2. The zeta potential of hydrated amorphous silica was ≈ -43 mV at pH of 6.5 which corresponds well with literature data (Miller et al., 2007), while the zeta potential of brucite was positive ≈ 2 mV at pH = 10.5 and is expected higher at lower pH (Pokrovsky and Schott, 2004). The negative effective charge of M-S-H indicates that the Si-OH groups on the Q^1 and Q^2 silicates are at least partially deprotonated: $Si\text{-}O^-$ and that the low cation concentrations in solution does not fully balanced these negative charges i.e., that all the CEC are not in the Stern layer. The decrease in zeta potential from pH 8 to 9 may be related to the deprotonation of more silanol groups as the pH increases.

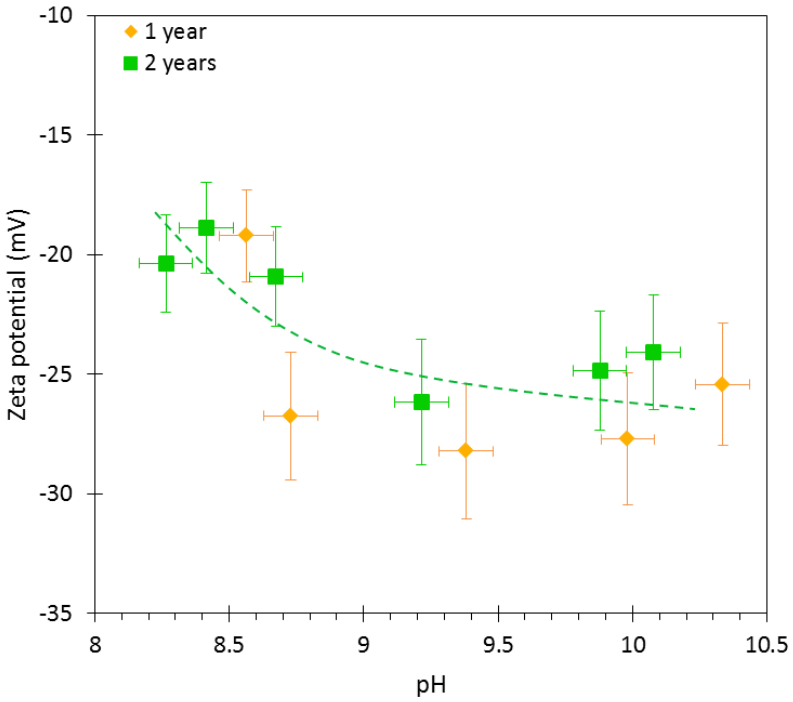

Figure 43: Zeta potential of M-S-H with Mg/Si=0.8-1.2 as a function of pH, M-S-H particles aged of 1 and 2 years at 20°C. The line is only guide to eye.

3.3.1.3.3. Measured pH values: effect of filtration

The pH of the filtrated liquid was systematically lower than the pH measured in the corresponding suspension as detailed in Table 21. The decrease of pH due to the

filtration indicated that not only Mg^{2+} but also OH^- probably as $MgOH^+$ were associated with the surface of M-S-H. In fact, in the pH range 8-10, $MgOH^+$ becomes more important as the pH increases (Figure 44). The OH^-/Si filtrated with the solid shown in Table 21 was calculated from the pH differences between the suspension and the corresponding filtrated supernatant. It indicates that the content of $MgOH^+$ counter-ions is actually very low compared to amount of Mg^{2+} found on the cation exchange sites (Table 19), which is in agreement with Figure 44.

Table 21: pH measured in the M-S-H samples after 3.3 years at 20°C.

initial Mg/Si	pH measured in suspension	pH measured in filtrated solution	[OH] filtrated with the solid (mmol/l)	OH filtrated with the solid / Si
0.7	8.3	8.0	0.0007	0.000003
0.8	8.3	7.9	0.0008	0.000003
0.9	8.5	8.2	0.0011	0.000005
1.0	9.1	8.8	0.0043	0.00002
1.1	9.7	9.1	0.0255	0.00012
1.2	9.9	9.6	0.0269	0.00013
1.3	10.3	10.0	0.0675	0.00034
1.4	10.4	10.1	0.0850	0.00045

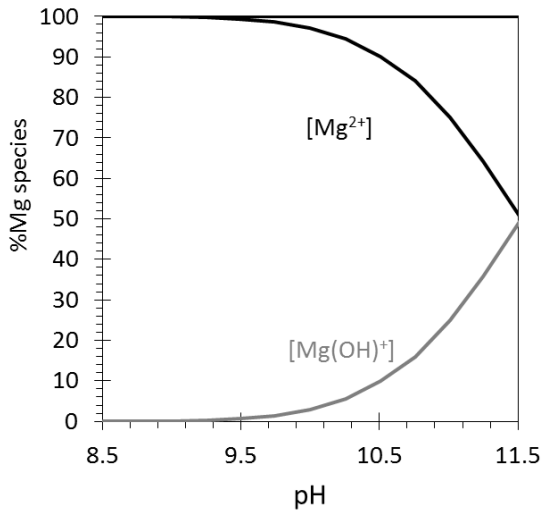

Figure 44: Distribution of magnesium speciation (Mg_{tot} = 100 mol/l) in solution at 20°C as a function of the pH.

3.3.1.3.4. Discussion

The CEC measurements indicated the presence of exchangeable cations (mainly Mg^{2+}) at the surface of M-S-H. Its amount increased while the zeta potential decreased,

when the pH raised, indicating an increase of the negative surface charge density of M-S-H with pH due to the deprotonation of the silanol groups of M-S-H.

The comparison of the CEC of 0.04 to 0.06 meq/Si (0.02 - 0.03 Mg_{exch}/Si) with the fraction of silanol groups of 0.3 to 0.6 per Si, indicated that only approximately 10% of the silanol groups were deprotonated in the pH range studied.

The zeta potentials measured in the M-S-H suspension were negative but decreased only moderately at higher pH values in contrast to the CEC measurements, in agreement with the presence of more Mg^{2+} at the surface at higher pH values. The presence of more magnesium on the cation exchange sites of M-S-H could also explain why the amount of *very confined* water quantified by ^{1}H NMR relaxometry increases with the Mg/Si, as Mg^{2+} in water is surrounded by 6 to 18 water molecules $Mg[H_2O]_6^{2+}[H_2O]_{12}$ (Markham et al., 2002), such the amount of water should increase strongly with the amount of Mg^{2+} on the cation exchange sites. In addition, also the silanol groups are associated with additional water as observed by FTIR and ^{1}H-^{29}Si CP MAS-NMR measurements. Thus the increase of the fraction of silanol groups (as observed by ^{29}Si MAS NMR spectroscopy) at high Mg/Si contributes also to the presence of more adsorbed water.

3.3.2. Conclusions

X-ray diffraction, X-ray pair distribution function results, and N_2 physio-sorption data confirmed that M-S-H phases were poorly ordered and nanosized phyllosilicates as already suggested in (Roosz et al., 2015). The presence of 30% to 55% Q^1 and Q^2 sites at low and high Mg/Si, respectively, as observed by ^{29}Si NMR, indicates a high fraction of silanol (Si-OH) groups present at edges sites or defects in the silicates layers. Hydrothermal treatment resulted in M-S-H with a slightly better ordered structure, as observed by ^{29}Si MAS NMR spectroscopy, X-ray diffraction data and thermogravimetric analysis. In all cases, M-S-H showed a small coherence length of about 1.2 nm, as measured by X-ray PDF analyses, and a relatively high specific surface area of 300 to 500 m^2/g and micro- and nano-porosity similar to poorly ordered synthetic phyllosilicates.

The samples were observed to swell slightly in the presence of ethylene glycol and the water content was highly dependent on the relative humidity. ^{1}H NMR relaxometry performed on the 84% RH samples combined with TGA measurement showed that hardly any bulk water was present, while the water was rather present in micro-pores as gel water. The amount of gel water depended strongly on the relative

humidity. Also the amounts of more confined water (either present at the surface or as water associated with Mg^{2+} cations) and hydroxyl groups were observed increasing at higher Mg/Si. This higher content of hydroxyl groups at high Mg/Si was related to the higher content of magnesium and thus of Mg-OH groups and to the increase of the density of silanol groups at higher Mg/Si.

M-S-H exhibited a negative surface charge indicating a partial deprotonation of the silanol groups. The small negative surface charge also leads to the presence of a low amount of magnesium on cation exchange sites (equal to 0.02 - 0.03 Mg/Si) compensating the negative charge similar as has been observed for phyllosilicates. The negative surface of the M-S-H particle might explain the weak cohesion and small particle size observed.

The ill-defined and nano-sized structure of M-S-H with its large number of silanol sites resulted in the presence of exchangeable cations. The strong resemblance of M-S-H to hydrated 2:1 / 1:1 phyllosilicates could also indicate that an aluminum uptake in the octahedral and tetrahedral layers of M-S-H could be possible similar to phyllosilicates. Further investigations have been carried out to investigate the possible incorporation of aluminum in the structure.

3.4. Main findings on the magnesium silicate hydrate

- M-S-H forms very slowly from SiO_2 and MgO in batch experiments
- A "transitional" M-S-H with a Mg/Si ratio of ~ 1 is formed at early age
- Mg/Si ratio in M-S-H is variable between 0.8 and 1.3
- Solubility of M-S-H can be described with a solid-solution model
- Solubility of M-S-H is comparable to solubility of talc and antigorite
- M-S-H is a poorly ordered, nanosized and hydrated phyllosilicate
- M-S-H synthetized in batch experiment shows high surface specific and rather short coherence length
- Structural, sorbed, gel, and bulk water were found in M-S-H
- M-S-H shows a negative surface charge due to the presence of deprotonated silanol groups
- A small quantity (35-40 meq/100 g) of exchangeable magnesium is present at the surface
- Negatively charged surface could explain the poor cohesion and small particle size observed for M-S-H

Chapter 4:
Calcium silicate hydrate and magnesium silicate hydrate

Contents

4.1. Introduction

As described in chapter 1, leaching and carbonation of the hydrated cement paste at the interaction zone with the clayey rocks lead to the decalcification of C-S-H and to the formation of amorphous silica. Magnesium reacts with silica from the cement leading, under water saturated conditions, to form M-S-H.

Portlandite and high Ca/Si C-S-H, the most important hydrates in hydrated Portland cement, are observed at pH ≥ 12.5. Lower pH values between 10 to 12.5 are measured for synthetic C-S-H (Hong and Glasser, 1999; Bach et al., 2013; Haas and Nonat, 2015; Lothenbach and Nonat, 2015; L'Hôpital et al., 2016a; Walker et al., 2016) and also in "low pH" cements in the absence of portlandite where a low Ca/Si C-S-H (0.7-1.3) is present (Cau Dit Coumes et al., 2006; Codina, 2007; Codina et al., 2008; Lothenbach et al., 2012a; Lothenbach et al., 2014).

This chapter focusses on the stability of C-S-H at low Ca/Si (< 1) in the presence of magnesium, on how M-S-H forms from C-S-H and on the relative stability C-S-H and M-S-H.

The composition of C-S-H is well investigated and depends mainly on the total Ca/Si and the pH (Cong and Kirkpatrick, 1996; Klur et al., 1998; Richardson, 2008; Renaudin et al., 2009; Lothenbach and Nonat, 2015). C-S-H consists of calcium oxide layers sandwiched on both side by silicate chains with the typical dreierketten structure (Richardson, 2008); i.e. with repeating building blocks composed of two pairing silicate tetrahedra attached to the calcium oxide layer and a bridging position, which can be occupied by a bridging silicate tetrahedra or be empty, depending on the C-S-H composition. Thus, silicate in C-S-H, investigated by ^{29}Si MAS NMR, is either bound to one silicate neighbor (Q^1) at high Ca/Si or to two neighbors, Q^2 at low Ca/Si ratio. In contrast, M-S-H gels have a layered silicate structure as detailed in the previous chapter. Similar to clays, M-S-H is stable at lower pH values than C-S-H, i.e. at pH between 7.5 and 10.5 ((Zhang et al., 2011; Nied et al., 2016) and chapter 1). Given the different structures and stability domains, most studies (Brew and Glasser, 2005b; Chiang et al., 2014; Lothenbach et al., 2015) have reported the precipitation of two distinct phases and not of a mixed magnesium calcium silicate hydrate phase.

Replacement of magnesium oxide by calcium oxide in octahedral sheets of magnesium silicate minerals, or vice versa, is not reported in the literature. Mixed magnesium calcium minerals exist as dolomite ($CaMg(CO_3)_2$), which has an alternating structural arrangement of calcium and magnesium ions. In this case, calcium or

magnesium oxides are not mixed in octahedral layers, but in alternate layers of calcium or magnesium as the crystallographic radius of calcium (0.99Å (Conway, 1981)) in the octahedral layer is significantly higher than that of magnesium (0.65Å (Conway, 1981)). The uptake of calcium in magnesium silicate clay as, e.g. in saponite occurs at the negatively charged surface and in its interlayer to compensate the charge. Similarly, in the amphibole group, the uptake of calcium can occur as charge balancing Ca^{2+} in the M4 sites. The larger size of the anhydrous calcium cation indicates that it would rather outbalance the possible negative charge of the interlayer and/or of the surface of M-S-H than a substitute to magnesium in the main layer.

Even if the formation of a magnesium calcium silicate hydrate phase does not seem very likely, the possible uptake of small amounts of magnesium by C-S-H (Lothenbach et al., 2015) may be envisaged. The uptake of alkalis, sulfate, or aluminum in C-S-H has indeed been observed (Richardson et al., 1993; Skibsted et al., 1993; Richardson, 2008; Renaudin et al., 2009; Bach et al., 2013; L'Hôpital et al., 2015; Lothenbach and Nonat, 2015; L'Hôpital et al., 2016b; Plusquellec and Nonat, 2016). Alkali and sulfate uptake in C-S-H occur mainly by sorption onto the surface or in the interlayer, while aluminum is taken up both in the interlayer and in the silicate chains. A high calcium concentration and/or a low pH decrease the alkali uptake (L'Hôpital et al., 2016b). The adsorption of ions on C-S-H also decreases with the ion concentration in solution. Magnesium is, like calcium, a doubly charged cation, with a similar ionic radius in its hydrated state (4.3 Å for Mg^{2+}, 4.1 Å for Ca^{2+}) (Conway, 1981). However, its aqueous concentration is much lower (0.0001-0.1mmol/l) than that of calcium (0.1-1.5mmol/l) in the presence of M-S-H and C-S-H (Lothenbach et al., 2015). Thus the sorption of magnesium on the C-S-H surface is expected to be smaller than that of calcium.

This chapter investigates the effect of magnesium on the stability of C-S-H, the possible uptake of calcium by M-S-H and of magnesium by C-S-H.

4.2. Effect of magnesium on calcium silicate hydrate (C-S-H)

This part is shortened version of the publication: Ellina Bernard, Barbara Lothenbach, Fabien Le Goff, Isabelle Pochard, Alexandre Dauzères, Effect of magnesium on calcium silicate hydrate (C-S-H), **Cement and Concrete Research**, 97 (2017) 61-72 (Bernard et al., 2017a).

In the present part, the effect of magnesium on the stability of C-S-H has been investigated by batch experiments where magnesium oxide or magnesium chloride were added to C-S-H with a Ca/Si ratio equal to 0.8 as detailed in part 2.1.2. The part 2.3.3.1 resumes the analytical techniques and the part 2.3.3.2 the thermodynamic modelling.

4.2.1. Results and discussions

4.2.1.1. C-S-H + $MgCl_2$

The addition of $MgCl_2$ to pre-synthesized C-S-H lowered the pH values (as discussed below) and destabilized the C-S-H. The TGA curves of M-S-H, C-S-H and C-S-H plus $MgCl_2$ and the derivative weight losses are shown in Figure 45. The first water loss region between 30 °C and 250 °C is characteristic for both C-S-H (L'Hôpital et al., 2016a; Lothenbach et al., 2016; Roosz et al., 2016) and M-S-H (chapter 3) and was related to poorly bound water on the surface or in the interlayer. In the case of pure C-S-H, the second water loss between 250 °C and 800 °C was related to the calcium or silanol hydroxyl groups (Lothenbach et al., 2016; Roosz et al., 2016). In M-S-H this second water loss corresponds to magnesium and silanol hydroxyl groups (Jin and Al-Tabbaa, 2013; Roosz et al., 2015; Lothenbach et al., 2016; Nied et al., 2016). It is more distinct and centered at 570 °C (Figure 45) as already reported by (Lothenbach et al., 2015). The TGA data indicated the presence of hydrates (C-S-H or M-S-H) in the samples, while no brucite (water loss in a narrow range at around 400 °C), nor portlandite (water loss in a narrow range at around 550 °C (Lothenbach et al., 2016)) were detected, indicating their absence. Traces of calcite (< 1 wt.%) were observed (weight loss at around 750-800 °C (Lothenbach et al., 2016)). The presence of M-S-H was clearly detected in the sample with the maximum of $MgCl_2$ addition, while at lower $MgCl_2$ additions mainly C-S-H and only small quantities of M-S-H seemed to be present.

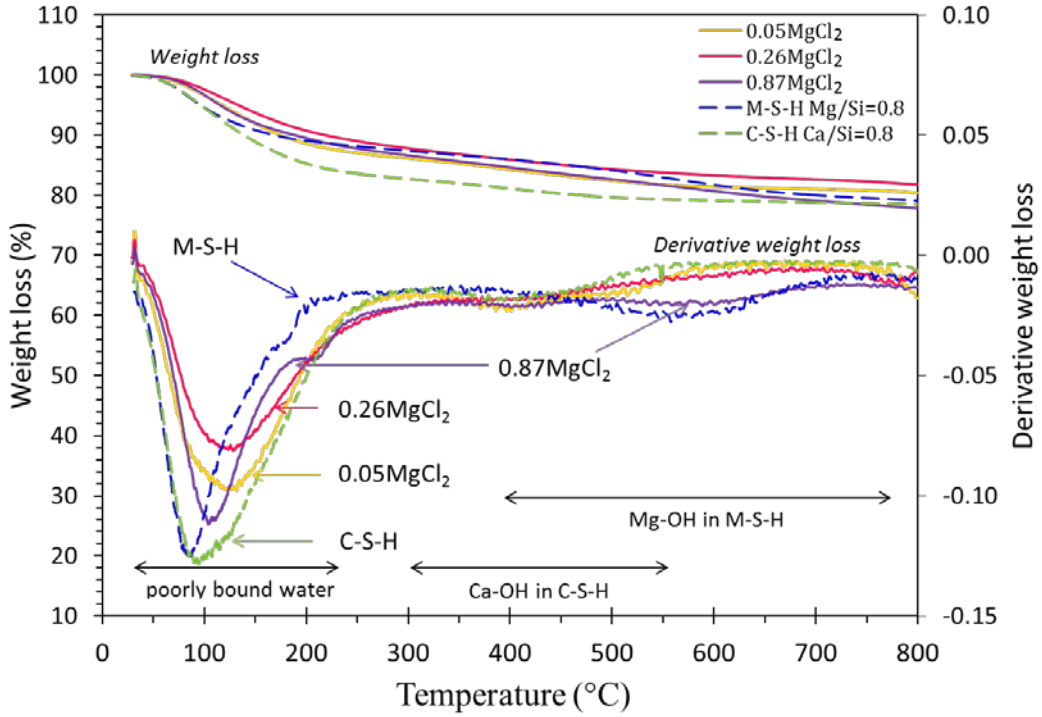

Figure 45: Thermogravimetric analysis (TGA) of C-S-H samples where $MgCl_2$ has been added: 0.05$MgCl_2$, 0.26 $MgCl_2$ and 0.87 $MgCl_2$ (solid lines) after 1 year of curing at 20 °C, TGA of M-S-H 0.8 and C-S-H 0.8 (dashed lines) are shown as references.

The XRD measurements are shown in Figure 46. The patterns of pure C-S-H and M-S-H showed broad reflections related to the nanosize of the particles (Allen et al., 2007; Skinner et al., 2010; Haas, 2012; Roosz et al., 2015).The characteristic reflections of C-S-H are located at 16.3, 29.2, 32.0 and 43.0° 2θ (Lothenbach et al., 2015) as detailed in Figure 46. With the addition of $MgCl_2$, the reflections of C-S-H decreased while M-S-H was observed by the additional broad reflections at 19.7 and 35.0° 2θ (Nied et al., 2016) in the samples 0.26$MgCl_2$ and 0.87$MgCl_2$. Peak shifts relative to pure phases, i.e. M-S-H or C-S-H, were not observed confirming the presence of C-S-H and/or M-S-H as separate phases, as previously observed by a few authors (Mitsuda, 1973; Lothenbach et al., 2015).

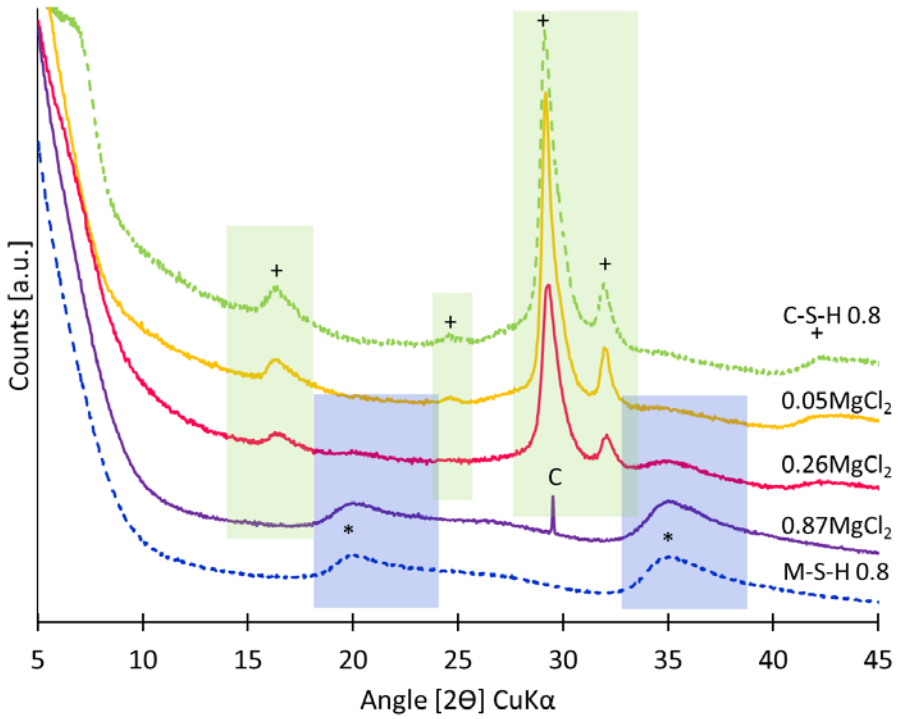

Figure 46: XRD patterns of C-S-H samples where $MgCl_2$ has been added: $0.05MgCl_2$, $0.26\ MgCl_2$ and $0.87\ MgCl_2$ (solid lines) after 1 year of curing at 20 °C, patterns of M-S-H 0.8 and C-S-H 0.8 (dashed lines) shown as references, C= calcite. The area of the main reflections of C-S-H and M-S-H are shaded (+ = C-S-H, * = M-S-H).

The FTIR spectra of these samples are shown in Figure 47. The characteristic bands of C-S-H with a Ca/Si equal to 0.8 were centered at ~ 950-980 cm^{-1} and at 800-825 cm^{-1} and were assigned to Si–O stretching vibrations of the Q^2 and Q^1 respectively (Yu et al., 1999), while the bands centrered at ~ 990-1000 cm^{-1} and ~ 870-880 cm^{-1} corresponded to the Q^3 and Q^2 of the M-S-H (Nied et al., 2016) as detailed in Figure 47. The Raman bands characteristic of C-S-H (Kirkpatrick et al., 1997; Black et al., 2007; Garbev et al., 2007; Richardson et al., 2010a) are given in Figure 48. Raman bands of M-S-H (Lothenbach et al., 2015; Nied et al., 2016) attributed by (Nied et al., 2016) by comparison with spectra of talc (Kirkpatrick et al., 1997) and antigorite (Gunnarsson and Arnórsson, 2005) are detailed in Figure 48 as well. The Si-O-Si bending of M-S-H was at a higher wavenumber (675 cm^{-1}) than the one of C-S-H (660 cm^{-1}). A broadening of the C-S-H bands due to the apperance of M-S-H (675 cm^{-1}) was already observed at the smallest $MgCl_2$ addition. At higher $MgCl_2$ additions, a clear band at 1000 cm^{-1} was visible. Similar to the XRD data, FTIR and Raman measurements indicated the absence of any significant amount of C-S-H in the $0.87MgCl_2$ sample.

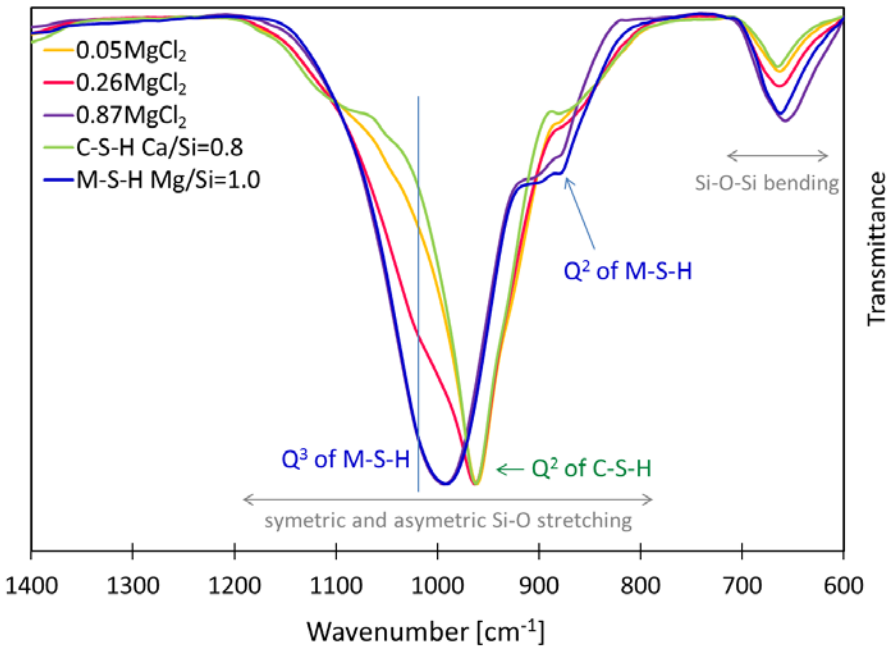

Figure 47: FTIR spectra of C-S-H samples where $MgCl_2$ has been added: $0.05MgCl_2$, $0.26\ MgCl_2$ and $0.87\ MgCl_2$after 1 year of curing at 20 °C, spectra of M-S-H 0.8 and C-S-H 0.8 shown as references (the vertical line indicates the shoulder due to the Q^3 silicate sites in M-S-H).

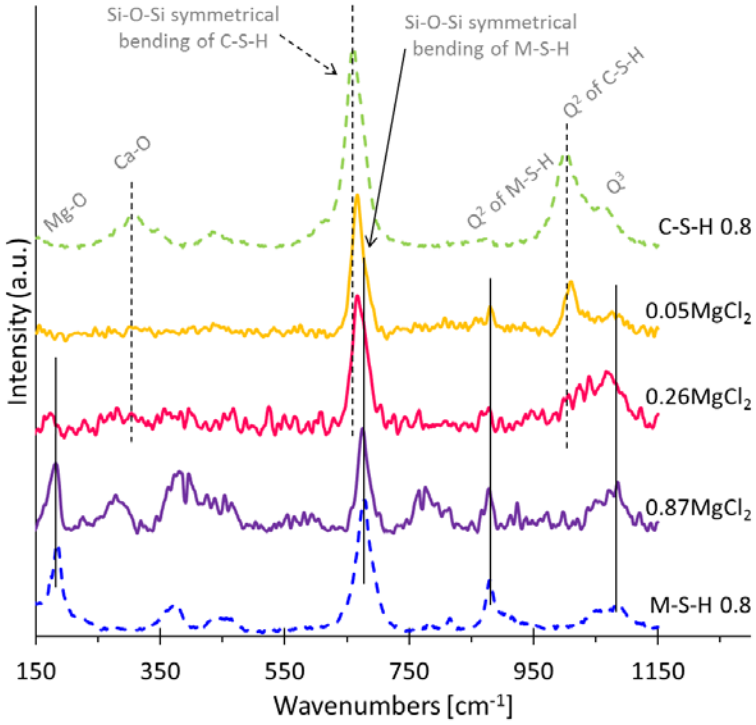

Figure 48: Raman spectra of C-S-H samples where $MgCl_2$ has been added: $0.05MgCl_2$, $0.26\ MgCl_2$ and $0.87\ MgCl_2$, C-S-H and M-S-H, after 1 year of curing at 20°C, assignments of the band according to [31-34] for C-S-H and [10, 21] for M-S-H.

The ^{29}Si MAS NMR spectra of these samples are shown in Figure 49. The structure of C-S-H is well investigated (Bell et al., 1990; Klur et al., 1998; Andersen et al., 2003; Chen et al., 2004; Richardson et al., 2010b; L'Hôpital et al., 2015); the characteristic shifts at ≃ -79.7, -82.9, -85.5 and -88.4 ppm, which correspond to Q^1 (end of chains), Q^2_b (bridging position), Q^2_p (pairing position) and Q^2_u (bridging position with binding to H^+ (Sato and Grutzeck, 1991; Le Saout et al., 2006; L'Hôpital et al., 2015)) of the tetrahedral silicate in C-S-H are visible in Figure 49. ^{29}Si MAS NMR studies have shown that at high Ca/Si, no cross linked silicate groups (Q^3) exist in pure C-S-H, while very small quantities of Q^3 with a chemical shift between -95 and -97 ppm (Le Saout et al., 2006; Myers et al., 2015a) have been reported for C-S-H with low Ca/Si. Our C-S-H reference sample contained approximately 4 % (quantification detailed below) of the total silica in a broad signal at -93.5 ppm. The presence of Q^3 signals in higher quantities between -92 and -97 ppm indicated the formation of M-S-H even at very low $MgCl_2$ addition ($0.05MgCl_2$) (Figure 49). At higher $MgCl_2$ addition the intensity of the chemical shifts of the C-S-H decreased while the amount of Q^3 tetrahedral sites, indicating the presence of M-S-H, increased. Although the peaks decreased, the relative intensity and the position of the chemical shifts of C-S-H, when present, did not change significantly, indicating that the polymerization of the silicates in the C-S-H remained constant. The $0.87MgCl_2$ sample spectrum, similar to M-S-H spectra (Mg/Si=0.80 and 1.0), indicated no or very little C-S-H. However the shift of the Q^2 signal to less negative values could indicate the persistence of some C-S-H in the $0.87MgCl_2$ sample.

The deconvolutions of the ^{29}Si MAS NMR spectra were done following the procedure outlined in (L'Hôpital et al., 2016a; Nied et al., 2016) and are presented in Table 22. The deconvolutions of the samples with additional $MgCl_2$ were associated with considerable (±10%) error due to the overlapping of the chemical shifts of ^{29}Si for M-S-H and C-S-H. The Q^3 tetrahedral sites have been attributed to M-S-H with the exception of the 3-4 % at -93.5 ppm which was already present in pure C-S-H. The attribution of the Q^2 tetrahedral signal of M-S-H has been made with keeping the ratio Q^2/Q^3 in M-S-H low (0.4-0.6), respecting Equation (9) and allowing a high MCL (>20) in the structure of C-S-H.

Deconvolutions of the ^{29}Si MAS NMR data attributed approximately 7 % ± 3 % to silica in M-S-H in the sample $0.05MgCl_2$, 44 % ± 7 % in the sample $0.26MgCl_2$ while 87 % ± 11 % and 53 % ± 8 % were attributed to C-S-H in the samples $0.05MgCl_2$ and $0.26MgCl_2$. The silica content in C-S-H decreased as M-S-H was formed. All the silica (98 %) was attributed to M-S-H in the sample $0.87MgCl_2$ although the Q^2 signal is broader than in pure M-S-H. The Ca/Si in C-S-H, when present, were estimated from the MCL (Lothenbach and Nonat, 2015) and is detailed in Table 22.

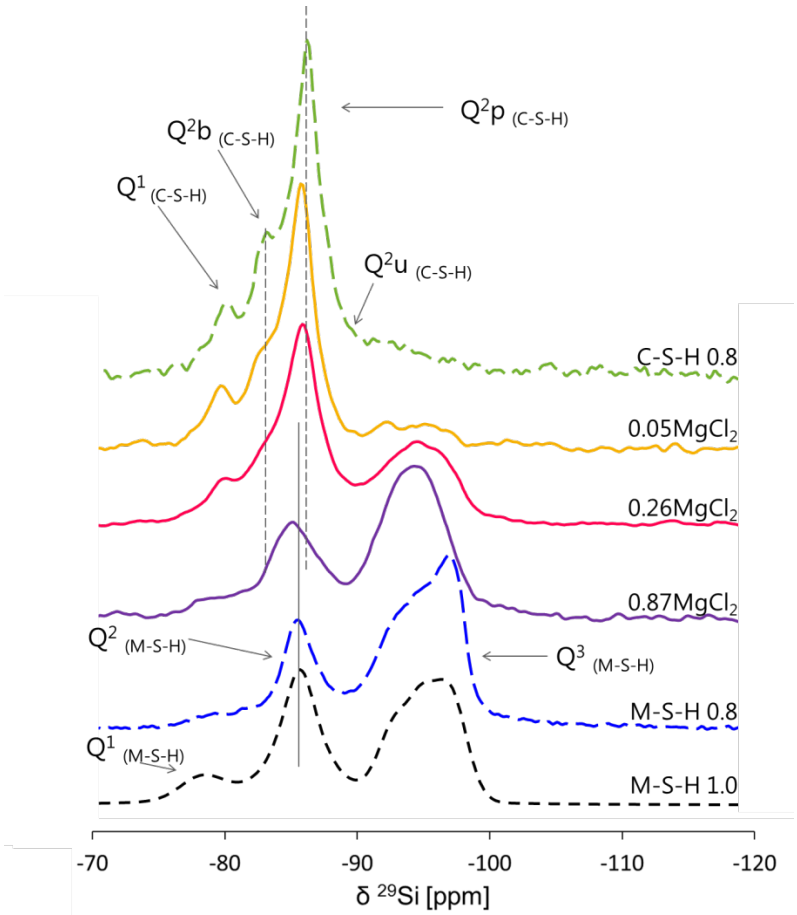

Figure 49: ^{29}Si MAS NMR spectra of C-S-H samples where $MgCl_2$ has been added: 0.05$MgCl_2$, 0.26 $MgCl_2$ and 0.87 $MgCl_2$ after 1 year of curing at 20°C, (C-S-H and M-S-H shown as references).

Table 22 : Peak shifts and relative intensities (quantifications) of different silicon shifts obtained from the deconvolution of the ^{29}Si MAS NMR spectra for C-S-H samples where $MgCl_2$ has been added: 0.05$MgCl_2$, 0.26 $MgCl_2$ and 0.87 $MgCl_2$after 1 year of curing at 20°C (C-S-H and M-S-H shown as references) (δ^{29}Si in ppm ± 0.3 ppm).

	δ^{29}Si (C-S-H)							δ^{29}Si (M-S-H)						Am. silica	Total in C-S-H	M-S-H
	Q^1	Q^2b	Q^2p	Q^2u	MCL	Ca/Si	Q^3	Q^1	Q^2	Q^3a	Q^3b	Q^3c		$Q^3(SiO_2)$		
	-79.6	-82.8	-85.8	-88.2			-93.5	-78.3	-85.5	-92.7	-94.7	-96.7	Q^2/Q^3	-100.9	% of silica	
C-S-H 0.8	8	22	59	7	25		4	-	-	-	-	-	-	-	96	-
0.05 $MgCl_2$	8	25	53	2	22	0.77	4	1	2	1	2	1	0.6	1	87	7
0.26 $MgCl_2$	5	12	32	3	21	0.78	3	2	11	14	8	9	0.4	1	53	44
0.87 $MgCl_2$	-	-	-	-	-		-	2	42	22	20	11	0.8	2	-	98
M-S-H 0.8	-	-	-	-	-		-	2	34	23	8	27	0.6	6	-	94
M-S-H 1.0	-	-	-	-	-		-	5	43	17	9	26	0.8	-	-	100

Quantification error ≃ ± 10% of absolute amount of (%Si) +2.5%.

The pH values and measured concentrations of the solution for samples cured for 3 months and 1 year at 20 °C are plotted in Figure 50 and detailed with the additional results at 50°C in Table 23. The addition of $MgCl_2$ to C-S-H decreased the pH value from 10.5 in the solution equilibrated with C-S-H only (Ca/Si = 0.8) to pH 7.7 at the maximum $MgCl_2$ addition (1.34$MgCl_2$ sample). The calcium concentrations increased with the addition of $MgCl_2$ up to 130 mmol/l [Ca] at 20°C and up to 140 mmol/l [Ca] at 50°C and

reached a plateau at Mg/Si ≥ 0.87. Thus 93 to 100 % of the initially present calcium (Table 3) was in the solution indicating the dissolution of C-S-H and possibly the uptake of some calcium in the M-S-H. This is in agreement with the ^{29}Si MAS NMR results showed in Figure 49, where only M-S-H was clearly observed. The destabilization of C-S-H at pH values below 9.5 is in agreement with studies on the stability of C-S-H upon leaching (Shi and Stegemann, 2000; Peyronnard et al., 2009; Leisinger et al., 2014; Swanton et al., 2016). The silicon concentrations, however, remained below the concentrations in equilibrium with respect to amorphous silica (1-2 mmol/l), which indicated the formation of another silica containing solid, i.e. M-S-H.

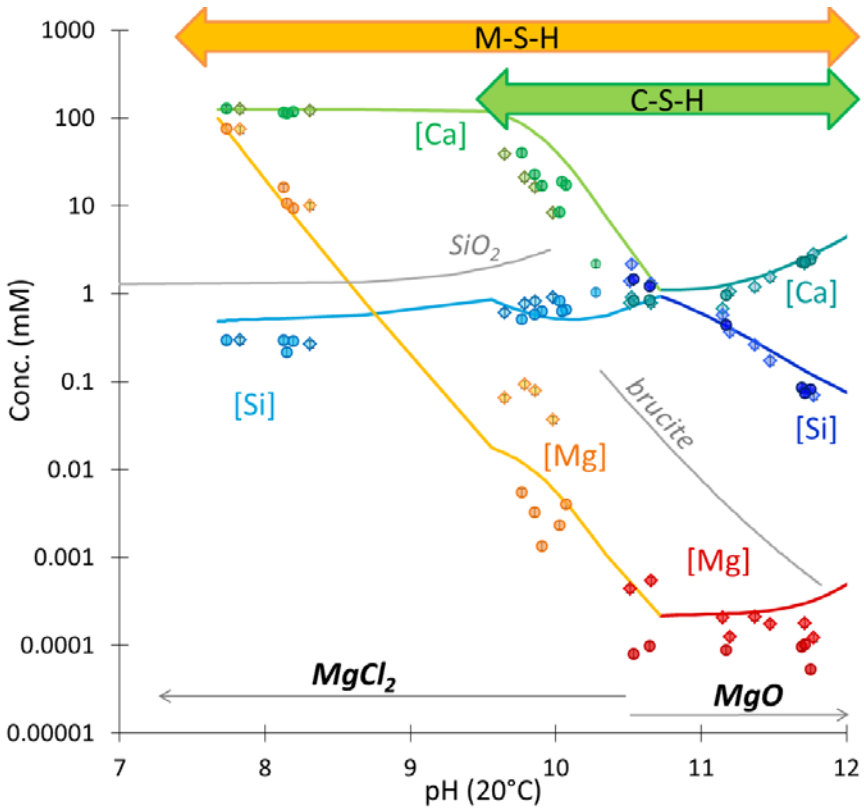

Figure 50: Measured silicon, magnesium, and calcium as a function of pH (diamond: 3 months, circles: 12 months) and calculated solubility curves of C-S-H and M-S-H using the solid-solution's models. Solubility's of brucite and amorphous SiO_2 are indicated in grey.

The magnesium concentrations were very low in the case of low $MgCl_2$ additions (samples $0.05MgCl_2$ up to $0.26MgCl_2$) at the pH values ≥ 9.7, indicating that the magnesium initially added reacted directly with the amorphous silica from the dissolution of C-S-H, consistent with the observation of M-S-H by ^{29}Si MAS NMR. Only for relatively high $MgCl_2$ additions ($0.87MgCl_2$, $1.33MgCl_2$) at pH values lower than 8.3, higher magnesium concentrations were observed. The magnesium concentrations increased with the $MgCl_2$ addition up to ≈ 80 mmol/l at pH 7.7, i.e. up to one third of the total magnesium present (see Table 3). The strong increase of magnesium could indicate that M-S-H is expected to be not stable below a pH of ~ 7.5. The measured concentrations showed little variations between 3 and 12 months indicating that the

formation of M-S-H was relatively fast under these lower pH conditions, while the formation of M-S-H from MgO and SiO_2 needs several months to years to reach equilibrium (Zhang et al., 2011; Szczerba et al., 2013; Li et al., 2014; Nied et al., 2016).

Table 23: Summary of the presence of brucite and unreacted silica in the solid composition, the measured dissolved concentrations, pH values in the solutions in equilibrium with the C-S-H and the magnesium additions samples at 20°C and 50°C after 3 months and 1 year. M-S-H samples, from chapter 3, have been added as references (bold samples indicate that the solid has been analyzed in details).

			Mg/Si	time [months]	brucite[a]	unreacted silica[b]	[OH][c]	[Ca]	[Mg]	[Si]	[Cl]	pH
									mmol/l			
20°C	C-S-H	Ca/Si=0.8		*3*			0.239	0.91	---	2.16	0.18	10.5
				12			0.136	1.04	---	2.19	0.01	10.3
	M-S-H	Mg/Si=0.8		*3*	✓	✓	0.028	---	0.28	1.54	0.02	9.6
				12		✓	0.0022	---	0.33	1.36	0.03	8.5
50°C	C-S-H	Ca/Si=0.8		*3*			0.114	0.96	---	2.36	0.09	9.5
				12			0.025	1.23	---	4.61	0.01	9.0
	M-S-H	Mg/Si=0.8		*3*		✓	0.0028	---	0.22	2.81	0.02	8.3
				12		✓	0.0014	---	0.10	2.57	0.03	8.1
20°C	**C-S-H+$MgCl_2$**		**0.05**	*3*		*n.d.*	0.076	8.23	0.037	0.90	18.61	10.0
				12		✓	0.084	**8.48**	**0.002**	**0.84**	**19.28**	**10.0**
			0.11	*3*		*n.d.*	0.059	16.38	0.078	0.82	37.77	9.9
				12		*n.d.*	0.066	17.12	0.001	0.64	38.91	9.9
			0.15	*3*		*n.d.*	0.051	21.09	0.092	0.77	48.80	9.8
				12		*n.d.*	0.060	22.94	0.003	0.59	52.65	9.9
			0.26	*3*		*n.d.*	0.039	38.53	0.064	0.61	91.72	9.6
				12		✓	0.051	**40.36**	**0.006**	**0.52**	**96.62**	**9.8**
			0.87	*3*		*n.d.*	0.0019	120.83	10.00	0.26	319.00	8.3
				12		✓	0.0014	**117.72**	**9.44**	**0.29**	**305.34**	**8.2**
			1.34	*3*		*n.d.*	0.0006	125.32	73.98	0.29	482.65	7.8
				12		*n.d.*	0.0005	128.31	76.32	0.30	535.93	7.7
50°C			*0.03*	*3*		*n.d.*	*0.073*	*8.76*	*0.002*	*0.72*	*17.34*	*9.4*
				12		*n.d.*	*0.058*	*8.83*	*0.001*	*0.79*	*15.24*	*9.3*
			0.11	*3*		*n.d.*	*0.061*	*18.21*	*0.001*	*0.68*	*35.39*	*9.3*
				12		*n.d.*	*0.051*	*17.24*	*0.001*	*0.68*	*32.27*	*9.2*
			0.15	*3*		*n.d.*	*0.055*	*22.78*	*0.001*	*0.63*	*45.54*	*9.2*
				12		*n.d.*	*0.047*	*23.51*	*0.001*	*0.70*	*44.48*	*9.2*
			0.26	*3*		*n.d.*	*0.044*	*41.88*	*0.002*	*0.63*	*86.65*	*9.2*
				12		*n.d.*	*0.038*	*45.46*	*0.001*	*0.70*	*84.20*	*9.1*
			0.87	*3*		*n.d.*	*0.0009*	*125.40*	*7.03*	*0.61*	*288.18*	*7.8*
				12		*n.d.*	*0.0007*	*135.72*	*10.67*	*0.68*	*328.61*	*7.7*
			1.34	*3*		*n.d.*	*0.0003*	*134.32*	*77.00*	*0.66*	*433.25*	*7.4*
				12		*n.d.*	*0.0003*	*145.38*	*84.57*	*0.64*	*466.22*	*7.4*
20°C	**C-S-H+MgO**		**0.04**	*3*	✓	*n.d.*	0.324	0.79	0.0005	1.31	0.17	10.7
				12	✓		0.243	**0.84**	**0.0001**	**1.47**	**0.01**	**10.5**
			0.23	*3*	✓	*n.d.*	2.176	1.54	0.0002	0.17	0.1	11.5
				12	✓	✓	1.066	**0.97**	**0.0001**	**0.44**	**0.01**	**11.2**
			0.59	*3*	✓	*n.d.*	4.427	2.85	0.0001	0.07	0.09	11.8

		12	✓		3.614	**2.30**	**0.0001**	**0.09**	**0.01**	**11.7**
	0.86	*3*	✓	*n.d.*	3.780	2.21	0.0002	0.08	0.01	11.7
		12	✓	*n.d.*	3.790	2.31	0.0001	0.07	0.01	11.7
	0.04	*3*	✓	*n.d.*	*0.298*	*0.79*	*0.0002*	*1.15*	*0.16*	*9.9*
		12	✓	*n.d.*	*0.276*	*0.84*	*0.0001*	*1.05*	*0.01*	*9.8*
	0.23	*3*	✓	*n.d.*	*2.587*	*1.84*	*0.0002*	*0.11*	*0.46*	*10.6*
		12	✓	*n.d.*	*1.619*	*1.43*	*0.0001*	*0.14*	*0.01*	*10.4*
	0.59	*3*	✓	*n.d.*	*4.763*	*3.17*	*0.0002*	*0.07*	*0.14*	*10.8*
		12	✓	*n.d.*	*4.127*	*2.96*	*0.0001*	*0.06*	*0.01*	*10.8*
	0.86	*3*	✓	*n.d.*	*5.844*	*3.68*	*0.0001*	*0.06*	*0.49*	*10.9*
50°C		*12*	✓	*n.d.*	*5.217*	*3.48*	*0.0001*	*0.05*	*0.01*	*10.8*

[a]from TGA,

[b]from ^{29}Si MAS NMR,

[c] Hydroxide concentrations calculated from the measured pH values

Magnesium's detection limit: 0.00001mmol/l

To investigate whether any calcium remained in the M-S-H, three of the samples were dissolved in 0.1 M HCl. The results in Table 24 showed a Ca/Mg ratio in the M-S-H of only 0.006 ± 0.01 for the sample with Mg/Si = 0.87, thus confirming the complete destabilization of C-S-H and pointing towards no or a very low uptake of calcium within the M-S-H structure.

The magnesium measurements summarized in Table 24 agreed well with the total amounts present as given in Table 3, which indicated a good accuracy of the measured aqueous concentrations. The measured calcium content in the solid together with the liquid phase was with 13.1±1.5 to 14.5±1.6 mmol somewhat lower than the 15.2 mmol of calcium initially used, which indicates either an underestimation of the measured calcium concentrations, the presence of less calcium in the C-S-H than expected or the removal of calcium ions loosely associated in the diffusive layer of M-S-H and C-S-H during washing with isopropanol and water. The slight decrease of the amount of measured total calcium in the samples with very high dissolved calcium (sample 0.87$MgCl_2$), could point towards a removal of calcium during the washing process and thus to the presence of some calcium at the surface of M-S-H even if effect of errors during the preparation of the samples, filtration and IC measurements cannot be excluded.

The Mg/Si and Ca/Si in M-S-H and C-S-H were calculated from the measured Ca and Mg in the solid part taking into account only the amount of silicate associated with M-S-H or C-S-H from the ^{29}Si MAS NMR analysis. For the 0.26$MgCl_2$ sample Ca/Si (0.5±0.3) and Mg/Si (0.6 ± 0.2) ratios were determined. These ratios were in agreement with the 0.67 usually reported for C-S-H and the 0.67-0.8 (Brew and Glasser, 2005b; Zhang et al., 2011; Szczerba et al., 2013; Nied et al., 2016) for M-S-H.

In summary, the different techniques indicated the destabilization of C-S-H and the formation of M-S-H upon the addition of $MgCl_2$ even if only little $MgCl_2$ (0.05$MgCl_2$) was added. C-S-H was observed to be unstable at pH values lower than 9.5 and M-S-H is expected to be destabilized at pH lower than 7.5.

Table 24: Composition of the solids from dissolution, of the aqueous phase from filtration, the total experimentally determined and the experimentally determined ratios Mg/Si in M-S-H and Ca/Si in C-S-H from mass balance and ^{29}Si MAS NMR deconvolutions.

	In the solid (from diss.)		+ In the liquid (IC)			= total $_{experimental}$ (mass balance)[a]		% Si[b] in M-S-H	Mg/Si	Ca/Si
Initial Mg/Si	mmol		mmol			mmol				
	Ca	Mg	Ca	Mg	Si	Ca	Mg	(NMR)		
0.05	13.6±1.5	0.9±0.2	0.9±0.1	~0[c]	0.1±0.01	14.5±1.6	0.9±0.2	7	0.7±0.5	0.8±0.2
0.26	9.6±0.9	5.3±0.5	4.4±0.5	~0[c]	0.1±0.01	14.0±1.4	5.3±0.5	44	0.6±0.2	0.5±0.3
0.87	0.1±0.1	15.4±1.9	13.0±1.4	1.0±0.1	~0[c]	13.1 ±1.5	16.4±2.0	98	0.8±0.2	0.005[1]

[a] solid part + liquid part

[b] error detailed in the text

[c] detected by IC (cf. Table 23) but below 0.01mmol and neglected in the calculations

4.2.1.2. C-S-H + MgO

The addition of MgO to C-S-H increased the pH, in contrast to the $MgCl_2$ additions. The XRD patterns and the TGA curves of the C-S-H samples with the different additions, 0.04MgO, 0.23MgO and 0.59MgO (cf. Table 3), are shown in Figure 51 and Figure 52 respectively. Independently of the MgO additions, C-S-H was clearly observed by XRD and TGA in all the samples while no clear XRD reflections of M-S-H can be observed in contrast to the samples where $MgCl_2$ was added, as discussed previously. TGA data could indicate the formation of small quantities of M-S-H as visible by the minor water loss between 400-700°C.

[1] It is difficult to detect small calcium concentrations in the presence of high magnesium concentrations by IC. CEC measured later on the 0.87$MgCl_2$ samples (1 year, 20 and 50°C) showed a $Ca_{exch}/Si \sim 0.03$. This value is more precise.

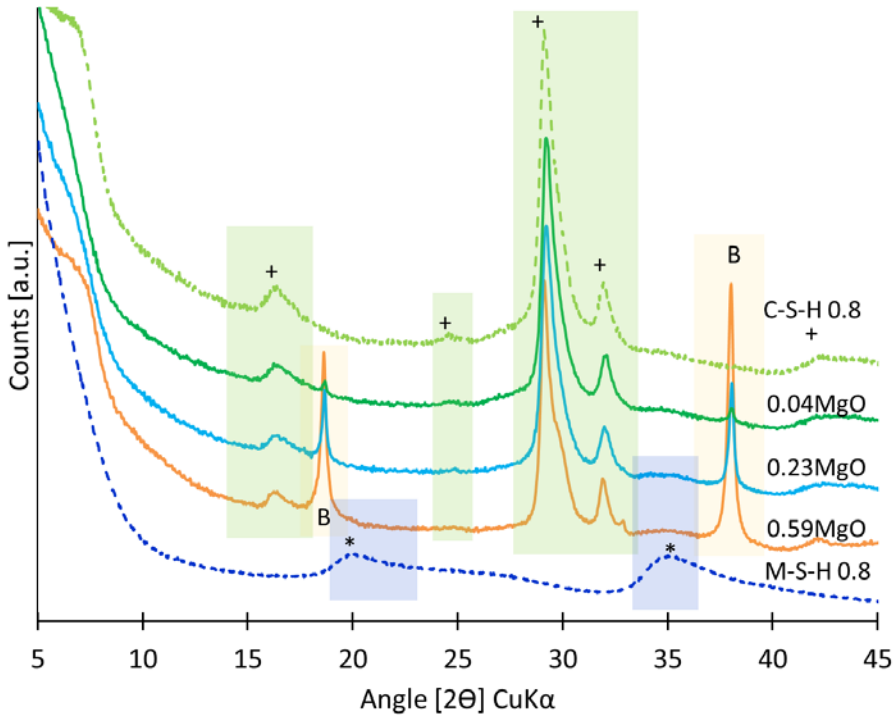

Figure 51: XRD patterns of C-S-H samples where MgO has been added: 0.04MgO, 0.23MgO and 0.59MgO after 1 year of curing at 20°C, patterns of M-S-H 0.8 and C-S-H 0.8 shown as references (B=brucite ($Mg(OH)_2$), +=C-S-H, *= M-S-H).

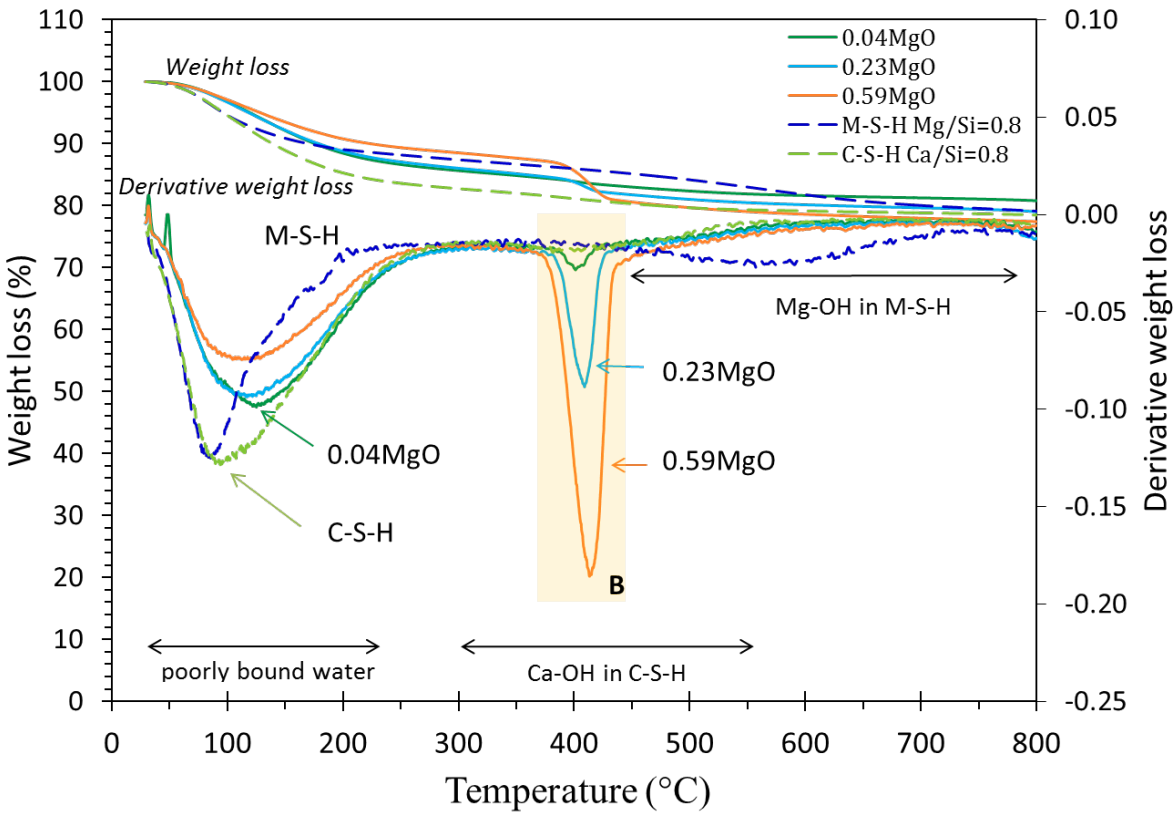

Figure 52: Thermogravimetric analysis of C-S-H samples where MgO has been added: 0.04MgO, 0.23MgO and 0.59MgO after 1 year of curing at 20°C, patterns of M-S-H 0.8 and C-S-H 0.8 shown as references. B=brucite ($Mg(OH)_2$).

^{29}Si MAS NMR spectra are shown in Figure 53 and the deconvolution is given in Table 25. The presence of MgO and the increase of pH (see below) resulted in shorter silicate chains in the C-S-H as visible in the higher amount of the Q^1 tetrahedral site attributed to C-S-H at -79.6 ppm. This is in accordance with (L'Hôpital et al., 2016a), where a shortening of the silicate chains of pure C-S-H has been observed when the pH is increasing. The increase of the Q^1 signal points towards an increase of Ca/Si in C-S-H (L'Hôpital et al., 2015; Lothenbach and Nonat, 2015), which agrees with the calculated Ca/Si in C-S-H in Table 25.

In contrast to the XRD and TGA data, the ^{29}Si MAS NMR data indicated clearly the formation of a small amount of M-S-H with the chemical shift between -92 and -97 ppm, characteristic of M-S-H's Q^3 tetrahedral sites, in addition of the signals characteristic of C-S-H. The quantifications based on the deconvolutions of the Q^3 bands gave 9± 3 %, 14± 3.5 % and 19± 4 % of the silica (Table 25) attributed to M-S-H in the 3 samples.

The total intensity of the sites attributed to C-S-H decreased slightly but remains high: 80 % of the silica was attributed to C-S-H even for the highest addition. The formation of some M-S-H is consistent with the observed increase of the Ca/Si in the remaining C-S-H as some silica is used to form M-S-H.

The FTIR and Raman spectra (Figure 54 and Figure 55) of all samples confirmed the ^{29}Si MAS NMR results; the samples were mainly composed of C-S-H as the spectra were similar to the pure C-S-H spectra. The FTIR band (Figure 54) at ~ 970 cm^{-1}, characteristic of C-S-H, developped a small shoulder at 1045 cm^{-1} if MgO was added confirming the precipitation of a small amount of M-S-H as did the additional presence of a band at 870 cm^{-1} in the Raman spectra, characteristic of Si-O symmetrical stretching of Q^2 tetrahedral site in M-S-H.

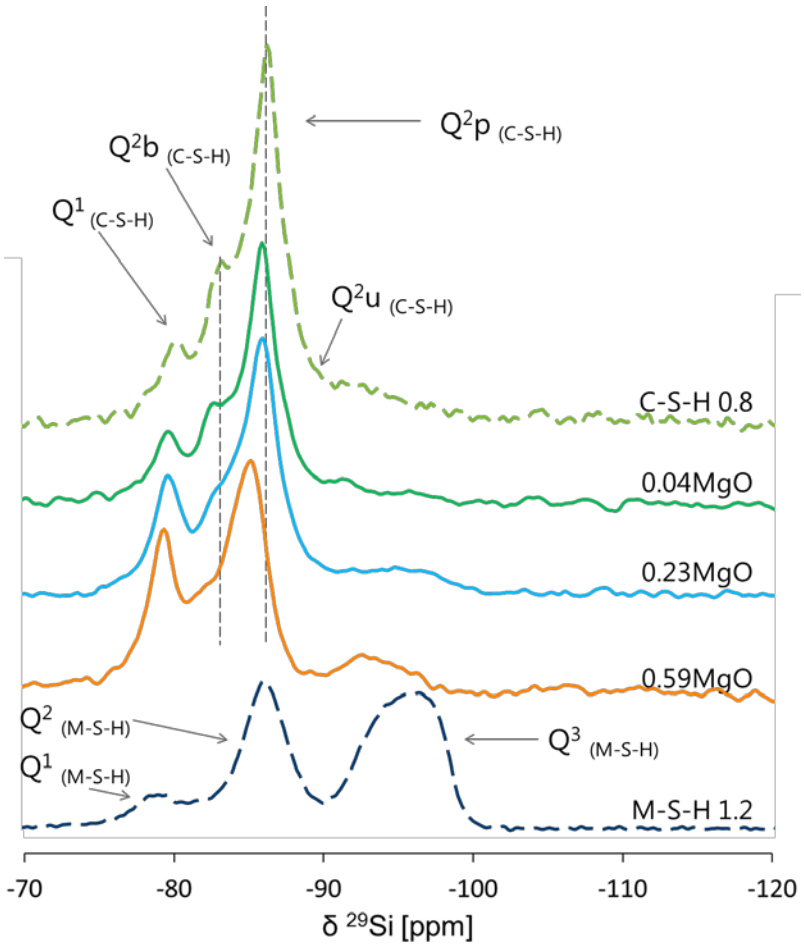

Figure 53: ^{29}Si MAS NMR spectra of C-S-H samples where MgO has been added: 0.04MgO, 0.23MgO and 0.59MgO after 1 year of curing at 20 °C, (C-S-H and M-S-H shown as references).

Table 25: Relative intensities (% ± 2.5 %) of different silicon shifts obtained from the deconvolution of the ^{29}Si MAS NMR spectra for the samples 0.04MgO, 0.23MgO and 0.59MgO after 1 year of curing at 20 °C (C-S-H and M-S-H shown as references) (δ^{29}Si in ppm ± 0.3 ppm).

	δ^{29}Si (C-S-H)							δ^{29}Si (M-S-H)						Am. silica	Total	
	Q^1	Q^2b	Q^2p	Q^2u	MCL	Ca/Si	Q^3	Q^1	Q^2	Q^3a	Q^3b	Q^3c		$Q^3(SiO_2)$	C-S-H	M-S-H
	-79.6	-82.8	-85.8	-88.2			-93.5	-78.3	-85.5	-92.7	-94.7	-96.7	Q^2/Q^3	-100.9	% of silica	
C-S-H 0.8	8	22	59	7	25		4	-	-	-	-	-	-	-	96	-
0.04 MgO	14	20	51	5	13	0.85	3	-	4	3	0	2	0.9	0	89	9
0.23 MgO	18	18	43	5	9	0.90	2	-	6	2	2	3	0.9	2	83	14
0.59 MgO	26	18	36	0	6	1.00	1	-	9	5	2	2	0.9	0	80	19
M-S-H 0.8	-	-	-	-	-		-	2	34	23	8	27	0.6	6	-	94
M-S-H 1.2	-	-	-	-	-		-	6	47	14	12	21	1.0	-	-	100

Quantification error ≃ ± 10% of absolute amount of (%Si) +2.5%.

In addition, the presence of brucite ($Mg(OH)_2$) was observed by XRD and TGA with the characteristic reflection peaks at 18.6, 32.7, 38.0° 2θ (Figure 51) and the water loss located at ~ 400°C in the TGA curves (Figure 52). Brucite was also visible by FTIR with a band at 3692 cm^{-1} (Frost and Kloprogge, 1999; Nied et al., 2016) in all the samples (data not shown). The amount of brucite quantified from TGA is compiled in Table 26. This amount was lower than the theoretical maximum brucite content and corresponded to 31, 41 and 74 % ± 20 % of the total magnesium content in the different samples, confirming the presence of magnesium bound in M-S-H. Table 26 also shows the quantification of brucite by TGA in the samples cured at 50 °C. In all cases, less brucite was present and more magnesium was found bound in M-S-H at 50°C than at 20 °C. This difference is related to the very slow reaction kinetics of brucite dissolution and M-S-H formation at 20 °C, while the reaction kinetics are faster at higher temperature, as discussed in more detail in chapter 3.2.

Table 26: Theoretical maximum amount of brucite calculated from total amount of magnesium added, experimental measured brucite content, and magnesium distribution between brucite and M-S-H.

Temperature	20°C			50°C		
Mg/Si	0.04	0.23	0.59	0.04	0.23	0.59
Theo. max $Mg(OH)_2$[a] (g/100 g)	3.9	17.1	30.3	2.9	14	33
Exp. $Mg(OH)_2$[b] (g/100 g)	1.2	7	22.5	0.8	3.5	19.2
% of Mg in brucite	31	41	74	28	25	58
% of Mg in M-S-H	69	59	26	72	75	42
Mg in M-S-H (mmol)	0.5	2.7	2.9	0.4	2.9	5.6

[a] Theo. max % of $Mg(OH)_2$ is the amount of brucite formed based on the initial amount of MgO added considering the total mass of solid, the initial MgO is obtained by dissolution

[b] calculated from TGA

The presence of only a small quantity of M-S-H was observed by FTIR, Raman and ^{29}Si MAS NMR for C-S-H if MgO was added, while 30 to 70 % of magnesium was present as brucite.

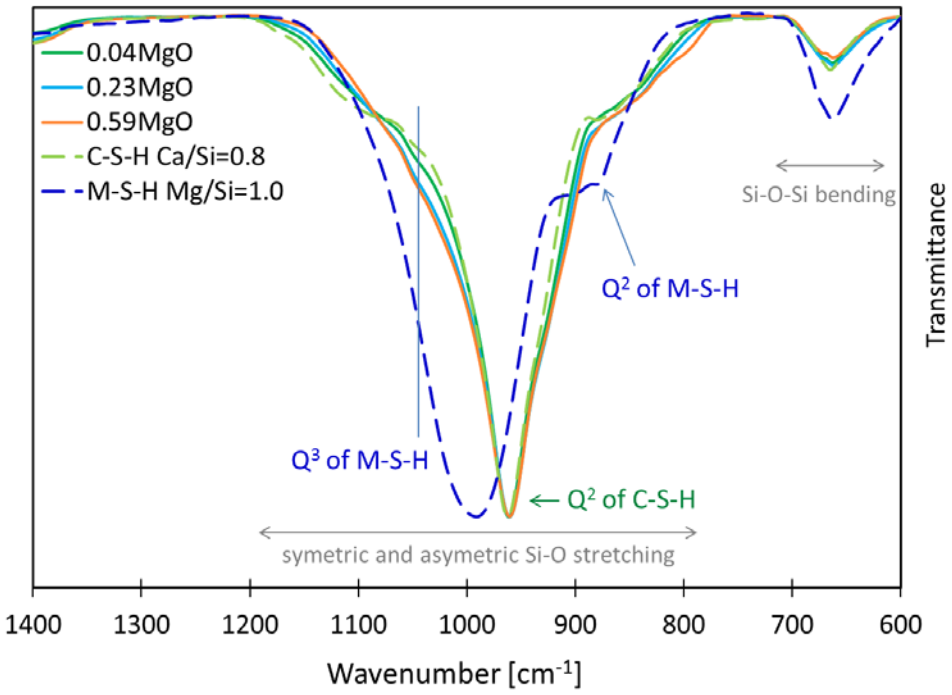

Figure 54: FTIR spectra of C-S-H samples where MgO has been added: C-S-H +0.04MgO, C-S-H +0.23MgO and C-S-H +0.59MgO after 1 year of curing at 20°C, spectra of M-S-H 0.8 and C-S-H 0.8 shown as references (the vertical line indicates the shoulder due to the Q^3 silicate sites in M-S-H).

The experimentally determined Mg/Si and Ca/Si in M-S-H and C-S-H were calculated from the quantification of the brucite by TGA (Table 26), the quantification of the silica attributed to C-S-H or M-S-H (^{29}Si MAS NMR, Table 25) and taking into account the dissolved ions in solution and are summarized in Table 27. The increase of Ca/Si in the C-S-H corresponded to the experimental observations with the decrease of MCL in C-S-H. A Mg/Si of ≈ 0.9 was observed in M-S-H. However, the data derived from mass balance calculations are associated with a high experimental error.

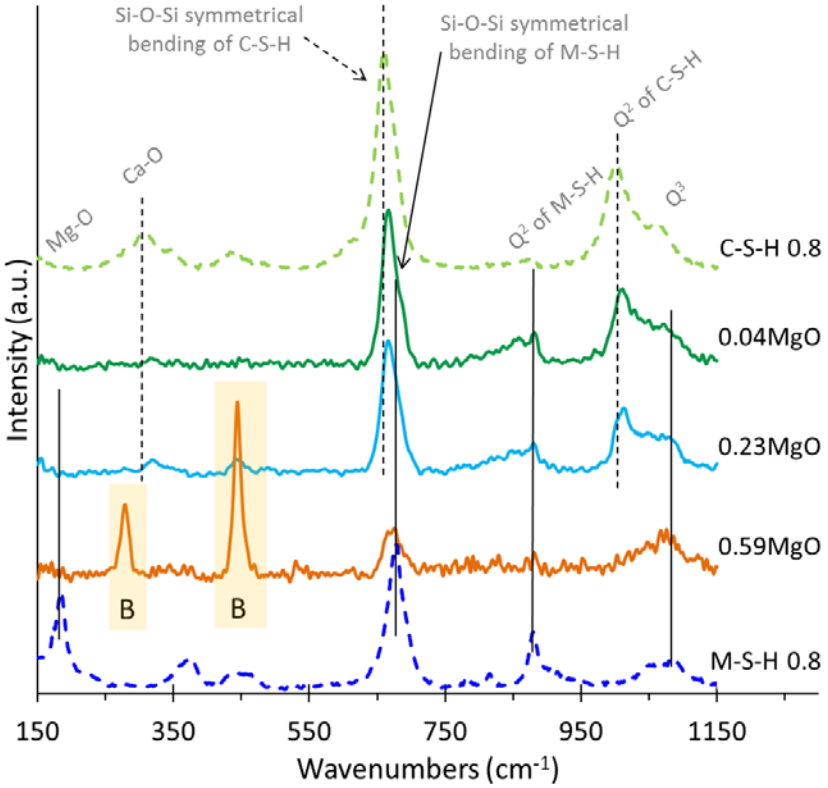

Figure 55: Raman spectra of C-S-H samples where MgO has been added: C-S-H +0.04MgO, C-S-H +0.23MgO and C-S-H +0.59MgO after 1 year of curing at 20°C, (C-S-H and M-S-H shown as references), B=brucite ($Mg(OH)_2$).

Table 27: Initial composition of the samples C-S-H +0.04MgO, C-S-H +0.23MgO and C-S-H +0.59MgO in mmol, amount of Ca, Si and Mg attributed to the solution at equilibrium, % of silica attributed to M-S-H and C-S-H, experimental % of magnesium attributed to M-S-H, and experimentally determined Mg/Si and Ca/Si in M-S-H and C-S-H.

initial Mg/Si	initial[a] mmol			liquid part (from IC) mmol			% Si (NMR) in		% Mg (TGA) in	Mg/Si	Ca/Si
	Ca[a]	Si[a]	Mg[a]	Ca	Si	Mg	M-S-H	C-S-H	M-S-H		
0.04	15.2	19.1	0.7	0.1	0.2	~0[b]	9	89	69	-	0.9 ± 0.1
0.23	15.2	19.1	4.5	0.1	0.1	~0[b]	15	84	59	0.9 ± 0.5	1.0 ± 0.1
0.59	15.2	19.1	11.2	0.3	~0[b]	~0[b]	19	77	26	0.8 ± 0.5	1.0 ± 0.1

[a] from Table 3,

[b]detected by IC (cf. Table 23) but ≤ 0.01mmol and not taking account in the calculations

The addition of MgO to pure water leaded to the formation of brucite and a pH value of 10.5. Interestingly, the addition of MgO to C-S-H increased the pH well above the pH 10.5 observed for pure C-S-H (Ca/Si = 0.8) (Table 23) and the solutions were clearly undersaturated with respect to brucite (Figure 50) This increase in pH and hydroxide concentrations is related to the release of calcium from C-S-H at higher Ca/Si as visible in the increased calcium concentrations (Table 23 and Figure 50). While the calcium and hydroxide concentrations increases, the silicon concentrations were

lowered (Figure 50) in agreement with the changes expected for pure C-S-H phase if the Ca/Si of C-S-H is increased from 0.8 to 1.0 (Lothenbach and Nonat, 2015; L'Hôpital et al., 2016a; Walker et al., 2016). This confirmed that the addition of MgO to C-S-H leaded to the formation of C-S-H with a higher Ca/Si as indicated in Table 27 in agreement with the higher fraction of Q^1 tetrahedral silicate which was observed by ^{29}Si MAS NMR. The magnesium concentrations remained clearly below the solubility of brucite as shown in Figure 50, although brucite was still present. This is due to the very slow dissolution of brucite when silicon and M-S-H are present, as discussed in details in chapter 3.2.

Comparable calcium and silicon concentrations were measured after 3 months and 1 year, while the magnesium concentrations decreased with time. At 50°C, similar concentrations were measured as at 20°C as detailed in Table 23, in agreement with the observations in pure M-S-H (chapter 3.2) and in pure C-S-H (Barbarulo, 2002; Lothenbach et al., 2008). However, less brucite was present at 50°C where the dissolution of brucite, even in the presence of silicon, proceeded faster than at 20°C as in pure M-S-H (chapter 3.2).

4.2.1.3. Comparison with thermodynamic modelling

The measured calcium, magnesium and silicon concentrations and the solubility curves calculated by GEMS (Kulik et al., 2013a) at 20°C are plotted as a function of pH in Figure 50. The results of thermodynamic modelling, using the thermodynamic data for C-S-H and M-S-H as detailed in Table 7, showed in general a good agreement with the changes observed. The modelling predicted the formation of C-S-H and M-S-H for pH values between 9.6 and 12. At lower pH values (7.8 to 9.6) only M-S-H was predicted. Figure 56 shows that the calculated Mg/Si and Ca/Si decreased if $MgCl_2$ was added to the C-S-H and increased if MgO was added to C-S-H. The trends compared well with the experimentally determined Mg/Si and Ca/Si from mass balance (Table 6 & Table 9) except the Mg/Si at pH values above 10.5. The Ca/Si in C-S-H estimated from the MCL (Table 22 & Table 25) showed in all cases comparable trends.

The $MgCl_2$ additions lowered the pH values from above 10 to 8 as the magnesium precipitated as M-S-H while the chloride ions remained in solution. The addition of low quantities of $MgCl_2$ led to the formation of M-S-H while the Ca/Si in C-S-H was lowered. Higher additions lowered the pH below 9.5 which resulted in the destabilization of C-S-H as shown in Figure 56. The modelled decrease of both Ca/Si and Mg/Si in the C-S-H and M-S-H was in the same range as the experimentally determined atomic ratios (Table 24, Figure 56).

Also the modelled effect of MgO addition to C-S-H Figrue 50 and Figure 56) fitted well to the measured calcium and silicon concentrations and to the increase of the Ca/Si

(Table 27 and Figure 56) in C-S-H. The formation of M-S-H was predicted, which agreed with the very low magnesium concentrations. No brucite formation was predicted up to pH 12, although brucite was observed experimentally. The strong under saturation of the solution with respect to brucite visible in Figure 50 indicated a kinetic hindrance of brucite dissolution in the presence of dissolved silicon, which was observed also in M-S-H systems if brucite is present (Zhang et al., 2011; Szczerba et al., 2013; Li et al., 2014), which can be explained by the partial reaction of brucite. It can be expected that, after longer reaction times or higher temperature, higher Mg/Si would be reached as indicated by the presence of less brucite at 50 °C.

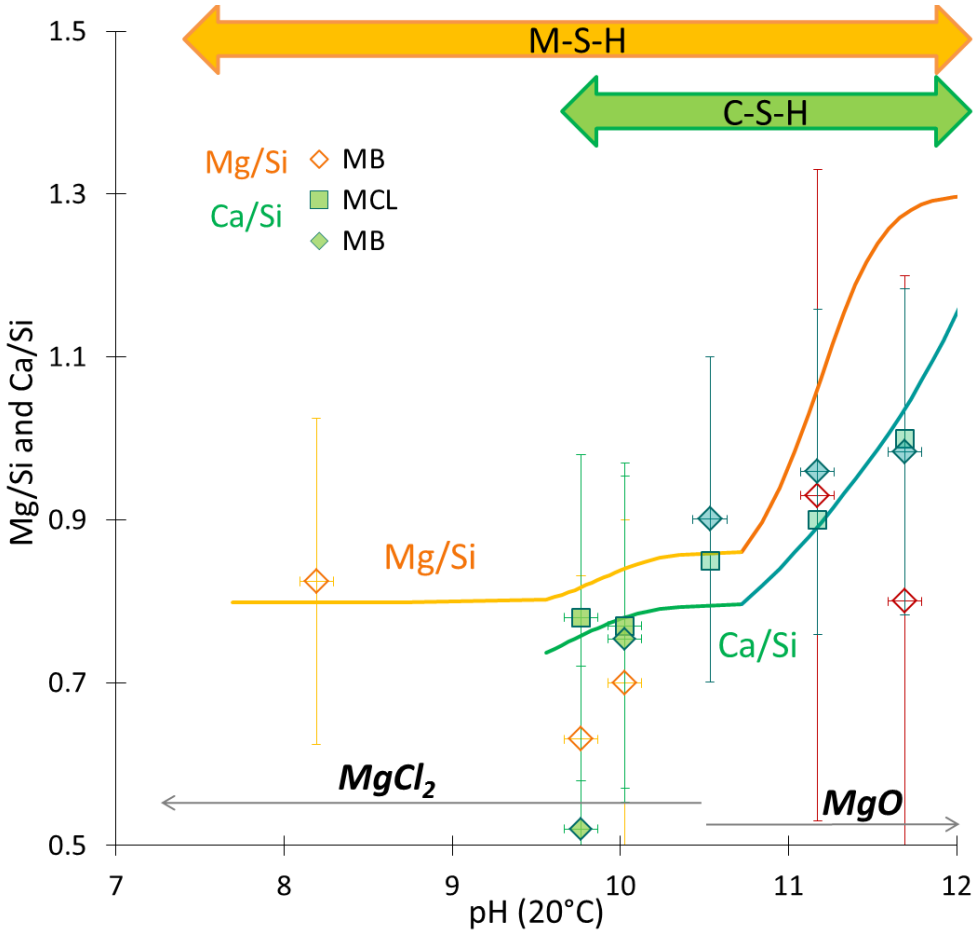

Figure 56: Evolution of atomic ratios calculated by GEMS and comparison with the ratios obtained experimentally (from MCL (^{29}Si MAS NMR, Table 3 & Table 7), and from MB, mass balance (Table 24 & Table 27)).

4.2.2. Conclusions

It was observed experimentally that low Ca/Si C-S-H was stable in the pH range 9.6 to 11.5. Lowering the pH due to the addition of low quantities of $MgCl_2$ leads to a decrease of the Ca/Si in C-S-H and to the formation of M-S-H. At pH values below 9.6, C-S-H was destabilized while M-S-H remained stable down to pH values ~ 7.5. The M-S-H formed from the dissolution of C-S-H and $MgCl_2$ was comparable to M-S-H prepared from MgO and SiO_2 (Brew and Glasser, 2005b; Szczerba et al., 2013; Nied et al., 2016).

Increasing the pH values from 10 to 11.5 by the addition of MgO leads to an increase of the Ca/Si ratio in C-S-H, i.e. to shorter silicate chains, higher calcium concentrations and lower silicon concentrations. M-S-H formation was observed up to a pH of 11.5. Experimentally, the persistence of some brucite was observed as the dissolution of brucite is very slow in the presence of silicon while modelling predicted only the presence of M-S-H which is thermodynamically more stable. It was shown that M-S-H is stable in the pH range 7.5 to 12. A small incorporation of calcium in M-S-H seems possible, although it could not be proven and further investigations are needed.

The present chapter has demonstrated that C-S-H can be destabilized in the presence of magnesium in the pH range 7.5 to 12. The destabilization is fast at pH values below 10 and proceeds very slowly at pH values above 10. This fast kinetic at lower pH values might explain why M-S-H has been observed clearly after 2 and 5 years at the interface between clays and “low pH cements”, where pH values ranges from 10 to 12 (Codina et al., 2008; Lothenbach et al., 2012a; Lothenbach et al., 2014), but not at the interface between clays and Portland cements (Dauzères et al., 2010; Jenni et al., 2014; Mäder et al., 2017), where pH values above 13 are present (Vollpracht et al., 2015). In the long-term, however, M-S-H could be expected to form also at the interface with Portland cement, as M-S-H has been observed in both Portland cement and in blended concretes exposed for long times to seawater, which also contains significant quantities of magnesium (Jakobsen et al., 2016).

4.3. Investigation of the possible magnesium incorporation in calcium silicate hydrate (C-S-H) and of the calcium in magnesium silicate hydrate (M-S-H)

This part corresponds to the shortened and adapted version of the publication: Ellina Bernard, Barbara Lothenbach, Cau-Dit-Coumes, Christophe Chlique, Alexandre Dauzères, Isabelle Pochard, Magnesium and calcium silicate hydrates, Part I: Investigation of the possible magnesium incorporation in calcium silicate hydrate (C-S-H) and of the calcium in magnesium silicate hydrate (M-S-H), **Applied Geochemistry**, 89, (2018), 229-242 (Bernard et al., 2018b).

Given the different structures and stability domains, the previous part showed and confirmed that, at pH<9.5, C-S-H was not stable and only M-S-H precipitated and that, at pH>9.5, the precipitation of two distinct phases.

This part investigates the possible uptake of calcium by M-S-H and of magnesium by C-S-H in batch experiments at 9 < pH < 10.5.

M-S-H was synthesized in batch experiments in the presence of calcium (6.25 to 12.5 molar %). Similarly, C-S-H was synthesised in the presence of magnesium (6.25 to 12.5 molar %) as detailed in part 2.1.2. The surface charge of the particles in suspension was investigated by zeta potential measurements and their cation exchange capacity (CEC) was determined. The composition of the solutions at equilibrium was analysed by pH measurements and ion chromatography. The solid phases were characterized by thermogravimetry analysis (TGA), powder X-ray diffraction (XRD) and ^{29}Si solid-state MAS NMR. The part 2.3.3.1 details the analytical techniques and the part 2.3.3.2 the thermodynamic modelling.

4.3.1. Results and discussions

4.3.1.1. Co-0.05 and Co-0.10 samples

This section focusses on M-S-H syntheses labelled Co-0.05 and Co-0.10. The (Mg+Ca)/Si ratio was set to 0.8 and a small fraction of MgO was substituted by CaO (Ca/Si=0.05 and 0.10).

.

4.3.1.1.1. Aqueous phase composition

The pH values and measured concentrations of the solutions equilibrated with the co-precipitated samples are plotted in Figure 57 and compared to the data obtained for pure C-S-H (chapter 4.2) and pure M-S-H (chapter 3.2).

In the solution at equilibrium with the pure M-S-H sample, a pH of 8.3 was measured, together with magnesium and silicon concentrations of 0.38 mmol/l and 1.44 mmol/l respectively. The substitution of magnesium by calcium at constant (Mg+Ca)/Si ratio of 0.8 increased the pH (Figure 57, Appendix E) from 8.3 to 8.9 (sample Co-0.05) or 9.3 (sample Co-0.10). A comparable decrease of magnesium has been observed for pure M-S-H at higher pH values (chapter 3.2) and for M-S-H in the presence of some calcium (Lothenbach et al., 2015). Little difference was observed in the concentrations and pH values between 1 and 2 years confirming that the samples were very close to equilibrium.

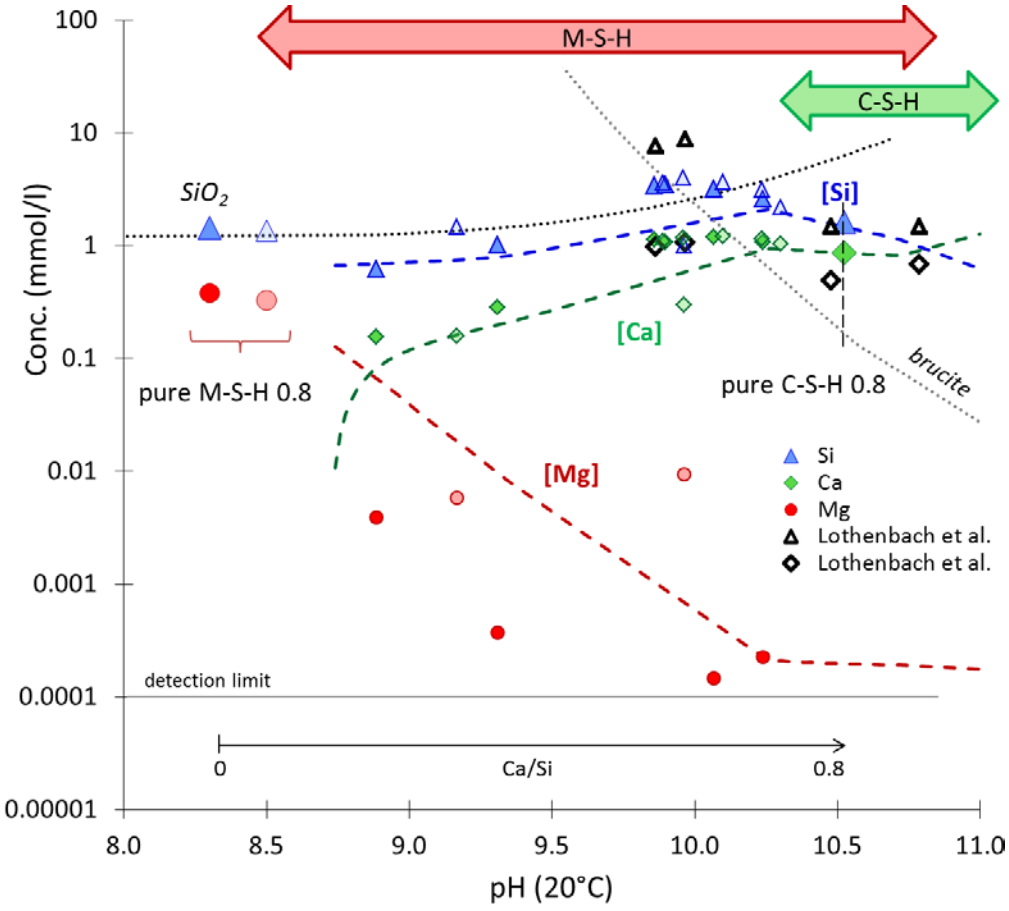

Figure 57: Measured silicon (triangles), magnesium (circles), and calcium (diamonds) concentrations at 20°C at 1 year (lighter symbols) and 2 years (full symbols) as a function of pH. Empty symbols are from Lothenbach et al. (Lothenbach et al., 2015). The solubility of M-S-H, C-S-H (dashed lines), brucite and amorphous silica (dotted lines) were calculated from the thermodynamic data (solid solutions for M-S-H and C-S-H) in Table 28 without considering the formation of mixed M-(C)-S-H phase.

C-S-H phases are not stable at this range of pH (<9.5) as detailed in the previous chapter. It can be noted however that the calcium concentrations were much lower (0.15 to 0.46 mmol/l, depending on the initial calcium content, temperature and time) than the total amount of calcium that could theoretically be present in solution (11.93 ± 1.50 and 23.66 ± 2.60 mmol/l), which suggests the uptake of calcium by the solid phases.

4.3.1.1.2. Solid phase analysis

The solid analysis focused on the samples equilibrated for 1 year at 50°C. However, similar results were obtained for the samples equilibrated for 2 years at 20°C indicating that the equilibrium was reached in both conditions.

The XRD patterns of the two co-precipitated (Co-0.05 and Co-0.10) samples are compared to those of M-S-H and C-S-H in Figure 58. The broad peaks at 19.7, 26.7, 35.0, 60.3° 2Θ (Nied et al., 2016) were attributed to M-S-H, the main phase observed in the samples. In addition, traces of calcite ($CaCO_3$, PDF-00-005-0586) and brucite ($Mg(OH)_2$, PDF-01-083-0114) were present. Their amount was less than 1%, as assessed from TGA (Figure 59).

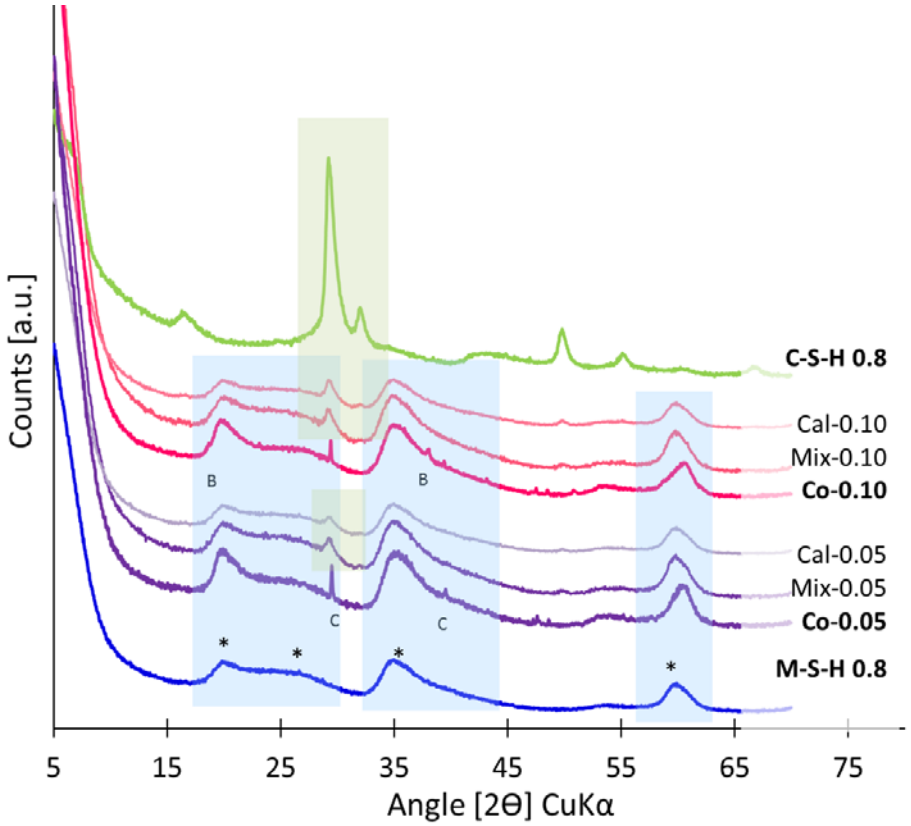

Figure 58: XRD patterns of samples Co-0.05 and Co-0.10 after 1 year of curing at 50°C compared to XRD patterns of M-S-H 0.8 (1 year at 50°C), C-S-H 0.8 (1 year at 50°C), mixed samples (0.10mix and 0.05mix), calculated reference patterns (Cal-0.05 and Cal-0.10) B=$Mg(OH)_2$ (brucite); C= $CaCO_3$ (calcite)..

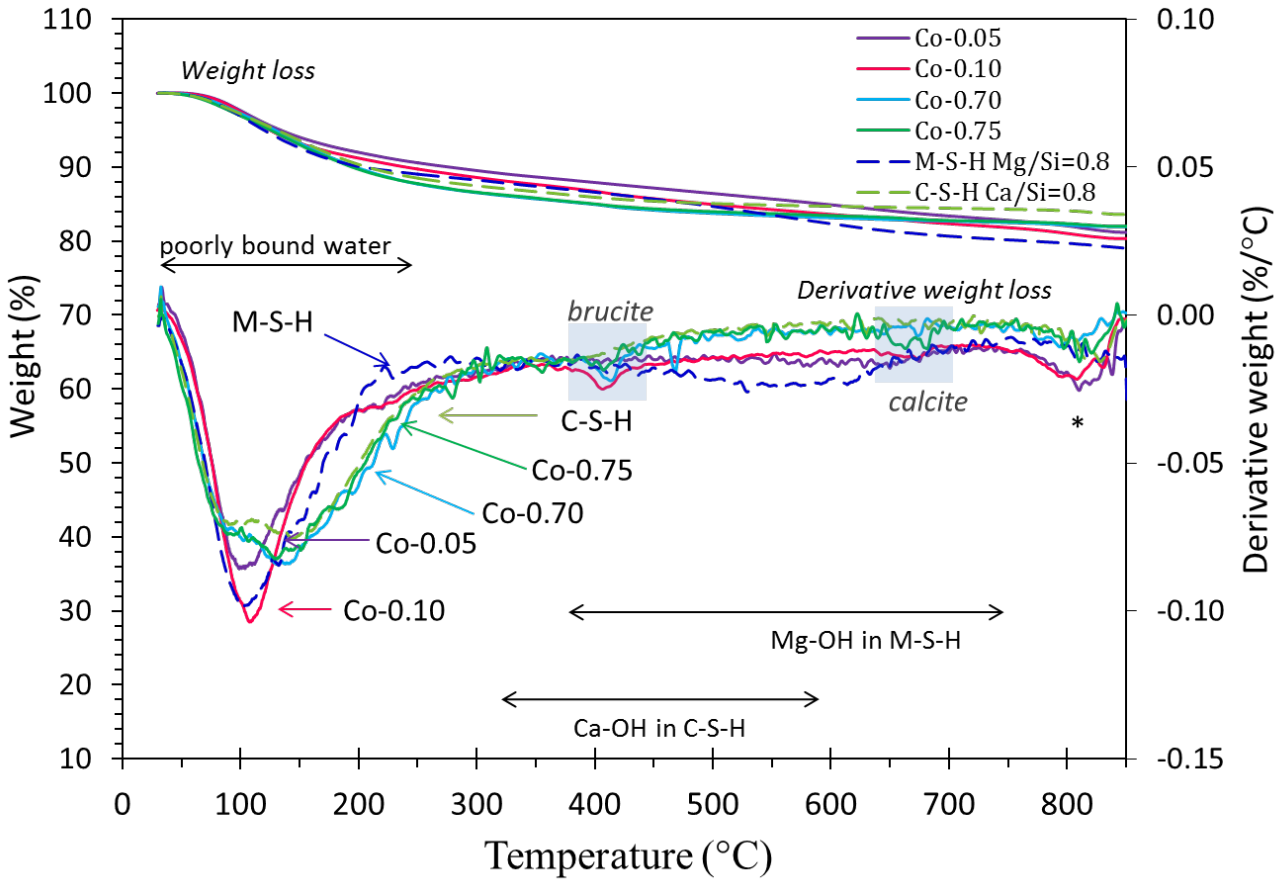

Figure 59: Thermogravimetric analysis of coprecipitated samples after 1 year of curing at 50°C compared to TGA of C-S-H 0.8 and M-S-H 0.8 (1 year, 50°C), * indicates the formation of wollastonite from C-S-H (Martin et al., 2017) and enstatite from M-S-H (as observed from talc (MacKenzie and Meinhold, 1994a)).

Complementary XRD patterns were measured and calculated for mixes of separately synthetized M-S-H and C-S-H phases. These mixes (Mix-0.05 and Mix-0.10) contained the same Mg/Si and Ca/Si ratios than samples Co-0.05 and Co-0.10, but the presence of any magnesium calcium silicate hydrate (M-C-S-H) could be excluded. The calculated XRD patterns (Cal-0.05, Cal-0.10) resulted from linear combinations of the patterns of plain M-S-H and C-S-H respecting the Mg/Si and Ca/Si ratios. Mix-0.05 and Mix-0.10 samples exhibited the same XRD patterns as the calculated ones (Figure 58), but slight differences were noticed for the co-precipitated samples. C-S-H, characterized by a main reflection peak at ~ 29.2° 2Θ, was present in the separately mixed samples but not in the co-precipitated ones. The sole observation of M-S-H by XRD was in good agreement with the low pH of the solution which should prevent the precipitation of C-S-H. The main part of the

calcium initially added was thus neither present in the solution nor in C-S-H (or only in very small quantities not observable by XRD).

The reflection at approx. 60.3° 2Θ in pure M-S-H is shifted to 60.4 and 60.5° 2Θ in the Co-0.05 and Co-0.10 samples, respectively. The reflection at higher angles is usually rather characteristic for talc structure, i.e. for a low Mg/Si (0.75) phyllosilicate.

^{29}Si MAS NMR spectra of the co-precipitated samples are presented together with the calculated spectra of the linear combination of pure M-S-H and C-S-H in Figure 60. Pure M-S-H 0.8 usually contains a small amount of amorphous silica (3-5% of SiO_2) ((Nied et al., 2016) and chapter 3) with a resonance at -110 ppm (Q^4) and a resonance at -100.9 ppm Q^3(-OH) (d'Espinose de Lacaillerie et al., 1995; Nied et al., 2016). The comparison of the calculated spectra with those of samples Co-0.05 and Co-0.10 shows the absence of amorphous silica in the co-precipitated samples.

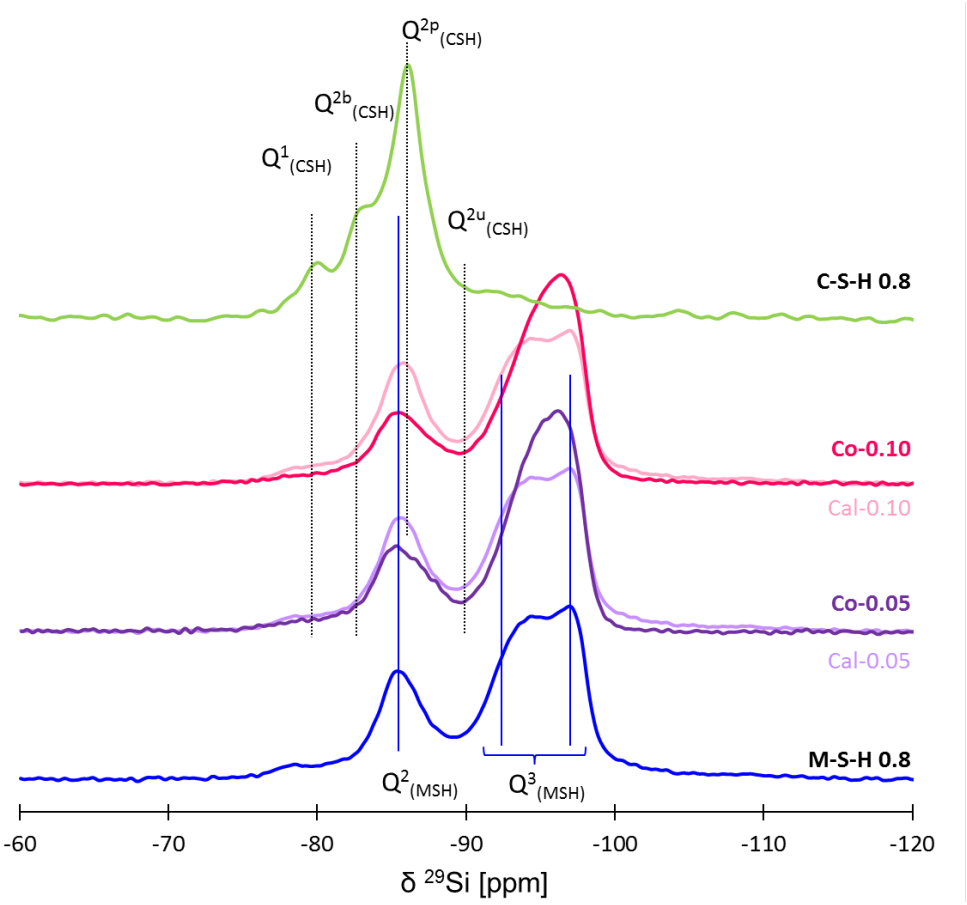

Figure 60: ^{29}Si MAS NMR spectra of Co-0.05 and Co-0.10 samples (1 year at 50°C) compared to spectra of C-S-H 0.8, M-S-H 0.8 and calculated samples Cal-0.05 and Cal-0.10.

The ^{29}Si MAS NMR spectra of Co-0.05 and Co-0.10 samples were similar to that of M-S-H 0.8 (Figure 60) with the presence of Q^2 tetrahedral silicate (chemical shifts at approx. -85.6 ppm) and Q^3 tetrahedral silicate (chemical shift between -92 and -97 ppm. No C-S-H could be detected. The comparison with the calculated spectra in Figure 60 points out a lower intensity of the Q^2 signal, but a higher content of Q^3 species. The Q^2 signal was broader and the Q^3 signal was less symmetrical and shifted to slightly more negative chemical shifts. This would be consistent with the presence of calcium in the vicinity of silicon since calcium shields silicon stronger than magnesium (Mägi et al., 1984; Lothenbach et al., 2015).

The associated deconvolutions are detailed in Table 28. The fraction of Q^3 silicate sites in M-S-H 0.8 (61% ±7%) increased to 73% (±8%) in Co-0.05 and Co-0.10 samples. The Q^2/Q^3 ratio calculated in the co-precipitated samples of ~0.4 (Table 28) was lower than the 0.6 usually found in pure M-S-H 0.8 (chapter 3). As the Q^2/Q^3 in M-S-H decreases with the decrease of Mg/Si (chapter 3), this low Q^2/Q^3 ratio suggests that the co-precipitated samples might have a Mg/Si lower than 0.8 (approx. to 0.7-0.75). The higher polymerization of the silicate network in the co-precipitated sample, together with the shift observed by XRD at high angles, seems to indicate a lower content of magnesium rather than the presence of calcium in the octahedral layers and thus that calcium might rather be adsorbed than incorporated in the octahedral layers. This is further investigated by complementary analyses.

Table 28: Relative peak area of the different silicon chemical shifts obtained from the deconvolution of the ^{29}Si MAS NMR spectra for the co-precipitated samples after 1 year of curing at 50°C (C-S-H (1 year at 20°C) and M-S-H (1 year at 50°C) shown as references).

	C-S-H				MCL		M-S-H						% of Si in		
	Q^1	Q^2_b	Q^2_p	Q^2_u		Q^3(?)	Q^1	Q^2	Q^3_a	Q^3_b	Q^3_c	App. Q^2/Q^3	$Q^3(SiO_2)$	C-S-H	M-S-H
	-79.6	-82.8	-85.8	-88.2		-93.5	-78.3	-85.5	-92.7	-94.7	-96.7		-100.9		
M-S-H 0.8	-	-	-	-	-	-	1	35	24	10	28	0.6	3	-	97
Co-0.05	-	-	-	-	-	-	1	27	18	25	29	0.4	-	-	100
Co-0.10	-	-	-	-	-	-	1	27	17	28	28	0.4	-	-	100
Co-0.70	6	17	42	3	23	3	0	9	8	5	7	0.4	0	69	28
Co-0.75	7	19	47	5	22	3	0	5	5	3	5	0.4	1	78	18
C-S-H 0.8	8	22	59	7	25	4	-	-	-	-	-	-	-	96	-

Quantification error ≃ ± 10% of absolute amount of (%Si) +2.5%.

The decrease in the fraction of Q^2 sites (resonance at -85.6 ppm) from 35±5% in M-S-H 0.8 to 27±4% for the co-precipitated samples (Co-0.05 and Co-0.10) also confirmed the absence of any significant amount of C-S-H (comparison between Co-0.05 and Co-0.10 and calculated spectra in Figure 60), which was consistent with

their characterization by XRD and with the low pH of their solution, outside the stability domain of C-S-H. ^{29}Si MAS NMR thus confirmed that the fraction of calcium in the solid phase was not precipitated as C-S-H.

However, it still remained unclear whether calcium substituted magnesium in the octahedral sheet or whether it was present as charge balancing cation at the surface and/or interlayer.

Additional characterizations of M-S-H 0.8, C-S-H 0.8, Co-0.05 and Co-0.10 solid fractions were performed using X-ray pair distribution function (PDF) analysis (Figure 61). The X-ray PDF analysis of pure M-S-H 0.8 indicated a structure where magnesium was bound to silicon and hydroxide.

The X-ray PDF analysis of M-S-H 0.8, Co-0.05 and Co-0.10 samples were very similar, and significantly different from that of C-S-H (Figure 61), which confirmed again that the products formed using the co-precipitation method had a M-S-H structure. The structural correlation peaks could be tentatively assigned using the structure of talc as a reference (Gruner, 1934): they mainly corresponded to Mg-Mg distances (r = 3.13 Å, 5.36 Å, 8.21 Å, 9.42 Å, 11.06 Å) and Mg-O (2.03 Å) within a same layer as well as Si-Si (3.20 Å) and Si-O distances in silicate tetrahedra (r =1.61 Å). Two additional peaks at r = 2.41 Å and 7.06 Å might be observed in the presence of calcium. The first distance is related Ca-O distances in the solid (detailed below). The peak at 2.4 Å would indicate the presence of CaO_7 polyhedra (Skinner et al., 2010) as also present in C-S-H or in other octahedral layer minerals such as e.g. dolomite or tobermorite, indicating either the presence of small quantities of C-S-H or the incorporation of some calcium in the octahedral layers of M-S-H.

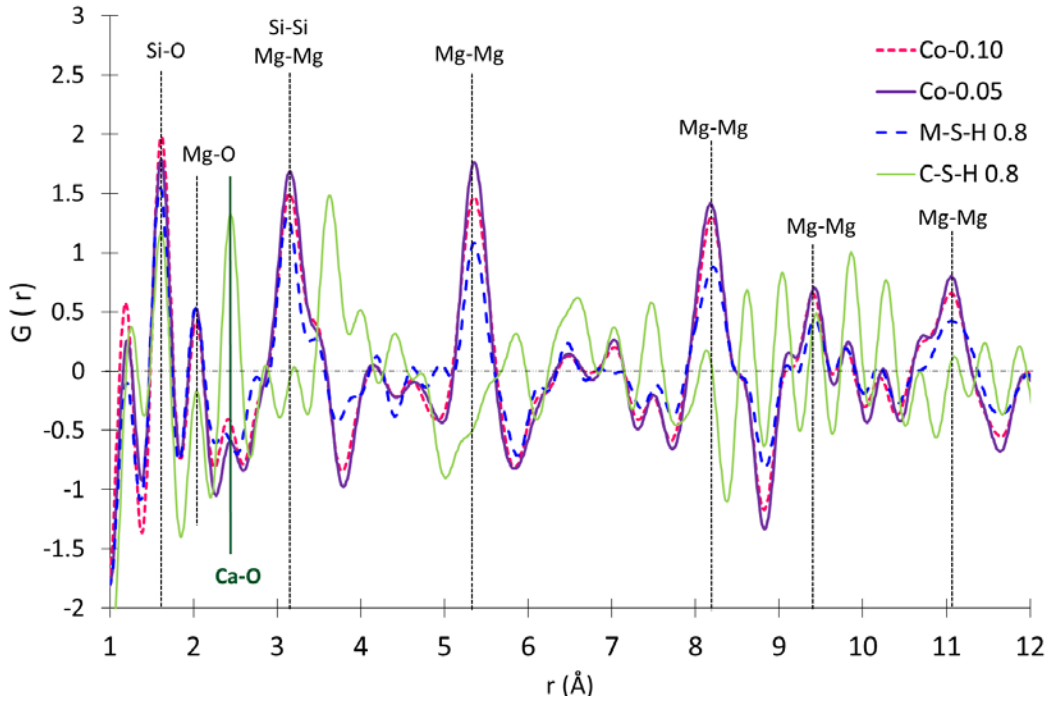

Figure 61: Reduced pair distribution function of M-S-H, C-S-H compared to co-precipitated Co-0.05 and Co-0.10 samples.

4.3.1.1.3. Surface properties

The zeta potential of M-S-H 0.8, M-S-H 1.0 and of the co-precipitated samples (cured during 2 years at 20°C) are plotted versus the calcium concentrations in solution in Figure 62a and versus the magnesium concentrations in solution in Figure 62b. After 2 years, the less than 2 wt. % of brucite is present; such a low amount would not affect the zeta potential measured. The zeta potential (-8.1 mV ± 0.9 mV) measured for the C-S-H (Ca/Si = 0.8) reference is consistent with data from the literature (Viallis-Terrisse et al., 2001; Labbez et al., 2007; Haas and Nonat, 2015).

The effective surface charge of M-S-H was negative with zeta potential values between -19 ± 3 mV and -25 ± 3 mV depending on the pH of the solution (within the pH range 8.3 - 9.2) (see chapter 3.3).

The substitution of MgO by CaO increased the pH from 8.3 to 8.9 and 9.3 for Co-0.05 and Co-0.10 samples respectively. This pH increase will thus lead to more negatively charge silanol groups of the Q^1 & Q^2 silicon species at the surface and edge sites of M-S-H, and should result in an increase of the negative surface charge density as detailed in chapter 3.3.

At the same time, the calcium concentration in solution increased from 0 to 0.15 and 0.29 mmol/l respectively and the magnesium concentration in solution dropped from 0.38 to 0.004 and below the detection limit of 0.001 mmol/l respectively. The Co-0.05 sample exhibited almost the same zeta potential as pure M-S-H with – 22 ± 3 mV at pH 8.9, which is an intermediate value between the two points of pure M-S-H (in zeta potential as well as in pH) whereas the zeta potential of the Co-0.10 sample was significantly less negative (-10 ±1 mV). These three samples having similar pH values, the surface charge of M-S-H thus depended on the calcium concentration as shown in Figure 62a. As with C-S-H (Viallis-Terrisse et al., 2001; Labbez et al., 2007; Labbez et al., 2011; Haas and Nonat, 2015; Plusquellec and Nonat, 2016), the zeta potential became less negative at higher concentration of dissolved calcium, indicating a sorption of calcium at the surface. One may postulate that, in the case of Co-0.05 sample, calcium substituted a similar amount of magnesium at the surface, resulting in little change of the zeta potential. The strong increase in the zeta potential of the second sample (Co-0.10) would indicate that calcium was more effectively adsorbed at the surface of M-S-H than magnesium, thus partially compensating the negative charge of the silicate sites.

The magnesium concentration in solution did not seem to influence the zeta potential of M-S-H as strongly as the calcium concentration, as shown in Figure 62b. In this Figure, we can see no influence of the magnesium concentration on the effective negative surface of M-S-H. Calcium has been observed to sorb stronger than magnesium on quartz (Conway, 1981; Dove and Nix, 1997) probably due its slight smaller hydrated size. Such a preferential sorption of calcium could explain the strong increase in zeta potential when the calcium concentration increased.

The measurement of the cation exchange capacity of M-S-H showed a positive CEC of 35 meq/100g (Figure 63), which indicated a negative surface charge of the M-S-H particle. This is in agreement with the effective negative surface charge obtained by zeta potential measurement. The exchangeable magnesium in pure M-S-H 0.8 was was equal was equal to 0.02 per silicon. The CEC of the Co-0.05 and Co-0.10 samples was slightly higher in the presence of calcium. It increased from 35 meq/100g to 47 meq/100g for Co-0.10 sample. This sample thus contained slightly more exchangeable calcium, about 0.03 per silicon. In the Co-0.05 sample, most of the magnesium at the surface was replaced by calcium (Table 29) and all of it in the Co-0.10, in agreement with the much higher calcium concentration than magnesium one in solution. The general CEC increase from the pure M-S-H to the Co-0.05 and Co-0.10 indicates a more negative surface charge.

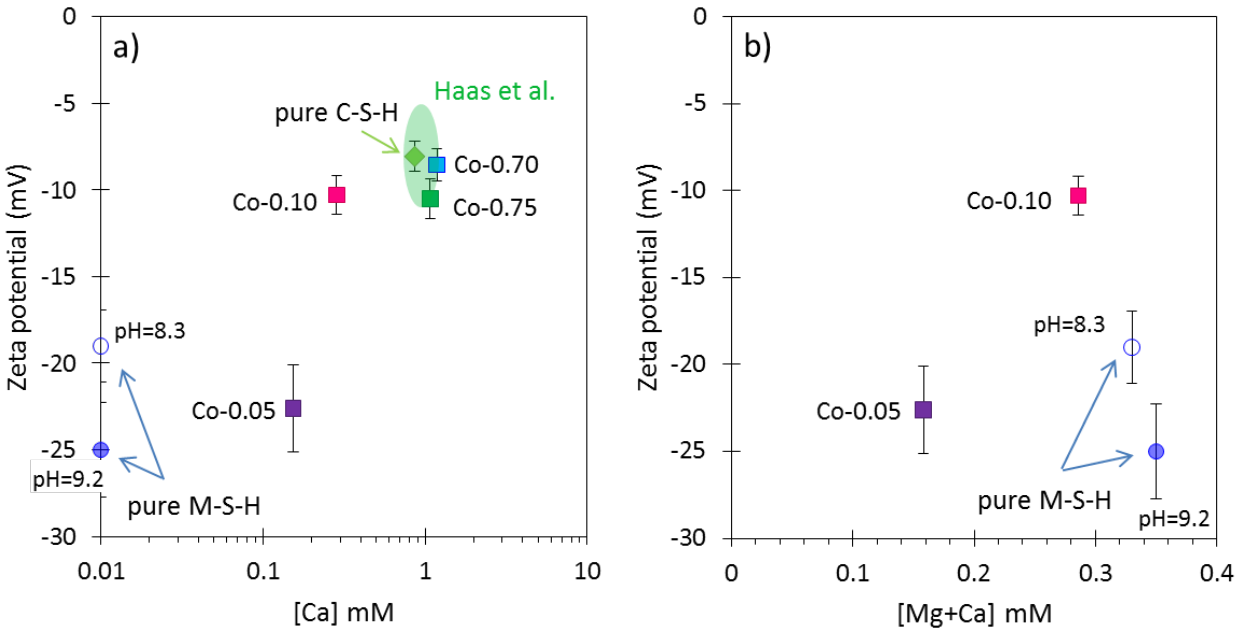

Figure 62: Zeta potential of M-S-H, co-precipitated sample particles a) versus calcium concentration in suspension (range of values for C-S-H from Haas et al. (Haas and Nonat, 2015) added for comparison) and b) versus magnesium and calcium concentration.

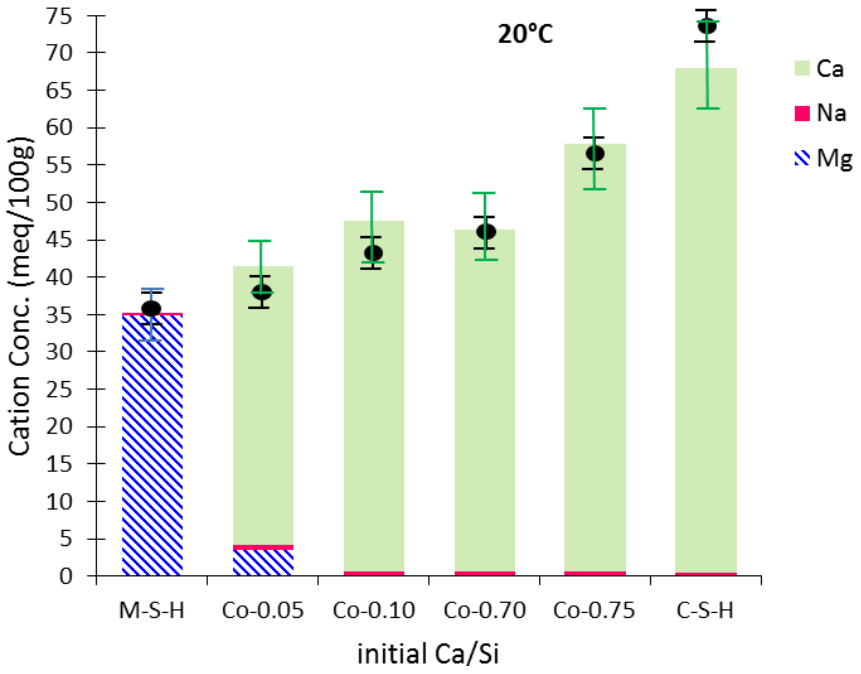

Figure 63: Concentrations of the cations sorbed on co-precipitated samples compared to M-S-H 0.8 and C-S-H 0.8 measured by the cobalt hexamine method as a function of the initial Ca/Si. CEC measurements by colorimetry (black circles) have been added for comparison.

Table 29: Exchangeable magnesium and calcium per silicon in co-precipitated samples compared to M-S-H 0.8 and C-S-H 0.8 calculated from CEC

sample	exchangeable Mg^{2+} per Si	exchangeable Ca^{2+} per Si	total
M-S-H	0.021	--	0.021
Co-0.05	0.002	0.022	0.024
Co-0.10	<0.001	0.028	0.028
Co-0.70	<0.001	0.032	0.032
Co-0.75	<0.001	0.040	0.040
C-S-H	<0.001	0.048	0.048

The uptake of 0.022 and 0.028 Ca_{exch}/Si (CEC in Table 29) at exchangeable sites compared to the total calcium uptake of 0.05 and 0.10 Ca/Si (if all the initially added calcium would be on CEC sites in the solid) showed that only a part of calcium was found adsorbed at the surface of M-S-H at the surface of M-S-H. CEC was also measured on the samples synthetized at 50°C. Similar results were obtained with Ca/Si ratios of 0.03 and 0.04 at CEC sites in the Co-0.05 and Co-0.10 samples (Appendix F & Appendix G). The remaining calcium may substitute some magnesium in the octahedral layer. Although substitution of magnesium by calcium (with a bigger size) is unusual, it might occur during co-precipitation within the poorly ordered M-S-H.

Alternatively, a part of calcium might have been washed during the filtration process. To check whether calcium was still present in the solid phase (i.e. in the octahedral layers) after the CEC and to account for the missing calcium, the co-precipitated samples after cation exchange by cobalt hexamine trichloride were dissolved in 0.1 mol/l HCl, to differentiate between surface-sorbed calcium and calcium in the structure. As the CEC measurement should remove the surface-sorbed calcium, any calcium still found is present as non-exchangeable. $Ca_{not\ exch}$/Si ratios of 0.02 and 0.05 were measured in the solids after dissolution (Table 30), confirming the presence of calcium in the solid part and the total Ca/Si found by the addition of the Ca_{exch}/Si and $Ca_{not\ exch}$/Si was approximatively equal to the initial Ca/Si added to the suspensions

In summary, the different analyses indicated an adsorption of calcium on the surface of M-S-H; a small calcium uptake in the M-S-H main layers might occured; alternatively a small amount of C-S-H could be present although this seemed unlikely due to the low pH value and based on different solid analyses. Thus, M-(C)-S-H corresponds to a M-S-H phase containing small quantities of adsorbed and/or incorporated calcium. The exact nature of calcium incorporation, however, still remains unclear.

Table 30: Ca/Si and Mg/Si in the solids synthetized at 50°C from mass balance and dissolution, before and after the CEC.

	Mass balance		Dissolution		
			Before CEC	After CEC	**Not exchangeable cation***
	Ca/Mg	Mg/Si	Ca/Mg	Ca/Mg	**Ca/Si***
Co-0.05	0.06±0.02	0.76±0.02	0.07±0.02	0.03±0.01	**0.02±0.02**
Co-0.10	0.14±0.02	0.71±0.02	0.13±0.02	0.08±0.02	**0.05±0.02**

*Ca/Si=Ca/Mg (After CEC) x Mg/Si (Mass balance).

4.3.1.2. Co-0.75 and Co-0.70 samples

This second section investigates the effect of small amounts of MgO (Mg/Si=0.05 and 0.10) added during the synthesis of C-S-H. The (Ca+Mg)/Si ratio was set to 0.8, and the resulting samples were labelled Co-0.75 and Co-0.70.

4.3.1.2.1. Aqueous phase composition

The aqueous phase equilibrated with pure C-S-H (Ca/Si ratio of 0.8) exhibited a pH of 10.5 and dissolved calcium and silicon concentrations of 0.86 mmol/l and 1.62 mmol/l respectively (Figure 57, Appendix E). These results are in good agreement with previously reported data (Lothenbach and Nonat, 2015). At the later age (2 years at 20°C where only traces of brucite were present), the partial replacement of CaO by MgO in Co-0.75 and Co-0.70 samples caused a decrease in pH to 10.2 and 10.1 respectively, and an increase in the calcium and silicon concentrations.

Compared to pure M-S-H, the higher pH values resulted in very low concentrations of magnesium in solution (Figure 57, Appendix E), as also observed when only M-S-H is formed at pH 10. The high pH and the very low concentration of magnesium tentatively indicated the presence of C-S-H and M-S-H and/or brucite.

4.3.1.2.2. Solid analysis

The solid analysis focused on the samples synthesized 1 year at 50°C; similar analyses were done on the samples synthesized 2 years at 20°C and only traces of brucite were present in both cases. Since the formation of M-S-H is very slow at 20°C, especially at high pH (Lothenbach et al., 2015), the presence of brucite ($Mg(OH)_2$) was observed up to 1 year (Appendix E). After 2 years however, only traces of brucite were detected. The samples cured at 50°C reacted faster and equilibrium was reached after 1 year.

The XRD patterns of Co-0.75 and Co-0.70 samples are compared to pure C-S-H pattern in Figure 64. C-S-H was the main phase present in these samples. However, a

small amount of M-S-H (10-20wt.%) is difficult to detect by XRD in the presence of C-S-H (chapter 4.2). As for the magnesium co-precipitated samples (see 4.3.2.1), complementary XRD patterns were measured and calculated to make the comparison easier. Some reference samples (Mix-0.75 and Mix-0.70) were prepared by mixing pure M-S-H and C-S-H phases with total (Mg+Ca)/Si ratios corresponding to those of experiments Co-0.75 and Co-0.70. Their diffraction patterns were recorded and calculated by linear combination of the patterns of plain M-S-H and C-S-H (Cal-0.75 and Cal-0.70). The calculated and separately mixed samples showed the same reflections. Similarly, all the patterns exhibited almost the same diffraction patterns and M-S-H phases were very difficult to observe. The co-precipitated samples could thus contain small amounts of M-S-H, but other characterizations were needed to ascertain the presence of this phase.

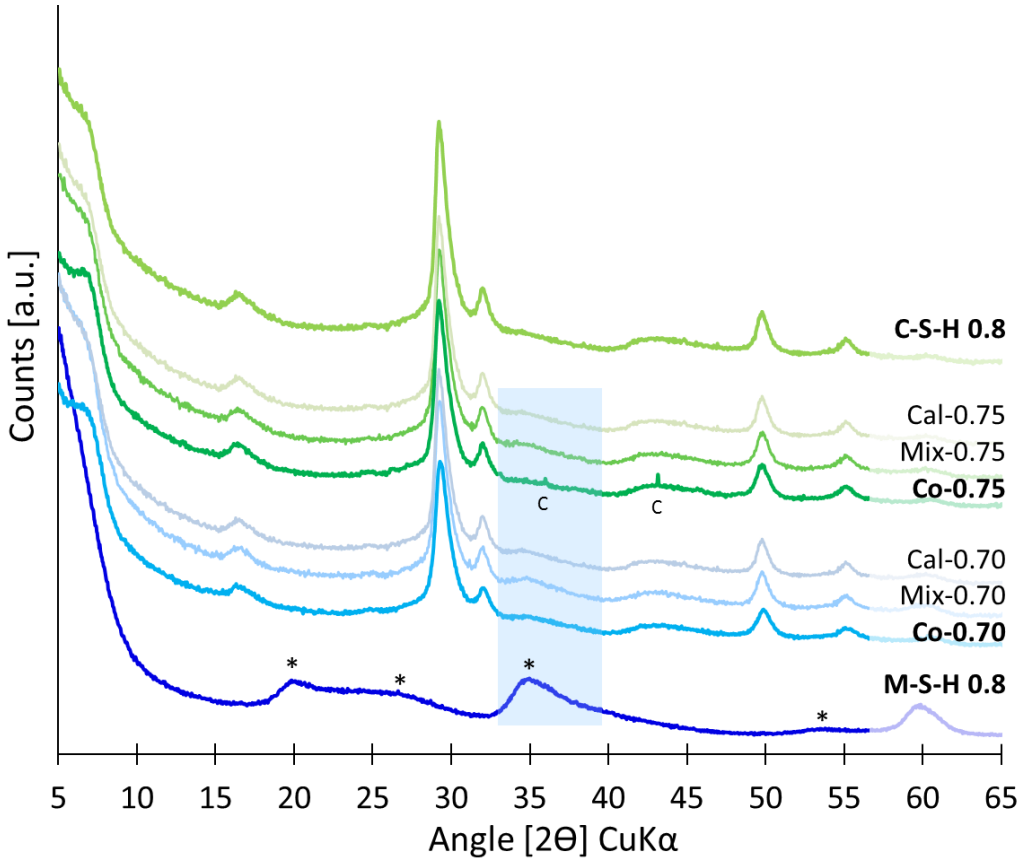

Figure 64: XRD patterns of Co-0.70 and Co-0.75 samples (1 year at 50°C) compared to XRD patterns of C-S-H 0.8, M-S-H 0.8 and calculated and mechanically mixed samples. C=calcite, *=M-S-H.

The X-ray PDF of Co-0.70 and Co-0.75 and C-S-H (Figure 65) bore strong resemblance. According to the literature (Lequeux et al., 1999; Skinner et al., 2010; Meral et al., 2011; Grangeon et al., 2013; White et al., 2015; White, 2016), the correlations peaks might correspond to Si-O distances (r = 1.61 Å and 3.63 Å), Ca-O

distances (r = 2.44 Å), Ca-Ca distances (r = 3.80 Å and 6.63 Å) Si-Ca distances (r = 3.20 Å and 3.63 Å) and possibly Si-Si distances (r = 3.20 Å). Small differences were however noticed between the pure C-S-H and the co-precipitated samples: the correlation peaks observed at r = 3.14 Å and 5.38 Å in the co-precipitated samples were characteristic of Mg-Mg distances observed in M-S-H. The intensity of the correlation peaks assigned to Ca-Ca distances was also lower. These results might suggest the presence of small amounts of M-S-H in the samples, but this again needed to be confirmed by other techniques.

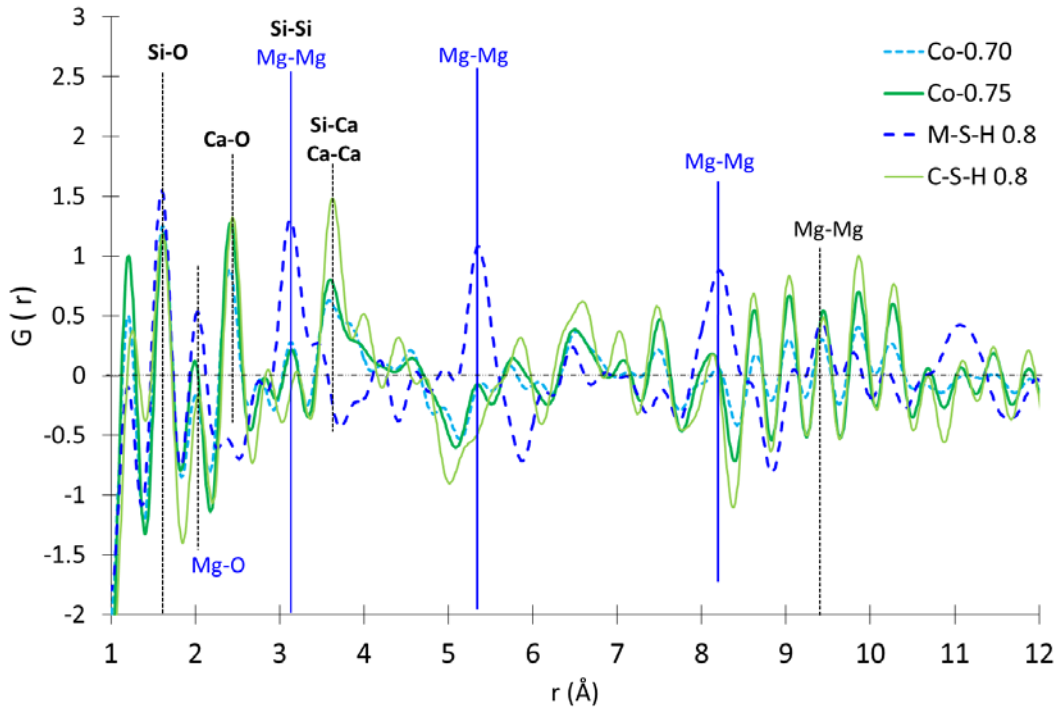

Figure 65: Reduced pair distribution function of M-S-H, C-S-H compared to co-precipitated Co-0.75 and Co-0.70 samples.

The ^{29}Si MAS NMR spectra of the co-precipitated (Co-0.75 and Co-0.70) samples are shown in Figure 66. ^{29}Si MAS NMR data confirmed the presence of C-S-H with typical chemical shifts (Bell et al., 1990; Klur et al., 1998; Andersen et al., 2003; Chen et al., 2004; Richardson et al., 2010b; L'Hôpital et al., 2015) at ≃ -79.7, -82.9, -85.8 and -88.4 ppm corresponding to Q^1 (end of chains), Q^2_b (bridging position), Q^2_p (pairing position) and Q^2_u (bridging position with binding to H^+ (Sato and Grutzeck, 1991; Le Saout et al., 2006; L'Hôpital et al., 2015)) of the tetrahedral silicate in C-S-H, as shown in Figure 66. The pure C-S-H sample with a Ca/Si ratio of 0.8 contained mainly Q^2 species, and only very small amounts of Q^3 species (broad signal at -93.5 ppm which accounted for ≃ 4% of the total silicate), in agreement with previous studies of C-S-H with low Ca/Si ratio (Le Saout et al., 2006; Myers et al., 2015a).The

presence of M-S-H in the samples was evidenced by the presence of the resonance peaks between -92 and -97 ppm corresponding to Q^3 tetrahedral sites of M-S-H.

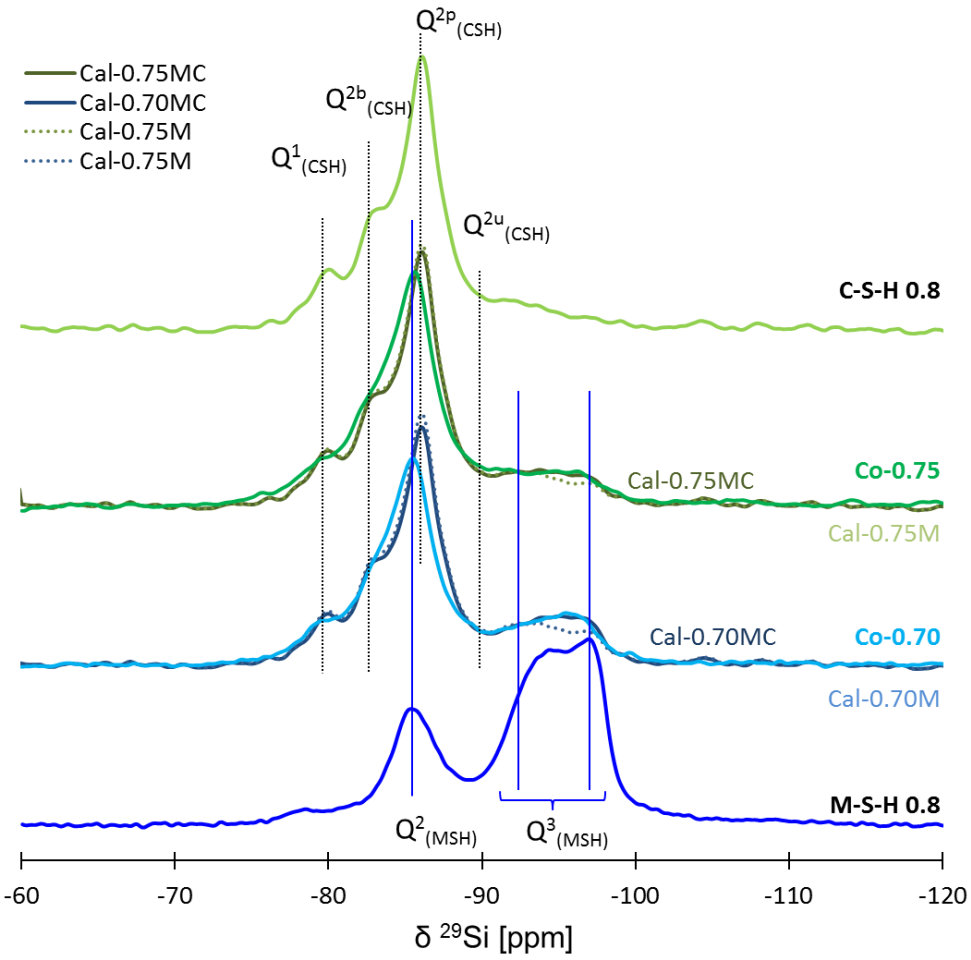

Figure 66: ^{29}Si MAS NMR spectra of Co-0.70 and Co-0.75 samples (1 year at 50°C) compared to spectra of C-S-H 0.8, M-S-H 0.8 and the calculated samples with M-S-H 0.8 (Cal-0.70M, Cal-0.75M) and with Co-0.05 (Cal-0.70MC, Cal-0.75MC).

Deconvolution of the ^{29}Si MAS NMR spectra was carried out following the procedure outlined in literature (detailed earlier) and the results are detailed in Table 28. Because of the formation of M-S-H, the content of silicate in C-S-H decreased from 96 (±5%) in pure C-S-H to 69 (±8%) in the Co-0.70 sample. The content of Q^1 and Q^2 sites attributed to C-S-H decreased with the replacement by magnesium. The calculated MCL remained above 20, which is typical for C-S-H with a low Ca/Si ratio.

The content of Q^3 tetrahedral sites between -92 and -97 ppm increased from 0 to 28% (±5%) (see Table 28) with the magnesium addition, confirming the presence of M-S-H. The amount of silicate attributed to M-S-H was higher than expected in Co-

0.75 and Co-0.70 samples. The Mg/Si=0.8 in M-S-H and Ca/Si=0.8 in C-S-H should distribute the tetrahedral silicate to 6% in M-S-H and 94% in C-S-H and in 13% in M-S-H and 87% in C-S-H, respectively, for the two co-precipitated samples. ^{29}Si MAS NMR indicated the presence of significantly more tetrahedral silicate attributed to M-S-H (18% instead of 6% and 28% instead of 13%), indicating that the content of M-S-H is higher than expected (as detailed in Table 28).

The recorded ^{29}Si MAS NMR data were compared to those calculated (Cal-0.70MC and Cal-0.75MC) using a linear combination of the spectra of C-S-H 0.8 and Co-0.05 samples. This latter was preferred to pure M-S-H (Cal-0.70M and Cal-0.75M) since it provided a better fit of the experimental spectra, as shown in Figure 66.

This better agreement together with the high fraction of silicate attributed to pure M-S-H could be explained by some uptake of calcium by M-S-H at higher pH. However, it remained unclear whether calcium was sorbed on the surface and edge sites of M-S-H only or whether it could be present in the octahedral layer as well.

Given the large amount of silicate associated with the M-(C)-S-H phase (28 and 18 % respectively, Table 28), all the magnesium in the solid fraction of samples Co-0.70 and Co-0.75 seemed to be in M-(C)-S-H phase. This, together with the low magnesium concentration in solution, suggested no or very little incorporation of magnesium in C-S-H. The uptake of magnesium at the exchangeable sites of C-S-H could also be excluded as the CEC measurements showed the presence of mainly calcium (Table 29).

The TEM observations of Co-0.70 sample (Appendix H) and the corresponding EDS measurements (Figure 67) showed two different types of products in the sample. The first one contained mainly calcium and silicon and thus corresponded to C-S-H. The second one, in smaller amount, contained significant amounts of magnesium and silicon, which confirmed the presence of M-S-H. The M-S-H particles exhibited a layered texture which agreed well with the sheet-like morphology already observed for pure M-S-H or mixed samples containing calcium (Lothenbach et al., 2015; Roosz et al., 2015). The (Mg+Ca)/Si ratio remained lower than 0.8 regardless the type of product. The mean Ca/Si and Mg/Si ratios were 0.65 ± 0.15 and 0.05 ± 0.05 respectively for the C-S-H particles, and 0.15 ± 0.05 and 0.65 ± 0.15 for the M-S-H particles (Figure 67). This confirms the uptake of no or only very small amounts of magnesium in C-S-H, in agreement with the ^{29}Si MAS NMR and PDF observations and indicates the possibility of a more substantial uptake of calcium by M-S-H. However, as the EDS measurements were performed on areas with a typical diameter of 100-150 nm, some intermixing of C-S-H and M-S-H phases can be

expected, such as for the data at Ca/Si ratios of 0.5 and 0.6 and Mg/Si ratios 0.3 to 0.6 which are based on intermixing of C-S-H and M-S-H.

In summary, separate M-S-H (henceforward, M-(C)-S-H) and C-S-H phases were observed in the Co-0.70 and Co-0.75 samples by TEM/EDS observations, ^{29}Si MAS NMR spectra, XRD and X-ray PDF analysis. The data seemed to indicate that a significant uptake of calcium in M-S-H occurred also at high pH. Traces of brucite were observed at 20°C after 2 years, due to the slow kinetic of brucite dissolution in batch experiments (Szczerba et al., 2013). In C-S-H, however, no or very limited uptake of magnesium seemed to occur. This result could be explained by the very low magnesium concentrations in solution which resulted in a negligible fraction of charge balancing magnesium at the C-S-H surface. The very low concentration of magnesium could also prevent its incorporation in C-S-H during the precipitation process.

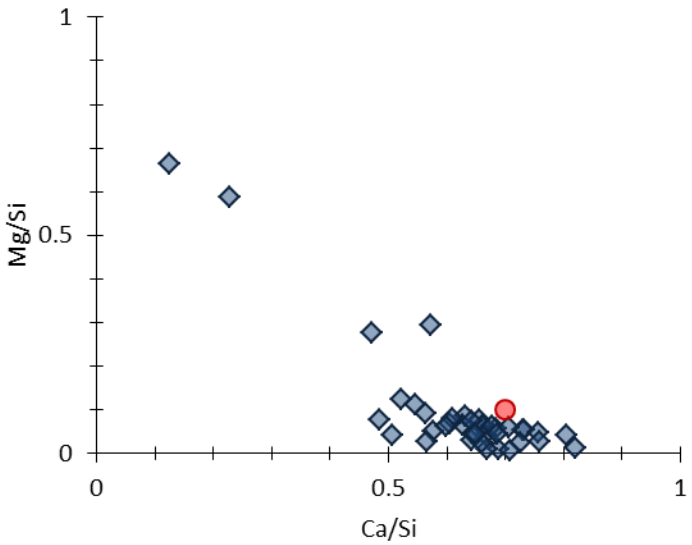

Figure 67: Measured elemental ratios (EDS) in Co-0.70 sample (cured 2 years at 20°C), red circle added as reference (Mg/Si= 0.1, Ca/Si=0.7).

4.3.1.3. Effect on solubility

The solubility products of $C_{0.80}SH_{1.94}$ and $M_{0.78}SH_{1.48}$ were calculated using the measured concentrations in solution at equilibrium (Figure 68). The solubility product of $C_{0.80}SH_{1.94}$ remained approximatively constant at ≃ -12 regardless of the presence or absence of magnesium. This indicates that the uptake of magnesium by C-S-H and the formation of a solid-solution are rather unlikely. In contrast, the decrease in the calculated solubility product of pure $M_{0.78}SH_{1.48}$ in the presence of calcium by up to 1 log unit at the maximum showed a stabilization of M-S-H in the presence of calcium (Figure 68). This supported the formation of a solid-solution

with an incorporation of calcium in M-S-H, in agreement with the experimental observations.

The expected concentrations of calcium, magnesium and silicon were calculated using separate C-S-H (Kulik, 2011) and M-S-H (chapter 3.2) phases, i.e. M-S-H without calcium and compared with the measured data in Figure 57. The thermodynamic modelling pointed out that C-S-H was stable only at pH higher than 10, in agreement with the experimental results. However, the calculated pH (10.4) in the presence of magnesium (Co-0.05 and Co-0.10) was notably higher than the pH experimentally observed (8.9 and 9.3 respectively), while the calculated calcium and silicon concentrations were lower than the experimental ones (Figure 57). Such deviations between experiments and calculations may have resulted from the occurrence of calcium in M-S-H which was neglected in this calculation. The uptake of calcium by M-S-H would indeed reduce its concentration in solution as well as the pH values.

To check this assumption, two additional end-members with a Ca/Si ratio of 0.1 were introduced in the M-S-H solid solution model developed previously. The total of cation to silica ratios of 0.78 and 1.30 were kept constant, leading to the following stoichiometries: $M_{0.68}C_{0.1}SH_{1.48}$ and $M_{1.2}C_{0.1}SH_{1.80}$ as detailed in Table 6.

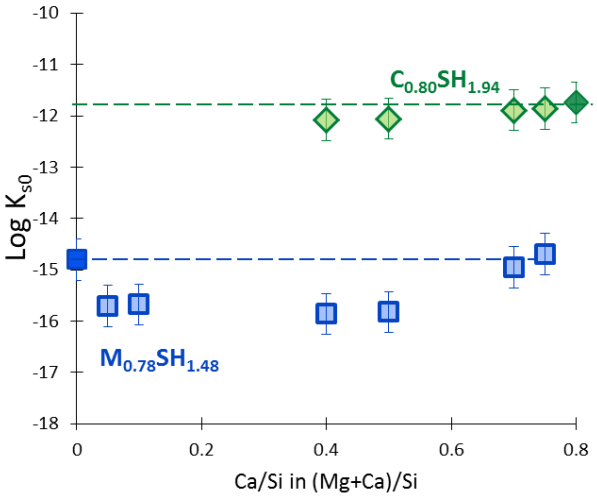

Figure 68: Solubility products of $M_{0.78}SH_{1.48}$ (squares) and solubility products of $C_{0.80}SH_{1.94}$ (diamonds) calculated for the co-precipitated samples at 20°C after 2 years. The M-S-H calculation is based on the end-members from chapter 3, the C-S-H calculation is derivated from Kulik et al. (Kulik, 2011).

The calculated concentrations and atomic ratios in C-S-H and M-S-H (solid lines) are compared to the results obtained by the model containing only M-S-H and C-S-H (dashed lines) and with the experimental data (dots) in Figure 69. . The experimentally observed calcium and silicon concentrations and pH measured

experimentally were better described by the model taking into account the possible incorporation of calcium in M-S-H. The model was also able to predict the presence of calcium (Ca/Si up to 0.07) in M-S-H, in agreement with the experimental observations.

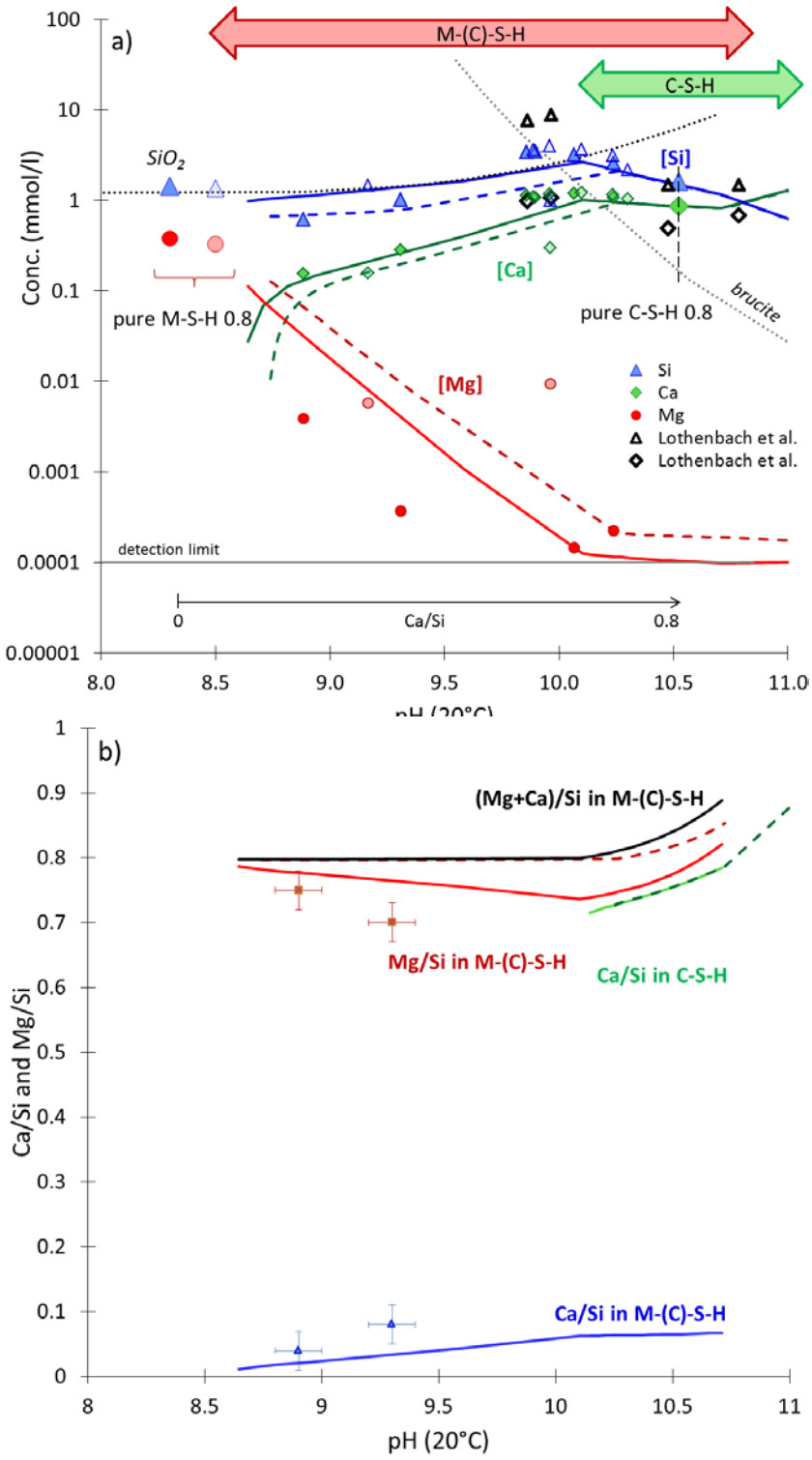

Figure 69: a) Calculated solubility curves (solid lines) associated to the co-precipitated samples using the M-(C)-S-H solution and C-S-H solid-solution models compared to the calculated solubility curves (dashed lines) using the M-S-H(Bernard et al., 2017b) and C-S-H solid-solution models. Solubilities of brucite and amorphous SiO_2 are shown in dotted lines. Empty symbols are from Lothenbach et al. (Lothenbach et al., 2015). b) Evolution of atomic ratios calculated by GEMS using the M-(C)-S-H solution and C-S-H solid-solution models compared to the M-S-H (Bernard et al., 2017b) and C-S-H solid-solution models and compared to the experimental results from mass balance.

4.3.2. Conclusions

This work aimed at investigating the relative stabilities of M-S-H and C-S-H and the possibility to incorporate small amounts of calcium into M-S-H, or small amounts of magnesium into C-S-H. The main conclusions can be summarized as follows.

1- C-S-H is unstable at pH values below 10.

2- When small amounts of calcium were added during the synthesis of M-S-H ((Mg+Ca)/Si = 0.8, Ca/Si = 0.05 or 0.10), the uptake of calcium by M-S-H is evidenced. CEC measurements showed that calcium is present as an exchangeable cation on the surface of M-S-H and is responsible for the less negative surface charge density of M-S-H particles pointed out by zeta potential determinations. Nevertheless, a small fraction of the calcium incorporated into M-S-H may be non-exchangeable. Thermodynamic calculations confirm that an incorporation of calcium into M-S-H is likely since the presence of calcium stabilizes the M-S-H formed. A solid solution may thus occur between pure M-S-H and a M-C-S-H phase containing small amounts of calcium. The site of incorporation is not yet fully elucidated, nor the maximal uptake. However, the two end-members ($M_{0.68}C_{0.1}SH_{1.48}$ and $M_{1.2}C_{0.1}SH_{1.80}$) make it possible to describe the aqueous concentrations and solid compositions observed experimentally.

3- At pH values above 10, both M-S-H and C-S-H phases are stable and coexist. A similar uptake of calcium by M-S-H as at lower pH values is suggested. The simultaneous presence of C-S-H and M-S-H makes it difficult to evidence a possible uptake of magnesium by C-S-H. However, if such uptake occurs, it is not in the cation exchangeable sites and the incorporation of magnesium in the structure should be strongly limited by the very low concentration of magnesium in solution controlled by M-S-H.

The new solid solution model developed in this study to describe the uptake of calcium by M-S-H may offer new prospects to simulate the deterioration of calcium silicate cement-based materials in the presence of magnesium (provided by clayey minerals, ground- or seawater) or to optimize the design of novel binders containing calcium, magnesium and silicates.

4.4. Mg-exchange at the interface "low-pH" cement - magnesium environment studied by a C-S-H - M-S-H model system

This part corresponds to the shortened and adapted version of the publication: Ellina Bernard, Alexandre Dauzères, Barbara Lothenbach, Magnesium and calcium silicate hydrates, Part II: Mg-exchange at the interface "low-pH" cement and magnesium environment studied in a C-S-H and M-S-H model system, **Applied Geochemistry**, accepted (2017) (Bernard et al., 2018a).

Previously, it was observed that the addition of magnesium and/or pH values lower than 10 destabilize C-S-H (chapter 4.2), while a low amount of calcium can be taken up by M-S-H (chapter 4.3).

Even though several papers have pointed towards the existence of a magnesium silicate hydrate phase at the interface in field experiments, proof of M-S-H formation and the study of their properties is complicated by the presence of clay minerals, which have the same silicate sheet structure as M-S-H. Thus the present study focuses on the characterization of the changes occurring at the interface of C-S-H and M-S-H only, using a simplified model system.

This study focuses on the evolution of a simplified interface between pure C-S-H and pure M-S-H in an experimental setup which allows studying the changes in the solid phases and in the pore solutions, using SEM/EDS analyses of solids, the chemical compositions of solutions and the reactive transport modelling (details of the techniques and methods are given in 2.3.4).

4.4.1. Results and discussions

4.4.1.1. Experiments

4.4.1.1.1. Solid analysis

The changes at the interface between the C-S-H and the M-S-H disk were studied by SEM/EDS. The SEM scattering electrons picture of the interface after 12 months is presented in Figure 70a. An overview of the different zones where EDS quantifications were carried out is given in Figure 70b.

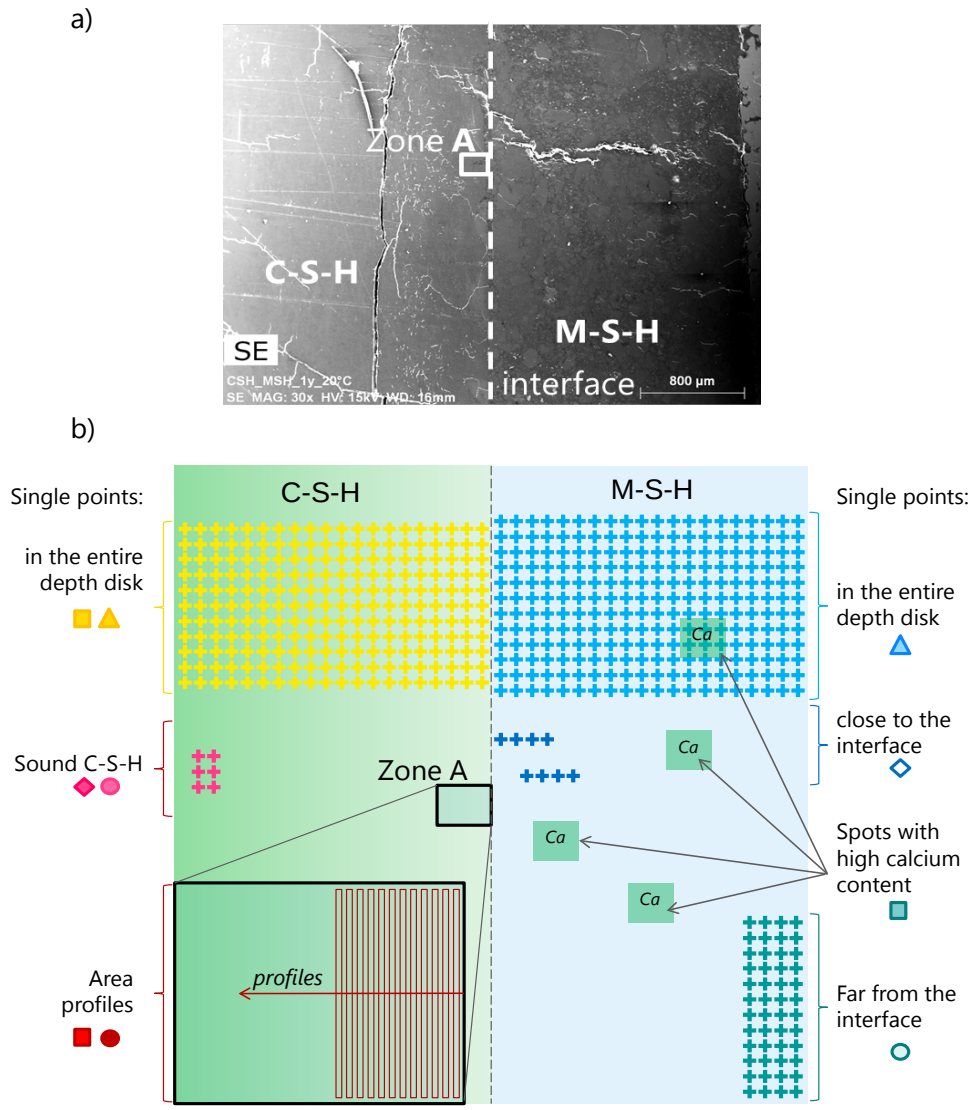

Figure 70: a) SEM picture of the interface C-S-H and M-S-H disks after 12 months at 25°C, b) overview of the different zones where the composition has been determined by EDS quantifications. Depth=the distance from the interface the symbols showed in this figure are used in the next figures to represent the results obtained in the different zones.

C-S-H disk

The EDS mapping of the area near the interface (zoom A, Figure 70) after 3 and 12 months are presented in Figure 71a. Some cracks occurred after equilibration during the dismantling of the cells and due to the high vacuum used for SEM/EDS analysis. The C-S-H in some distance from the interface showed no evident changes except the occurrence of a few spots where calcium carbonate might have formed. FTIR analysis on the scratched zone of sound C-S-H confirmed the presence of only C-S-H with a band at ~964 cm^{-1} assigned to Si–O stretching vibrations of the Q^2 tetrahedra and of a low amount of carbonates with the carbonate bands at 1400–

1500 cm^{-1}. Near the interface of the C-S-H with the M-S-H a depletion of calcium was observed. After 3 month up to a depth of approximately 200µm; after 12 months this depletion of calcium reached 600 to 800 µm in depth. Also a depletion of silicon was observed which extended to comparable depths. In the area where the calcium and silicon were depleted the occurrence of some small crack filled by epoxy resin the near the interface were detected. The carbon detected by SEM in the cracks was mainly due to the epoxy resin used to embed the interface. However, possibly carbonates could also have formed in those cracks.

In addition a enrichment of magnesium was observed near to the interface at a depth of ~50-60 µm after 3 months and 200-220 µm after 12 months. The depth of the depletion of calcium and of magnesium enrichment increased at least by a factor 4 between 3 and 12 months. The large difference in the depths of decalcification and magnesium enrichment indicated that first the dissolution of C-S-H occurred and only later the precipitation of M-S-H. These two steps are consistent with the different structures of C-S-H, which contains silica chains, and M-S-H, which contains silica sheets (Brew and Glasser, 2005b; Lothenbach et al., 2015). Based on the EDS measurement it could not be decided whether two phases (C-S-H and M-S-H) were present or whether some magnesium might had been taken up in the C-S-H phase as the spot size was ~1 to 3 µm such that closely intermixed phases would be captured in the same analysis. Uptake of magnesium in C-S-H however, seems little probable as dedicated batch experiments have shown no measurable uptake of magnesium in C-S-H (chapter 4.3). Although Figure 71a clearly shows a magnesium front in the C-S-H disk, only a small fraction of the magnesium moved from the M-S-H disk to the C-S-H disk as visualized in Figure 71b based on the relative intensity of magnesium of the M-S-H side.

The FTIR analysis of the C-S-H disk far from the interface and at the interface confirmed the presence of C-S-H plus a small amount of calcium carbonate. Additionally, some amorphous silica was observed at the interface with a band at 1190 cm^{-1} and some shoulders related to M-S-H could be identified at 1100 cm^{-1}. The presence of only a weak shoulder indicating Q^3 characteristic of M-S-H at the interface (Figure 72) indicates the presence of much less M-S-H than C-S-H in the sample scratched off the interface.

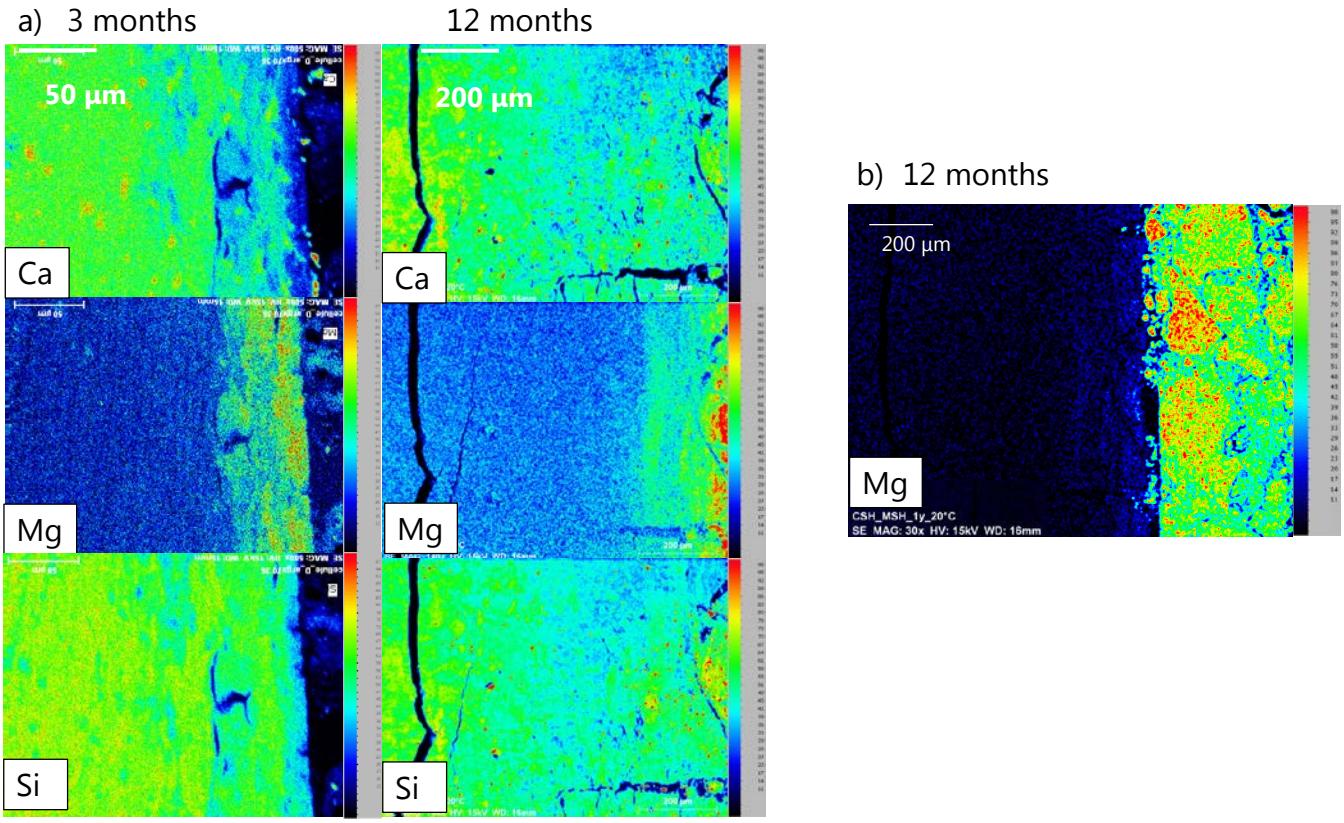

Figure 71: a) EDS elemental mapping of the C-S-H near the interface (zoom A as detailed in Figure 70) and b) magnesium enrichment in C-S-H compared to the M-S-H disk (colors were normalized to the lowest and the highest content).

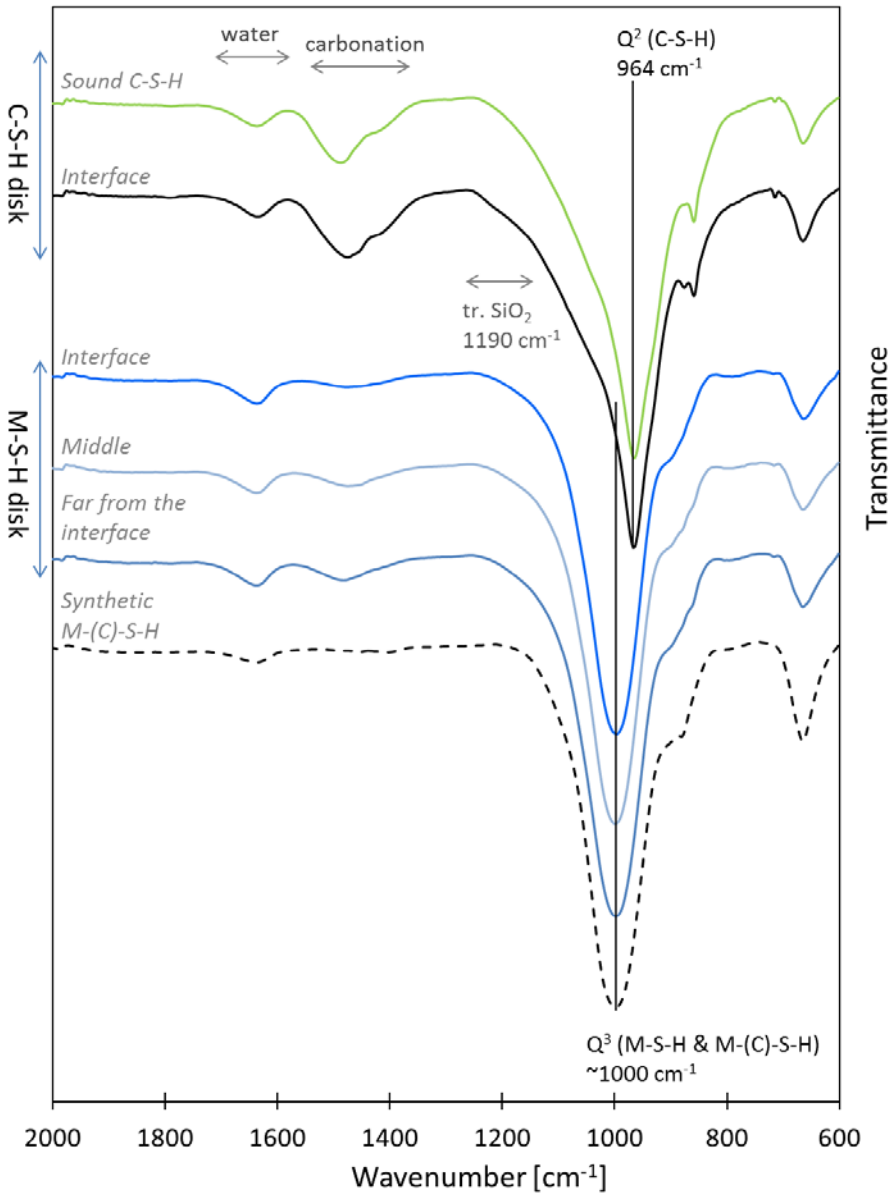

Figure 72: FTIR spectra of scratched off samples at the interfaces, in the sound C-S-H disk and M-S-H disk (experiment dismantled after 3 months) , spectrum of synthetic M-(C)-S-H from (Bernard et al., 2018b) shown as reference. The spectra were scaled to ease comparison.

The Ca/Si_{tot} and Mg/Si_{tot} quantified by EDS are plotted as a function of the distance to the interface in Figure 73. Mg/Si_{tot} decreased from 0.4 at the interface to 0 far from the interface. Far from the interface a Ca/Si= 0.8±0.1 was maintained but it decreased to Ca/Si_{tot} of about 0.6±0.1 at the interface. The EDS maps in Figure 71 illustrate that both the calcium but also the silicon moved away from the interface between 3 and 12 months. However, as both calcium and silicon were depleted, a similar Ca/Si was observed after 3 and 12 months in Figure 73.

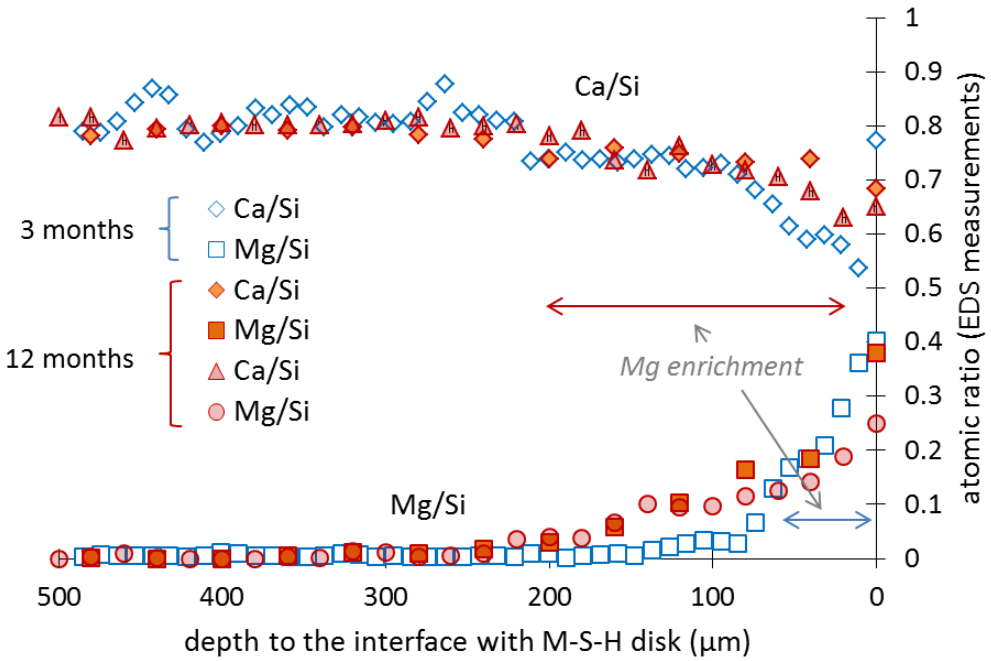

Figure 73: Mg/Si and Ca/Si ratios determined by EDS in the C-S-H disk as a function of the distance to the interface (1 profile at 3 months and 2 profiles); the errors associated with the ratios are about ± 0.1.

The EDS data are summarized in a ternary diagram in Figure 74. The EDS points include C-S-H far from the interface as well as C-S-H near the interface as detailed in Figure 70b. The composition of the C-S-H far from the interface remained unchanged at Ca/Si = 0.8, although a bigger spread of the data (0.8 ±0.3) was observed after 12 months. Nearer to the interface, a gradient in direction of M-S-H was visible already after 3 months and much clearer after 12 months. As the spot size of the EDS analysis was ~1 to 3 µm such closely intermixed phases are captured in the same analysis resulting in many cases in mixed analysis. In addition, a trend towards amorphous silica was observed after 12 months as well a few points towards high calcium content. As in these small calcium rich areas very little and no silica or no magnesium was observed, these points indicated that a small amount of calcium carbonate had formed either during the interaction with M-S-H or during the drying and impregnation procedure. No trends towards magnesium hydroxide or carbonate were visible indicating the absence of brucite or magnesite in the C-S-H disk.

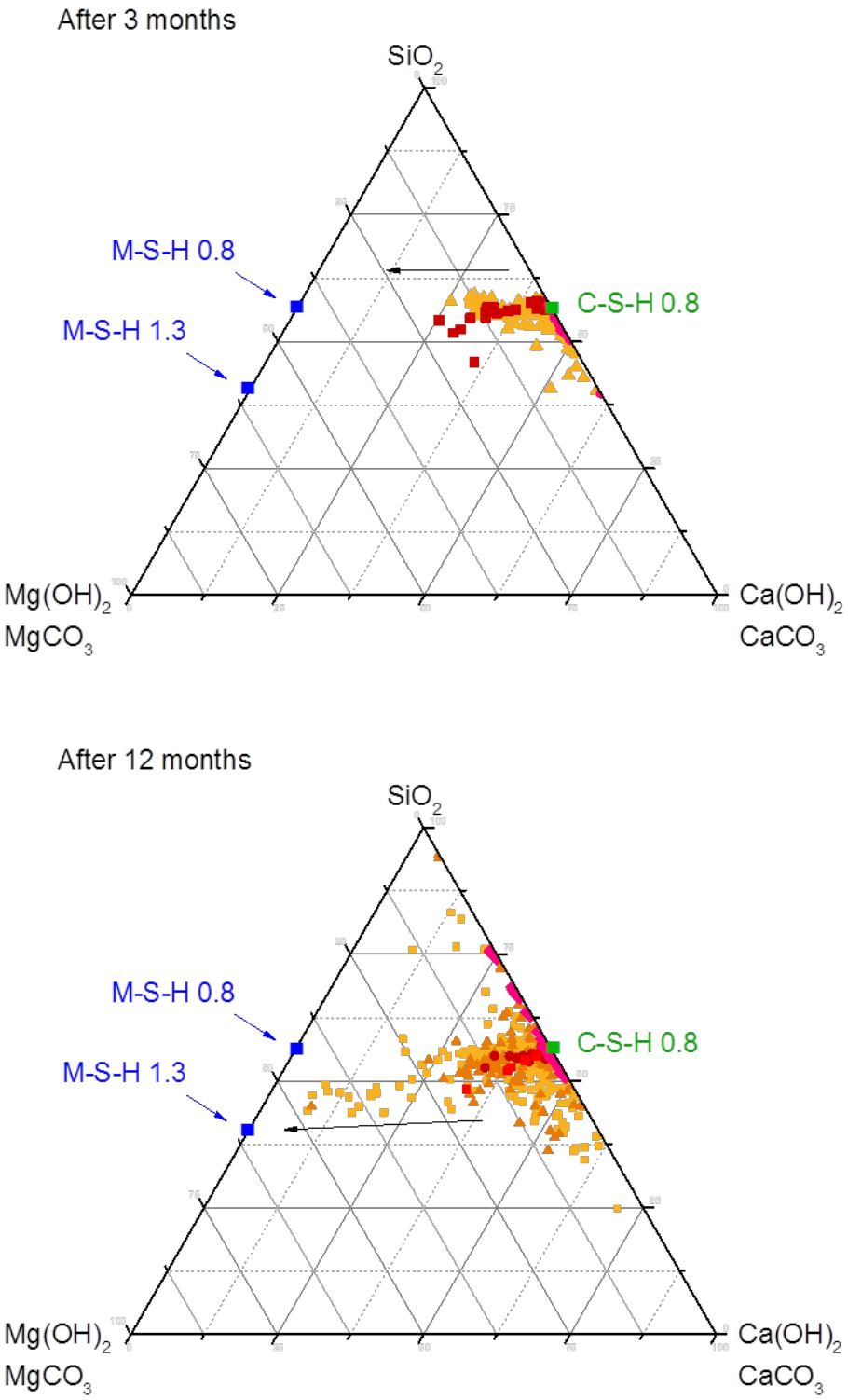

Figure 74: Ca-Si-Mg ternary plots (in molar units) obtained from EDS measurements of the C-S-H disk after 3 and 12 months in contact with M-S-H. Yellow triangles and squares: singles points in the entire depth disks, red squares and red circles: area profiles, pink diamonds: far from interface C-S-H.

M-S-H disk

The analysis of the M-S-H disk focused on the 3 months results where a homogeneous M-S-H was prepared, as the disk analyzed after 12 months was not well compacted and was partially disintegrated already prior to exposure as shown in Figure 71b. Second electron images and the EDS mapping of the M-S-H disk are summarized in Figure 75. In contrast to the C-S-H disk, no front was observed in the M-S-H disk and neither silicon nor magnesium were leached near the interface. The measured Mg/Si molar ratio (Figure 76) was found to vary between 0.8 to 0.6 independent from the distance to the interface.

The calcium distribution in the M-S-H was heterogeneous. Defined areas with high calcium content but no or very little silicon and magnesium are visible in Figure 75, again indicating the presence of calcium carbonate in the samples, as also visible in the ternary diagram summarizing the EDS data in Figure 76a. A more detailed analysis, however, indicated that in all measurements a small amount of calcium was present in M-S-H as shown in Figure 76b. All measured points, even those far from the interface, contained calcium, and the Ca/Si varies between 0.03 to 0.08 as shown in Figure 76b, although initially no calcium had been present (Ca/Si=0).

The FTIR analysis of the M-S-H disk (Figure 72) showed almost identical spectra independently of the depth in the M-S-H disk. A much lower carbonation than in the C-S-H disk is observed and the spectra are similar to the spectrum of M-(C)-S-H (Mg/Si=0.75, Ca/Si=0.05).

The calcium uptake could either be due to finely and homogeneously distributed calcite intermixed with M-S-H or more probably due to an uptake of some calcium in M-S-H. In fact, the uptake of some calcium on the negatively charged M-S-H has been observed in dedicated batch experiments (chapter 4.3). Calcium (together with aluminum and iron) had also be observed in M-S-H collected from the interface between clays and cement (Lerouge et al., 2017).

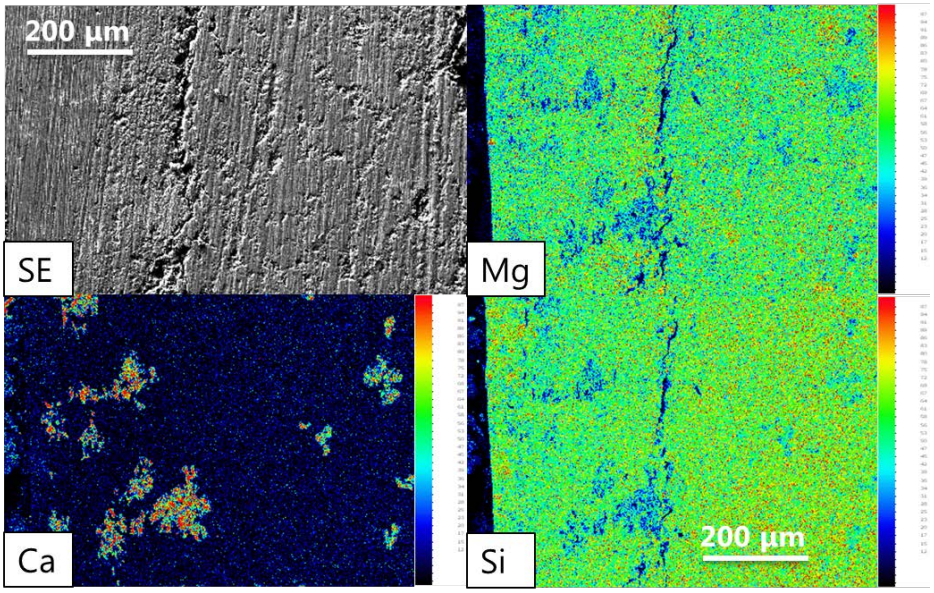

Figure 75: EDS elemental mapping of M-S-H disk close to the interface (interface on the left).

A few EDS data measured on the M-S-H disk after 12 months are also represented in Figure 76. Similar results, Mg/Si (0.8 ±0.1) and Ca/Si (0.07 ±0.02), were obtained even if the mean values of the two ratio were slightly higher after 12 months.

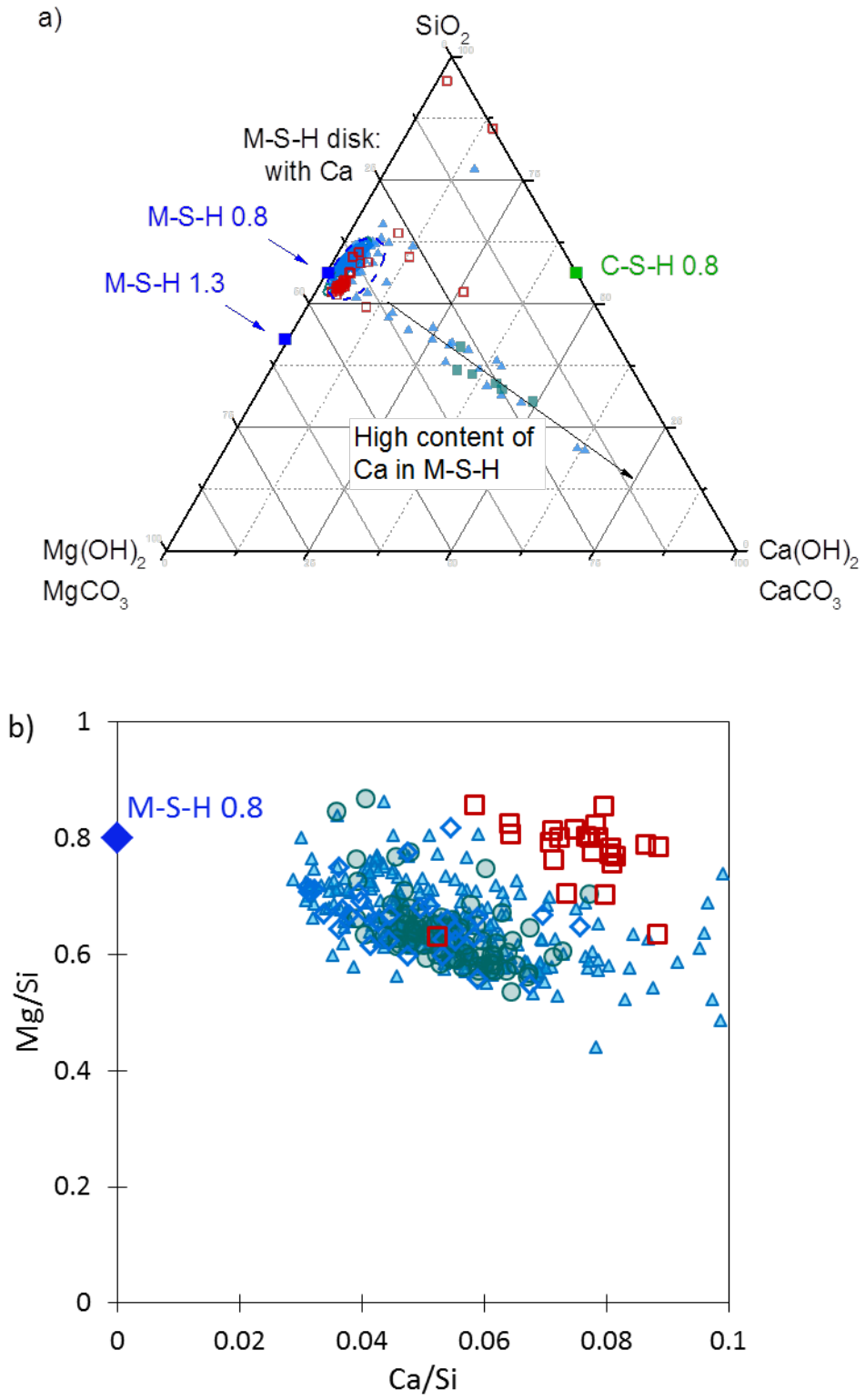

Figure 76: a) Ca-Si-Mg ternary plots from EDS measurements of the M-S-H disk at 3 months, b) zoom on measured elemental ratios in M-S-H disk. Triangles= points in the entire disk, squares= high calcium content spots, circles= far from the interface, diamonds= close to the interface cf. Figure 70, empty red squares= results after 12 months.

4.4.1.1.2. Liquid analysis

The Solutions of the both reservoirs were followed for any physico-chemical changes. Figure 77 shows the pH values and the main species measured in solutions in the two reservoirs at t=0, after 3 and after 12 months. In addition traces of potassium and chloride were observed.

Initially, the solution in equilibrium with C-S-H contained mainly silicon (1.5 mmol/l), some calcium (0.8 mmol/l), no sodium (<0.003 mmol/l) and had a measured pH of 10.5. With time a decrease of pH was observed together with a small increase of the silicon and calcium concentrations. In addition, some sodium diffused from the M-S-H reservoir through the M-S-H and C-S-H disk. The increase of dissolved silicon in the C-S-H reservoir and the pH decrease with time were consistent with a decalcification of C-S-H (Lothenbach and Nonat, 2015; L'Hôpital et al., 2016a) confirming the EDS observations at the interface.

The solution in contact with M-S-H had initially a pH of 8.5 and contained 2.0 mmol/l silicon, 0.1 mmol/l of magnesium and 0.3 mmol/l sodium. After 3 months, a migration of calcium from the C-S-H side to the M-S-H solution was observed, while the pH increased from 8.5 initially to 9.3 after 3 months and to 9.6 after 12 months. The dissolved magnesium concentrations decreased from initially 0.1 mmol/l to <0.01 mmol/l as pH increased, This decrease of magnesium concentration at higher pH is consistent with results from batch experiments.

The occurrence of calcium in the M-S-H reservoir indicated that calcium diffused within 3 months completely through the M-S-H disk, in agreement with the homogeneous distribution of calcium in the M-S-H disk as observed by EDS. The pH of 9.5 in the M-S-H reservoir was below the range of stability of the C-S-H which was consistent with the absence of C-S-H precipitation in the M-S-H disk as already observed in chapter 4.2.

In summary, the interaction of C-S-H with magnesium decreased the pH, leading to the decalcification of C-S-H and the precipitation of M-S-H. In contrast to C-S-H, M-S-H remained stable and took up a small amount of calcium.

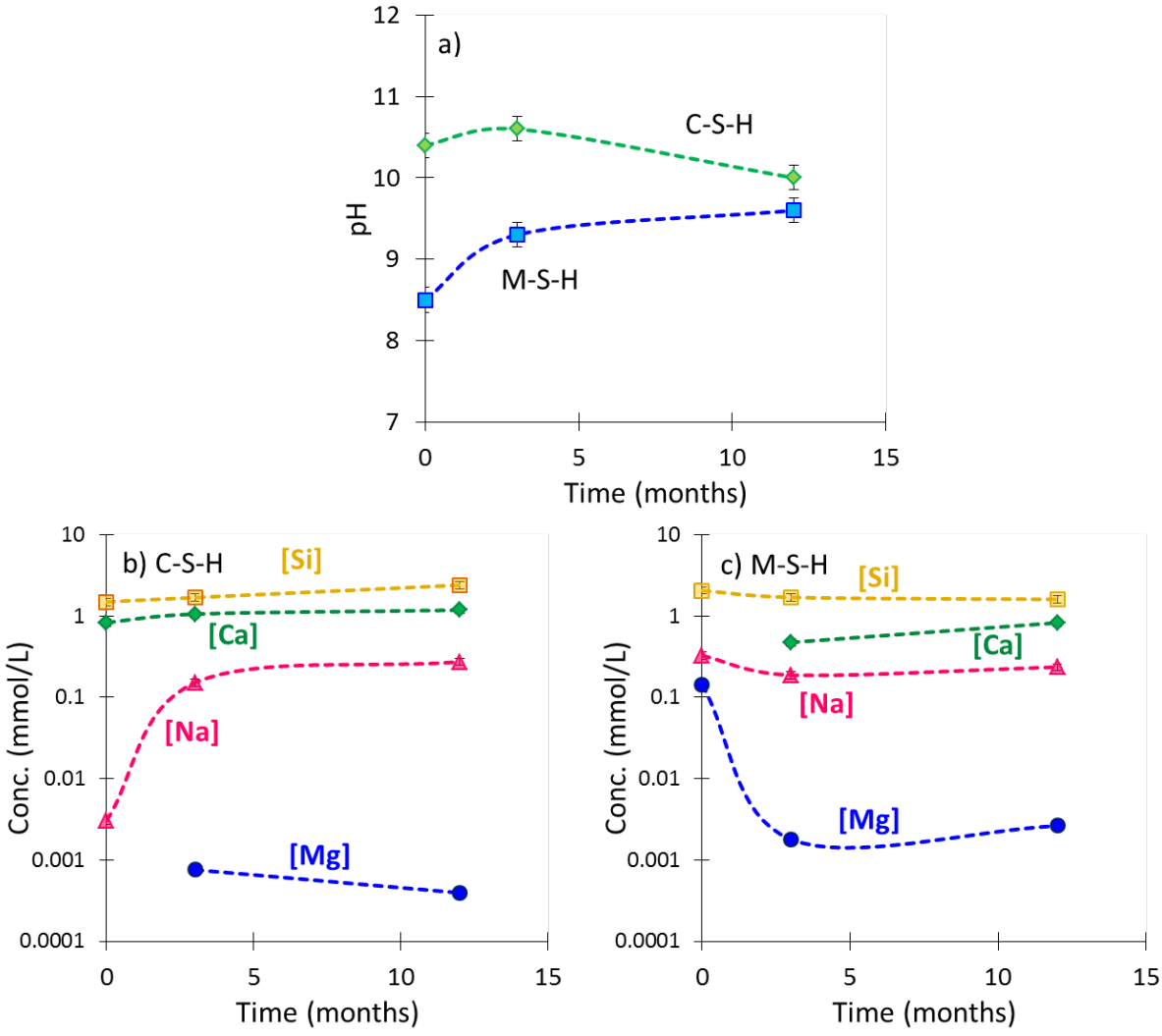

Figure 77: Chemical evolution of the solutions as function of time. (a) pH of the both solutions; (b) Si, Ca, Na and Mg concentration in the CSH reservoir; (c) idem in the MSH reservoir ([K] and [Cl] < 0.05mmol/l).

4.4.1.2. Modelling of the chemical evolution of the interface

Reactive transport modelling assuming thermodynamic equilibrium was used to better understand the underlying mechanisms.

The C-S-H disk used in the calculations contained C-S-H with a Ca/Si of 0.8 and traces of C-S-H with a Ca/Si of 0.67 resulting in a pH value of 10.5. The disk of M-S-H was constituted of M-S-H with Mg/Si=0.83 and with Mg/Si=0.78 to obtain M-S-H with a Mg/Si of 0.8 as used experimentally and a pH of 8.5. Both disk resulting in a total Ca/Si equal to 0.80 and Mg/Si equal to 0.80. The initial configuration and the solid compositions of the modelling are detailed in Figure 78a. The solution compositions of the reservoirs were set to the experimental solution compositions

and are given in Figure 78b. The pore solutions in the disks calculated by modelling agreed well with the solution composition reservoir as visible in the pH values. The measured calcium was with 0.83 mmol/l slightly lower than the 1.09 mmol/l in the modelled pore solution, while the measured modelled magnesium (0.07 mmol/l) agreed well. The silicon concentrations of the reservoirs differed slightly within ± 0.6 mmol/l to the modelled pore solution of the disks.

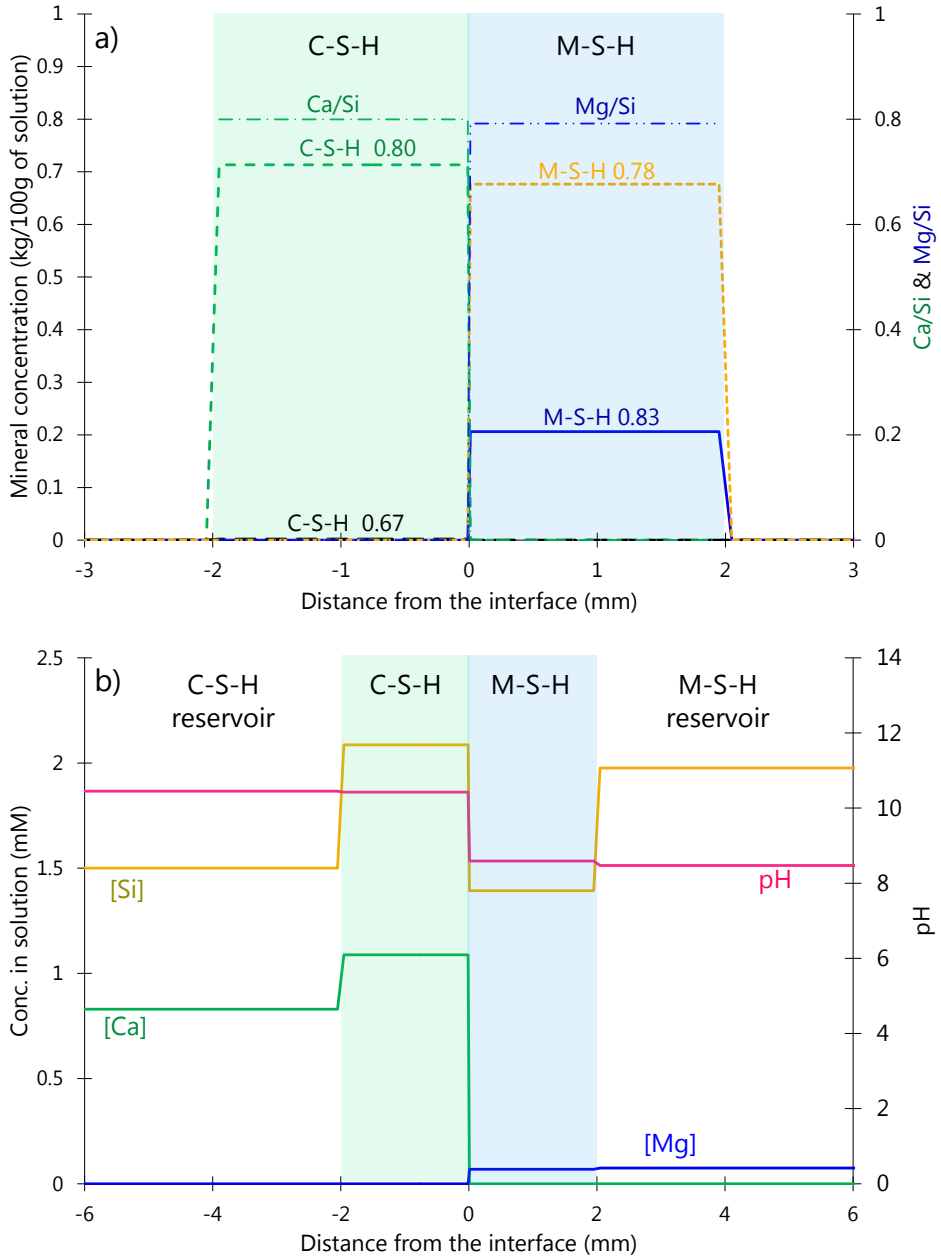

Figure 78: Modelling of the initial state of the mineral concentration at the C-S-H 0.8 / M-S-H 0.8 interface.

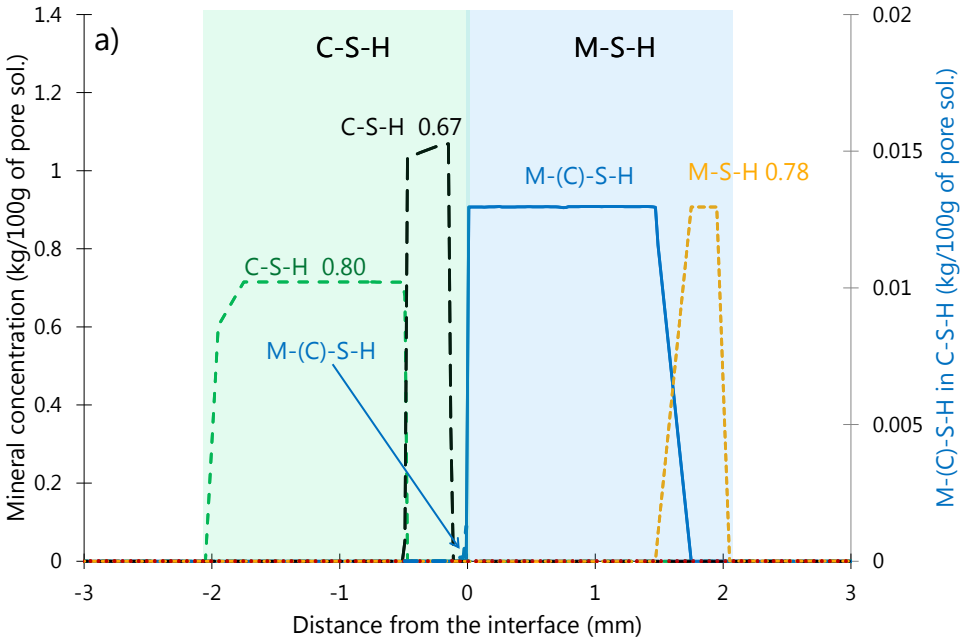
a)
C-S-H
M-S-H
C-S-H 0.67
M-(C)-S-H
M-S-H 0.78
C-S-H 0.80
M-(C)-S-H
Mineral concentration (kg/100g of pore sol.)
M-(C)-S-H in C-S-H (kg/100g of pore sol.)
Distance from the interface (mm)
1.4
1.2
1
0.8
0.6
0.4
0.2
0
0.02
0.015
0.01
0.005
0
-3
-2
-1
0
1
2
3

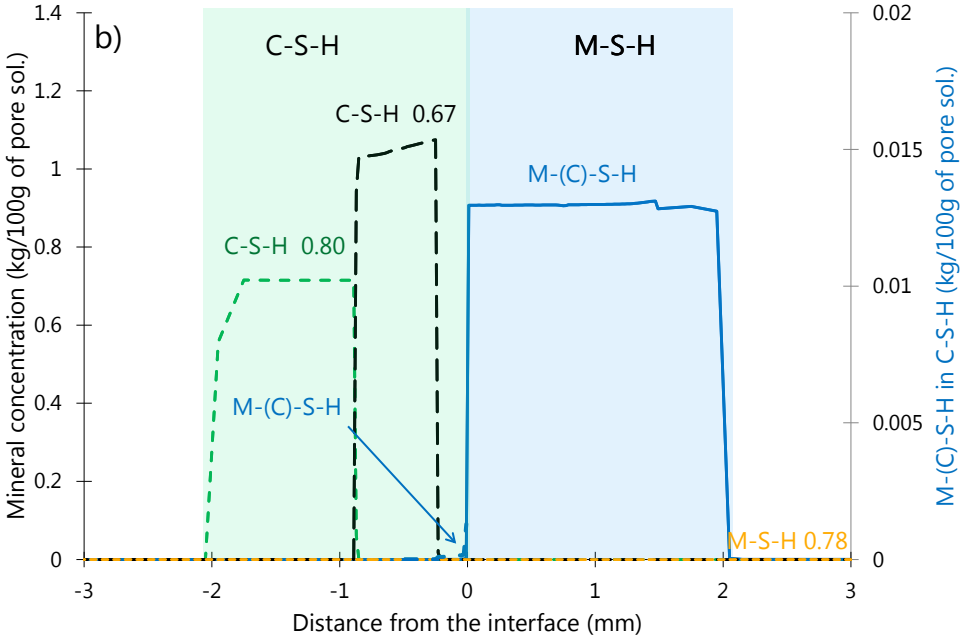
b)
C-S-H
M-S-H
C-S-H 0.67
M-(C)-S-H
C-S-H 0.80
M-(C)-S-H
M-S-H 0.78
Mineral concentration (kg/100g of pore sol.)
M-(C)-S-H in C-S-H (kg/100g of pore sol.)
Distance from the interface (mm)
1.4
1.2
1
0.8
0.6
0.4
0.2
0
0.02
0.015
0.01
0.005
0
-3
-2
-1
0
1
2
3

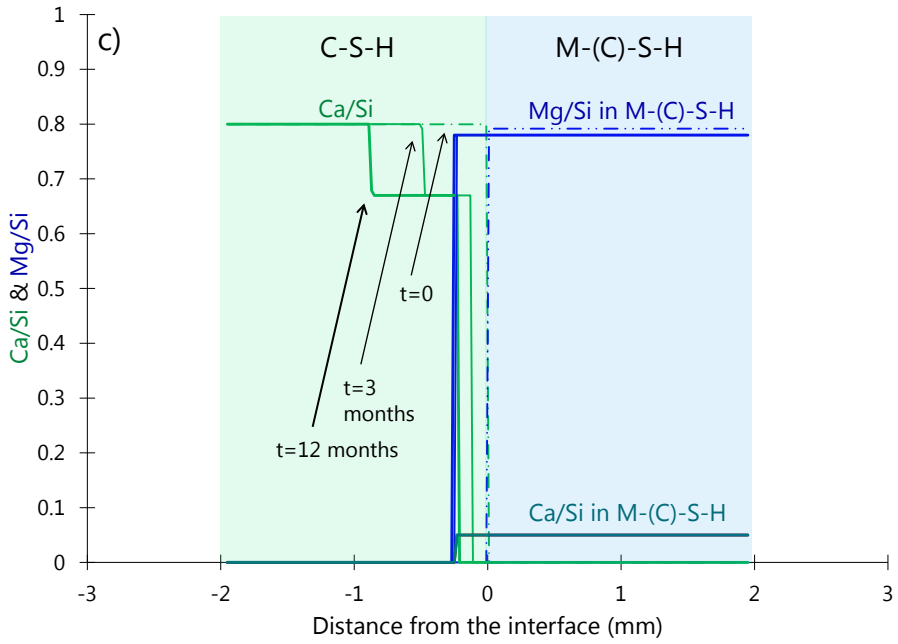

Figure 79: Modelling of the main phases' evolution with M-S-H, M-(C)-S-H and C-S-H phases a) after 3 months, b) 12 months of interaction at the C-S-H / M-S-H interface at 25°C and c) the evolution of the molar ratios in the phases with time.

The modelling results after 3 and 12 months are summarized in Figure 79. They indicated decalcification of the C-S-H disk in contact with the M-S-H disk near to the interface where the Ca/Si dropped from 0.8 to 0.67 while no amorphous silica was predicted. With time the decalcification front was calculated to move further away from the interface. The modelling indicated that a net loss of silicon and calcium from the C-S-H to the M-S-H occurred as detailed in Figure 80. Twice as much calcium as silicon loss was predicted by the modelling. On the opposite direction, a very low amount of magnesium diffused from the M-S-H disk into the C-S-H side as shown in Figure 80. The very low amount of magnesium which was due to the very low concentration of magnesium (Figure 78) imposed by the pH values of the two reservoirs. Thus the magnesium diffusion resulted in the formation of a small quantity of M-(C)-S-H only in the C-S-H disk (Figure 79 and Figure 81). In the M-S-H disk, the M-S-H present initially was calculated to be destabilized while M-S-H containing some calcium, M-(C)-S-H, was calculated to form, after 3 months in the major parts of the M-S-H disk and after 12 months over the whole disk.

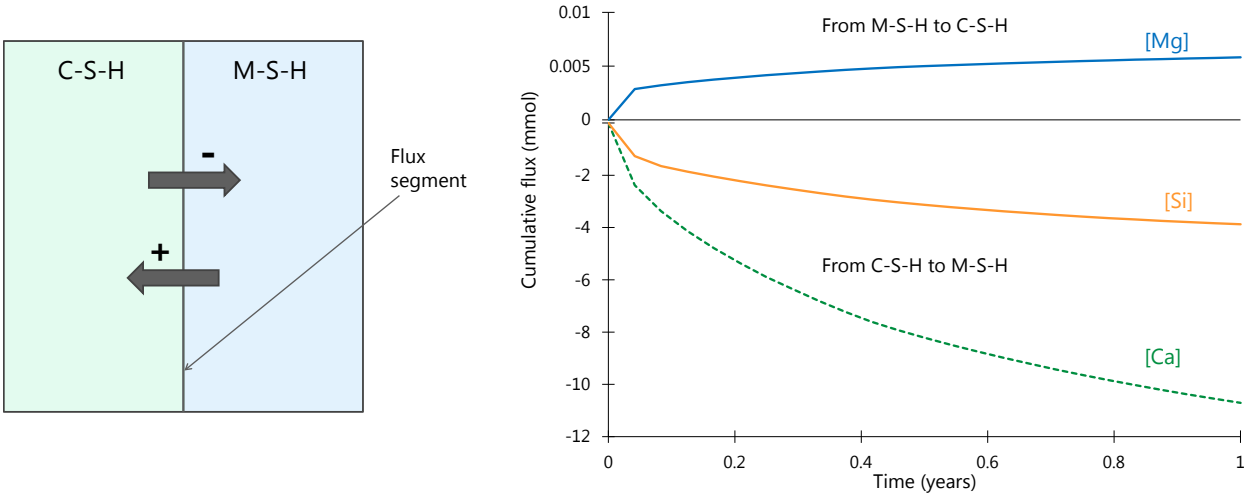

Figure 80: Modelling of the cumulative flux at the C-S-H/M-S-H interface.

After 12 months, the calculated depth of the M-(C)-S-H formation had increased. The modelling predicted the loss of silicon in the first 50 µm through diffusion and thus a strong increase of porosity in the area where all C-S-H 0.67 was dissolved, while experimentally a limited increase of the porosity was observed and the formation of much more M-(C)-S-H.

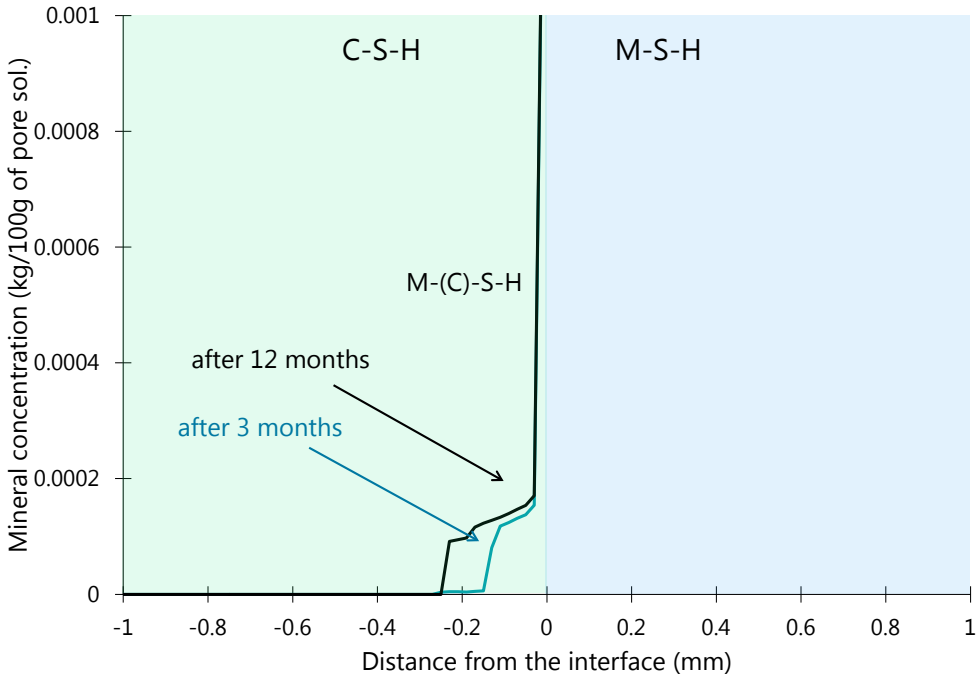

Figure 81: Modelling with M-S-H, M-(C)-S-H and C-S-H phases of the M-S-H phases' evolution inside the C-S-H disk after 3 months and 12 months of interaction at the C-S-H/M-S-H interface at 25°C.

The general phenomena observed experimentally, i.e. the decalcification of the C-S-H, in increasing porosity at the interface, the precipitation of M-S-H in the C-S-H disk and the precipitation of calcium in the M-S-H phase were well described by the modelling.

Also the extent of degradation in both materials was more or less consistent with the experimental results. After 3 months, the decrease of Ca/Si in C-S-H from 0.8 to 0.67 is with 490 µm calculated to be somewhat deeper than the 200 µm observed experimentally. However, after 12 months a good agreement between modeled and experimental data was obtained. Also the calculated depths of M-(C)-S-H formation in the C-S-H disk of 230 µm agreed with the experimental observation after 1 year, while after 3 months the calculated progress of 130 µm was further than the experimental observations. The main differences to the experiments were the much lower amount of M-(C)-S-H calculated and the nearly complete dissolution of the zone at the interface. Both were related to the very low amount of magnesium transported in the calculations from the M-S-H disk into the C-S-H due to the stability of the M-S-H phases.

In the experiments reservoirs filled with the respective solutions were used in order to maintain the disks water saturated during the experiments and to be able to observe the changes in the solution during the experiments. The modelling of the changes in the solutions is depicted in Figure 82 by the solid lines. With time, the calcium concentrations and the pH values increased in the M-S-H solution while the dissolved magnesium was calculated to decrease. The trends were in good agreement with the experimental observations. The modelled concentrations of silicon change little with time, while experimentally they decreased slightly. Also the changes in the C-S-H reservoir were well described by the modelling, which predicted an increase of calcium and silicon concentrations and little change in the pH values, while the experimental data after 12 months showed a slight decrease of the pH. The slight decrease of the measured pH in the C-S-H solution could be due to small carbonation of the system which were not been taken into account in the modelling.

The modelling has also been carried out neglecting the uptake of calcium in M-S-H which gave similar results (see Appendix I) with the exception that no calcium uptake in the M-S-H disk was predicted.

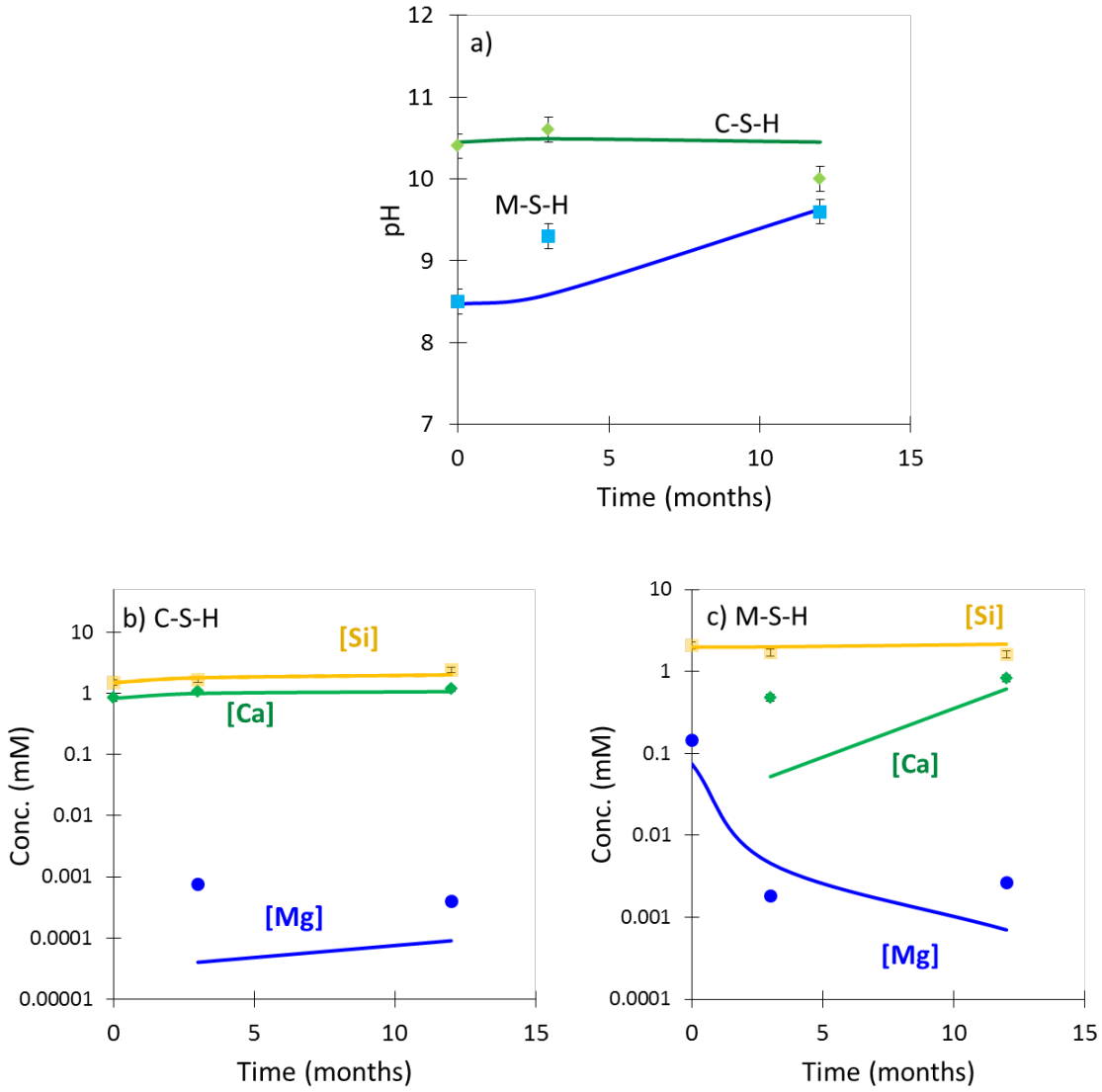

Figure 82: Modelling of the evolution of the reservoir chemistry in parallel to the mineralogical changes compared to the experimental results (symbols): a) pH values over time; b) C-S-H reservoir over time c) M-S-H reservoir over time (solid lines: modelled changes).

4.4.2. Conclusions

Both experimental observations and reactive transport calculations of the cell experiments showed the partial destabilization of C-S-H in the presence of M-S-H within a few months. Experimentally, C-S-H was decalcified (drop of Ca/Si from 0.8 to 0.6±0.1) followed by the formation of amorphous silica and visual cracks. In addition the precipitation of M-S-H already observed after 3 months in the place where originally C-S-H phases were present. No incorporation of magnesium was observed in sound C-S-H phase in agreement with observations in batch

experiments (chapter 4.3). Magnesium was observed near the interface only together with amorphous silica.

These cell experiments clearly proved that M-S-H formation occurs within a relatively short time and that M-S-H forms from the dissolution of C-S-H, as postulated in (Jenni et al., 2014; Dauzères et al., 2016; Lerouge et al., 2017; Mäder et al., 2017) based on field observations. In contrast to such field studies, where the experimental differentiation between M-S-H and the clay minerals was difficult, the absence of clay minerals in the present study and the clear separation of C-S-H and M-S-H at the beginning of the diffusion experiments, allowed an unbiased interpretation of the results.

Calcium available from the dissolution of C-S-H was observed to diffuse to the M-S-H, where calcium was partially bound to M-S-H. This agrees with the calcium uptake in M-S-H observed in batch experiments (chapter 4.3).

The good agreement between thermodynamic modelling and experiments underlined the applicability of transport modelling to study the deterioration of cementitious material in contact with claystone; the magnesium perturbation can be considered simultaneously with leaching, carbonation, or sulfate uptake in a transport modelling. From now on, thermodynamic data concerning M-S-H but also M-(C-)S-H in solid solution (chapter 4.3) or single phases (this chapter) can correctly model the magnesium perturbation occurring during the aging of low-pH cementitious materials in deep storage.

Further steps for a better understanding of the formation of M-S-H would be to consider the possible aluminum and alkali uptake in M-S-H and the effect of porosity on the diffusion of magnesium and other ions.

4.5. Main findings on the calcium and magnesium silicate system

- C-S-H is unstable at pH values below 10 (in batch and cell experiments)
- C-S-H (Ca/Si=0.8) + $MgCl_2$ lead to pH values below 10, the destabilization of C-S-H and the formation of M-S-H
- At pH values between 10 and 10.5, both M-S-H and C-S-H phases are stable and coexist
- C-S-H (Ca/Si=0.8) + high MgO content leads to the pH up to 11.5 where the Ca/Si in C-S-H increases and brucite & M-S-H form
- M-S-H formed from C-S-H has a structure comparable to the structure of pure M-S-H prepared from MgO and SiO_2, i.e. a poorly ordered hydrated phyllosilicate
- M-S-H are stable between pH 7.5 to 11.5
- A limited uptake of calcium occurs in M-S-H, mainly at the cation exchange sites at the surface, potentially calcium may also be present in other sites
- A solid solution model can be used to describe the uptake of calcium in M-S-H: M-C-S-H

Chapter 5:
Binding of alkalis and incorporation of aluminum in magnesium silicate hydrate

Contents

5.1. Introduction

The alkalis or aluminum incorporation in M-S-H are of interest due to the presence of aluminum both in the cement paste and in the clay environment and to understand whether its presence influences the ability of M-S-H for alkali uptake.

Although the existence of a magnesium silicate hydrate phase at the cement paste/clay interface or degraded cement by sea water is established, it remains unclear i) if aluminum is incorporated in a magnesium alumino-silicate phase (M-(A-)S-H) or intermixed as hydrotalcite-like phases and i) if the binding of alkalis occurs in M-S-H. Brew and Glasser (Brew and Glasser, 2005a) showed a good immobilization potential of M-S-H for potassium; no other indication of the ability of M-S-H for alkali uptake is available in literature.

M-S-H phases have an ill-defined structure comparable to hydrated nano-sized 2:1 and/or 1:1 phyllosilicates ((Roosz et al., 2015; Nied et al., 2016; Lerouge et al., 2017), chapter 3.3). In chapter 3.3, the effective negative surface charge of M-S-H particles was measured by zeta potential measurement (acoustophoresis) directly in the suspensions. The negative surface charge was explained by the presence of some deprotonated silanol groups at the edges and/or in vacancy in the silicate layers of the M-S-H and low cation concentrations in solution. An increase of pH at similar magnesium concentrations resulted in a more negative surface charge density of M-S-H particles indicating a higher deprotonation of the silanol groups. The cations exchange capacity measured on the solid after filtration showed only a small amount of cations such as magnesium and sodium might be sorbed onto the surface of M-S-H to outbalance its negative charges. In the presence of calcium (chapter 4.3), the surface charge density of M-S-H was measured to be less negative, and a higher calcium sorption on the surface of the silicate layers was measured by CEC.

Natural phyllosilicates contain commonly aluminum in the tetrahedral and/or octahedral sheets. Theoretically, saponite and montmorillonite are typical trioctahedral and dioctahedral smectites, respectively, composed of mainly magnesium, silicate, and aluminum in the main layers. A negative surface charge is characteristic for all smectites. The simplified composition of saponite can be expressed as $(Ca_{0.5}Mg_{0.5}Na{\cdot}nH_2O)_xMg_3[(Si,Al)_4O_{10}](OH)_2{\cdot}mH_2O$. In the case of saponite, its negative charge comes from the substitution of Al^{3+} for Si^{4+} in the tetrahedral sheets. In montmorillonite, instead, a part of the Mg^{2+} of octahedral sites is substituted by Al^{3+}: $(NaCa_{0.5}{\cdot}nH_2O)_x(Al, Mg,\square)_2\ [Si_4O_{10}](OH)_2{\cdot}mH_2O$ and only two third of the octahedral

sites are filled. Vermiculite contains aluminum in both octahedral and tetrahedral layers: $(Ca_{0.5}Mg_{0.5}Na{\cdot}nH_2O)_x(Mg,Al,\square)_3[(Al,Si)_4O_{10}]$ $(OH)_2{\cdot}mH_2O$ indicating excellent abilities of aluminum incorporation in magnesium silicate hydrate phases.

This chapter studies: i) the ability of M-S-H to bind alkali at different pH values by adding either sodium nitrate or sodium hydroxide to M-S-H during the synthesis; ii) the M-A-S-H phases formation at different temperatures (20, 50 and 70°C), at Mg/Si = 1.1 and 1.7 and varying Al/Si ratios. M-A-S-H samples with Mg/Si=0.8 and 1.2 were also synthesized in the presence of sodium nitrate.

5.2. Binding of alkali in M-S-H depending on the pH

This part studies the ability of M-S-H to bind alkali at different pH values by adding either sodium nitrate or sodium hydroxide to M-S-H during the synthesis. Additionally, some alkali hydroxide solution were tested. The details of the syntheses are given in 2.1.3. Ion chromatography (IC) technique, pH measurements, thermogravimetry analysis (TGA), X-ray diffraction (XRD) characterizations, ^{29}Si MAS NMR spectroscopy, Zeta potential and CEC measurements used in this study are detailed in chapter 2.2.

5.2.1. Results and discussions

5.2.1.1. M-S-H as the main reaction product

5.2.1.1.1. M-S-H synthetized in the presence of sodium nitrate

The presence of sodium nitrate in the solution during synthesis led to the formation of M-S-H as the main product after 1 year, i.e. at or near equilibrium (chapter 3).

X-ray diffraction patterns of the M-S-H 0.8 synthesized in the presence of sodium nitrate are compared with X-ray diffraction pattern of pure M-S-H 0.8 in Figure 83. Pure M-S-H and M-S-H synthesized in sodium nitrate solution presented similar patterns with broad X-rays humps characteristic of M-S-H at 19.7, 26.7, 35.0, and 59.9 °2θ (λ=1.54Å) (Roosz et al., 2015; Nied et al., 2016). Residual sodium nitrate was found in the samples where the solution used during synthesis contained [$NaNO_3$] = 500 mmol/l, maybe due to its re-precipitation during the drying process. In the presence of sodium nitrate, the large hump at 26.7 °2θ which had been related to the basal specing in chapter 3.3 seems more intense. The reflection at approx. 60 °2θ characteristic for trioctahedral smectites as stevensite or saponite appears narrower. TGA analysis (Figure 84) of those samples revealed the presence of physically bound water (weight loss 30-250°C) and structurally bound water, i.e., the hydroxyl groups (250-800°C) comparable to M-S-H as detailed in chapter 3. The physically bound water content is strongly dependent on the relative humidity and the drying methods, but it seems that its content increases with the addition of sodium nitrate.

Their ^{29}Si MAS-NMR spectra are compared to the pure M-S-H 0.8 in Figure 85, and the silicate layers were also very similar, independent whether sodium nitrate was

present or not. The ^{29}Si MAS NMR spectrum of pure M-S-H had been deconvoluted using resonances at around -78.6 ppm assigned to Q^1, -85.5 ppm (Q^2) and Q^3 (large hump between -92.5 and -96.7 ppm) tetrahedral silicates. The large Q^3 content indicated a structural similarity to phyllosilicates (chapter 3). In the presence of sodium nitrate, the samples contained a comparable amount of amorphous silica (~4% of the initial silica fume) as without sodium nitrate. Also the content of Q^1 and Q^2 tetrahedral silicate (1-2% Q^1 and ~30% Q^2 of the total silicon present) was comparable to the pure M-S-H sample as well as the total amount of Q^3 tetrahedral silicate. However, the addition of sodium nitrate slightly increased the amounts of Q^3a and Q^3b and decreased the amount of Q^3c as shown in Figure 85. Sodium in the vicinity of silicate should lead to less negative chemical shifts (Mägi et al., 1984). However, the Q^2 position peak should be more affected than the Q^3 position peaks due to the exchangeable sites in the surrounding of the silanol groups (chapter 3.3). But Q^2 position peak is not affected by the sodium nitrate addition, thus it seems that the higher Q^3a content is more related to the T:O structure than to sorbed sodium.

Also, in the M-S-H 1.2 samples synthesized in the presence of sodium nitrate, M-S-H-like phases were observed as the main reaction products with a comparable content of water and silicate sheets arrangement (see Appendix J & Appendix K).

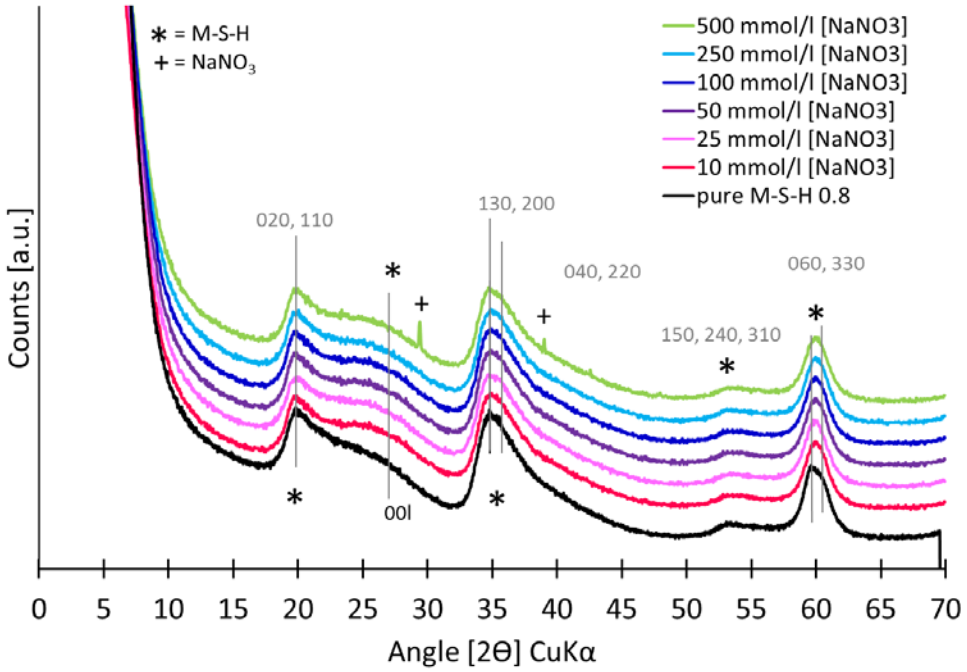

Figure 83: XRD patterns of M-S-H 0.8 samples synthesized in the presence of sodium nitrate compared to pure M-S-H 0.8 after 1 year of curing at 50 °C.

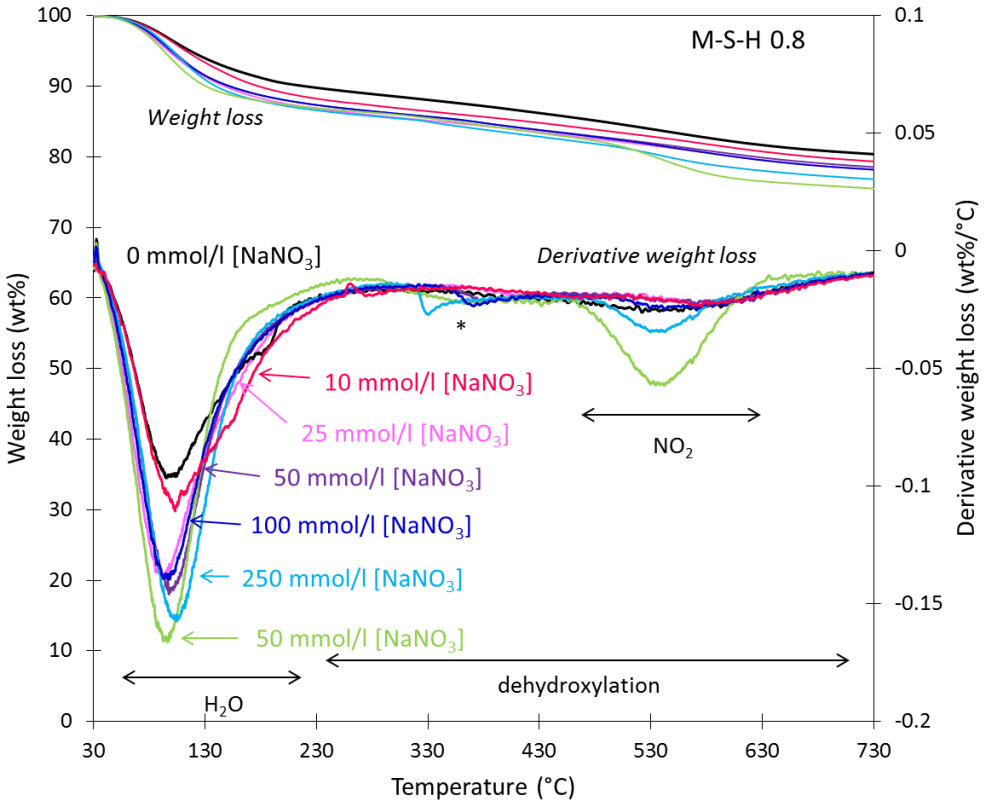

Figure 84: Thermogravimetric analysis of the M-S-H samples synthesized in the presence of sodium nitrate after 6 months of curing at 50°C compared to TGA of pure M-S-H 0.8 (*=impurities).

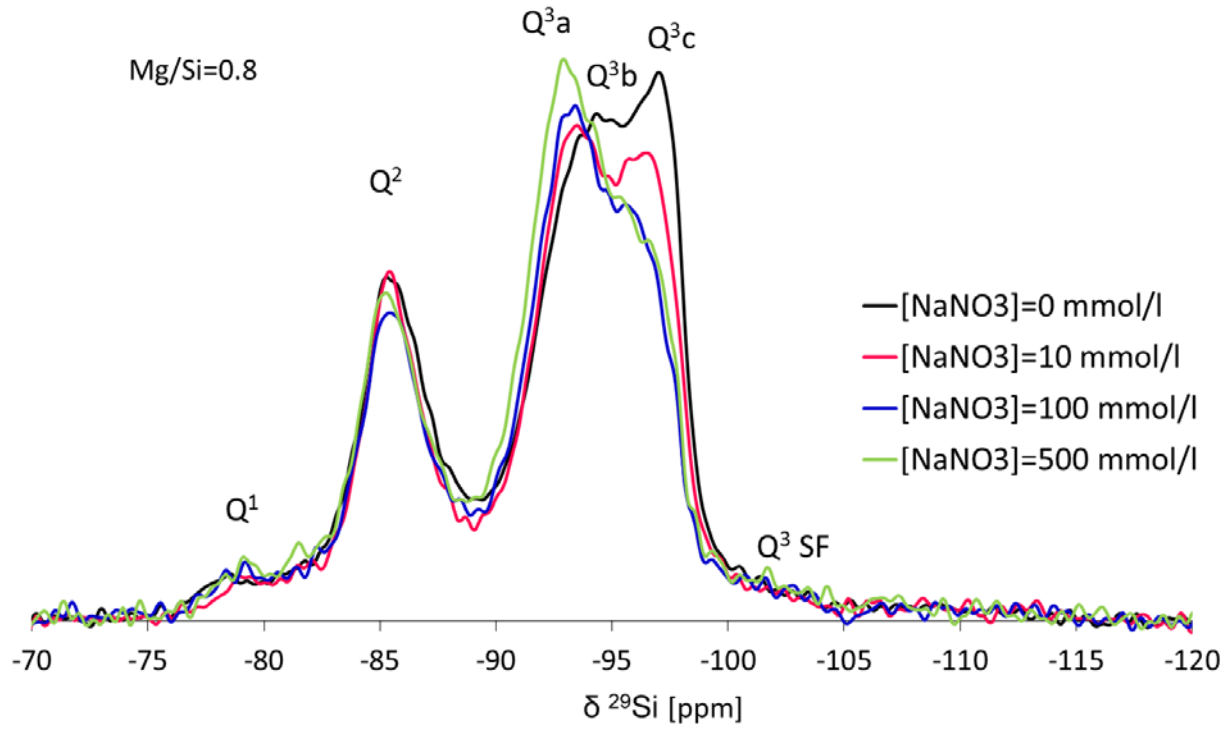

Figure 85: ^{29}Si MAS NMR spectra of M-S-H 0.8 samples synthesized in the presence of sodium nitrate after 1 year of curing at 50 °C.

The presence of sodium nitrate did not change the solutions at equilibrium with the M-S-H fundamentally. A summary of the solution compositions of the samples synthesized at 20°C is given in Table 31. The addition of sodium nitrate lowered the pH from 8.3 to 7.7 at Mg/Si=0.8 and from 10 to 9.7 at Mg/Si=1.2 (Table 31). This decrease of the measured pH could be due to the increase in ionic strength, due to the effect of Na^+ on the pH electrode or due to the uptake of more sodium than nitrate by the solid.

IC measured no or only a small reduction of sodium or nitrate in solution at equilibrium with the M-S-H samples, indicating a limited uptake of sodium or nitrate by the solid phases. At high alkali concentrations, such indirect determination of sodium and nitrate uptake based on the difference in concentration measurements and mass balance calculations are not very accurate as they are associated with a significant error, due to 10% relative error of the ionic chromatography as discussed in (L'Hôpital et al., 2016b) or below.

The measured magnesium concentrations were slightly higher in the presence of sodium nitrate. The increase of dissolved magnesium concentrations could be due to a partial substitution of magnesium by sodium as counter-ions of the negative surface charge of M-S-H, due to the increase in the ionic strength, or due to the formation of Mg-nitrate complexes in solution or due to the lower pH values which might destabilized the M-S-H or which might protonated the silanol groups.

Table 31: pH values and measured dissolved concentrations in the solutions in equilibrium with the M-S-H synthesized in the presence of sodium nitrate (at 20°C, curing time: 1 or 2 years).

Mg/Si	$[NaNO_3]_{init}$ mmol/l	pH	[Na] mmol/l	$[NO_3]$	[Mg]	[Si]
0.8	0	8.3	0.4	---	0.4	1.4
	10	8.1	9.1	10.4	1.3	1.4
	25	8.1	22.8	25.9	1.9	1.4
	50	8.0	47.8	53.6	2.8	1.4
	100	7.7	107.2	95.1	4.3	1.2
	250	7.6	251.1	236.1	5.1	1.0
	500	7.7	495.3	470.9	5.9	1.2
1.2	0	10.0	0.5	---	0.1	0.008
	10	10.0	9.0	10.4	0.8	0.002
	25	9.8	23.4	26.1	1.3	0.001
	50	9.8	48.4	53.2	1.8	<0.001
	100	9.7	99.1	88.9	2.9	0.002

To conclude, X-ray diffraction and ^{29}Si MAS-NMR spectroscopy showed that M-S-H was the main reaction product in the samples and thus independently of the initial addition of sodium nitrate. The slight changes in the repartition of the Q^3 tetrahedral silicate sites observed by ^{29}Si MAS-NMR spectroscopy and the slight variations in the solution composition might show a little uptake of sodium in M-S-H. Similar results were observed at 50 and 70°C.

5.2.1.1.2. M-S-H synthesized in presence of sodium hydroxide

This second section investigates the effect of sodium hydroxide on M-S-H. Sodium hydroxide increases the pH of the solution which should result in brucite formation at high magnesium contents. Therefore the focus was on M-S-H with Mg/Si=0.8.

At equilibrium (after 1 or 2 years at 20°C), only traces of brucite were detected by XRD at high sodium hydroxide content (≥100 mmol/l) (Figure 86 and Table 33). The weight loss data from TGA (Figure 87), the XRD patterns (Figure 86) and the presence mainly Q^2 and Q^3 (Figure 88) indicated that also in the presence of NaOH, M-S-H was the main reaction product.

The intensity of the broad XRD signal at 19.7 °2θ in the XRD patterns, which relates to signals from the main layers (020, 110), decreased in the presence of sodium hydroxide. Similarly to the addition of sodium nitrate, the shape of the hump at ~ 60 °2θ was modified compared to the pure M-S-H and seemed shifted to higher angles. The layer-to-layer reflection (001) was observed at high sodium hydroxide concentration ([NaOH]=500 mmol/l) at 12.1 Å. This (001) reflection is usually observed at higher Mg/Si (chapter 3.3) in M-S-H.

Interestingly, the physically bound water (weight loss 30-250°C) seems to increase with the addition of sodium hydroxide.

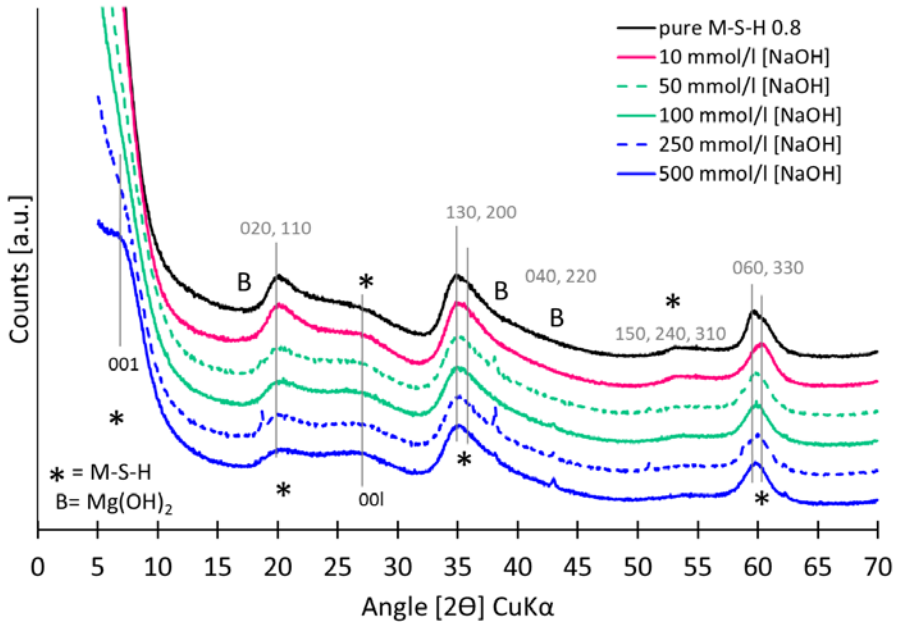

Figure 86: XRD patterns of M-S-H 0.8 samples synthesized in the presence of sodium hydroxide compared to pure M-S-H 0.8 after 2 years of curing at 20 °C.

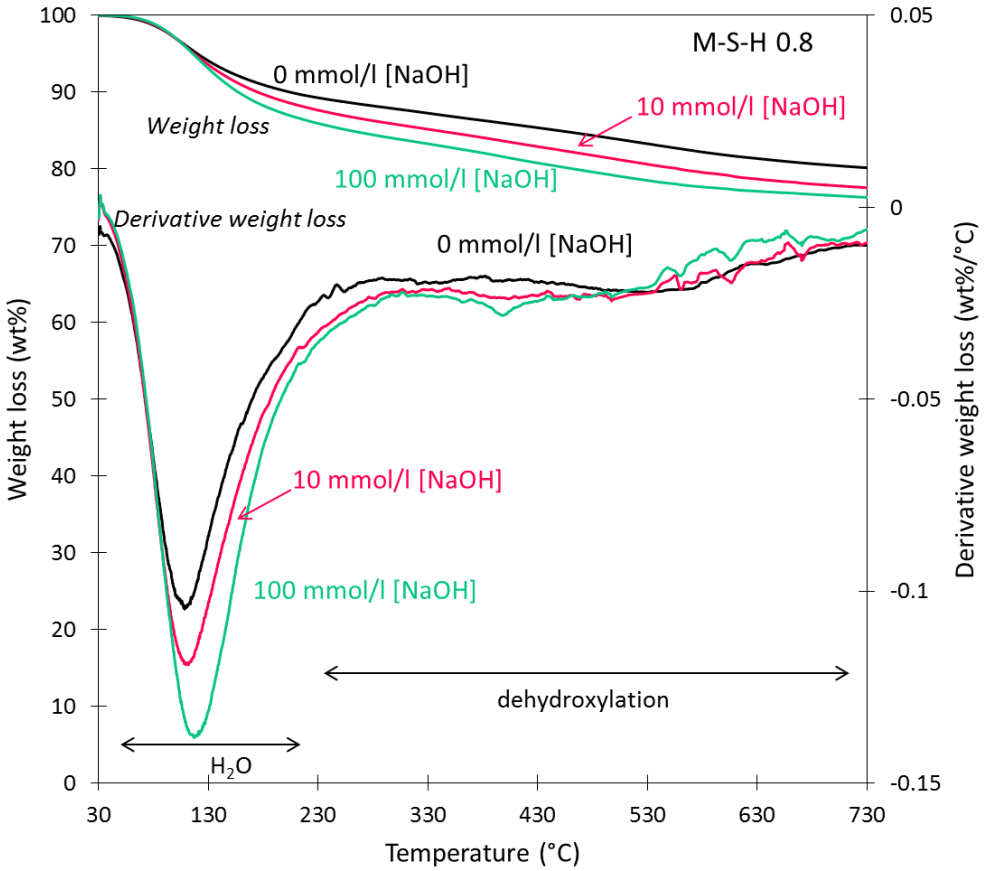

Figure 87: Thermogravimetric analysis of the M-S-H samples synthesized in the presence of sodium hydroxide after 1 year of curing at 20°C compared to TGA of pure M-S-H 0.8.

The ^{29}Si MAS NMR spectra of the M-S-H samples in the presence of sodium hydroxide, in Figure 88, indicates changes in the surrounding of the silicate layer structure. The associated deconvolutions are detailed in Table 32. For pure M-S-H (Mg/Si = 0.8) a small amount of unreacted silica is generally present, which is absent if sodium hydroxide was present. This is comparable to the results obtained for M-S-H synthesized in the presence of calcium (chapter 4.3). The content of Q^3 tetrahedral sites decreased with the addition of sodium hydroxide. In particular the content of Q^3c was lowered while somewhat more Q^3a environement was found at high sodium hydroxide content. At [NaOH] ≥ 100 mmol/l, only the Q^3a environment was observed.

The Q^2 resonance was broadened with the increase of sodium hydroxide content (Figure 88). The Q^1 and Q^2 contents increased with the addition of sodium hydroxide. An additional band at ~ -83 ppm was observed indicating the presence of Na in the surrounding of silanol groups at the surface. The presence of sodium instead of magnesium changed the chemical shift of the Q^2 to less negative values. The band at -83 ppm, assigned to Q^2 tetrahedral silicate in the surrounding of sodium, increased up to 15 % ±4% in the presence of 100 mmol/l NaOH. Thus the Q^2_{tot}/Q^3_{tot} increased with the sodium hydroxide addition indicating a depolymerization of the silicates.

The presence of alkali hydroxide solution or rather the presence of hydroxides are creating “defects”, possibly due to the increased deprotonation of the silanol groups at higher pH resulting in more negative surface charges which limits the growth or assembly of silicate sheets as suggested in chapter 3.3. Similarly, for synthetic C-S-H a shortening of the silicate chains at high pH was reported (Lothenbach and Nonat, 2015; L'Hôpital et al., 2016b). The observation of more Q^3a and less Q^3c might be due to the presence of more defects in the silicate layers. Similar trends were observed at 50°C (Table 32).

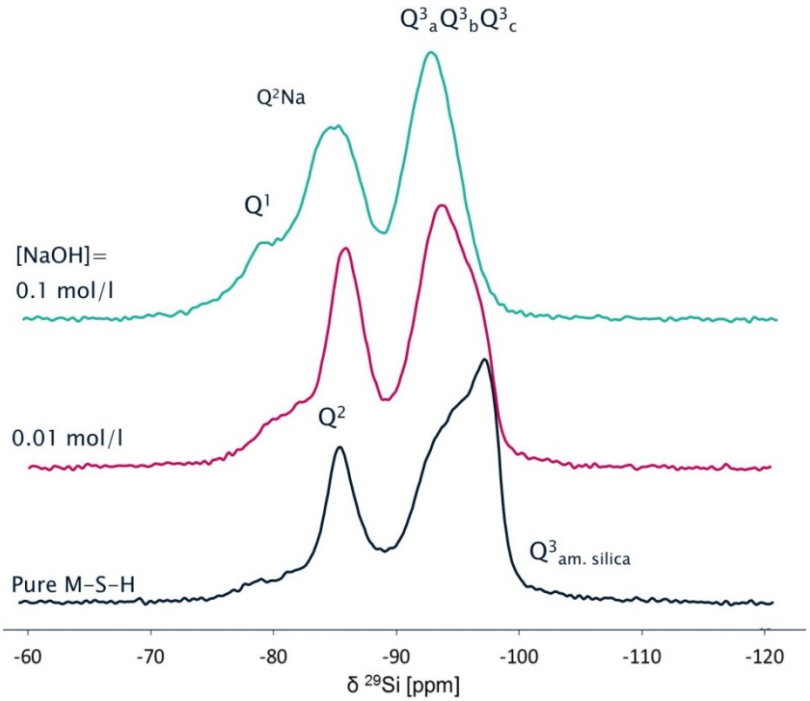

Figure 88: ^{29}Si MAS NMR spectra with assignments of single sites of M-S-H samples synthesized in the presence of sodium hydroxide after 1 year at 20°C compared to a pure M-S-H.

Table 32: Peak shifts and relative intensities (quantifications) of different silicon shifts obtained from the deconvolution of the ^{29}Si MAS NMR spectra for M-S-H synthesized in the presence of sodium hydroxide (1year) (δ^{29}Si in ppm ± 0.3 ppm).

			δ^{29}Si (M-S-H)							
			Q^1	Q^2 Na	Q^2	Q^3a	Q^3b	Q^3c	Q^2/Q^3	Am. silica $Q^3(SiO_2)$
	Mg/Si	[NaOH] mmol/l	-78.3	-83	-85.5	-92.7	-94.7	-96.7		-100.9
20°C	0.8	0	2	0	35	25	8	26	0.6	4
		10	4	9	28	37	14	9	0.6	0
		100	10	15	27	48	0	0	0.9	0
50°C	0.8	0	1	0	34	24	10	28	0.6	3
		50	2	7	28	30	5	27	0.6	1
		100	3	13	31	35	15	2	0.8	0

Quantification error ≃ ± 10% of absolute amount of (%Si) +2.5%.

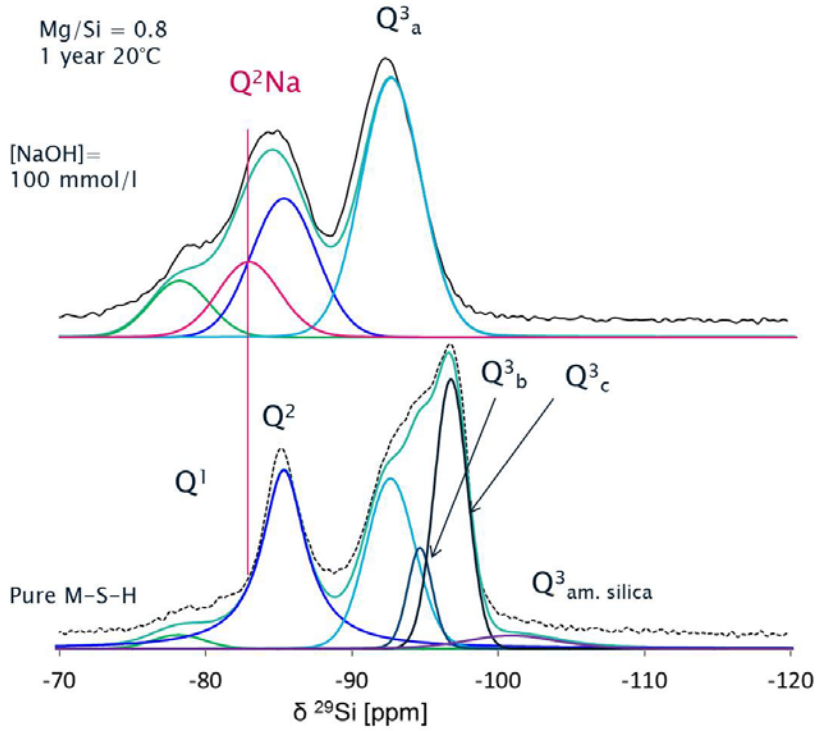

Figure 89: Example of the deconvolutions ^{29}Si MAS NMR spectra for pure M-S-H 0.8 and M-S-H 0.8 synthesized in 100 mmol/l of sodium hydroxide (1 year 20°C).

The solutions compositions of the samples synthetized in the presence of sodium hydroxide during 2 years at 20°C are detailed in Table 33. The addition of sodium hydroxide to M-S-H increased the pH value from 8.3 in the solution of pure M-S-H to pH 13.3 in the presence of 500 mmol/l NaOH. The magnesium concentrations increased from 0.4 mmol/l with the addition of NaOH up to 9.9 mmol/l at pH 12.5 in the absence of any brucite. At higher pH values the formation of brucite lowered the magnesium concentration to <0.06 mmol/l. The silicon concentrations increased from 1.4 mmol/l at pH 8.3 to 35 mmol/l at pH 13.3 although they remained below the concentrations in equilibrium with respect to amorphous silica above pH 9. The relative high magnesium concentrations observed between pH 10 to 12.5 could possibly be related to the formation of aqueous magnesium silica complexes, which had not yet been described in literature.

The measured sodium concentrations were considerably lower than what was initially added. 80% of sodium was associated with the solid phase in 10 mmol/l NaOH. Up to 50 mmol/l of sodium were taken up in the M-S-H phase at higher NaOH concentrations, in agreement with the ^{29}Si MAS NMR data which shows the presence of sodium in the neighboring of the silicates. The sodium in the solid could be i) be

adsorbed on M-S-H surface to compensate the negative surface charge (either in the Stern layer near the surface or in the diffuse layer; which both are partitioned with the solid during filtration) or ii) be in the octahedral layer substituting magnesium.

Table 33: Summary of the presence of brucite and unreacted silica in the solid composition, the measured dissolved concentrations, pH values in the solutions in equilibrium with the M-S-H synthesized 2 years at 20°C.

Initial NaOH (mmol/l)	Brucite	Amorphous silica	Na	Mg	Si	pH (20°C)
			mmol/l			
3		traces	0.38	0.39	1.44	8.3
10			2.07	0.25	0.58	9.9
25			8.06	7.64	5.17	10.2
50			19.03	9.60	5.83	11.8
100			61.75	9.89	10.56	12.5
250	traces		198.29	0.06	21.23	13.0
500	traces		449.87	0.001	34.86	13.3

The data presented above showed that at high pH values, i.e. in sodium hydroxide solutions, sodium is present in the vicinity of the tetrahedral silicates and more defects are present in the silicate sheets; an effect which was hardly observed in $NaNO_3$ solutions.

5.2.1.2. Surface properties

The measurement of the cation exchange capacity (CEC) on the samples synthesized in 10 and 100 mmol/l sodium nitrate or sodium hydroxide solution are shown in Figure 90.

In agreement with the observations by ^{29}Si MAS NMR spectroscopy and the solution analysis, the CEC showed the progressive replacement of magnesium at the surface by sodium. As expected in $NaNO_3$ solution, a CEC of 31 meq/100g 30 meq/100g and 34 meq/100g was measured in the 10, 50,and 100 mmol/l $NaNO_3$ samples, respectively, similar to the 35 meq/100g of pure M-S-H (chapter 3.3) (Figure 90a). At 10 mmol/l where 1 mmol/l magnesium and 9 mmol/l sodium were present, 20 meq/100g of magnesium and 10 meq/100g of sodium were found on the cation exchange sites indicating a higher preference for the bivalent magnesium than the monovalent sodium (Skluzacek et al., 2006; Bruzzoniti et al., 2009; de Lara et al., 2015). At higher sodium concentration, most of the cation exchange sites are occupied by sodium due to its very large concentration compared to magnesium.

The total CEC of the 10 mmol/l NaOH sample increased slightly to 41 meq/100g, while the CEC in 100 mmol/l NaOH was measured at 170 meq/100g (Figure 90b). The high CEC measured in 0.1NaOH sample confirmed a high content of cations sorbed.

The 10 mmol/l NaOH sample contained more exchangeable sodium than magnesium which might be due to the lower magnesium concentration (0.25 mmol/l compared to 1.3 mmol/l in the 0.01$NaNO_3$ sample). In 100 mmol/l NaOH where more sodium was present most of the magnesium at the surface was replaced by sodium (Figure 90b).

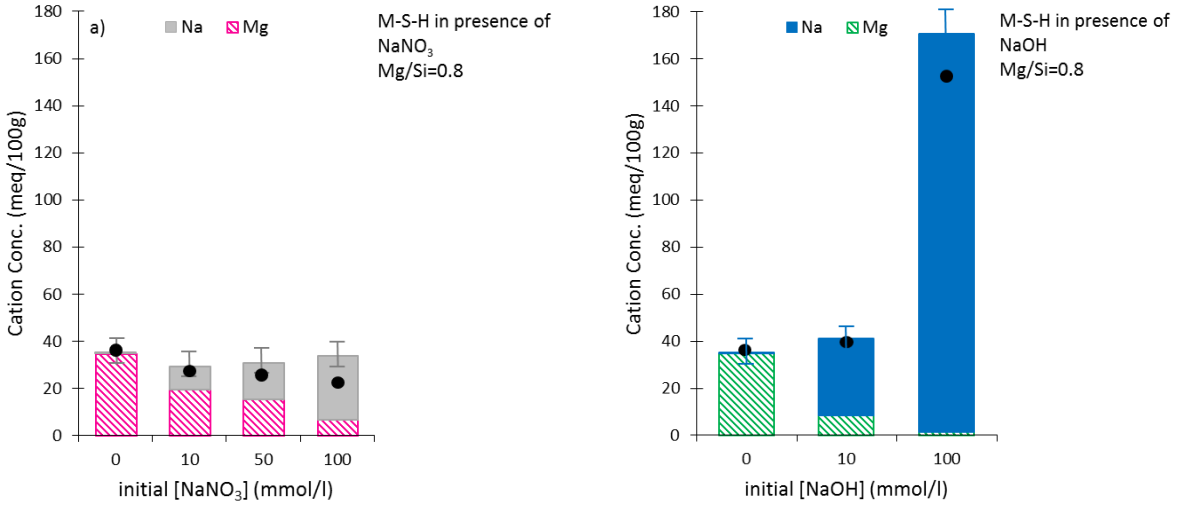

Figure 90: Concentrations of the cations sorbed on M-S-H samples synthesized in the presence of alkalis (1 or 2 years at 20°C) measured by the cobalt hexamine method as a function of the initial concentration added. CEC measurements by colorimetry (black circles) have been added for comparison.

The zeta potentials of M-S-H 0.8 samples synthesized in sodium nitrate or sodium hydroxide are plotted versus the pH measured in suspension in Figure 91. The increase of the sodium nitrate or sodium hydroxide increases the ionic strength which compresses the electric double layer and results in the measurement of a less negative zeta potential in our case. Thus the zeta potential was measured only in the suspension were the initial sodium concentration was lower or equal to 50 mmol/l.

Similarly to the pure M-S-H, the effective charge of M-S-H samples in sodium nitrate was negative with zeta potential values of -19 ± 2 mV. The observed relatively constant values are consistent with a relatively constant pH and a similar content of Q^1 and Q^2 sites in the silicate layers. The negative effective charge similar to M-S-H confirms the small sodium adsorption upon high sodium nitrate addition.

The sample with 10 mmol/l of sodium hydroxide showed a drop of zeta potential value close to -60 ± 6 mV due to the increase of pH and thus, the deprotonation of the silanol groups. At higher sodium hydroxide concentrations the zeta potentials re-increased up to around -20 ± 5 mV although the pH was even higher, 10.2 and 11.8 for 25 and 50 mmol/l NaOH.

The ^{29}Si MAS NMR spectroscopy has shown a higher content of Q^1 and Q^2 tetrahedral silicate sites in the presence of sodium hydroxide, which are deprotonated at high pH values resulting in a decrease of the surface charge, as had been visible in the measured increase of the cation exchange sites at higher pH values (Figure 90). The measured zeta potential, which reproduces the potential at some distance to the surface, is thus the result of several opposing effects; lowered by the higher negative surface charge at high pH values, increased by the stronger attraction of cations to the negative surface and by the higher ionic strength. These competing effects make the result difficult to interpret in contrast to the results of the CEC measurements.

However, combined the CEC results and the zeta potential data indicates that the little exchangeable cations, found in the 10 mmol/l NaOH sample, did not compensate the negative charge of the silicate sites.

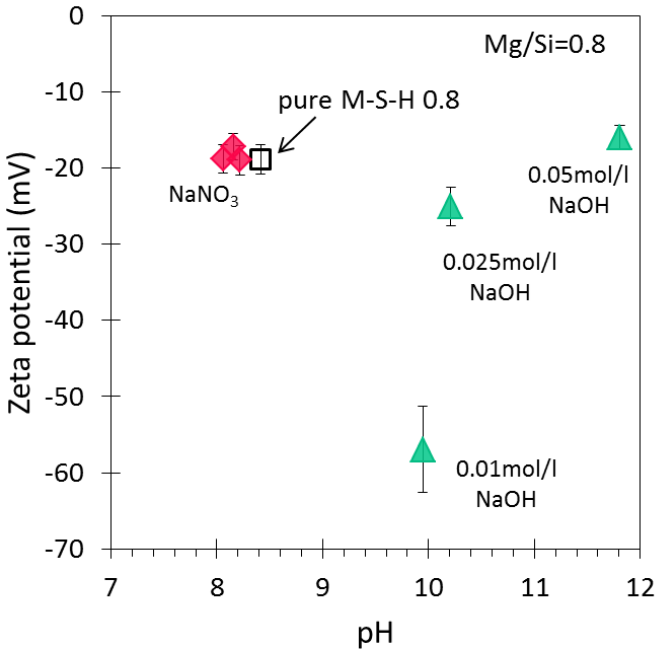

Figure 91: Zeta potential of M-S-H 0.8 samples synthesized in sodium nitrate and sodium hydroxide solutions versus the pH measured in the suspensions.

5.2.1.3. Alkali uptakes

The alkali uptake obtained in the presence of NaOH and $NaNO_3$ is compared to the alkali uptake measured on M-S-H (Mg/Si=0.8, 1.0) synthesized in LiOH or KOH solutions.

The uptake of alkali can be obtained by different methods: 1) the indirect method based on massbalance, where the alkalis in solution after the filtration are subtracted from the initial alkali content, 2) the direct method, where a part of the solid, after washing, is completely re-dissolved 3) the CEC method, where the concentration of the ions exchanged by cobalt is used. In all the methods, the alkalis in the diffuse layer are treated as part of the solid. The washing (Milli-Q/ethanol and ethanol) applied before the direct and the CEC method could potentially lead to an underestimation of the alkali content as the washing might have eliminated some of the cations as detailed in (L'Hôpital et al., 2016b). The direct and indirect method will include cations present in the main layer as well as on the surface, while the CEC method will only include the cations at surface. At low concentrations (≤100 mmol/l sample)and when the uptake is significant, the three methods give comparable results, indicating that the indirect method is sufficiently precise (Appendix M) and that the washing is not an issue and that the alkalis are mainly present at the surface and no/or very little in the octahedral main layer. At higher concentrations, the indirect method can be associated with a large relative error due to the uncertainty of the solution measurement.

In the presence of $NaNO_3$, the error of the indirect method was too large to capture the low small sodium uptake; the alkali uptakes were obtained from the direct method as reported in Figure 92. The content of sodium in the solid is low, and Na/Si increased only very moderately from 0 to 0.04. In the presence of hydroxide and high pH values, the Na/Si, K/Si, and Li/Si increased much more strongly with the additions. The maximum alkali/Si observed was in the range 0.2 (at 100 mmol/l) and did not depend on the Mg/Si or on the kind of alkali (Na, K, Li). These alkali uptake results confirmed the finding from ^{29}Si MAS NMR and the CEC data.

The CEC data gave similar Na_{exch}/Si as observed by the direct and indirect method as reported in Figure 92, which indicates that sodium is present in M-S-H only at the surface sites. Although the CEC does not allow distinguishing clearly between specifically sorbed cations at the surface and charge balancing cations present in the diffuse layer, the comparable uptake of Na, K and Li tends to indicate that the alkali ions are mainly present as exchangeable cations in the Stern and diffuse layers. The presence of more physically bound water measured by TGA in the presence of sodium hydroxide is linked to the increased sodium sorption onto M-S-H as already observed in clay materials as sodium is associated with 4 water molecules in a first hydration shell.

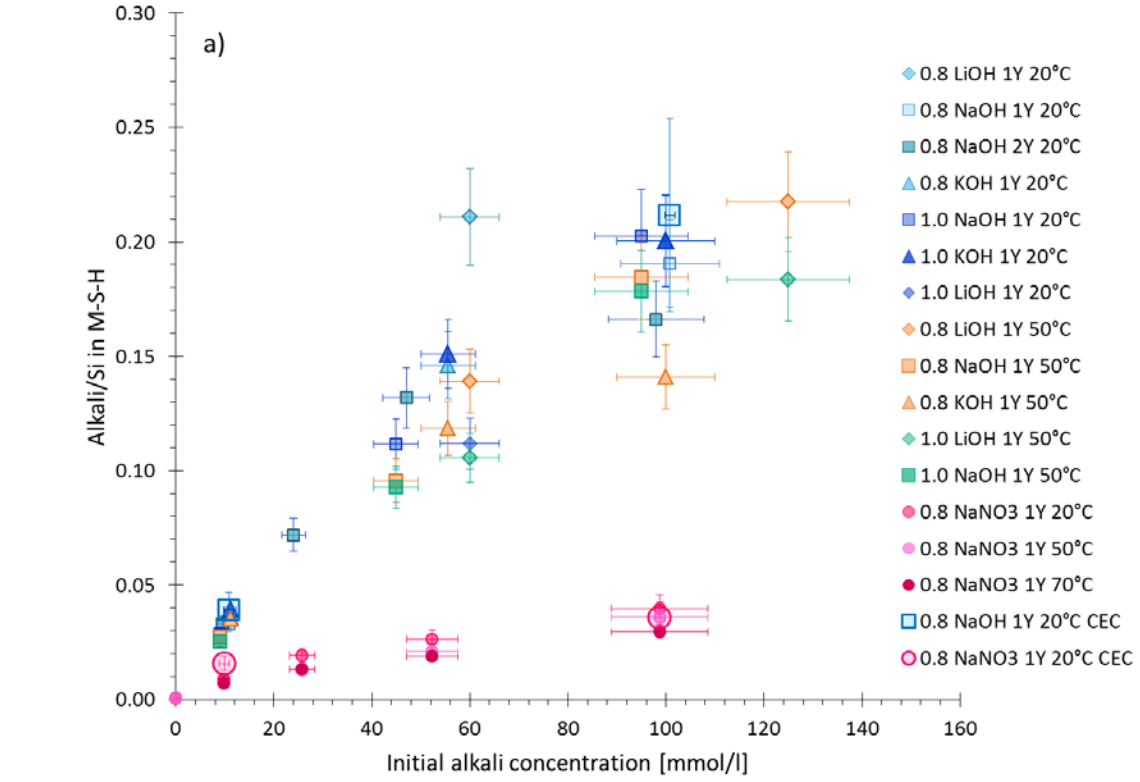
a)
Alkali/Si in M-S-H
Initial alkali concentration [mmol/l]
0.8 LiOH 1Y 20°C
0.8 NaOH 1Y 20°C
0.8 NaOH 2Y 20°C
0.8 KOH 1Y 20°C
1.0 NaOH 1Y 20°C
1.0 KOH 1Y 20°C
1.0 LiOH 1Y 20°C
0.8 LiOH 1Y 50°C
0.8 NaOH 1Y 50°C
0.8 KOH 1Y 50°C
1.0 LiOH 1Y 50°C
1.0 NaOH 1Y 50°C
0.8 NaNO3 1Y 20°C
0.8 NaNO3 1Y 50°C
0.8 NaNO3 1Y 70°C
0.8 NaOH 1Y 20°C CEC
0.8 NaNO3 1Y 20°C CEC

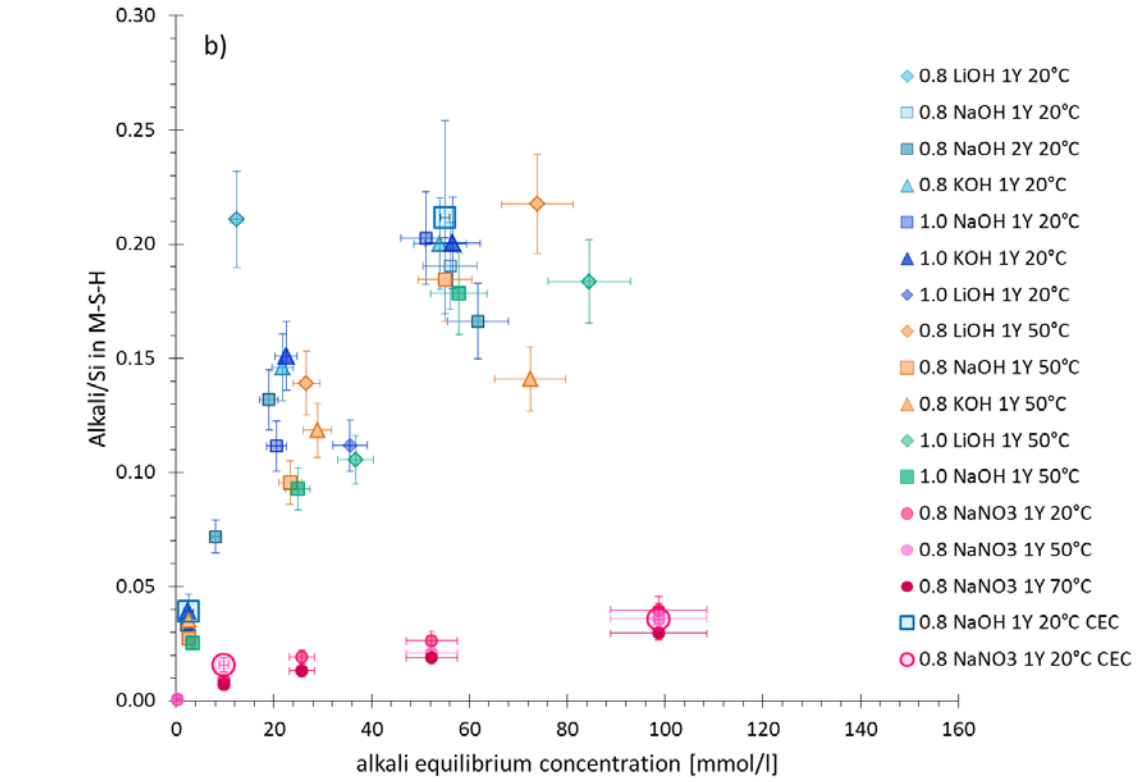
b)
Alkali/Si in M-S-H
alkali equilibrium concentration [mmol/l]
0.8 LiOH 1Y 20°C
0.8 NaOH 1Y 20°C
0.8 NaOH 2Y 20°C
0.8 KOH 1Y 20°C
1.0 NaOH 1Y 20°C
1.0 KOH 1Y 20°C
1.0 LiOH 1Y 20°C
0.8 LiOH 1Y 50°C
0.8 NaOH 1Y 50°C
0.8 KOH 1Y 50°C
1.0 LiOH 1Y 50°C
1.0 NaOH 1Y 50°C
0.8 NaNO3 1Y 20°C
0.8 NaNO3 1Y 50°C
0.8 NaNO3 1Y 70°C
0.8 NaOH 1Y 20°C CEC
0.8 NaNO3 1Y 20°C CEC

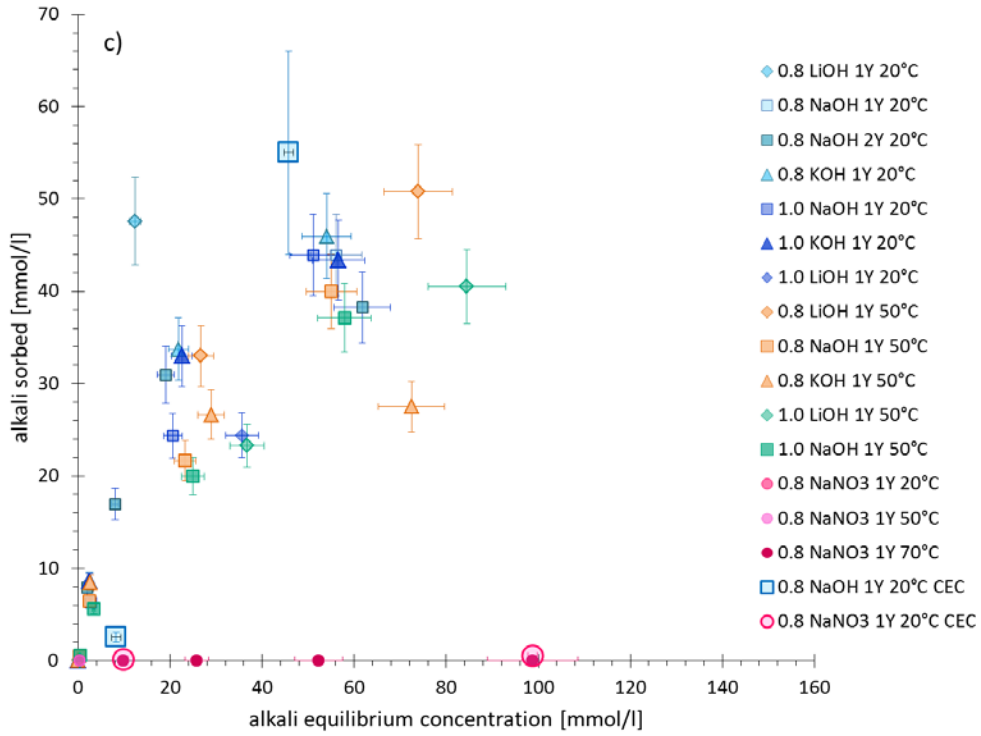

Figure 92: Alkalis uptake in M-S-H (Mg/Si=0.8 and Mg/Si=1.0) as a function of a) the initial alkali concentration (measured); b) the alkali concentration at equilibrium (measured) c) sorption isotherms, the results for LiOH, NaOH, KOH were calculated from mass balance (indirect method), the results for $NaNO_3$ were calculated from dissolution (direct method).

5.2.2. Conclusions

A very limited sodium uptake was observed in the presence of sodium nitrate at pH values ranging 7 to 8. The uptake of sodium was much more significant in the presence of sodium hydroxide, which increased the pH of the solution strongly, than in the presence of $NaNO_3$. The ^{29}Si MAS NMR data showed a higher content of Q^1 and Q^2 tetrahedral silicate sites in the presence of alkali hydroxide solution. The silanol sites are deprotonated at high pH values, which leads to an increased alkali binding on M-S-H as also visible in the increased cation exchange sites at higher pH. The alkali uptake was observed to be influenced by the pH and dissolved alkali concentrations. The molar Na/Si ratio in M-S-H raised from 0.03 in 10 mmol/l NaOH to ~0.2 in 100 mmol/l NaOH. A comparable uptake as for NaOH was observed for KOH and LiOH. The alkalis are present as exchangeable cations in the interlayer or at the surface of M-S-H.

It might be speculated the alkali uptake will be similar at high Mg/Si as the CEC and zeta potential measured hardly vary with the Mg/Si as the concentration of magnesium remain low also at a high Mg/Si (chapter 3 and 4), which limits the competition of dissolved magnesium with alkali sorption. However, calcium, a divalent cation, present in higher concentration than magnesium, is preferentially bound on the surface of M-S-H as observed in chapter 4.3.

The formation of M-S-H phases with Mg/Si ≤1 up to pH values of 12.5 was observed without that brucite which confirms the possible formation of M-S-H at high pH values as suggested from the addition of MgO to C-S-H.

5.3. Incorporation of aluminum in M-S-H

In this study, magnesium silicate hydrate with aluminum, M-A-S-H phases, were synthesized in batch experiments at different temperatures (20, 50 and 70°C), at Mg/Si = 1.1 and 1.7 and varying Al/Si ratios. M-A-S-H samples with Mg/Si=0.8 and 1.2 were also synthesized in the presence of sodium nitrate; the syntheses are described in 2.1.4. The aqueous phase was analyzed by ion chromatography and pH measurements and the solid phase by thermogravimetric analysis, X-ray diffraction, and FT-infrared, ^{29}Si and ^{27}Al MAS NMR spectroscopy. Surface properties were determined by measurement of zeta potential and cation exchange capacity. The analytical techniques used are detailed in 2.2.

5.3.1. Results and discussions

5.3.1.1. Influence of the amount of aluminum

The effect of varying amounts of aluminum (Al/Si 0.05 to 0.20) was investigated using metakaolin at Mg/Si =1.1 and 1.7 to study aluminum uptake at high and low Mg/Si.

5.3.1.1.1. M-A-S-H 1.1

To mimic the relatively high pH above 9 observed at the interface between cement and clays (Jenni et al., 2014; Dauzères et al., 2016) and to avoid the presence of unreacted silica or brucite, an intermediate Mg/Si of ~1.1 varying amounts of aluminum (Al/Si 0.05 to 0.20) was investigated.

The addition of small amount of metakaolin ($Al_2O_3{\cdot}2SiO_2$) to magnesium oxide (MgO) and silica fume (SiO_2) led in the samples M-A-S-H 1.1 to the formation of M-(A-)S-H as the main product, i.e., magnesium (alumino) silicate hydrate. After 2 years of equilibration at room temperature, little difference was observed between the TGA curves, XRD patterns, FTIR and ^{29}Si MAS NMR spectra of pure M-S-H and M-(A-)S-H samples (Al/Si equal to 0, 0.05, 0.10 and 0.15) as partially shown in Figure 93 and Figure 94 for Al/Si=0 and 0.10.

The XRD pattern (Figure 93a) of the M-A-S-H 1.1 sample was comparable to the pattern of pure M-S-H and showed a similar poor crystallinity or nanocrystallinity as M-S-H with broad X-rays humps at 19.7, 26.7, 35.0, and 59.9 °2θ (λ=1.54Å) (Nied et al., 2016), although in the presence of aluminium the signals showed a slightly higher intensity which indicates tentatively a better ordering of the M-A-S-H samples than M-S-H. In the M-A-S-H 1.1 sample in addition to M-A-S-H also the presence of a small amount of unreacted quartz and anatase from the metakaolin used (Figure 3, chapter 2) was observed.

TGA analysis (Figure 93b) of M-A-S-H 1.1 sample revealed the presence of physically bound water (weight loss 30-250°C) and structurally bound water i.e. the hydroxyl groups (250-800°C) (Mitsuda and Taguchi, 1977; Zhang et al., 2011; Nied et al., 2016) comparable to M-S-H.

The FTIR data (Figure 94a) indicated that the silicate networks in the M-A-S-H 1.1 was comparable to M-S-H. The bands centered at ~ 990-1000 cm^{-1} and ~ 870-880 cm^{-1} correspond to vibrations of Q^3 and Q^2 of silica as also characteristic for pure M-S-H (Nied et al., 2016). The ^{29}Si MAS NMR spectroscopy shown in Figure 94b confirmed that M-A-S-H had a comparable silica layer structure as M-S-H with Q^2 signal at approx. -85 ppm and Q^3 signals between -92 and -97 ppm.

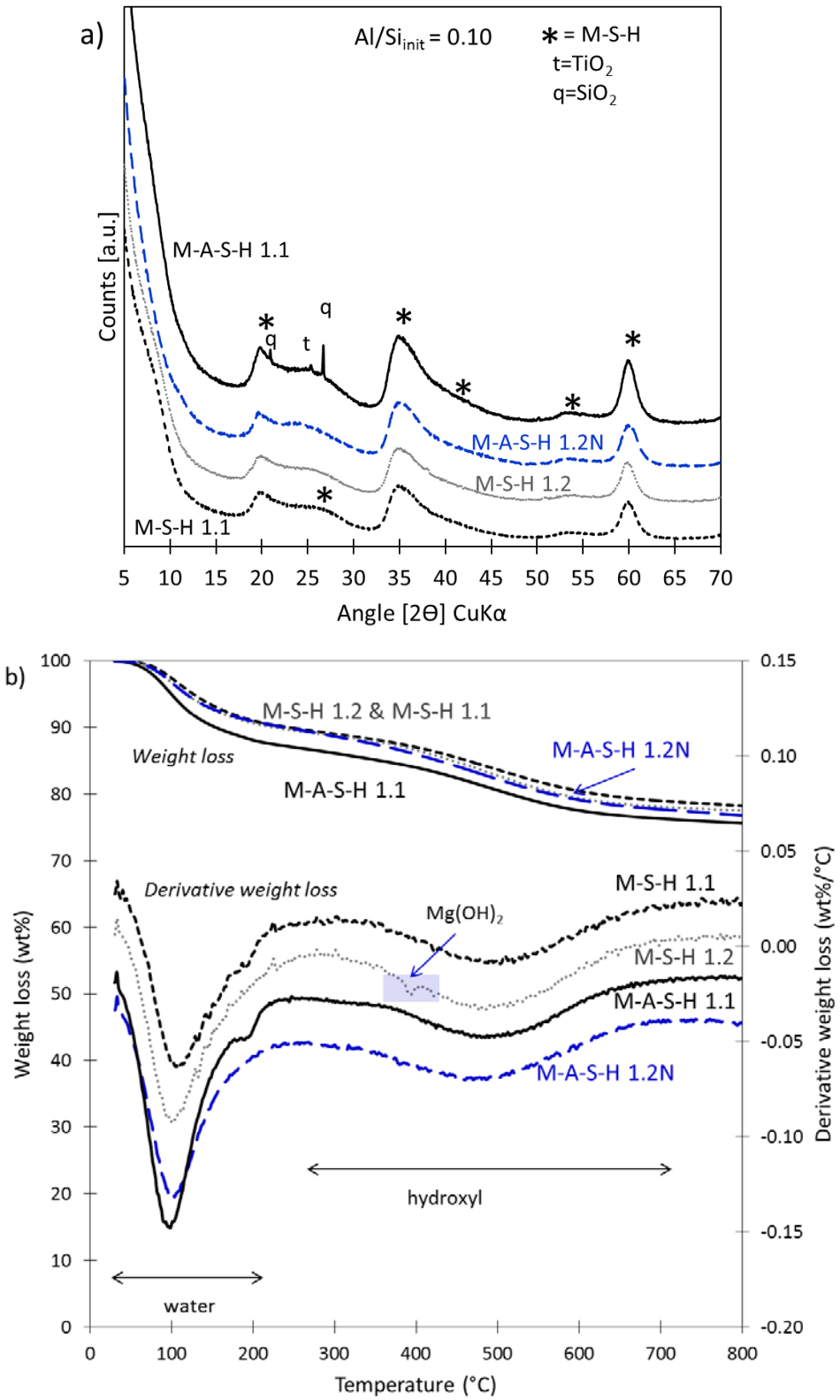

Figure 93: a) XRD patterns and b) TGA of the samples from M-A-S-H and M-A-S-H N with initial Mg/Si=1.1-1-2 and Al/Si = 0.1 cured 1 year at 50°C.

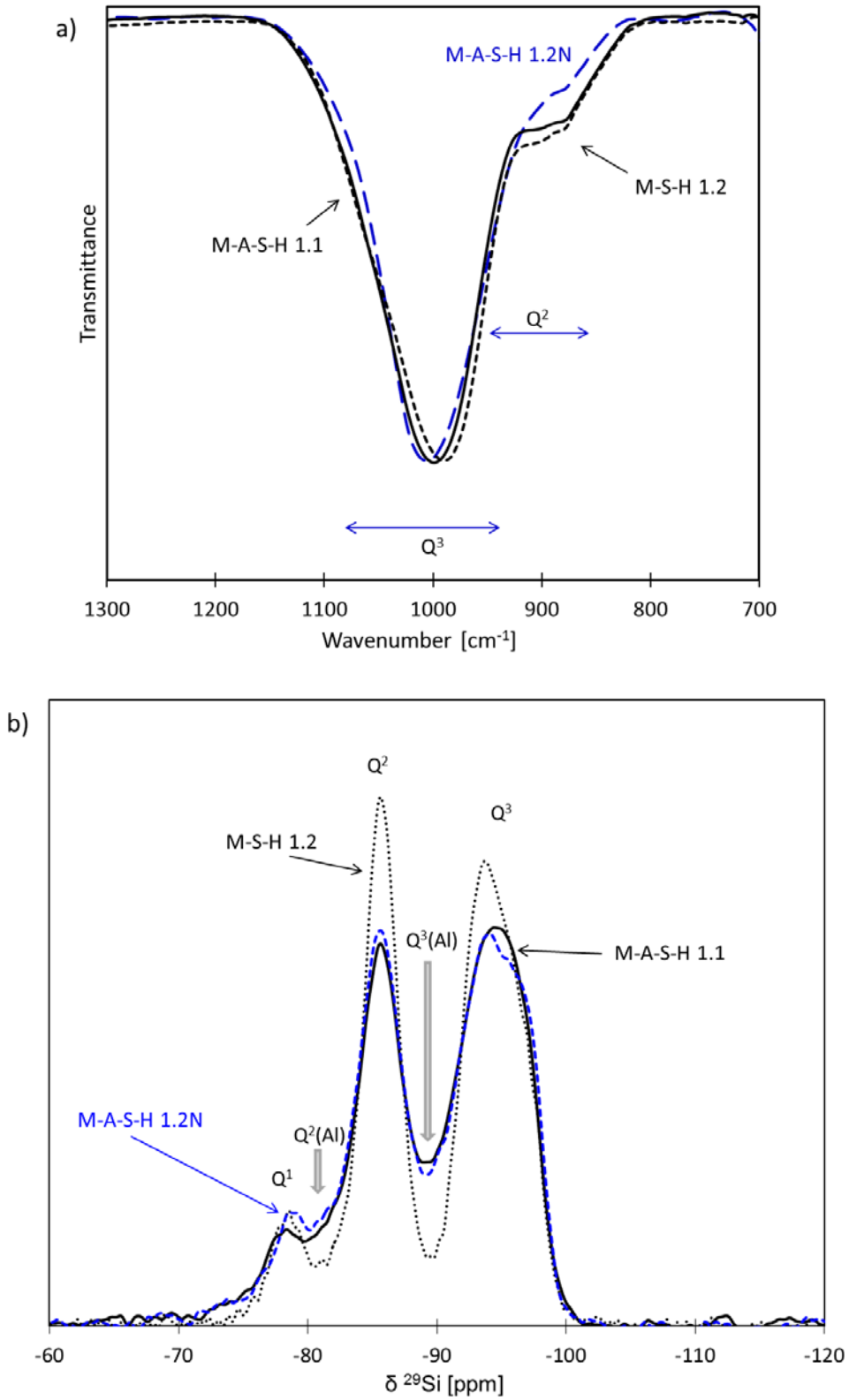

Figure 94: a) FTIR and b) ^{29}Si MAS NMR spectra of the samples from M-A-S-H and M-A-S-H N with initial Mg/Si=1.1-1-2 and Al/Si = 0.1 cured 1 year at 50°C.

No brucite, aluminum hydroxide, hydrotalcite or amorphous silica was detected at Al/Si=0.05, 0.10, 0.15 samples, as summarized in Table 34.

Only in the M-A-S-H 1.1 sample synthesized at room temperature with the highest addition of aluminum (Al/Si=0.2), ^{29}Si MAS NMR showed traces of unreacted silica and TGA and XRD a small amount of brucite. However, the analog samples equilibrated at 50 (Figure 95) and 70°C (Table 34) contained only M-A-S-H, no silica, brucite nor hydrotalcite. This indicates that the samples at 20°C were not completely at equilibrium even after 2 years of equilibration, similar to the observations for pure M-S-H (chapter 3), while the faster kinetic at 50°C and 70°C allowed the complete reaction of silica and brucite. Thus, all samples with Al/Si from 0 to 0.20 contained only M-(A-)S-H at 20, 50 and 70°C, excepted M-A-S-H 1.1 with Al/Si=0.2 at 20°C, where brucite and silica had not yet reacted completely.

Table 34: Summary of the presence of hydrotalcite, brucite and unreacted silica in the solid composition, the measured dissolved concentrations, pH values in the solutions in equilibrium with the M-A-S-H (errors: calculated Mg/Si±0.1, Al/Si±0.03, brucite ±2 wt%, pH ±0.1, concentrations: ±10%).

	initial Mg/Si - Al/Si	calculated Mg/Si - Al/Si	Age (y)	Hydrotal.	Brucite	Unreacted silica	pH (20°C)	[Mg] mmol/l	[Si]	[Al]
20°C	1.1	*1.1*	*1*				*9.9*	*0.13*	*0.004*	---
		1.1	*2*				9.8	0.15	0.008	---
	1.1 - 0.05	*1.1-0.05*	*1*				*9.9*	*0.29*	*0.01*	*<0.0001*
		1.1-0.05	*2*				9.8	0.35	0.01	0.0005
	1.1- 0.10	*1.1 - 0.10*	*1*				*10.0*	*0.18*	*0.01*	*<0.0001*
		1.1 - 0.10	*2*				9.8	0.41	0.01	0.0002
	1.1- 0.15	*1.1-0.15*	*1*		✓		*10.0*	*0.37*	*0.02*	*<0.0001*
		1.1- 0.15	*2*				9.9	0.27	0.01	0.0003
	1.1- 0.20	*n.d.*	*1*		✓	✓	*9.5*	*0.02*	*0.29*	*0.0031*
		1.2-0.22	*2*		✓	✓	9.5	0.60	0.30	0.0005
	1.6	*1.4*	*1*		✓		*10.5*	*0.12*	*0.003*	---
		1.4	*2*		✓		10.5	0.12	0.001	---
	1.7 - 0.05	*1.4-0.05*	*1*		✓		*10.4*	*0.09*	*0.003*	*0.0007*
		1.4-0.05	*2*		✓ *(20wt%)*		10.5	0.20	0.002	0.0004
	1.7 - 0.10	*1.4-0.10*	*1*		✓		*10.5*	*0.07*	*0.005*	*0.0007*
		1.4-0.10	*2*		✓ *(20wt%)*		10.5	0.18	0.002	0.0004
	1.7 - 0.15	*1.4-0.15*	*1*		✓		*10.3*	*0.13*	*0.013*	*0.0017*

		1.4-0.15	*2*		*✓ (20wt%)*		10.5	0.11	0.003	0.0005
	1.7 - 0.20	*n.d.*	*1*		*✓*	*✓*	*9.6*	*0.12*	*0.384*	*0.0117*
		1.1-0.20	*2*		*✓ (20wt%)*		10.1	0.29	0.038	0.0005
50°C	1.1	1.1	1			✓	9.3	0.43	0.04	---
	1.1 - 0.05	1.1-0.05	1				9.3	0.36	0.01	<0.0001
	1.1 - 0.10	1.1 - 0.10	1				9.4	0.22	0.02	<0.0001
	1.1 - 0.15	1.1 - 0.15	1				9.4	0.20	0.02	<0.0001
	1.1 - 0.20	1.1 - 0.20	1				9.4	0.15	0.04	<0.0001
	1.6	1.4	1		✓		10.3	0.17	0.002	---
	1.7 - 0.05	1.5-0.05	1		*✓ (20wt%)*		10.3	0.17	0.001	<0.0001
	1.7 - 0.10	1.5-0.10	1		*✓ (20wt%)*		10.4	0.09	0.001	<0.0001
	1.7 - 0.15	1.5-0.15	1	✓	*✓ (20wt%)*		10.4	0.06	0.001	<0.0001
	1.7 - 0.20	1.5-0.20	1	✓	*✓ (20wt%)*		10.5	0.03	0.001	<0.0001
70°C	1.1	1.1	1			✓	9.2	0.29	0.005	---
	1.1 - 0.05	1.1-0.05	1				9.4	0.30	0.02	<0.0001
	1.1 - 0.10	1.1 - 0.10	1				9.4	0.29	0.02	<0.0001
	1.1 - 0.15	1.1 - 0.15	1	✓			9.3	0.25	0.02	<0.0001
	1.1 - 0.20	1.1 - 0.20	1	✓			9.5	0.20	0.02	<0.0001
	1.6	1.4	1				10.2	0.23	0.001	---
	1.7 - 0.05	1.4-0.05	1		*✓ (21wt%)*		10.3	0.21	0.001	<0.0001
	1.7 - 0.10	1.5-0.10	1		*✓ (21wt%)*		10.4	0.14	0.001	<0.0001
	1.7 - 0.15	1.5-0.15	1	✓?	*✓ (22wt%)*		10.4	0.10	0.001	<0.0001
	1.7 - 0.20	1.5-0.20	1	✓?	*✓ (23wt%)*		10.5	0.07	0.001	<0.0001

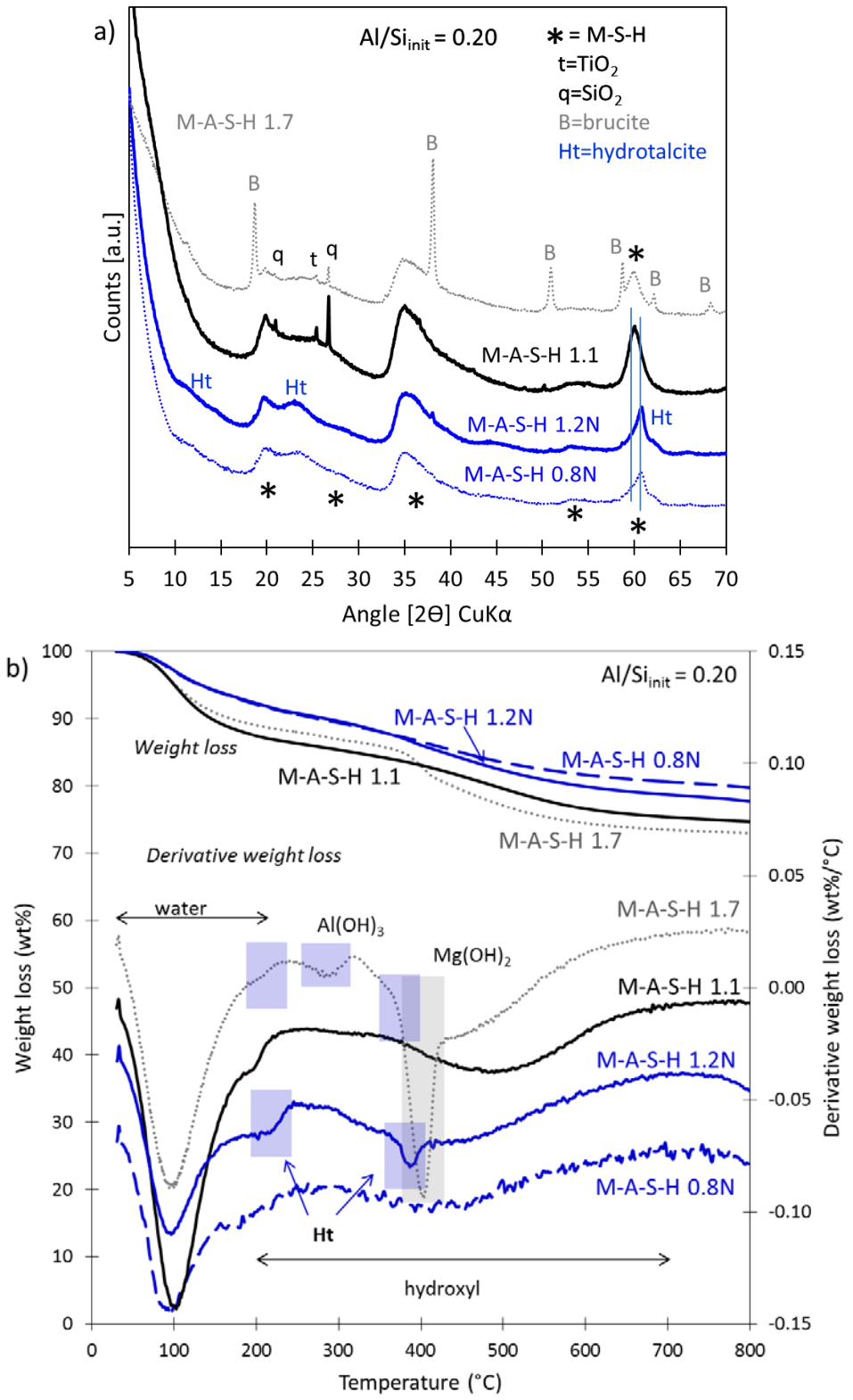

Figure 95: a) XRD patterns and b) TGA curves and derivatives associated with M-A-S-H samples with initial Al/Si = 0.20 cured 1 year at 50°C.

The presence of M-(A-)S-H phase only, indicates a gradual uptake of aluminum. The ^{29}Si MAS NMR spectra of the M-A-S-H 1.1 samples (Figure 96) showed, in fact, some small differences indicating changes in the structure of the silicate layers. In the presence of aluminum, the resonances were broadened (Figure 96) and two additional bands at ~ -82 and -91 ppm occurred. The presence of aluminum induces a less negative chemical shift than silicon (Sanz and Serratosa, 1984; Komarneni et al., 1986). Hence, the first one was attributed to Q^2(Al), i.e., silicate with one aluminate and one silicate neighbor, and the second one to the Q^3(Al) tetrahedral silicate, i.e., silicate with one aluminate and two silicate neighbors. The comparison with ^{29}Si MAS NMR spectrum of saponite (Appendix O) confirmed the assignment of the band ~ -91 ppm to Q^3(Al) tetrahedral silicate sites (Li et al., 1993). The chemical shift of silicate is mainly affected by changes in the adjacent tetrahedral silicate layer (and only weakly by replacement in the octahedral magnesium layer (Mägi et al., 1984; Sanz and Serratosa, 1984)) such that the observed shifts indicate an uptake of aluminum in the silicate sheets.

The intensity increase of the band at ~ -91 ppm and the decrease of the Q^3 signal between -93 and -97 ppm shows qualitatively that the content of silicate next to aluminum increased in the presence of more aluminum.

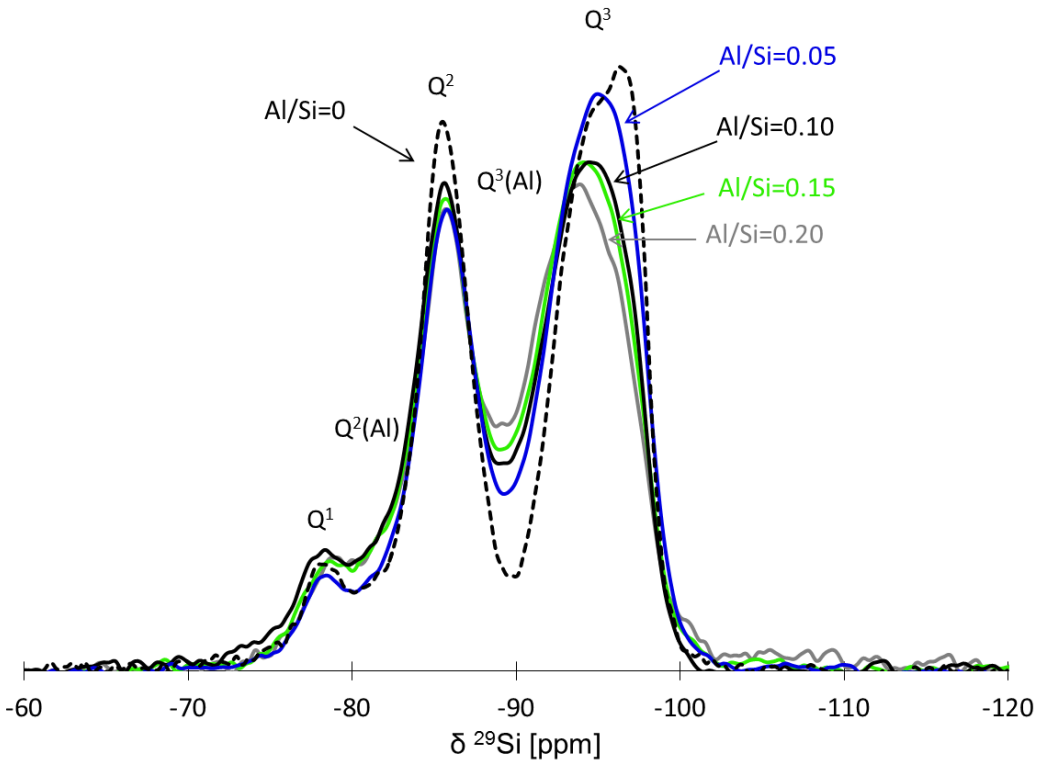

Figure 96: ^{29}Si MAS NMR spectra of the M-(A-)S-H samples, Mg/Si=1.1 and Al/Si=0.05-0.20 compared to M-S-H 1.0.

^{27}Al MAS NMR spectra of M-A-S-H 1.1 with different Al-contents are presented, together with the spectra recorded for the raw metakaolin used for the synthesis, in Figure 97. The spectra indicated that the metakaolin reacted completely or nearly completely (< 5% MK). The ^{27}Al MAS NMR data of M-A-S-H showed mainly the presence of IV- and VI-fold coordinated aluminum in the M-A-S-H. Comparison with literature attributed the first signal between 0 to 20 ppm to octahedrally coordinated Al(VI) environment (Sanz and Serratosa, 1984; Lippmaa et al., 1986). The signal could be divided into two Al(VI) signals, a signal centered at ~9 ppm which seemed symmetric and a large asymmetric signal at about ~5 ppm. The broad asymmetric shoulder at ~5 ppm is related to poor ordering of the layers (Bisio et al., 2008; Costenaro et al., 2012). The Al(VI) band in clay mineral is usually between 0 and 10 ppm depending on the structure of the octahedral sheet. in dioctahedral minerals, where only 2 out of 3 sites are occupied Al(VI) is close to 0 ppm while in trioctahedral phyllosilicates, where all octahedral positions are filled, Al(VI) appears at 5-10 ppm (Sanz and Serratosa, 1984). In hydrotalcite-like phases, a symmetric Al(VI) signal centered at ~ 9-11 ppm ((Hibino and Tsunashima, 1998)) and for poorly ordered aluminum hydroxide an asymmetric signal at around 11 ppm is observed as shown in Appendix Q.

The comparable chemical shifts of the Al(VI) in trioctahedral phyllosilicates and hydrotalcite is consistent with the aluminum neighboring magnesium in the octahedral layers and confirms that the shift of Al(VI) is mainly affected by the first neighbors in the octahedral sheets (Sanz and Serratosa, 1984). TGA and XRD data indicated neither hydrotalcite nor aluminum hydroxide presence and the solutions were undersaturated with respect to both solids as discussed below, making the presence of hydrotalcite or aluminum hydroxide little probable. The observed chemical shift of the Al(VI) at ~ 9 ppm indicates that aluminum in octahedral sites is present mainly in a trioctahedral environment such as in the case of vermiculite, although some defects in the octahedral sheets may occur as pointed out by the shoulder at ~ 5 ppm.

A further broad signal at approximatively 62 ppm confirmed the presence of tetrahedrally coordinated Al(IV), as e.g. in saponite ((Bisio et al., 2008) &Appendix P). The Al(IV) signal was visible as a broad asymmetric signal in the M-A-S-H phases. The broad signal could again indicate the presence of two tetrahedral sites and/or poorly ordered aluminum sites in the tetrahedral layers (Bisio et al., 2008). A minor amount of Al(V) at ~35 ppm was also observed. The deconvolution of the ^{27}Al NMR was carried out using two octahedral and two tetrahedral sites to only approximatively estimate the distribution of aluminum between Al(VI) and Al(IV),

while Al(V) at ~35 ppm was neglected. The positions of the single sites are only estimated. The calculated Al(VI)/Al(IV) ratios are detailed in Table 35.

The ^{27}Al MAS NMR spectra of the M-A-S-H 1.1 showed similar repartition of the aluminum in the samples; in each sample, approximately 50% of the aluminum was in Al(IV) sites, another 50% in Al(VI) sites. This approximate 50-50% distribution of the aluminum in the M-A-S-H 1.1 indicates a comparable uptake of aluminum in the octahedral magnesium and tetrahedral silicate layer and would thus imply no or only minor changes in the surface charge compared to pure M-S-H.

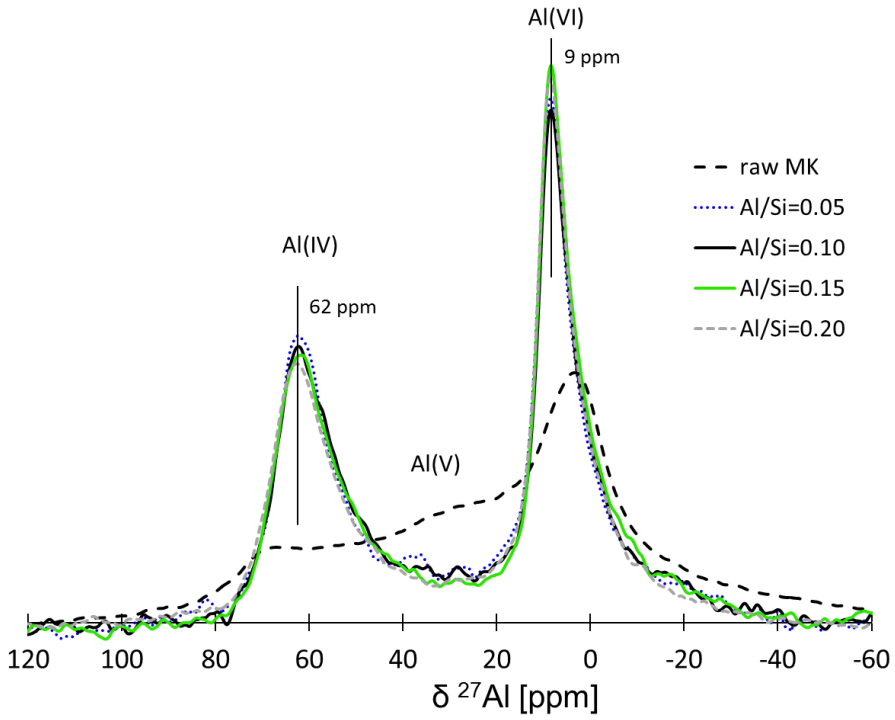

Figure 97: ^{27}Al MAS NMR spectra of the M-A-S-H samples, Mg/Si=1.1 and Al/Si=0.05-0.20, equilibrated for 2 years at 20°C compared to the raw metakaolin (MK).

Table 35: Percentages attributed to the Al (IV) and Al(VI) sites in the ^{27}Al MAS NMR spectra of the M-A-S-H samples synthesized at 50°C (error ± 10%).

	Al(IV)a	Al(IV)b	Al(VI)	Al(VI)	
	antisym	antisym	symmetric	antisym	Al(VI)/Al(IV)
ppm	69	64	9	5	
1.1-0.1	14	33	35	18	~1
1.7-0.1	14	14	52	20	~2.5

The composition of the solutions at equilibrium with the M-A-S-H samples is detailed in Table 34. At 20°C, a pH value of 9.8 and magnesium and silicon concentrations of 0.15 mmol/l and 0.008 mmol/l, respectively, were measured. In the presence of metakaolin, pH values remained in the range from 9.8 to 10.0 and silicon concentrations between 0.01 to 0.02 mmol/l with the exception of the sample with the highest metakaolin dosage (Al/Si = 0.2), where the presence of unreacted silica indicated that equilibrium had not yet been reached. The magnesium concentrations fluctuated between 0.15 and 0.41 mmol/l. Similarly, the results for the samples equilibrated at 50 and 70°C showed comparable trends. The addition of metakaolin had no significant effect on the pH values, magnesium, and silicon concentrations, and the aluminum concentrations were near or below the detection limit of 0.0001 mmol/l, confirming that the aluminum from metakaolin was precipitated in a solid phase.

Saturation indices (SI) were calculated from the measured concentrations and pH values in the pore solution and compiled in Table 36. The SI showed that the solutions at 20°C were undersaturated with respect to amorphous silica and brucite, in agreement with the absence of these phases (except the sample with the highest aluminum content, where only a moderate undersaturation with respect to silica was observed). The solutions with aluminum were slightly oversaturated with respect to M-S-H indicating that the uptake of aluminum in M-S-H had some effect on its solubility. Some aluminum concentrations were below the detection limit, such that only maximum SI could be calculated for Al-containing solids (using the detection limit of 0.0001 mmol/l as maximum aluminum concentration). In all cases, the solutions were undersaturated with respect to microcrystalline aluminum hydroxide and hydrotalcite, again in agreement with the analysis of the solid phases. The solutions were calculated oversaturated with respect to crystalline saponite (which was used as a proxy for M-A-S-H phases in the calculations). The measured concentrations were also used to calculate ion activity products (IAP) for two possible aluminum containing end-members, resulting in log IAP = -19.2 ± 0.2 for $M_{0.76}A_{0.20}SH$ from the samples with low Mg/Si and in log IAP = -29.1 ± 0.4 for $M_{1.50}A_{0.20}SH$ from the samples with high Mg/Si.

Table 36: Calculated saturation indices of the M-A-S-H calculated from the measured concentrations (Table 34) and the thermodynamic data given in Table 8. Solid phases observed experimentally are marked as bold.

	initial Mg/Si & Al/Si	saturation indices						log IAP	
		Brucite	MSH-SS	Amor SiO_2	$Al(OH)_3$ micro	Ht 2:1	Saponite[a]	$M_{0.76}A_{0.2}SH_{1.5}$	$M_{1.5}A_{0.2}SH_2$
20°C	1.1 - 0	-1.5	**-0.8**	-2.8					
		-1.6	**-0.5**	-2.4					
	1.1 - 0.05	-1.1	**0.4**	-2.4	<-2.1	<-5.0	>9.8		
		-1.1	**0.4**	-2.4	-1.4	-3.3	10.0	**-19.2**	-29.3
	1.1 - 0.10	-1.2	**0.5**	-2.3	<-2.2	<-5.0	>9.9		
		-1.1	**0.6**	-2.3	-1.7	-4.0	10.2	**-19.2**	-29.3
	1.1 - 0.15	-0.8	**1.6**	-2.1	<-2.2	<-9.3	>11.9		
		-1.2	**0.4**	-2.4	-1.6	-3.8	9.9	**-19.2**	-29.4
	1.1 - 0.20	**-3.1**	**-0.1**	**-0.7**	-0.5	-9.3	10.3	*-18.8**	*-30.4**
		-1.6	**2.9**	**-0.7**	-1.3	-5.0	14.8	*-17.8**	*-28.3**
	1.6 - 0	**-0.3**	**0.6**	-3.3					
		-0.3	**-0.1**	-3.8					
	1.7 - 0.05	**-0.5**	**0.3**	-3.3	-1.8	-1.7	8.6	-19.7	**-29.3**
		-0.1	**0.6**	-3.6	-2.1	-0.5	8.7	-19.7	**-29.1**
	1.7 - 0.10	**-0.7**	**0.4**	-3.0	-1.8	-2.3	9.0	-19.5	**-29.3**
		-0.1	**0.8**	-3.4	-2.1	-0.8	9.1	-19.6	**-29.0**
	1.7 - 0.15	**-0.7**	**1.2**	-2.5	**-1.3**	**-1.2**	11.1	-18.9	**-28.7**
		-0.4	**0.4**	-3.3	-1.9	-1.7	8.7	-19.7	**-29.3**
	1.7 - 0.20	**-2.1**	**2.0**	**-0.7**	**0.0**	**-4.6**	13.8	*-17.9**	*-28.8**
		-0.8	**1.9**	-1.9	**-1.6**	**-2.4**	12.9	*-18.5**	*-28.3**

[a] $Mg_{0.15}Mg_3Al_{0.3}Si_{3.7}O_{10}(OH)_2 \cdot 4H_2O$ * Not considered as samples not equilibrium

The zeta potential measurements on M-S-H and M-A-S-H 1.1 particles are plotted versus the measured pH in Figure 98a. Similar to the zeta potential of M-S-H (chapter 3.3 and 4.3), the zeta potential of the M-A-S-H is negative. The zeta potential values measured for the pure M-S-H 1.1 suspension was about -25 mV, while it was slightly less negative for the M-A-S-H 1.1 suspensions with -20 ± 2 mV (Figure 98). Only the sample with the highest aluminum addition (Al/Si = 0.2) where amorphous silica was still present, showed a lower value of -25 ±3 mV, which was probably related to the very negative zeta potential of amorphous silica (< - 40 ± 4 mV) (chapter 3.3)., The pH of the solutions of the other samples were between 9.8-9.9 and can thus not explain the slightly less negative zeta potentials. The measured zeta potential became less negative with the increase of the magnesium concentrations from 0.15 for the pure M-S-H to 0.41 mmol/l for the sample with

Al/Si = 0.1 (Figure 98b), which indicates the specific sorption of some magnesium on the M-A-S-H surface resulting in a slightly less negative zeta potential.

The slightly less negative zeta potential seems to be related to the increase of magnesium concentration while the incorporation of aluminum in the samples did not affect the effective surface charge density. This is coherent with the uptake of aluminum half in tetrahedral and half in octahedral layers of the M-A-S-H 1.1 samples.

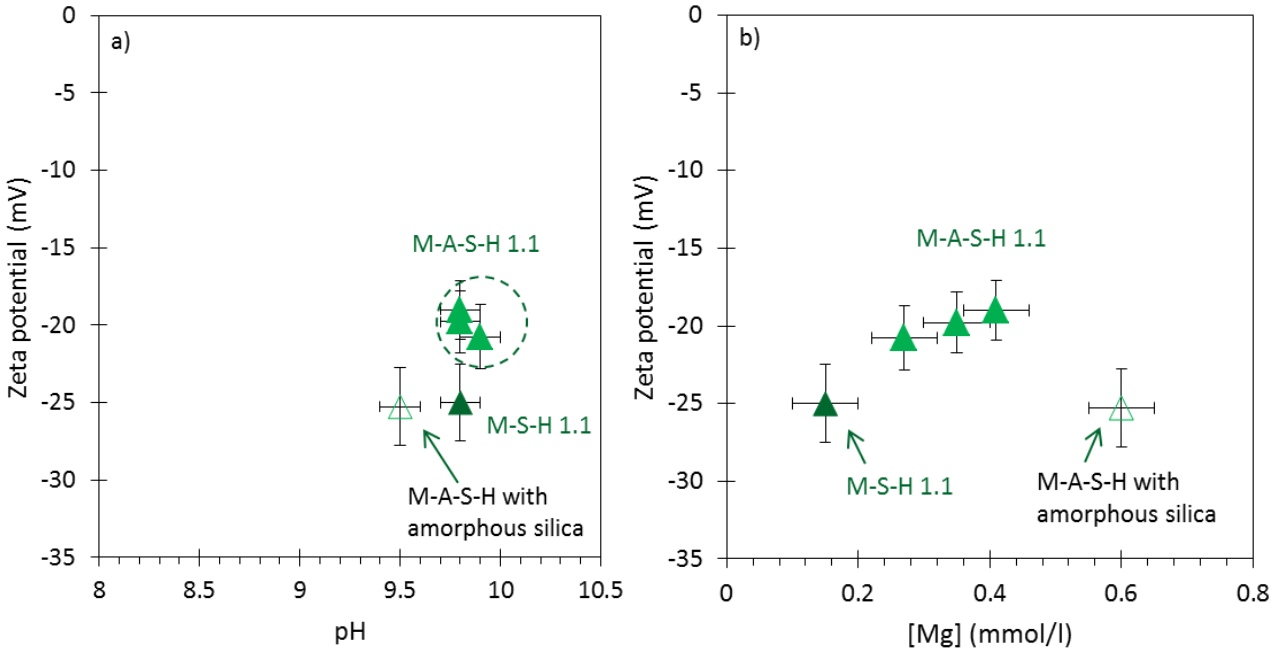

Figure 98: Measured zeta potentials a) as a function of the measured pH values in the M-A-S-H samples (2 years, 20°C) Mg/Si=1.1, b) as a function of the dissolved magnesium measured; M-S-H references from chapter 3.3.

In agreement with the slight variation of the zeta potential measurement, the measurement of the cation exchange capacity of the pure M-S-H 1.1 and M-A-S-H 1.1 showed a comparable CEC of around 35 ± 5 meq/100g independent of aluminum addition as illustrated in Figure 99.

The CEC calculated from the total of the cations released by the cobalt(III) replacement agreed well with the CEC measured by colorimetry (Figure 99). As for pure M-S-H (chapter 3.3), the exchangeable cations were mainly magnesium plus a low quantity of alkalis (lithium, sodium, and potassium from the metakaolin). Aluminum was not detected as exchangeable cation in agreement with its negligible

concentration, indicating that aluminum was completely incorporated in the sheets of the magnesium silicate phase.

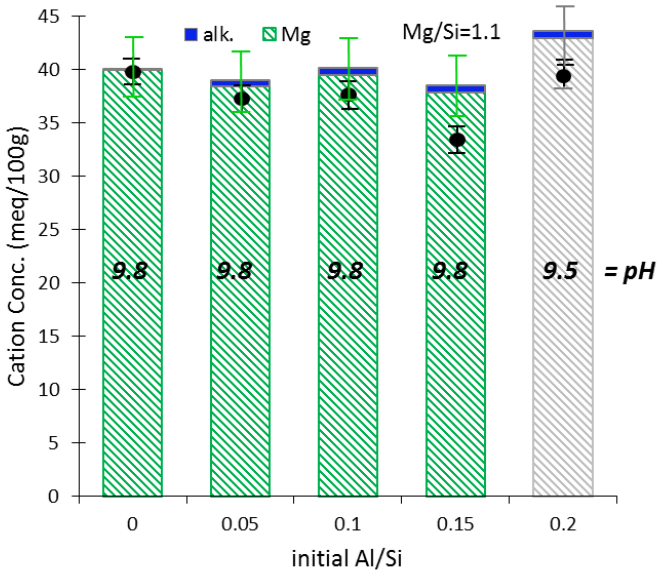

Figure 99: Concentrations of the cations sorbed on M-A-S-H 1.1 measured by the cobalt hexamine method as a function of the initial Al/Si. The cation exchange capacity (CEC) measurements by colorimetry (black circles) have been added for comparison. Al/Si=0.2 sample not at equilibrium in grey.

5.3.1.1.2. M-A-S-H 1.7

In the samples prepared at higher Mg/Si ratio (Mg = 1.6 and 1.7), some brucite was present in addition to M(-A)-S-H phases, as indicated by TGA with a narrow water loss at 400°C (Figure 95b) and by XRD, (Figure 95a). Independent on the quantity of metakaolin initially added, approximately 20 wt.% of brucite was observed at the 20, 50 and 70°C, indicating a maximum Mg/Si of 1.4 at all temperatures in agreement with the observations in pure M-S-H ((Nied et al., 2016) and chapter 3). In the M-A-S-H 1.7 sample with the highest Al/Si=0.20 after 1 year, unreacted amorphous silica was detected by FTIR and ^{29}Si MAS NMR at 20°C; after 2 years, however, all silica had reacted (Table 34). Contrary to Mg/Si = 1.1, traces of amorphous aluminum hydroxide and hydrotalcite were detected at Al/Si=0.2 (Figure 95).

The ^{27}Al MAS NMR spectra of the M-A-S-H 1.7 were identical independently of the amount of metakaolin added (Figure 100). A higher aluminum fraction (~70%) was present in the octahedral MgO layer than in the tetrahedral silica layer (~30%) as detailed in Table 35, in agreement with the higher fraction of magnesium than silica in these M-S-H with Mg/Si =1.4.

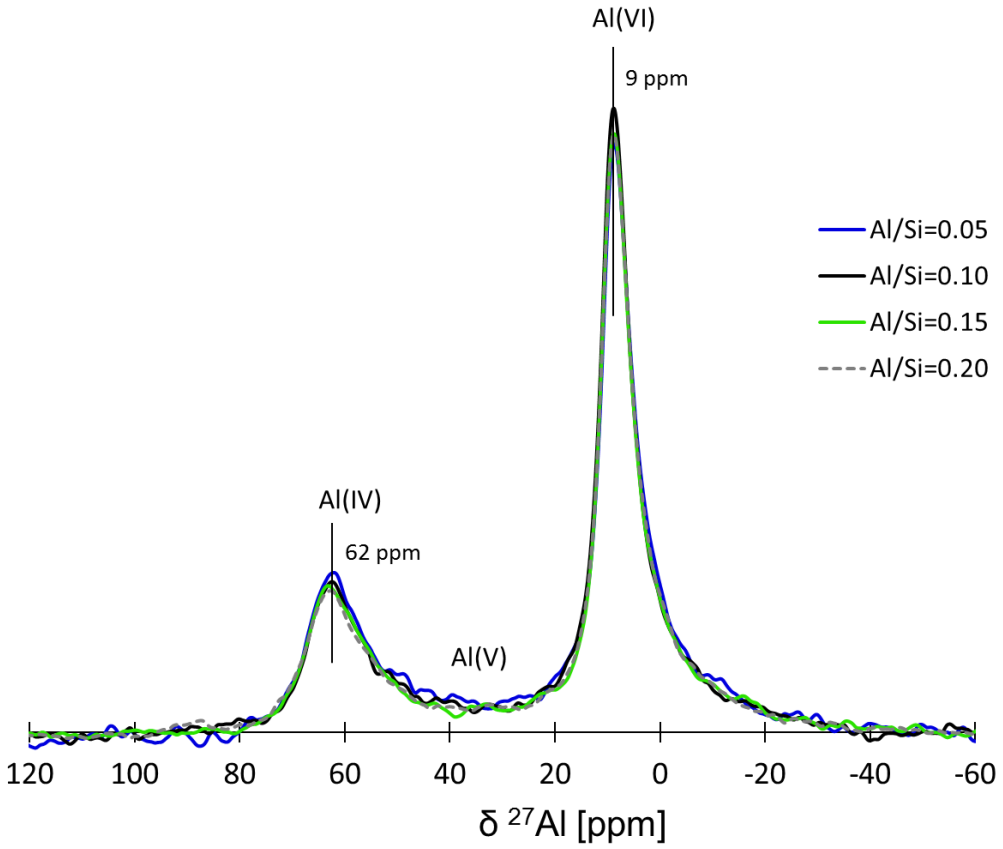

Figure 100: ^{27}Al MAS NMR spectra of the M-A-S-H samples, Mg/Si=1.7 and Al/Si=0.05-0.20, equilibrated for 2 years at 20°C.

In pure M-S-H 1.6 equilibrated at 20°C, a pH value of about 10.5, and magnesium and silicon concentrations of 0.12 mmol/l and 0.001 mmol/l were determined (Table 34), in agreement with the observations for other high Mg/Si samples, where brucite had been present (chapter 3 and 4.2). The addition of metakaolin did again not change the pH of the solution, which remained at 10.5. Also, the magnesium and silicon concentrations in the M-A-S-H 1.7 were relatively similar to the pure M-S-H 1.6, except for the highest addition of aluminum (Al/Si=0.2) where the equilibrium had not been completely reached at 20°C.

The saturation indices (SI) calculated from the measured concentrations and pH values in the pore solution, compiled in Table 39, showed that the solutions at 20°C were undersaturated with respect to amorphous silica (with the exception of the sample with the highest aluminum content, were only a moderate undersaturation was observed), but saturated with respect to brucite. The solutions were slightly oversaturated with respect to M-S-H indicating that the uptake of

aluminum in M-S-H influences M-S-H solubility. Again, most concentrations of aluminum were close to the detection limit, and the solutions were undersaturated with respect to microcrystalline aluminum hydroxide and hydrotalcite consistent with their absence in XRD and TGA (except at Al/Si=0.2).

The presence of more aluminum in octahedral sites than in tetrahedral sites is expected to reduce the negative charge of M-S-H, which agrees with the less negative zeta potential measured for the samples containing aluminum as shown in Figure 101. In fact, in pure M-S-H a zeta potential of -23 mV was measured, while the Al-containing samples all had a less negative zeta potential of -18±2 mV. As discussed above, the concentration of magnesium and the pH values remained constant independent on the amount of metakaolin, such that the decrease of the negative zeta potential seems to be related directly to the higher amount (70%) of Al^{3+} in the octahedral Mg^{2+} layer than in the tetrahedral Si^{4+} layer. However, one would expect a further increase of the effective negative charge with the aluminum content, indicating that further factors influence the effective surface charge of the M-A-S-H samples. Also the CEC of the samples with aluminum comparable to the CEC measured in its absence, (Figure 102). Again, no significant variation of the CEC with higher aluminum content was observed.

Magnesium and sodium were the only exchangeable cations measured by CEC, indicating again that aluminum was present exclusively in the M-S-H layers.

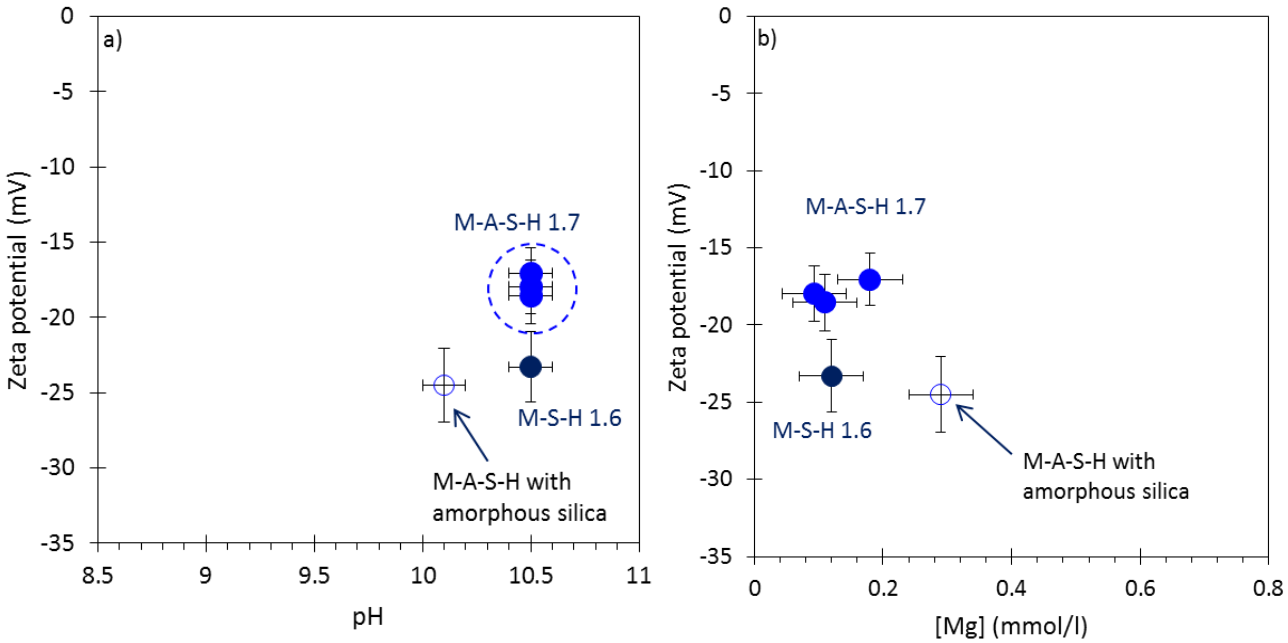

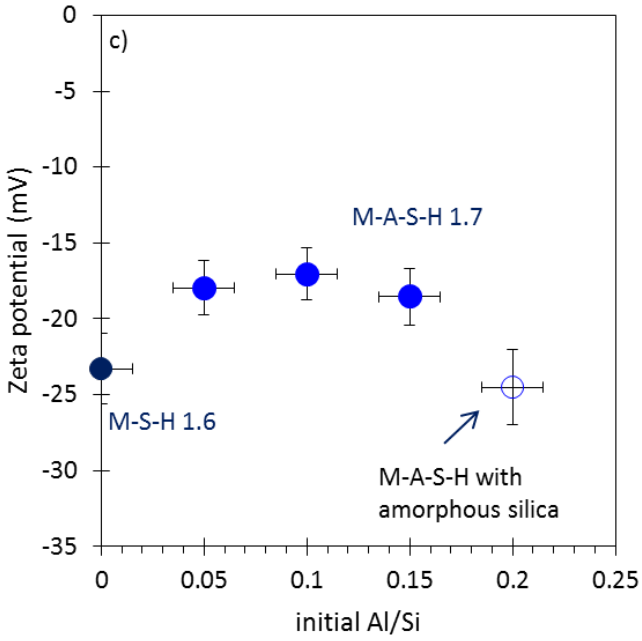

Figure 101: Measured zeta potentials a) as a function of the measured pH values in the M-A-S-H samples (2 years, 20°C) Mg/Si=1.7, b) as a function of the measured magnesium concentrations and c) as a function of the initial Al/Si.

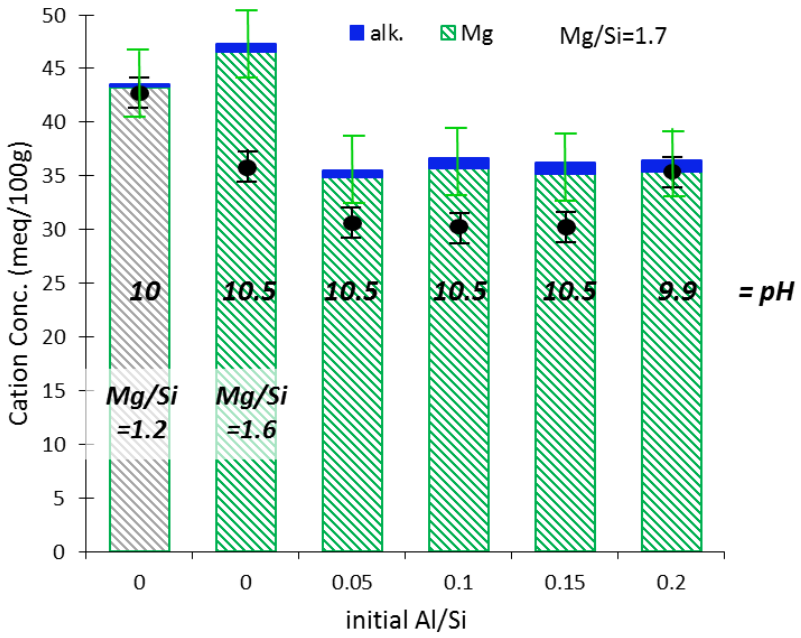

Figure 102: Concentrations of the cations sorbed on M-A-S-H 1.7 measured by the cobalt hexamine method as a function of the initial Al/Si compared to the CEC of the M-S-H 1.2 (grey). CEC measurements by colorimetry (black circles) have been added for comparison. Note that the M-A-S-H samples contained in addition to M-A-S-H also 20% brucite, that the M-S-H 1.2 is pure and that 80 wt % of M-A-S-H give similar CEC values (44.3, 43.9, 43.4 and 43.7 meq/100g of M-A-S-H).

Aluminum was found to be completely taken up in M-S-H at 20, 50 and 70°C as no other aluminum containing phases were observed. ^{29}Si and ^{27}Al MAS NMR data indicated an incorporation in both the octahedral and the tetrahedral layers. CEC results showed that similarly to M-S-H, magnesium is the main exchangeable cation while no aluminum was observed as exchangeable cation, consistent with the very low aluminum concentrations in solution.

5.3.1.2. Effect of sodium nitrate on aluminum in M-S-H

Sodium aluminate was used to avoid the presence of unreacted quartz and anatase from the metakaolin addition. To prevent a pH increase and the precipitation of brucite, the addition of sodium was matched by nitric acid. Sodium nitrate was used to obtain a constant sodium nitrate concentration of approx. 100 mmol/l in all samples. No or only a small reduction of sodium or nitrate in solution at equilibrium with the M-S-H and M-A-S-H samples was measured by IC (Table 37), indicating a limited uptake of sodium or nitrate by the solid phases in agreement with the observations for the M-S-H samples (chapter 5.2). At high concentrations and low uptake, such indirect determination of sodium and nitrate uptake based on the difference in concentration measurements and mass balance calculations are not very accurate, as discussed in the previous chapter, and thus the uptake of sodium was obtained directly from CEC measurements (see below).

Table 37: The measured dissolved concentrations, pH values in the solutions in equilibrium with the M-A-S-H N. (in mmol/l, errors: pH ±0.1, concentrations: ±10%).

	initial Mg/Si - Al/Si	Age (years)	pH (20°C)	[Mg]	[Si]	[Al]	[Na]	[NO_3]	initially added [Na]	initially added [NO_3]
20°C	*0.80 (no $NaNO_3$)*	*1*	*8.5*	*0.33*	*1.36*	---	*0.33*	---	---	---
	0.80	1	7.7	4.27	1.18	---	107	95	100	95
	0.80 - 0.10	1	8.2	3.44	1.36	0.0002	103	111	106	115
		2	8.1	3.67	1.18	<0.0001	103	102	107	106
	0.08 - 0.20	1	9.1	0.014	1.57	0.009	101	102	111	106
		2	9.4	0.004	1.71	<0.0001	106	97	113	98
	1.20 (no $NaNO_3$)	*1*	*10.3*	*0.10*	*0.004*	---	*0.44*	---	---	---
	1.20	1	9.7	2.90	0.002	---	99	89	96	99
	1.20 - 0.10	1	10.0	1.59	0.010	<0.0001	104	109	106	118
		2	8.9	3.84	0.019	<0.0001	106	106	108	109
	1.20 - 0.20	1	9.6	0.006	2.64	<0.0001	120	122	110	125
		2	9.4	0.006	1.33	<0.0001	123	113	111	117
50°C	*0.80 (no $NaNO_3$)*	*1*	*8.1*	*0.10*	*2.57*	---	*0.29*	---	---	---
	0.80	1	7.7	2.80	2.53	---	96	106	*	*
	0.80 - 0.10	**1**	**8.0**	**1.28**	**2.04**	**<0.0001**	**98**	**96**	*	*
	0.80 - 0.20	1	8.7	0.04	1.64	<0.0001	107	102	*	*
	1.20 (no $NaNO_3$)		*9.9*	*0.19*	*0.006*	---	*0.50*	---	---	---
	1.20	*Not measured*								
	1.20 - 0.10	**1**	**8.6**	**5.07**	**0.06**	**<0.0001**	**104**	**110**	*	*
	1.20 - 0.20	1	9.1	0.47	0.22	<0.0001	121	118	*	*

*not measured; solutions prepared for the samples at 20 and 50°C.

The M-S-H synthesized in the presence of sodium nitrate was comparable to pure M-S-H with the exception that sodium (Na/Si=0.04) instead of magnesium was present as exchangeable cation at the surface as discussed in chapter 5.2. Also, the Al-containing samples with $NaNO_3$ showed a comparable structure to M-A-S-H prepared from metakaolin as shown in Figure 93 to Figure 95. Similar to the M-A-S-H 1.1, no brucite or only traces were observed in the M-A-S-H 1.2N after 2 years at 20 and 1 year at 50°C (Table 38). Only M-A-S-H 1.2N Al/Si = 0.2, showed the presence of some persistent brucite and unreacted silica indicating a slower kinetic than in the M-A-S-H 1.1 samples with metakaolin.

The M-A-S-H 0.8N samples at 20 and 50°C contained some unreacted silica independent of the amount of aluminum at 20°C due to the low Mg/Si and the pH values (Table 38), comparable to the pure M-S-H 0.8 and M-S-H 0.8N. At Al/Si=0.2, a hydrotalcite-like phase was observed by TGA (Figure 95b) and by XRD (Figure 95a) at all temperatures, in contrast to the M-A-S-H 1.1 and 1.7 samples without $NaNO_3$. Hence, a part of magnesium and a part of aluminum were not in M-A-S-H phases.

The ^{27}Al MAS NMR spectra of M-A-S-H 0.8N and 1.2N are compared in Figure 103 with M-A-S-H 1.1, all with Al/Si=0.2. The Al(IV) environment in the presence of $NaNO_3$ was broader than for pure M-A-S-H and an additional signal at approx. 54 ppm was observed. The fraction of Al(VI) was higher for the M-A-S-H N and has a narrower full width at half maximum (FWHM), which would be consistent with the presence of a hydrotalcite-like phase, which contains Al(VI) in the octahedral position only, in agreement with the XRD and TGA data. ^{27}Al MAS NMR spectroscopy, in our case, does not allow clear distinction between Al(VI) in the octahedral layer of M-A-S-H and hydrotalcite-like phase. The Al(IV)/Al(VI) ratio in the total samples was calculated about approx. 2.5.

While the shape and position of the Al(VI) is mainly affected by the second neighbors in the octahedral sheets, the position of the Al(IV) environment depends on the nature of the second neighbors in the tetrahedral sheets, but also on the second neighbors in the octahedral sheets and second neighbors at the hydroxylated surface, i.e. on the ions at the surface of the tetrahedral layers. The shift of the Al(IV) band from 62 to 54 ppm could thus be related to the presence of sodium instead of magnesium at the surface, as the presence of magnesium leads to higher shifts than sodium. Similarly, Al(IV) in margarite ($CaAl_2(Al_2Si_2O_{10})(OH)_2$) was observed at 71 ppm, but at 67 ppm in muscovite ($KAl_2(AlSi_3O_{10})(OH)_2$), which contains K^+ instead of Ca^{2+} at the surface in (Sanz and Serratosa, 1984).

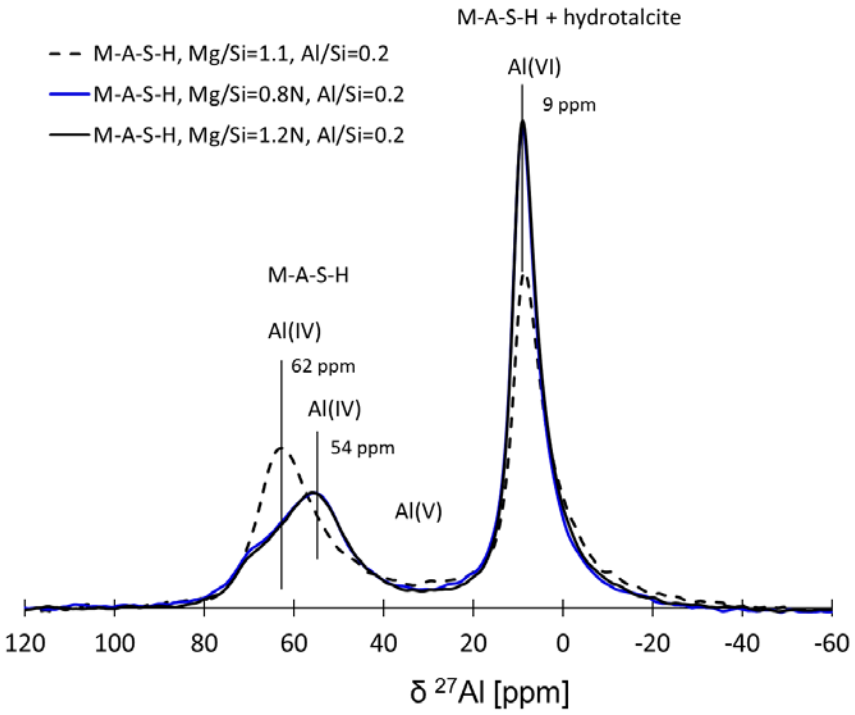

Figure 103: Comparison of the ^{27}Al MAS NMR spectra of the sample M-A-S-H 0.8N, M-A-S-H 1.2N, and M-A-S-H 1.1, Al/Si=0.2, 1 year 50°C).

Table 38: Summary of the presence of hydrotalcite, brucite, amorphous aluminum hydroxide and unreacted silica in the solid composition, Mg/Si and Al/Si in the samples were not calculated due to the difficulties to quantify the hydrotalcite, brucite and aluminum hydroxide.

	initial Mg/Si & Al/Si	Age (years)	hydrotal.	brucite	Al(OH)3	unreacted silica
20°C	0.80	1				✓
	0.80 - 0.10	1	✓ traces	✓ traces		✓
		2	✓ traces		✓ traces	✓
	0.08 - 0.20	1	✓	✓	✓	✓
		2	✓	✓	✓	✓
	1.20	1				
	1.20 - 0.10	1	✓ traces	✓ traces		
		2	✓ traces		✓ traces	
	1.20 - 0.20	1	✓	✓	✓	✓
		2	✓	✓	✓	✓
50°C	0.80	1				✓
	0.80 - 0.10	**1**				✓
	0.80 - 0.20	1	✓ traces		✓ traces	✓
	1.20	1				
	1.20 - 0.10	**1**				
	1.20 - 0.20	1	✓		✓ traces	✓

Although the phases synthesized in the presence of sodium nitrate showed a comparable structure as the pure M-S-H and M-A-S-H based on metakaolin, the

compositions of the solution were slightly different. The presence of approx. 100 mmol/l sodium nitrate lowered the pH of pure M-S-H solution from 8.3 to 7.7 at Mg/Si=0.8 and from 10 to 9.7 at Mg/Si=1.2 resulting in an increase of the magnesium concentrations as detailed in the previous chapter. Also for the Al-containing samples, slightly lower pH values (below 9.4) than in the samples without $NaNO_3$ were observed. The solutions of the M-S-H 0.8, M-S-H 0.8N and M-A-S-H 0.8N contained silicon concentrations between 1.2 and 1.7 mmol/l, thus in equilibrium with amorphous silica, as also observed by ^{29}Si MAS NMR in the solid phases (Table 38). At Al/Si = 0 and 0.1 relatively high magnesium concentrations were measured in the presence of sodium nitrate due to the lower pH values (and/or due to replacement of magnesium at the cation exchange sites by sodium). At Al/Si = 0.2, however, much lower magnesium concentrations were measured, which could be related to the observed formation of a hydrotalcite like phase in these samples.

The solutions of the M-A-S-H 0.8N were undersaturated with respect to brucite consistent with the experimental observations where no or only traces of brucite were detected (Table 39), but saturated with respect to amorphous silica and M-S-H, consistent with the solid phase analyses.

Again, most concentrations of aluminum were below the detection limit, such that only maximum SI could be calculated (using the detection limit of 0.0001 mmol/l as maximum aluminum concentration). The solutions were again undersaturated with respect to microcrystalline aluminum hydroxide and OH-hydrotalcite, contrary to the experimental observations of a hydrotalcite-like phase at Al/Si=0.2. The presence of hydrotalcite might be explained by the presence of nitrate in solution and the formation of NO_3-hydrotalcite, $[Mg_{l-x}Al_x(OH)_2]^{x+}$ $[NO_3^- \cdot mH_2O]^{x-}$. The formation of NO_3-hydrotalcite would be consistent with the distinct decrease of magnesium concentration. Whether nitrate concentrations decreased (indicating its uptake in NO_3-hydrotalcite, cannot be assessed due to the inherent error of ±10% of the liquid phase analysis. If 50% of aluminum would be used to make hydrotalcite at Al/Si = 0.2 and assuming NO_3/Al ~1 in the hydrotalcite, a decrease of nitrate concentration by approx. 10 mmol/l would be expected, which within the error of the measurements. The formation of NO_3-hydrotalcite limits the uptake of aluminum and magnesium in the M-A-S-H samples.

The measured concentrations were also used to calculate ion activity products (IAP) for possible aluminum containing end-members, resulting in log IAP = -18.6 ± 0.2 for $M_{0.76}A_{0.20}SH$ from the samples with low Mg/Si, comparable to the log IAP of -19.2 ± 0.2 obtained from the samples without sodium nitrate.

Table 39: Calculated saturation indices of the M-A-S-H calculated from the measured concentrations (Table 37) and the thermodynamic data given in Table 8. Solid phases observed experimentally are marked as bold.

		saturation indices						log IAP	
	initial Mg/Si & Al/Si	Brucite	MSH-SS	Amor. SiO_2	$Al(OH)_3$ micro.	Ht 2:1	Saponite	$M_{0.76}A_{0.2}SH_{1.5}$	$M_{1.5}A_{0.2}SH_2$
20°C	0.8 - 0	-4.3	**-0.7**	**0.0**					
	0.8 - 0.10	-3.4	**1.2**	**0.1**	-1.0	**-11.8***	12.0	-18.4	-30.2
		-3.6	**0.7**	**0.0**	<-1.1	**<-12.8***	<11.2		
	0.8 - 0.20	**-4.0**	**0.0**	**0.1**	-0.3	**-12.7***	10.3	-18.7	-31.0
		-4.0	**0.1**	**0.1**	<-2.4	**<-16.8***	<9.9		
	1.2 - 0	-0.6	**0.6**	-3.0					
	1.2 - 0.10	-0.2	**2.2**	-2.5	<-2.2	**<-1.2***	<12.4		
		-2.0	**-0.2**	-1.8	<-1.2	**<-6.4***	<9.6		
	1.2 - 0.20	**-3.2**	**2.0**	**0.2**	<-2.8	**<-14.2***	<12.7		
		-3.5	**0.7**	**-0.1**	<-2.4	**<-14.9***	<10.8		

* refers to 2:1 OH-hydrotalcite. NO_3- rather than OH-hydrotalcite was present.

The cation exchange capacity (CEC) was measured on the M-A-S-H N solids after washing and drying. The measurement of CEC on the samples at Al/Si=0.2 are shown in Figure 104 and showed a CEC of ~35 meq/100g similar to pure M-S-H and M-S-H synthesized in the presence of sodium nitrate (chapter 5.2) and also to the M-A-S-H samples (Figure 99 and Figure 102). The cations sorbed on M-A-S-H N were found to be mainly sodium instead of magnesium as usually observed in M-S-H (chapter 3.3) or M-A-S-H (Figure 99 and Figure 102). The amount of sodium and magnesium at the cation exchange sites is directly influenced by the relative concentrations of sodium and magnesium in the solution confirming the findings in chapter 5.2.

From CEC a Na/Si of 0.04 and 0.05 was calculated for M-A-S-H 0.8N and M-A-S-H 1.2N, respectively (Al/Si=0.20). This is consistent with the results previously obtained for M-S-H synthesized in sodium nitrate solution. The CEC results confirmed the finding from ^{27}Al MAS NMR spectroscopy that sodium is sorbed on M-A-S-H N solid samples.

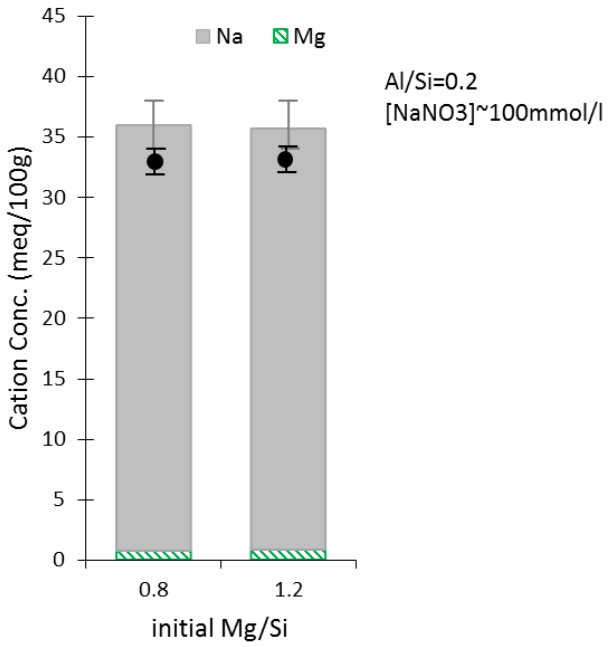

Figure 104: Concentrations of the cations sorbed on M-A-S-H N (Al/Si=0.20) measured by the cobalt hexamine method as a function of the initial Mg/Si.

5.3.2. Conclusions

This work aimed at investigating the aluminum incorporation into magnesium silicate hydrate phases. Up to 0.2 aluminum per silica has been observed to be incorporated in M-A-S-H. Samples with higher Al/Si had not been studied. Infrared spectroscopy (FT-IR), ^{29}Si and ^{27}Al MAS NMR data, thermogravimetric analysis (TGA), and X-ray diffraction (XRD) showed that M-(A-)S-H phases formed which had a similar silicate polymerization as pure M-S-H.

In batch experiments the kinetic of formation of M-A-S-H was similar to M-S-H: initially, brucite, or NO_3-hydrotalcite in the presence of sodium nitrate, formed which later reacted slowly with the amorphous silica to M-(A-)S-H. The presence of sodium nitrate slowed down the kinetic of M-A-S-H formation.

The incorporation of aluminum took place in both, the octahedral and tetrahedral sheets; aluminum was distributed more or less evenly between octahedral and tetrahedral positions at Mg/Si = 1.1. At high Mg/Si ratio, however, where more octahedral sites in the magnesium hydroxide layer than tetrahedral silicate sites were present, 70% of the aluminum was found in the magnesium hydroxide layer resulting in slightly less negative surface charge. CEC measurements showed that no significant amount of aluminum was present as an exchangeable cation in M-S-H.

In the presence of sodium nitrate, in addition to M-A-S-H also the formation of NO_3-containing hydrotalcite was observed, which somewhat limited the Al-uptake in M-A-S-H. A sodium concentration of 100 mmol/l was sufficient to replace the Mg^{2+} usually present on the cation exchange sites of M-A-S-H by Na^{+} as already observed in M-S-H in sodium nitrate (chapter 5.2).

Possibly more than 0.2 Al/Si could be taken up in M-S-H, which needs to be further investigated. Additionally, the incorporation of aluminum in presence of alkali hydroxide solution might change the uptake and the surface chage of the particle. Furthermore, more detailed characterizations of the M-A-S-H phases by e.g. PDF, DVS or N_2 sorption isotherms might allow getting coherence length, basal spacing, and particle size and giving further insights about the stability of those phases.

The variation of the ion activity products calculated for M-S-H in the presence of aluminum confirmed an incorporation of aluminum into M-S-H. Similar solution and solid compositions were observed at 50 and/or 70°C, indicating little influence of temperature on the stability of M-A-S-H as observed for M-S-H (chapter 3.2). The development of thermodynamic models for aluminum uptake in C-A-S-H, M-A-S-H and hydrotalcite-like solids will be needed to describe the changes on the interface of cement paste with a magnesium containing environment or within magnesia-silica based cementitious materials. This study gives both aqueous and solid compositions which could serve as a basis for the development of the end-members to add to the solid solution M-S-H phase developed in the chapters 3.2 and 4.3 or to that from (Nied et al., 2016).

5.4. Main findings on the alkali and aluminum uptake

- In the presence of sodium nitrate (pH ~ 7-8) little sodium uptake on the M-S-H surface and no influence of sodium nitrate on the M-S-H structure is observed
- More alkalis are preferentially associated with the surface of M-S-H at high pH values
- Li, Na and K show a comparable uptake and their uptake is independent of Mg/Si
- At low and high pH, alkalis are present to compensate the negative surface charge on M-S-H
- M-S-H with Mg/Si ≤1 is stable up to pH 12.5 without brucite formation
- Aluminum is incorporated in M-S-H up to at least Al/Si=0.20
- M-(A-)S-H phases are similar to M-S-H with comparable content of water, small particle size and polymerization in the tetrahedral silicate sheets
- M-(A-)S-H phases can be considered as ill-defined hydrated phyllosilicates
- The formation of NO_3-containing hydrotalcite was observed in the presence of sodium nitrate and relatively low pH, limiting the Al/Si ≤ 0.20
- Aluminum is incorporated in the main layers of M-S-H
- Aluminum was observed in both octahedral and tetrahedral sheets
- The aluminum incorporation does not change the surface charge of M-S-H significantly

Chapter 6:

Conclusions and outlook

Conclusions

The radioactive waste storage in Europe is a challenge. The envisaged storage in clayey environments, if adopted by civil society and validated by the scientific community, will constitute a significant challenge as the cementitious materials used for construction can interact with the clay, and they will interact with each other and the environment for a very long time span. After re-saturation of the disposal cell after several hundred to thousands of years, the clayey rock pore water will interact with the cementitious materials, especially in the sealing zones (Cigéo case - France). There, the durability of the concrete plugs should be maintained for several thousand years. The clayey water, with a pH close to neutrality and containing carbonates, sulfates, and magnesium, will inevitably cause leaching, carbonation, and the formation of sulfate and magnesium containing hydrates depending on the composition of the concrete used.

Alkaline to hyper-alkaline interstitial water of cementitious materials with their high pH values will alter the properties of the swelling clay core and the host rock. Among the options investigated so far, the low-pH concretes can limit the alkalinity of the interstitial water causing fewer changes to the clayey materials. The study of the physicochemical and mechanical evolutions of those new and less known cementitious materials showed, up to now, a relatively acceptable behavior under the conditions of storage. However, for the purpose of the stability of the repositories, good geochemical and reactive transport modelling has to be carried out with representative calculations of the perturbations observed experimentally. Hence, good thermodynamic databases are needed.

A review of the available literature showed that we are not able to model all relevant chemical changes of low-pH concretes in a storage environment. The formation of magnesium containing phases, such as M-S-H, is one of the major perturbations observed experimentally, but is generally neglected in modelling as the thermodynamic data for this phase were not available. Thus this thesis aimed to describe how M-S-H phases are formed, their stoichiometry, the uptake of other ions

and to calculate their thermodynamic properties to complete thermodynamic databases and allow considering such phases in transport models.

This study showed that low Ca/Si C-S-H as present in low-pH cements is easily destabilized in the presence of magnesium such that M-S-H is expected to be formed at interface concrete with a magnesium containing environment. C-S-H is destabilized in the presence of magnesium relatively fast in the pH range 7.5 to 9.5, which leads to significant quantities of dissolved calcium and amorphous silica. M-S-H forms from dissolved magnesium and the amorphous silica after relatively short times (3 months at 20°C in both diffusion cell and batch experiment and 1 month at 50°C in batch experiments).

Nevertheless, the formation of synthetic M-S-H from MgO and SiO_2 is a slow process which continues at least up to 3 years and possibly longer at 20°C. During the first days, the hydration of magnesium oxide to brucite results in a high pH where M-S-H forms very slowly only because the high silica concentrations inhibit brucite dissolution. Similarly, M-S-H formation is also slow if MgO is added to C-S-H as again brucite is formed initially. The pH of the solution is crucial in batch experiments with a significant amount of magnesium as pH values above 10.5 promote this initial brucite precipitation. Despite its slow formation in the presence of brucite, experiments and thermodynamic modelling have shown clearly that M-S-H is more stable than brucite and amorphous silica. Interestingly, no brucite was observed in the cell experiment at the interface even at a pH of 10.5 in the C-S-H, which can be explained by low dissolved magnesium concentrations. Brucite formation is, therefore, expected and observed only in batch experiments but not in cell or field experiments, also in agreement with thermodynamic modelling results.

For M-S-H synthesized in batch experiments, the Mg/Si range varied between 0.8 to 1.4. Detailed studies indicated that M-S-H has a nano-crystalline ill-defined structure comparable to hydrated swelling 2:1 and 1:1 phyllosilicates and contains a significant amount of water. M-S-H has a negative surface charge from the presence of deprotonated silanol groups in the silicate layers. The negative charge is counterbalanced by exchangeable magnesium cations at the surface if other cations are absent.

In the presence of aluminum, the uptake of aluminum in M-S-H is observed in M-A-S-H, while other aluminum containing hydrates such as hydrotalcite or aluminum hydroxide did not form. However, in the presence of 100 mmol/l sodium nitrate, a NO_3-hydrotalcite-like phase was observed at Al/Si=0.20. M-A-S-H phases incorporate aluminum both in octahedral sites and in tetrahedral sites. M-A-S-H phases are nano-sized as M-S-H, have a comparable content of water and a similar silicate

polymerization (tetrahedral silicate sheets). The aluminum incorporation does not change the surface charge of M-S-H significantly. However, the precipitation of hydrotalcite in addition to M-A-S-H at the interface might sorb different anions.

Only a little sodium uptake occurs at low pH (~ 7-9) on M-S-H and M-A-S-H (Na/Si ~ 0-0.04). Although the binding of magnesium, calcium, and alkalis was mainly investigated on M-S-H, comparable results are expected for M-A-S-H due to its similar surface charge. A much higher sorption of cations was observed at higher pH values (>10). At high pH values the silanol groups are deprotonated, and the negative surface charge is balanced by cations near the surface. No significant difference was observed between Li^+, Na^+ or K^+, but a clear preference for bivalent cations, with a preference of Ca^{2+} over Mg^{2+}. Even at high pH values, the calcium uptake in M-S-H was clearly below 0.12 Ca/Mg. Similar to the alkalis, Ca^{2+} was present on the cation exchange sites on the surface. It is not excluded that Ca^{2+} was present both on the cation exchange sites at the surface of M-S-H as well as in main layer sites.

Together the different experimental studies showed that M-S-H is stable between pH 7.5 to 12.5. The continuous changes in concentrations at different Mg/Si and pH values are best captured by a solid-solution model. The solubility products of the end-members were calculated from the solution composition from oversaturation and undersaturation experiments. The entropy, enthalpy, and heat capacity were calculated and describe the M-S-H stability as a function of temperature. Also, the calcium uptake in M-S-H could be outlined by a solid solution model between pure M-S-H and M-C-S-H.

The expected increase in temperature up to 70°C in the nearfield of a nuclear waste repository will not significantly impact the formation of M-S-H at the interface. Although M-S-H formation occurred faster at higher temperatures and it might be slightly more structured, M-S-H remains poorly ordered and nano sized, it exhibits a comparable range of Mg/Si ratio and a comparable solubility.

Finally, the nano-crystalline ill-defined structure of M-S-H (extended to M-A-S-H) and its similarity to hydrated swelling 2:1 and 1:1 phyllosilicates could indicate that in underground repositories such M-(A-)S-H phases could evolve into more crystalline, well-defined phyllosilicates over the life time of the repository.

Perspectives

Although many different aspects have been investigated, a number of topics will need to be addressed in more details in the future:

A thermodynamic model to account for the incorporation of aluminum and alkalis is still missing. The data collected in the last chapter (chapter 5) cover both aqueous, and solid-compositions in the presence of alkalis and aluminum and could serve as a basis for an extension of thermodynamic data to include M-A-S-H and M-N-S-H as well as other alkalis.

Also, an in-depth understanding of the stability field of M-A-S-H versus hydrotalcite-like phases (at different Mg/Al and with OH^-, NO_3^-, CO_3^{2-}, or other anions), calcium alumino-silicate phases (C-A-S-H) and zeolite at different pH values is needed. Systematic experiments and thermodynamic data for various hydrotalcites, zeolites and C-A-S-H phases are partially incomplete and contradictory. The adequate description of all relevant phases which might occur is needed for a reliable modelling of the precipitation of M-S-H at the interface between concrete and the environment or of the performance and durability of magnesia/silica cement-based materials where M-(A-)S-H is the main hydrate.

A study with diffusion cells containing C-A-S-H disks in contact with M-S-H-like phases and sodium aluminate solutions would give understandings about the stability in the presence of aluminium and alkalis under near field conditions.

Many other open questions remain which would be interesting to study in further investigations possibly using additional suitable experimental techniques:

- How much alumnium can be taken up in M-S-H ? The last chapter had shown that an aluminum incorporation in M-S-H occurs up to Al/Si = 0.2, but possible higher ratios still need to be investigated. Also the effect of aluminum on basal spacing, on swelling, on the crystallinity of the M-A-S-H phase and on calcium uptake has not yet been studied.

- Further insights in porosity, density, the content of water of pure M-S-H and its effect on swelling and swelling pressure must be investigated to complete the findings given in chapter 3. In particular, the swelling and generated swelling pressures conditions are worth to study during rewetting and in saturated conditions.

- The recording of complete sorption isotherms for alkali (including much lower as well as higher concentrations) might allow differentiating and quantifying active sorbing edge sites and weakly binding cation exchange sites on M-S-H and M-A-S-H. ^{23}Na solid state MAS NMR studies or spectroscopic techniques might give additional insights on the nature of the alkali sorption sites. That information will extend the knowledge on the cation uptake in M-S-H and provide insights on the retention ability of the M-(A-)S-H for other cations such as Cs^{+}, Sr^{2+} or Ra^{2+} relevant for nuclear safety.

In addition to the question outlined above on the general chemical properties, open questions also remain on porosity and diffusion of ions in M-S-H, M-A-S-H, M-C-S-H and their changes over time.

Finally, also the mechanical properties and the possible swelling pressure generated by such M-(A-)S-H phase are needed to be able to account for them in the design of radioactive waste disposals in deep geological strata.

References:

Adler, M., Mäder, U., Waber, H.N., 1999. High-pH alteration of argillaceous rocks: an experimental study. Schweiz. Mineral. Petrogr. Mitt 79, 445-454.

Allen, A.J., Thomas, J.J., Jennings, H.M., 2007. Composition and density of nanoscale calcium–silicate–hydrate in cement. Nature materials 6, 311-316.

Andersen, M.D., Jakobsen, H.J., Skibsted, J., 2003. Incorporation of aluminum in the calcium silicate hydrate (CSH) of hydrated Portland cements: a high-field ^{27}Al and ^{29}Si MAS NMR investigation. Inorganic Chemistry 42, 2280-2287.

Anderson, G.M., Crerar, D.A., 1993. Thermodynamics in Geochemistry: the Equilibrium Model. Oxford University Press, Oxford.

ANDRA, 2005. Evaluation of the feasibility of a geological repository in an argillaceous formation. Collection Les rapports 2005.

ANDRA, 2013. The Cigeo project, Meuse/Haute-Marne reversible geological disposal facility for radioactive waste.

ANDRA, 2016. Rapport Andra CG-TE-D-NTE-AMOA-SR1-0000-15-0060 – « Dossier d'options de sûreté - Partie exploitation » (DOS-Expl).

Aramendía, M., Borau, V., Jiménez, C., Marinas, J., Ruiz, J., 1997. Characterization of Spanish sepiolites by high-resolution solid-state NMR. Solid state nuclear magnetic resonance 8, 251-256.

Bach, T., Chabas, E., Pochard, I., Cau Dit Coumes, C., Haas, J., Frizon, F., Nonat, A., 2013. Retention of alkali ions by hydrated low-pH cements: Mechanism and Na^+/K^+ selectivity. Cement and Concrete Research 51, 14-21.

Barbarulo, R., 2002. Comportement des matériaux cimentaires: actions des sulfates et de la température, Université Laval Québec.

Barron, P.F., Slade, P., Frost, R.L., 1985. Solid-state silicon-29 spin-lattice relaxation in several 2: 1 phyllosilicate minerals. The Journal of Physical Chemistry 89, 3305-3310.

Bauer, A., Berger, G., 1998. Kaolinite and smectite dissolution rate in high molar KOH solutions at 35 and 80 C. Applied Geochemistry 13, 905-916.

Bell, G., Bensted, J., Glasser, F., Lachowski, E., Roberts, D., Taylor, M., 1990. Study of calcium silicate hydrates by solid state high resolution ^{29}Si nuclear magnetic resonance. Advances in Cement Research 3, 23-27.

Bernard, E., Dauzères, A., Lothenbach, B., 2018a. Magnesium and calcium silicate hydrates, Part II: Mg-exchange at the interface “low-pH” cement and magnesium environment studied in a C-S-H and M-S-H model system. Applied Geochemistry 89, 210-218.

Bernard, E., Lothenbach, B., Cau-Dit-Coumes, C., Chlique, C., Dauzères, A., Pochard, I., 2018b. Magnesium and calcium silicate hydrates, Part I: Investigation of the possible magnesium incorporation in calcium silicate hydrate (C-S-H) and of the calcium in magnesium silicate hydrate (M-S-H). Applied Geochemistry 89, 229-242.

Bernard, E., Lothenbach, B., Le Goff, F., Pochard, I., Dauzères, A., 2017a. Effect of magnesium on calcium silicate hydrate (C-S-H). Cement and Concrete Research 97, 61-72.

Bernard, E., Lothenbach, B., Rentsch, D., Pochard, I., Dauzères, A., 2017b. Formation of magnesium silicate hydrates (M-S-H). Physics and Chemistry of the Earth, Parts A/B/C 99, 142-157.

Bish, D.L., Brindley, G., 1978. Deweylites, mixtures of poorly crystalline hydrous serpentine and talc-like minerals. Mineral. Mag 42, 75-79.

Bisio, C., Gatti, G., Boccaleri, E., Marchese, L., Superti, G., Pastore, H., Thommes, M., 2008. Understanding physico–chemical properties of saponite synthetic clays. Microporous and Mesoporous Materials 107, 90-101.

Black, L., Breen, C., Yarwood, J., Garbev, K., Stemmermann, P., Gasharova, B., 2007. Structural features of C–S–H (I) and its carbonation in air—a Raman spectroscopic study. Part II: carbonated phases. Journal of the American Ceramic Society 90, 908-917.

Blanc, P., Lassin, A., Piantone, P., Azaroual, M., Jacquemet, N., Fabbri, A., Gaucher, E.C., 2012. Thermoddem: A geochemical database focused on low temperature water/rock interactions and waste materials. Applied Geochemistry 27, 2107-2116.

Bonen, D., Cohen, M.D., 1992. Magnesium sulfate attack on portland cement paste—II. Chemical and mineralogical analyses. Cement and Concrete Research 22, 707-718.

Brantley, S.L., Kubicki, J.D., White, A.F., 2008. Kinetics of Water-Rock Interaction. Springer.

Brew, D., Glasser, F., 2005a. The magnesia–silica gel phase in slag cements: alkali (K, Cs) sorption potential of synthetic gels. Cement and Concrete Research 35, 77-83.

Brew, D.R.M., Glasser, F.P., 2005b. Synthesis and characterisation of magnesium silicate hydrate gels. Cement and Concrete Research 35, 85-98.

Brindley, G., Bish, D., Wan, H.-M., 1979. Compositions, structures, and properties of nickel-containing minerals in the kerolite-pimelite series. American Mineralogist 64, 615-625.

Brindley, G., Bistt, D.L., Wan, H.-m., 1977. The nature of kerolite, its relation to talc and stevensite.

Brunauer, S., Emmett, P.H., Teller, E., 1938. Adsorption of gases in multimolecular layers. Journal of the American chemical society 60, 309-319.

Bruzzoniti, M.C., De Carlo, R.M., Fiorilli, S., Onida, B., Sarzanini, C., 2009. Functionalized SBA-15 mesoporous silica in ion chromatography of alkali, alkaline earths, ammonium and transition metal ions. Journal of Chromatography A 1216, 5540-5547.

Cases, J., Bérend, I., Besson, G., Francois, M., Uriot, J., Thomas, F., Poirier, J., 1992. Mechanism of adsorption and desorption of water vapor by homoionic montmorillonite. 1. The sodium-exchanged form. Langmuir 8, 2730-2739.

Cau Dit Coumes, C., Courtois, S., Nectoux, D., Leclercq, S., Bourbon, X., 2006. Formulating a low-alkalinity, high-resistance and low-heat concrete for radioactive waste repositories. Cement and Concrete Research 36, 2152-2163.

Chabrol, K., Gressier, M., Pebere, N., Menu, M.-J., Martin, F., Bonino, J.-P., Marichal, C., Brendle, J., 2010. Functionalization of synthetic talc-like phyllosilicates by alkoxyorganosilane grafting. Journal of Materials Chemistry 20, 9695-9706.

Chen, J.J., Thomas, J.J., Taylor, H.F., Jennings, H.M., 2004. Solubility and structure of calcium silicate hydrate. Cement and Concrete Research 34, 1499-1519.

Chevalier, S., Franck, R., Lambert, J., Barthomeuf, D., Suquet, H., 1994. Characterization of the porous structure and cracking activity of Al-pillared saponites. Applied Catalysis A: General 110, 153-165.

Chiang, W.-S., Ferraro, G., Fratini, E., Ridi, F., Yeh, Y.-Q., Jeng, U., Chen, S.-H., Baglioni, P., 2014. Multiscale structure of calcium-and magnesium-silicate-hydrate gels. Journal of Materials Chemistry A 2, 12991-12998.

Claret, F., Bauer, A., Schäfer, T., Griffault, L., Lanson, B., 2002. Experimental investigation of the interaction of clays with high-pH solutions: A case study from the Callovo-Oxfordian formation, Meuse-Haute Marne underground laboratory (France). Clays and Clay Minerals 50, 633-646.

Codina, M., 2007. Les bétons bas pH-Formulation, caractérisation et étude à long terme. INSA de Toulouse.

Codina, M., Cau-dit-Coumes, C., Le Bescop, P., Verdier, J., Ollivier, J., 2008. Design and characterization of low-heat and low-alkalinity cements. Cement and Concrete Research 38, 437-448.

Cong, X., Kirkpatrick, R.J., 1996. ^{29} Si MAS NMR study of the structure of calcium silicate hydrate. Advanced Cement Based Materials 3, 144-156.

Conway, B., 1981. Ion hydration co-sphere interactions in the double-layer and ionic solutions. Journal of Electroanalytical Chemistry and Interfacial Electrochemistry 123, 81-94.

Costenaro, D., Gatti, G., Carniato, F., Paul, G., Bisio, C., Marchese, L., 2012. The effect of synthesis gel dilution on the physico-chemical properties of acid saponite clays. Microporous and Mesoporous Materials 162, 159-167.

d'Espinose de la caillerie, J.-B., Fripiat, J., 1994. A reassessment of the ^{29}Si MAS-NMR spectra of sepiolite and aluminated sepiolite. Clay minerals 29, 313-318.

d'Espinose de Lacaillerie, J.-B., Kermarec, M., Clause, O., 1995. ^{29}Si NMR observation of an amorphous magnesium silicate formed during impregnation of silica with Mg(II) in aqueous solution. The Journal of Physical Chemistry 99(47), 17273-17281.

Dauzères, A., Achiedo, G., Nied, D., Bernard, E., Alahrache, S., Lothenbach, B., 2016. Magnesium perturbation in low-pH concretes placed in clayey environment - solid characterizations and modeling. Cement and Concrete Research 79, 137-150.

Dauzères, A., Le Bescop, P., Cau-Dit-Coumes, C., Brunet, F., Bourbon, X., Timonen, J., Voutilainen, M., Chomat, L., Sardini, P., 2014. On the physico-chemical evolution of low-pH and CEM I cement pastes interacting with Callovo-Oxfordian pore water under its in situ CO_2 partial pressure. Cement and Concrete Research 58, 76-88.

Dauzères, A., Le Bescop, P., Sardini, P., Cau Dit Coumes, C., 2010. Physico-chemical investigation of clayey/cement-based materials interaction in the context of geological waste disposal: Experimental approach and results. Cement and Concrete Research 40, 1327-1340.

de Lara, L.S., Rigo, V.A., Michelon, M.F., Metin, C.O., Nguyen, Q.P., Miranda, C.R., 2015. Molecular dynamics studies of aqueous silica nanoparticle dispersions: salt effects on the double layer formation. Journal of Physics: Condensed Matter 27, 325101.

De Weerdt, K., Justnes, H., 2015. The effect of sea water on the phase assemblage of hydrated cement paste. Cement and Concrete Composites 55, 215-222.

Deschner, F., Winnefeld, F., Lothenbach, B., Seufert, S., Schwesig, P., Dittrich, S., Goetz-Neunhoeffer, F., Neubauer, J., 2012. Hydration of Portland cement with high replacement by siliceous fly ash. Cement and Concrete Research 42, 1389-1400.

Dódony, I., Pósfai, M., Buseck, P.R., 2002. Revised structure models for antigorite: An HRTEM study. American Mineralogist 87, 1443-1457.

Dove, P.M., Nix, C.J., 1997. The influence of the alkaline earth cations, magnesium, calcium, and barium on the dissolution kinetics of quartz. Geochimica et Cosmochimica Acta 61, 3329-3340.

Dumas, A., Martin, F., Le Roux, C., Micoud, P., Petit, S., Ferrage, E., Brendlé, J., Grauby, O., Greenhill-Hooper, M., 2013. Phyllosilicates synthesis: a way of accessing edges contributions in NMR and FTIR spectroscopies. Example of synthetic talc. Physics and Chemistry of Minerals 40, 361-373.

Egami, T., Billinge, S.J.L., 2003. Chapter 3. The method of total scattering and atomic pair distribution function analysis. Pergamon Materials Series.

Evans, N., 2008. Binding mechanisms of radionuclides to cement. Cement and concrete research 38, 543-553.

Everett, D., 1972. Manual of symbols and terminology for physicochemical quantities and units, appendix II: Definitions, terminology and symbols in colloid and surface chemistry. Pure and Applied Chemistry 31, 577-638.

Falini, G., Foresti, E., Gazzano, M., Gualtieri, A.F., Leoni, M., Lesci, I.G., Roveri, N., 2004. Tubular-Shaped Stoichiometric Chrysotile Nanocrystals. Chemistry-A European Journal 10, 3043-3049.

Farrow, C., Juhas, P., Liu, J., Bryndin, D., Božin, E., Bloch, J., Proffen, T., Billinge, S., 2007. PDFfit2 and PDFgui: computer programs for studying nanostructure in crystals. Journal of Physics: Condensed Matter 19, 335219.

Fernández, R., Torres, E., Ruiz, A.I., Cuevas, J., Alonso, M.C., Calvo, J.L.G., Rodríguez, E., Turrero, M.J., 2017. Interaction processes at the concrete-bentonite interface after 13 years of FEBEX-Plug operation. Part II: Bentonite contact. Physics and Chemistry of the Earth, Parts A/B/C.

Fleury, M., Kohler, E., Norrant, F., Gautier, S., M'Hamdi, J., Barré, L., 2013. Characterization and quantification of water in smectites with low-field NMR. The Journal of Physical Chemistry C 117, 4551-4560.

Frost, R.L., Ding, Z., 2003. Controlled rate thermal analysis and differential scanning calorimetry of sepiolites and palygorskites. Thermochimica Acta 397, 119-128.

Frost, R.L., Kloprogge, J.T., 1999. Infrared emission spectroscopic study of brucite. Spectrochimica Acta Part A: Molecular and Biomolecular Spectroscopy 55, 2195-2205.

Frost, R.L., Locos, O.B., Ruan, H., Kloprogge, J.T., 2001. Near-infrared and mid-infrared spectroscopic study of sepiolites and palygorskites. Vibrational Spectroscopy 27, 1-13.

Frost, R.L., Mendelovici, E., 2006. Modification of fibrous silicates surfaces with organic derivatives: an infrared spectroscopic study. Journal of colloid and interface science 294, 47-52.

Gailhanou, H., Blanc, P., Rogez, J., Mikaelian, G., Horiuchi, K., Yamamura, Y., Saito, K., Kawaji, H., Warmont, F., Grenèche, J.-M., 2013. Thermodynamic properties of saponite, nontronite, and vermiculite derived from calorimetric measurements. American Mineralogist 98, 1834-1847.

Garbev, K., Stemmermann, P., Black, L., Breen, C., Yarwood, J., Gasharova, B., 2007. Structural features of C–S–H (I) and its carbonation in air—a Raman spectroscopic study. Part I: fresh phases. Journal of the American Ceramic Society 90, 900-907.

Garcia Calvo, J.L., Hidalgo, A., Alonso, C., Fernández Luco, L., 2010. Development of low-pH cementitious materials for HLRW repositories: Resistance against ground waters aggression. Cement and Concrete Research 40, 1290-1297.

Gartner, E., Gimenez, M., Meyer, V., Pisch, A., 2014. A Novel Atmospheric Pressure Approach to the Mineral Capture of CO_2 from Industrial Point Sources. Thirteenth annual conference on carbon capture, utilization and storage, Pittsburgh, Pennsylvania.

Gaucher, E., Lerouge, C., 2007. Caractérisation géochimique des forages PAC et nouvelles modélisations THERMOAR, BRGM Reports.

Gaucher, E.C., Blanc, P., 2006. Cement/clay interactions–a review: experiments, natural analogues, and modeling. Waste Management 26, 776-788.

Giese, J.R.F., Wu, W., Van Oss, C.J., 1996. Surface and electrokinetic properties of clays and other mineral particles, untreated and treated with organic or inorganic cations. Journal of dispersion science and technology 17, 527-547.

Gionis, V., Kacandes, G.H., Kastritis, I.D., Chryssikos, G.D., 2006. On the structure of palygorskite by mid-and near-infrared spectroscopy. American Mineralogist 91, 1125-1133.

Gollop, R., Taylor, H., 1992. Microstructural and microanalytical studies of sulfate attack. I. Ordinary Portland cement paste. Cement and Concrete Research 22, 1027-1038.

Golubeva, O.Y., Korytkova, E., Gusarov, V., 2005. Hydrothermal synthesis of magnesium silicate montmorillonite for polymer-clay nanocomposites. Russian journal of applied chemistry 78, 26-32.

Grangeon, S., Claret, F., Lerouge, C., Warmont, F., Sato, T., Anraku, S., Numako, C., Linard, Y., Lanson, B., 2013. On the nature of structural disorder in calcium silicate hydrates with a calcium/silicon ratio similar to tobermorite. Cement and Concrete Research 52, 31-37.

Gruner, J.W., 1934. The crystal structures of talc and pyrophyllite. Zeitschrift für Kristallographie-Crystalline Materials 88, 412-419.

Gunnarsson, I., Arnórsson, S., 2000. Amorphous silica solubility and the thermodynamic properties of H_4SiO_4 in the range of 0 to 350°C at P_{sat}. Geochimica et Cosmochimica Acta 64, 2295-2307.

Gunnarsson, I., Arnórsson, S., 2005. Precipitation of poorly crystalline antigorite under hydrothermal conditions. Geochimica et Cosmochimica Acta 69, 2813-2828.

Haas, J., 2012. Etude expérimentale et modélisation thermodynamique du système CaO-SiO_2-(Al_2O_3)-H_2O. Université de Bourgogne.

Haas, J., Nonat, A., 2015. From C–S–H to C–A–S–H: Experimental study and thermodynamic modelling. Cement and Concrete Research 68, 124-138.

Hair, M.L., 1975. Hydroxyl groups on silica surface. Journal of Non-Crystalline Solids 19, 299-309.

Halperin, W.P., Jehng, J.-Y., Song, Y.-Q., 1994. Application of spin-spin relaxation to measurement of surface area and pore size distributions in a hydrating cement paste. Magnetic Resonance Imaging 12, 169-173.

Helgeson, H.C., 1978. Summary and critique of the thermodynamic properties of rock-forming minerals. American Journal of Science 278, 1-229.

Hibino, T., Tsunashima, A., 1998. Characterization of repeatedly reconstructed Mg− Al hydrotalcite-like compounds: Gradual segregation of aluminum from the structure. Chemistry of materials 10, 4055-4061.

Holland, T., Powell, R., 1998. An internally consistent thermodynamic data set for phases of petrological interest. Journal of metamorphic Geology 16, 309-343.

Hong, S.-Y., Glasser, F., 1999. Alkali binding in cement pastes: Part I. The CSH phase. Cement and Concrete Research 29, 1893-1903.

Hummel, W., Berner, U., Curti, E., Pearson, F.J., Thoenen, T., 2002. Nagra/PSI Chemical Thermodynamic Data Base 01/01. Universal Publishers/uPUBLISH.com, USA, also published as Nagra Technical Report NTB 02-16, Wettingen, Switzerland.

Ivanova, V., Kasatov, B., Moskaleva, V., 1974. Thermographic studies of serpentines by ignition up to 1400° C. International Geology Review 16, 202-213.

Jakobsen, U.H., De Weerdt, K., Geiker, M.R., 2016. Elemental zonation in marine concrete. Cement and Concrete Research 85, 12-27.

James, M., Hunter, R.J., O'Brien, R.W., 1992. Effect of particle size distribution and aggregation on electroacoustic measurements of. zeta. potential. Langmuir 8, 420-423.

Jenni, A., Mäder, U., Lerouge, C., Gaboreau, S., Schwyn, B., 2014. In situ interaction between different concretes and Opalinus Clay. Physics and Chemistry of the Earth, Parts A/B/C 70, 71-83.

Jin, F., Al-Tabbaa, A., 2013. Thermogravimetric study on the hydration of reactive magnesia and silica mixture at room temperature. Thermochimica Acta 566, 162-168.

Kalousek, G.L., Mui, D., 1954. Studies on formation and recrystallization of intermediate reaction products in the system magnesia-silica-water. Journal of the American Ceramic Society 37, 38-42.

Kaya, A., Yukselen, Y., 2005. Zeta potential of clay minerals and quartz contaminated by heavy metals. Canadian Geotechnical Journal 42, 1280-1289.

Kirkpatrick, R.J., Yarger, J., McMillan, P.F., Ping, Y., Cong, X., 1997. Raman spectroscopy of CSH, tobermorite, and jennite. Advanced Cement Based Materials 5, 93-99.

Klur, I., Pollet, B., Virlet, J., Nonat, A., 1998. CSH structure evolution with calcium content by multinuclear NMR, Nuclear magnetic resonance spectroscopy of cement-based materials. Springer, pp. 119-141.

Komarneni, S., Fyfe, C.A., Kennedy, G.J., Strobl, H., 1986. Characterization of Synthetic and Naturally Occurring Clays by 27Al and 29Si Magic-Angle Spinning NMR Spectroscopy. Journal of the American Ceramic Society 69.

Kulik, D., 2002. Minimising uncertainty induced by temperature extrapolations of thermodynamic data: a pragmatic view on the integration of thermodynamic databases into geochemical computer codes, The use of thermodynamic databases in performance assessment. OECD, Barcelona, pp. 125-137.

Kulik, D., Wagner, T., Dmytrieva, S.V., Kosakowski, G., Hingerl, F., Chudnenko, K.V., Berner, U., 2013a. GEM-Selektor geochemical modeling package: revised algorithm and GEMS3K numerical kernel for coupled simulation codes. Computational Geochemistry 17, 1-24.

Kulik, D.A., 2011. Improving the structural consistency of CSH solid solution thermodynamic models. Cement and Concrete Research 41, 477-495.

Kulik, D.A., Wagner, T., Dmytrieva, S.V., Kosakowski, G., Hingerl, F.F., Chudnenko, K.V., Berner, U.R., 2013b. GEM-Selektor geochemical modeling package: revised algorithm and GEMS3K numerical kernel for coupled simulation codes. Computational Geosciences 17, 1-24.

Kunther, W., Lothenbach, B., Scrivener, K.L., 2013. Deterioration of mortar bars immersed in magnesium containing sulfate solutions. Materials and structures 46, 2003-2011.

Kunther, W., Lothenbach, B., Skibsted, J., 2015. Influence of the Ca/Si ratio of the C–S–H phase on the interaction with sulfate ions and its impact on the ettringite crystallization pressure. Cement and Concrete Research 69, 37-49.

L'Hôpital, E., Lothenbach, B., Kulik, D., Scrivener, K., 2016a. Influence of calcium to silica ratio on aluminium uptake in calcium silicate hydrate. Cement and Concrete Research 85, 111-121.

L'Hôpital, E., Lothenbach, B., Scrivener, K., Kulik, D., 2016b. Alkali uptake in calcium alumina silicate hydrate (CASH). Cement and Concrete Research 85, 122-136.

L'Hôpital, E., Lothenbach, B., Le Saout, G., Kulik, D., Scrivener, K., 2015. Incorporation of aluminium in calcium-silicate-hydrates. Cement and Concrete Research 75, 91-103.

Labbez, C., Nonat, A., Pochard, I., Jönsson, B., 2007. Experimental and theoretical evidence of overcharging of calcium silicate hydrate. Journal of Colloid and Interface Science 309, 303-307.

Labbez, C., Pochard, I., Jönsson, B., Nonat, A., 2011. CSH/solution interface: Experimental and Monte Carlo studies. Cement and Concrete Research 41, 161-168.

Lalan, P., Dauzères, A., De Windt, L., Bartier, D., Sammaljärvi, J., Barnichon, J.-D., Techer, I., Detilleux, V., 2016. Impact of a 70° C temperature on an ordinary Portland cement paste/claystone interface: An in situ experiment. Cement and Concrete Research 83, 164-178.

Le Saout, G., Lécolier, E., Rivereau, A., Zanni, H., 2006. Chemical structure of cement aged at normal and elevated temperatures and pressures: Part I. Class G oilwell cement. Cement and Concrete Research 36, 71-78.

Leisinger, S.M., Bhatnagar, A., Lothenbach, B., Johnson, C.A., 2014. Solubility of chromate in a hydrated OPC. Applied Geochemistry 48, 132-140.

Lequeux, N., Morau, A., Philippot, S., Boch, P., 1999. Extended X-ray Absorption Fine Structure Investigation of Calcium Silicate Hydrates. Journal of the American Ceramic Society 82, 1299-1306.

Lerouge, C., Gaboreau, S., Grangeon, S., Claret, F., Warmont, F., Jenni, A., Cloet, V., Mäder, U., 2017. In situ interactions between Opalinus Clay and Low Alkali Concrete. Physics and Chemistry of the Earth, Parts A/B/C 99, 3-21.

Li, L., Liu, X., Ge, Y., Xu, R., Rocha, J., Klinowski, J., 1993. Structural studies of pillared saponite. The Journal of Physical Chemistry 97, 10389-10393.

Li, Z., Zhang, T., Hu, J., Tang, Y., Niu, Y., Wei, J., Yu, Q., 2014. Characterization of reaction products and reaction process of $MgO–SiO_2–H_2O$ system at room temperature. Construction and Building Materials 61, 252.

Lin, L., Cornu, D., Daou, M.M., Domingos, C., Herledan, V., Krafft, J.-M., Laugel, G., Millot, Y., Lauron-Pernot, H., 2017. Role of Water on the Activity of Magnesium Silicate for Transesterification Reactions. ChemCatChem, Wiley Omline Library 9.

Lippens, B.C., De Boer, J., 1965. Studies on pore systems in catalysts: V. The t method. Journal of Catalysis 4, 319-323.

Lippmaa, E., Samoson, A., Magi, M., 1986. High-resolution aluminum-27 NMR of aluminosilicates. Journal of the American Chemical Society 108, 1730-1735.

Lothenbach, B., Bernard, E., Mäder, U., 2017. Zeolite formation in the presence of cement hydrates and albite. Physics and Chemistry of the Earth, Parts A/B/C.

Lothenbach, B., Durdzinski, P., DeWeerdt, K., 2016. Thermogravimetric analysis, in: Scrivener, K., Snellings, R., Lothenbach, B. (Eds.), A Practical Guide to Microstructural Analysis of Cementitious Materials. CRC Press, Oxford, UK, pp. 177-212.

Lothenbach, B., Le Saout, G., Ben Haha, M., Figi, R., Wieland, E., 2012a. Hydration of a low-alkali CEM III/B–SiO2 cement (LAC). Cement and Concrete Research 42, 410-423.

Lothenbach, B., Matschei, T., Möschner, G., Glasser, F.P., 2008. Thermodynamic modelling of the effect of temperature on the hydration and porosity of Portland cement. Cement and Concrete Research 38, 1-18.

Lothenbach, B., Nied, D., L'Hôpital, E., Achiedo, G., Dauzères, A., 2015. Magnesium and calcium silicate hydrates. Cement and Concrete Research 77, 60-68.

Lothenbach, B., Nonat, A., 2015. Calcium silicate hydrates: Solid and liquid phase composition. Cement and Concrete Research 78, 57-70.

Lothenbach, B., Pelletier-Chaignat, L., Winnefeld, F., 2012b. Stability in the system $CaO–Al_2O_3–H_2O$. Cement and Concrete Research 42, 1621-1634.

Lothenbach, B., Rentsch, D., Wieland, E., 2014. Hydration of a silica fume blended low-alkali shotcrete cement. Physics and Chemistry of the Earth, Parts A/B/C 70, 3-16.

Lothenbach, B., Winnefeld, F., 2006. Thermodynamic modelling of the hydration of Portland cement. Cem Concr Res 36, 209-226.

MacKenzie, K., Meinhold, R., 1994a. The thermal reactions of talc studied by 29 Si and 25 Mg MAS NMR. Thermochimica Acta 244, 195-203.

MacKenzie, K.J.D., Meinhold, R.H., 1994b. Thermal reaction of chrysotile revisited: a ^{29}Si and ^{25}Mg NMR study. American Mineralogist 79, 43-50.

Mäder, U., Jenni, A., Lerouge, C., Gaboreau, S., Miyoshi, S., Kimura, Y., Cloet, V., Fukaya, M., Claret, F., Otake, T., Shibata, M., Lothenbach, B., 2017. 5-year chemico-physical evolution of concrete-claystone interfaces. Swiss Journal of Geosciences 110, 307-327.

Mägi, M., Lippmann, E., Samoson, A., Engelhardt, G., Grimmer, A.R., 1984. Solid-state high-resolution silicon-29 chemical shifts in silicates. The Journal of Physical Chemistry 88, 1518-1522.

Markham, G.D., Glusker, J.P., Bock, C.W., 2002. The arrangement of first-and second-sphere water molecules in divalent magnesium complexes: Results from molecular orbital and density functional theory and from structural crystallography. The Journal of Physical Chemistry B 106, 5118-5134.

Martin, L.H., Winnefeld, F., Tschopp, E., Müller, C.J., Lothenbach, B., 2017. Influence of fly ash on the hydration of calcium sulfoaluminate cement. Cement and Concrete Research 95, 152-163.

Massiot, D., Fayon, F., Capron, M., King, I., Le Calvé, S., Alonso, B., Durand, J.O., Bujoli, B., Gan, Z., Hoatson, G., 2002. Modelling one-and two-dimensional solid-state NMR spectra. Magnetic Resonance in Chemistry 40, 70-76.

Matschei, T., Lothenbach, B., Glasser, F.P., 2007. Thermodynamic properties of Portland cement hydrates in the system $CaO–Al_2O_3–SiO_2–CaSO_4–CaCO_3–H_2O$. Cement and Concrete Research 37, 1379-1410.

Melekhova, E., Schmidt, M.W., Ulmer, P., Guggenbühl, E., 2006. The reaction talc + forsterite = enstatite + H_2O revisited: Application of conventional and novel experimental techniques and derivation of revised thermodynamic properties. American Mineralogist 91, 1081-1088.

Mellini, M., Zanazzi, P.F., 1987. Crystal structures of lizardite-1T and lizardite-2H1 from Coli, Italy. American Mineralogist 72, 943-948.

Meral, C., Benmore, C., Monteiro, P.J., 2011. The study of disorder and nanocrystallinity in C–S–H, supplementary cementitious materials and geopolymers using pair distribution function analysis. Cement and Concrete Research 41, 696-710.

Merkel, B.J., Planer-Friedrich, B., 2008. Groundwater geochemistry. A Practical Guide to Modeling of Natural and Contaminated Aquatic Systems Springer Berlin.

Michot, L., Villieras, F., François, M., Yvon, J., Le Dred, R., Cases, J., 1994. The structural microscopic hydrophilicity of talc. Langmuir 10, 3765-3773.

Miller, J.D., Nalaskowski, J., Abdul, B., Du, H., 2007. Surface characteristics of kaolinite and other selected two layer silicate minerals. The Canadian Journal of Chemical Engineering 85, 617-624.

Mitsuda, T., 1973. Paragenesis of 11 Å tobermorite and poorly crystalline hydrated magnesium silicate. Cement and Concrete Research 3, 71-80.

Mitsuda, T., Taguchi, H., 1977. Formation of magnesium silicate hydrate and its crystallzation to talc. Cement and Concrete Research 7, 223-230.

Momma, K., Izumi, F., 2011. VESTA 3 for three-dimensional visualization of crystal, volumetric and morphology data. Journal of Applied Crystallography 44, 1272-1276.

Muller, A.C.A., Mitchell, J., McDonald, P.J., 2016. Proton nuclear magnetic resonance relaxometry, in: Scrivener, K., Snellings, R., Lothenbach, B. (Eds.), A Practical Guide to Microstructural Analysis of Cementitious Materials. CRC Press, Oxford, UK, pp. 177-212.

Myers, R.J., L'Hôpital, E., Provis, J.L., Lothenbach, B., 2015a. Effect of temperature and aluminium on calcium (alumino)silicate hydrate chemistry under equilibrium conditions. . Cement and Concrete Research 68, 83-93.

Myers, R.J., Lothenbach, B., Bernal, S.A., Provis, J.L., 2015b. Thermodynamic modelling of alkali-activated slag cements. Applied Geochemistry 61, 233-247.

Nagata, H., Shimoda, S., Sudo, T., 1974. On dehydration f bound water of sepiolite, Clays & Clay Minerals. Citeseer.

NAGRA, 2002. Demonstration of feasibility of disposal ("Entsorgungsnachweis") for spent fuel, vitrified high-level waste and long-lived intermediate-level waste. Opalinus Clay Project.

Nied, D., Enemark-Rasmussen, K., L'Hopital, E., Skibsted, J., Lothenbach, B., 2016. Properties of magnesium silicate hydrates (MSH). Cement and Concrete Research 79, 323-332.

Nied, D., Lothenbach, B., L'Hopital, E., 2011. Synthesis, structural characterization and solubility of M-S-H gel. TN 2011-50 Part 2, Empa technical note.

Pearson, F.J., Arcos, D., Bath, A., Boisson, J.-Y., Fernandez, A.M., Gäbler, H.-E., Gaucher, E., Gautschi, A., Griffault, L., Hernan, P., Waber, H.N., 2003. Mont-Terri Project – Geochemistry of Water in the Opalinus Clay Formation at the Mont Terri Rock Laboratory. Reports of the FOWG, Geology Series 5, 319.

Pedone, A., Palazzetti, F., Barone, V., 2017. Models of Aged Magnesium–Silicate–Hydrate Cements Based on the Lizardite and Talc Crystals: A Periodic DFT-GIPAW Investigation. The Journal of Physical Chemistry C.

Peyronnard, O., Benzaazoua, M., Blanc, D., Moszkowicz, P., 2009. Study of mineralogy and leaching behavior of stabilized/solidified sludge using differential acid neutralization analysis: Part I: Experimental study. Cement and Concrete Research 39, 600-609.

Plusquellec, G., 2014. Analyse in situ de suspensions de silicate de calcium hydraté: application aux interactions ioniques à la surface des particules. Université de Bourgogne.

Plusquellec, G., Nonat, A., 2016. Interactions between calcium silicate hydrate (CSH) and calcium chloride, bromide and nitrate. Cement and Concrete Research 90, 89-96.

Pokrovsky, O.S., Schott, J., 2004. Experimental study of brucite dissolution and precipitation in aqueous solutions: surface speciation and chemical affinity control. Geochimica et Cosmochimica Acta 68, 31-45.

Poyet, S., Le Bescop, P., Cau Dit Coumes, C., Touzé, G., Moth, J., 2014. Formulating a low-alkanity and self-consolidating concrete for the DOPAS-FSS experiment. NUWCEM, 2nd international symposium on cement-based materials for nuclear waste, Avignon, France.

Qiu, X., Thompson, J.W., Billinge, S.J., 2004. PDFgetX2: a GUI-driven program to obtain the pair distribution function from X-ray powder diffraction data. Journal of Applied Crystallography 37, 678-678.

Ramírez, S., Cuevas, J., Vigil, R., Leguey, S., 2002. Hydrothermal alteration of "La Serrata" bentonite (Almeria, Spain) by alkaline solutions. Applied Clay Science 21, 257-269.

Renaudin, G., Russias, J., Leroux, F., Cau-dit-Coumes, C., Frizon, F., 2009. Structural characterization of C–S–H and C–A–S–H samples—Part II: Local environment investigated by spectroscopic analyses. Journal of Solid State Chemistry 182, 3320-3329.

Rhouta, B., Kaddami, H., Elbarqy, J., Amjoud, M., Daoudi, L., Maury, F., Senocq, F., Maazouz, A., Gerard, J.-F., 2008. Elucidating the crystal-chemistry of Jbel Rhassoul stevensite (Morocco) by advanced analytical techniques. Clay minerals 43, 393-403.

Richardson, I., Skibsted, J., Black, L., Kirkpatrick, R.J., 2010a. Characterisation of cement hydrate phases by TEM, NMR and Raman spectroscopy. Advances in Cement Research 22, 233-248.

Richardson, I.G., 2008. The calcium silicate hydrates. Cement and Concrete Research 38, 137-158.

Richardson, I.G., Brough, A.R., Brydson, R., Groves, G.W., Dobson, C.M., 1993. Location of aluminum in substituted calcium silicate hydrate (C-S-H) gels as determined by ^{29}Si and ^{27}Al NMR and EELS. Journal of the American Ceramic Society 76, 2285-2288.

Richardson, I.G., Skibsted, J., Black, L., Kirkpatrick, R.J., 2010b. Characterisation of cement hydrate phases by TEM, NMR and Raman spectroscopy. Advanced Cement Based Materials 22, 233-248.

Roosz, C., Gaboreau, S., Grangeon, S., Prêt, D., Montouillout, V., Maubec, N., Ory, S., Blanc, P., Vieillard, P., Henocq, P., 2016. Distribution of water in synthetic calcium silicate hydrates. Langmuir 32, 6794-6805.

Roosz, C., Grangeon, S., Blanc, P., Montouillout, V., Lothenbach, B., Henocq, P., Giffaut, E., Vieillard, P., Gaboreau, S., 2015. Crystal structure of magnesium silicate hydrates (MSH): The relation with 2: 1 Mg–Si phyllosilicates. Cement and Concrete Research 73, 228-237.

Salomão, R., Pandolfelli, V., 2008. Efeito da adição de microssílica na hidratação de óxido de magnésio em concretos refratários (Microsilica addition as anti-hydration technique of magnesia in refractory castables). Cerâmica 54, 43-48.

Sánchez del Río, M., García-Romero, E., Suárez, M., Silva, I.d., Fuentes-Montero, L., Martínez-Criado, G., 2011. Variability in sepiolite: Diffraction studies. American Mineralogist 96, 1443-1454.

Santhanam, M., Cohen, M.D., Olek, J., 2002. Mechanism of sulfate attack: a fresh look: part 1: summary of experimental results. Cement and concrete research 32, 915-921.

Sanz, J., Serratosa, J., 1984. Silicon-29 and aluminum-27 high-resolution MAS-NMR spectra of phyllosilicates. Journal of the American Chemical Society 106, 4790-4793.

Sato, H., Grutzeck, M., 1991. Effect of starting materials on the synthesis of tobermorite, MRS Proceedings, 245. Cambridge Univ Press, pp. 235-240.

Savage, D., Walker, C., Arthur, R., Rochelle, C., Oda, C., Takase, H., 2007. Alteration of bentonite by hyperalkaline fluids: A review of the role of secondary minerals. Physics and Chemistry of the Earth, Parts A/B/C 32, 287-297.

Shariatmadari, H., Mermut, A., Benke, M., 1999. Sorption of selected cationic and neutral organic molecules on palygorskite and sepiolite. Clays and Clay Minerals 47, 44-53.

Shi, C., Stegemann, J., 2000. Acid corrosion resistance of different cementing materials. Cement and Concrete Research 30, 803-808.

Sing, K., Everett, D., Haul, R., Moscou, L., Pierotti, R., Rouquerol, J., Siemieniewska, T., 1985. Reporting physisorption data for gas/solid systems with special reference to the determination of surface area and porosity. Pure and Applied Chemistry 57, 603-619.

Skibsted, J., Henderson, E., Jakobsen, H.J., 1993. Characterization of calcium aluminate phases in cements by aluminum-^{27}MAS NMR spectroscopy. Inorganic chemistry 32, 1013-1027.

Skinner, L., Chae, S., Benmore, C., Wenk, H., Monteiro, P., 2010. Nanostructure of calcium silicate hydrates in cements. Physical review letters 104, 195502.

Skluzacek, J.M., Tejedor, M.I., Anderson, M.A., 2006. An iron-modified silica nanofiltration membrane: Effect of solution composition on salt rejection. Microporous and mesoporous materials 94, 288-294.

Swanton, S., Heath, T., Clacher, A., 2016. Leaching behaviour of low Ca: Si ratio CaO–SiO 2–H 2 O systems. Cement and Concrete Research 88, 82-95.

Szczerba, J., Prorok, R., Śnieżek, E., Madej, D., Maślona, K., 2013. Influence of time and temperature on ageing and phases synthesis in the $MgO–SiO_2–H_2O$ system. Thermochimica Acta 567, 57-64.

Tardy, Y., Duplay, J., 1992. A method of estimating the Gibbs free energies of formation of hydrated and dehydrated clay minerals. Geochimica et Cosmochimica Acta 56, 3007-3029.

Thoenen, T., Hummel, W., Berner, U., Curti, E., 2014. The PSI/Nagra Chemical Thermodynamic Database 12/07. PSI report 14-04, Villigen PSI, Switzerland.

Tits, J., Iijima, K., Wieland, E., Kamei, G., 2006. The uptake of radium by calcium silicate hydrates and hardened cement paste. Radiochimica Acta 94, 637-643.

Tonelli, M., Martini, F., Calucci, L., Fratini, E., Geppi, M., Ridi, F., Borsacchi, S., Baglioni, P., 2016. Structural characterization of magnesium silicate hydrate: towards the design of eco-sustainable cements. Dalton Transactions 45, 3294-3304.

Tremosa, J., Arcos, D., Matray, J., Bensenouci, F., Gaucher, E.C., Tournassat, C., Hadi, J., 2012. Geochemical characterization and modelling of the Toarcian/Domerian porewater at the Tournemire underground research laboratory. Applied geochemistry 27, 1417-1431.

Valori, A., McDonald, P.J., Scrivener, K.L., 2013. The morphology of C–S–H: Lessons from 1 H nuclear magnetic resonance relaxometry. Cement and Concrete Research 49, 65-81.

Van der Lee, J., 1998. Thermodynamic and mathematical concepts of CHESS. Technical Report Nr LHM/RD/98/39 Ecole des Mines de Paris, Fontainebleau, France.

Van Der Lee, J., De Windt, L., Lagneau, V., Goblet, P., 2003. Module-oriented modeling of reactive transport with HYTEC. Computers & Geosciences 29, 265-275.

Viallis-Terrisse, H., Nonat, A., Petit, J.-C., 2001. Zeta-potential study of calcium silicate hydrates interacting with alkaline cations. Journal of colloid and interface science 244, 58-65.

Vidal, O., Baldeyrou, A., Beaufort, D., Fritz, B., Geoffroy, N., Lanson, B., 2012. Experimental study of the stability and phase relations of clays at high temperature in a thermal gradient. Clays and Clay Minerals 60, 200-225.

Vogels, R., Kloprogge, J.T., Geus, J.W., 2005. Synthesis and characterization of saponite clays. American Mineralogist 90, 931-944.

Vollpracht, A., Lothenbach, B., Snellings, R., Haufe, J., 2015. The pore solution of blended cements: a review. Materials and Structures, 1-27.

Walker, C.S., Sutou, S., Oda, C., Mihara, M., Honda, A., 2016. Calcium silicate hydrate (CSH) gel solubility data and a discrete solid phase model at 25° C based on two binary non-ideal solid solutions. Cement and Concrete Research 79, 1-30.

Walling, S.A., Kinoshita, H., Bernal, S.A., Collier, N.C., Provis, J.L., 2015. Structure and properties of binder gels formed in the system $Mg(OH)_2$-SiO_2-H_2O for immobilisation of Magnox sludge. Dalton Transactions 44, 8126-8137.

Wei, J., Yu, Q., Zhang, W., Zhang, H., 2011. Reaction products of MgO and microsilica cementitious materials at different temperatures. Journal of Wuhan University of Technology-Mater. Sci. Ed. 26, 745-748.

Weir, M.R., Kuang, W., Facey, G.A., Detellier, C., 2002. Solid-state nuclear magnetic resonance study of sepiolite and partially dehydrated sepiolite. Clays and Clay Minerals 50, 240-247.

Welch, M.D., Rocha, J., Klinowski, J., 1992. Characterization of polysomatism in biopyriboles: double-/triple-chain lamellar intergrowths. Physics and chemistry of minerals 18, 460-468.

White, C.E., 2016. Effects of temperature on the atomic structure of synthetic calcium–silicate–deuterate gels: A neutron pair distribution function investigation. Cement and Concrete Research 79, 93-100.

White, C.E., Daemen, L.L., Hartl, M., Page, K., 2015. Intrinsic differences in atomic ordering of calcium (alumino) silicate hydrates in conventional and alkali-activated cements. Cement and Concrete Research 67, 66-73.

White, C.E., Provis, J.L., Bloomer, B., Henson, N.J., Page, K., 2013. In situ X-ray pair distribution function analysis of geopolymer gel nanostructure formation kinetics. Physical Chemistry Chemical Physics 15, 8573-8582.

Wieland, E., Tits, J., Bradbury, M., 2004. The potential effect of cementitious colloids on radionuclide mobilisation in a repository for radioactive waste. Applied Geochemistry 19, 119-135.

Wollast, R., MacKenzie, F.T., Bricker, O.P., 1968. Experimental precipitation and genesis of sepiolite at earth-surface conditions. The American Mineralogist 53, 1645-1662.

Yang, J.C.S., 1960. The system magnesia-silica-water below 300° C.: I, Low-temperature phases from 100° to 300° C. and their properties. Journal of the American Ceramic Society 43, 542-549.

Yu, P., Kirkpatrick, R.J., Poe, B., McMillan, P.F., Cong, X., 1999. Structure of calcium silicate hydrate (C-S-H): Near-, Mid-, and Far-infrared spectroscopy. Journal of the American Ceramic Society 82, 742-748.

Zhang, T., Cheeseman, C., Vandeperre, L., 2011. Development of low pH cement systems forming magnesium silicate hydrate (MSH). Cement and Concrete Research 41, 439-442.

Zhang, T., Vandeperre, L.J., Cheeseman, C.R., 2012. Magnesium-silicate-hydrate cements for encapsulating problematic aluminium containing wastes. Journal of Sustainable Cement-Based Materials 1, 34-45.

Zhuravlev, L., 2000. The surface chemistry of amorphous silica. Zhuravlev model. Colloids and Surfaces A: Physicochemical and Engineering Aspects 173, 1-38.

Zigan, F., Rothbauer, R., 1967. Neutron diffraction measurement on brucite. Neues Jahrb Mineral, Monatsh 4, 137-143.

Appendix:

Appendix A: Sketches of the Cigéo project, based on (ANDRA, 2013).

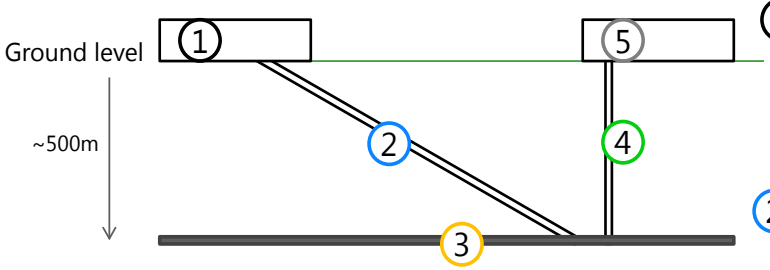

1 Waste package receipt and preparation zone
Located a few kilometers away from the excavation site, this zone will consist of buildings for receiving, inspecting and preparing waste packages before their transfer to the underground facility.

2 Ramps
One ramp will be used to transfer waste packages to the underground facility, while another will be used as a technical access drift.

3 Underground facility
The Cigeo underground facility will be expanded as needed during its operation and will be divided into various zones.

4 Shaft
Five vertical shafts will connect the underground facility to the surface work zone. They will be used to transport personnel, materials and equipment up and down, carry excavated rock to the surface and supply fresh air to the underground installations.

5 Base of underground excavation and construction work
Located directly above the underground facility, this zone will be used in particular as a base for excavating and building the underground structures. The rock excavated during the building of these structures will be piled in this zone.

Appendix B: Summary of the experimentally determined Mg/Si molar ratios, presence of brucite and/or silica fume, pH values, measured dissolved concentrations in the solutions in equilibrium with the synthesized M-S-H samples and calculated ion activity products of M-S-H with Mg/Si=0.78, 1.00 and 1.30.

temp.	equilibration time	initial Mg/Si	Mg/Si	brucite[a]	unreacted silica[b]	pH (20°C)	[Mg] mmol/l	[Si]	Log K_{s0} $M_{0.78}SH_{1.48}$	$MSH_{1.60}$	$M_{1.30}SH_{1.80}$
Undersaturation											
7°C	1.5 Years	0.8	*n.d.*		X	8.6	1.14	1.19	**-14.8**	-13.9	-22.7
		1.2	*n.d.*	X		9.7	1.35	0.003	-15.8	-14.4	**-22.6**
Oversaturation											
20°C	3 months	0.8	**0.81**	X	X	9.6	0.28	1.54	-13.6	-16.6	-20.7
		0.9	*n.d.*	X	X	9.3	0.26	1.53	-13.1	**-15.9**	-19.8
		1	*n.d.*	X	X	9.5	0.2	1.51	-12.7	**-15.4**	-19
		1.1	*n.d.*	X	X	9.5	0.18	1.52	-12.5	**-15**	-18.4
		1.2	*n.d.*	X	X	9.4	0.13	1.52	-12.5	-15.1	-18.5
		1.3	*n.d.*	X	X	9.5	0.26	1.29	-12.3	-14.7	-18
		1.4	**1.09**	X	X	9.3	0.21	1.14	-12.5	-14.9	-18.1
	6 months	0.8	*n.d.*		X	9.1	0.32	1.24	-14.5	-17.6	-22.1
		0.9	*n.d.*		X	9.5	0.34	0.2	-13.7	**-16.4**	-20.4
		1	1.00[c]	X		10	0.26	0.06	-13.6	**-16**	-19.5
		1.1	1.03[c]	X		10.5	0.29	0.05	-13	**-15**	-18.1
		1.2	1.14[c]	X		10.6	0.21	0.011	-13.5	-15.5	-18.7
		1.3	1.17[c]	X		10.7	0.17	0.013	-13.4:	-15.5	-18.6
		1.4	1.20[c]	X		10.7	0.03	0.42	-12.3	-14.4	-17.6

	1 Year	0.8	**0.84**		X	8.5	0.33	1.36	**-14.5**	-17.8	-22.3
		0.9	*n.d.*		X	8.7	0.32	0.66	**-14.6**	**-17.8**	-22.2
		1	**1**			9.3	0.26	0.07	-14.6	**-17.6**	-21.5
		1.1	1.10 [c]			9.9	0.13	0.02	-14.8	**-17.5**	**-21.2**
		1.2	**1.19**	X		10.3	0.1	0.004	-15.2	-17.8	**-21.3**
		1.3	1.17 [c]	X		10.4	0.1	0.003	-15.2	-17.8	**-21.2**
		1.4	**1.25**	X		10.4	0.13	0.004	-15	-17.6	**-21**
	2 Years	0.7	*n.d.*		X	8.2	0.37	1.47	**-14.9**	-18.2	-22.9
		0.8	**0.83**		X	8.3	0.38	1.44	**-14.7**	-18	-22.5
		0.9	*n.d.*		X	8.6	0.4	0.34	-14.9	**-18.1**	-22.5
		1	**1**			9.2	0.35	0.06	-14.9	**-17.9**	-21.9
		1.1	1.10 [c]			9.8	0.15	0.008	-15.2	**-18**	-21.8
		1.2	**1.2**			10	0.13	0.008	-15	-17.7	-21.4
		1.3	1.28 [c]	X		10.3	0.09	0.003	-15.3	-17.9	**-21.4**
		1.4	1.29 [c]	X		10.3	0.12	0.001	-15.7	-18.3	**-21.8**
50°C	1 month	0.7	*n.d.*	X	X	8.6	0.21	2.03	-13.5	-16.5	-20.7
		0.8	*n.d.*	X	X	8.6	0.22	2.03	-13.4	-16.4	-20.5
		0.9	*n.d.*	X	X	8.7	0.21	2.15	-13.3	**-16.3**	-20.4
		1	*n.d.*	X	X	8.8	0.25	1.89	-13.2	**-16.2**	-20.2
		1.1	*n.d.*	X	X	8.9	0.22	1.77	-13.2	**-16.1**	-20.1
		1.2	1.05 [c]	X		10.1	0.2	0.03	-13.7	-16.2	-19.7
		1.3	1.18 [c]	X		9.6	0.23	0.34	-13.1	-15.8	-19.5
		1.4	1.18 [c]	X		10	0.26	0.18	-13	-15.5	-19
	3 months	0.7	*n.d.*		X	8.5	0.21	2.93	**-13.5**	-16.6	-19.5
		0.8	*n.d.*		X	8.6	0.22	2.81	**-13.4**	-16.4	-19.3
		0.9	*n.d.*		X	8.6	0.25	1.57	**-13.6**	**-16.6**	-19.5
		1	*n.d.*	X	X	9.1	0.22	0.48	**-13.5**	**-16.4**	-19
		1.1	1.08 [c]	X		9.7	0.26	0.03	-14	**-16.6**	**-18.9**
		1.2	1.15 [c]	X		9.7	0.21	0.03	-14.1	-16.8	**-19.1**
		1.3	1.20 [c]	X		9.8	0.19	0.01	-14.4	-17	**-19.2**
		1.4	1.26 [c]	X		9.9	0.19	0.02	-14.1	-16.7	**-18.9**
	6 months	0.7	*n.d.*		X	8.0	0.12	2.57	**-13.9**	-17.1	-21.4
		0.8	*n.d.*		X	8.3	0.09	2.5	**-13.9**	-17.1	-21.4
		0.9	*n.d.*		X	8.3	0.16	1.81	**-13.8**	**-16.9**	-21.2
		1	*n.d.*		X	8.6	0.29	0.51	**-13.9**	**-16.9**	-20.9
		1.1	1.09 [c]	X		9.5	0.31	0.02	-14.2	**-16.8**	**-20.4**
		1.2	1.17 [c]	X		9.6	0.33	0.01	-14.4	-17	**-20.5**
		1.3	1.24 [c]	X		9.8	0.32	0.01	-14.4	-16.9	**-20.4**
		1.4	1.30 [c]	X		9.9	0.35	0.004	-14.5	-17	**-20.4**
	1 Year	0.7	*n.d.*		X	8.3	0.1	2.51	**-13.9**	-17.1	-21.4
		0.8	**0.85**		X	8.3	0.1	2.57	**-13.9**	-17.1	-21.4
		0.9	*n.d.*		X	8.5	0.14	1.38	**-13.9**	**-17**	-21.2
		1	**1**			8.7	0.35	0.27	-13.9	**-16.8**	-20.8
		1.1	1.10 [c]			9.3	0.43	0.04	-14.1	**-16.9**	**-20.6**
		1.2	**1.2**	X		9.9	0.19	0.006	-14.5	-17.1	**-20.5**

		1.3	1.25 [c]	X		10.1	0.17	0.002	-14.8	-17.3	**-20.7**
		1.4	**1.28**	X		10.2	0.15	0.002	-14.8	-17.3	**-20.7**
70°C	3 months	0.7	*n.d.*		X	8.5	0.05	3.76	**-13.3**	-16.4	-20.5
		0.8	*n.d.*		X	8.7	0.03	3.7	**-13.4**	-16.4	-20.6
		0.9	*n.d.*		X	8.4	0.04	3.77	**-13.6**	**-16.8**	-21.1
		1	*n.d.*	X	X	9	0.03	1.62	**-13.3**	**-16.3**	-20.3
		1.1	1.14 [c]	X		9.5	0.04	0.33	-12.9	**-15.7**	**-19.6**
		1.2	1.17 [c]	X		9.6	0.06	0.227	-13.3	-16.1	**-19.7**
		1.3	1.20 [c]	X		10	0.07	0.047	-13.7	-16.2	**-19.8**
		1.4	1.24 [c]	X		10.3	0.09	0.011	-14	-16.5	**-19.9**
	1 Year	0.7	*n.d.*		X	8.3	0.05	3.11	**-13.6**	-16.7	-21
		0.8	**0.86**		X	8.3	0.05	3.12	**-13.5**	-16.6	-20.8
		0.9	*n.d.*		X	8.4	0.07	2.28	**-13.5**	**-16.5**	-20.7
		1	**1**		X	8.9	0.06	0.51	**-13.7**	**-16.6**	-20.6
		1.1	1.10 [c]			9.2	0.29	0.05	-13.8	**-16.5**	-20.1
		1.2	**1.2**			9.8	0.28	0.014	-13.9	-16.4	-19.8
		1.3	1.25 [c]			10	0.24	0.004	-14.3	-16.8	-20.1
		1.4	**1.3**	X		10.1	0.25	0.003	-14.4	-16.8	**-20.2**
Undersaturation											
20°C	1 Year	0.75	talc			8.6	0.16	0.35	-15 [d]	-	-
		1.5	antigorite			8.2	0.18	0.13	-	-	-23 [d]

[a]X= observed by TGA and XRD, [b]X= observed by FT-IR and/or ^{29}Si MAS NMR (amount quantified is detailed in Figure 14 and Figure 12)

[c] = unreacted silica negligible as [Si] < 0.3mmol/l, n.d.= unreacted silica not determined

Mg/Si in bold correspond to experimentally determined ratios (amorphous silica has been quantified by ^{29}Si MAS NMR)

Calculated ion activity products in bold correspond to the values used for the averaged values in Table 12, values in grey correspond to samples dominated by transitional M-S-H and are given for comparison only

n.d.= not determined

[d]Synthetic talc (Alfa Aesar) log $K_{s0}(M_3S_4H_2)$=-58.0; natural antigorite (from Binntal) log $K_{s0}(M_3S_2H_2)$=-51.8

Appendix C: Details of the X-ray PDF analysis fitting.

Minerals used:

Sepiolite fiche CIF: 9014723

Formula : H_{12} $Mg_{3.592}$ O_{22} Si_6

Calculated formula: $Mg_{14.368}$ O_{68} Si_{24} Wa_{20}

Groupe d'espace : P n c n

α=β=γ= 90° ; a=13.3067 Å ; b=26.9720 Å ; c=5.2664 Å

Sanchez, M. , Garcia-Romero E. , Suarez, M. , Silva, I. , Fuentes-Montero L. , Martinez-Criado G. , Variability in sepiolite: Diffraction studies Note: Sample BAT25 Note: T = 25 C, Journal of American Mineralogist, Vol. 96, pp. 1443 – 1454, (2011)

Talc fiche CIF: 1011152

Formule : H_2 Mg_3 O_{12} Si_4

Groupe d'espace : C 1 2/c 1

a=5.26 ; b=9.1 ; c=18.81 ; α=γ=90° ; β=100.08°

Gruner, J. W. , The crystal structures of talc and pyrophyllite, Zeitschrift fuer Kristallographie, Kristallgeometrie, Kristallphysik, Kristallchemie (-144,1977), Vol. 88, pp. 412-419, (1934)

Antigorite-Tb (n = 17) fiche CIF: 19084

Formule : Mg_{48} O_{147} Si_{34}

Groupe d'espace : triclinique P 1 1
Dodony I, Posfai M, Buseck P R, Revised structure models for antigorite: An HRTEM study, American Mineralogist 87 (2002) 1443-1457
a=43.5 angstroms ; b=9.23 angstroms; c=7.27 angstroms; α= 90 ; β = 92°; =γ=90°

Antigorite-M fiche CIF: 9014625
Formule : Mg_{39} O_{120} Si_{28}
Groupe d'espace : monoclinique P 1 m 1
a=35.02 ; b=9.23 ; c=7.27 ; α= β=γ=90°
Dodony, I.; Posfai, M.; Buseck, P. R., Revised structure models for antigorite: An HRTEM study Note: n = 14, Journal of American Mineralogist, Vol. 87, pp. 1443 – 1457, (2002)

Chrysotile fiche CIF: 1010960
Formule : H_8 Mg_6 O_{18} Si_4
Groupe d'espace : C 1 2/m 1
a=14.66; b=18.5 ; c=5.33 ; α=γ=90° β=93.27°
Warren, B.E. ; Bragg, W.L., The crystal structure of chrysotile H_4 Mg_3 Si_2 O_9, Zeitschrift fuer Kristallographie, Kristallgeometrie, Kristallphysik, Kristallchemie (-144,1977), Vol. 76, pp. 201-210, (1931)

Lizardite fiche CIF: 0005585
Formule : Mg_3 Si_2 H_4 O_9
Groupe d'espace : P 3 1 m
a=b=5.332 ; c=7.332 ; α=β=90° ; γ=120°
Guggenheim S. and Zhan W. , Effect of temperature on the structures of lizardite-1T and lizardite-2H1, The Canadian Mineralogist, Vol. 36, pp. 1587-1594, (1998)

Fits:

For every fit, the Qdamp was set to 0.05 and Qmax was kept at 17, the fit range is detailed below.

			1.3 (1-20 Å) Figure 26	0.8 (1-20 Å) Figure 27	0.8 (1-12 Å) Figure 28
CIF file	Paramètre	Initial	Ajusté	Ajusté	Ajusté
sepiolite	Scale factor	1	0.739	0.61	
	Delta1	0	1.128	0	
	a	13.4	13.125	13.038	
	b	26.8	27.281	27.065	
	c	5.28	5.415	5.418	
	α	90	90	90	
	β	90	90	90	
	γ	90	90	90	
	adp Mg	0	0.00549	0.0077	
	adp Si	0	0.0281	0.012	
	adp O	0	0.0356	0.0188	
	r_w		0.61	0.60	
Talc	Scale factor	1	0.685	0.609	0.797
	Delta1	0	1.428	1.497	1.431
	a	5.26	5.39	5.352	5.356
	b	9.1	9.357	9.34	9.24
	c	18.81	18.019	18.266	18.39

	α	90	90	90	90
	β	100	100	100	100
	γ	90	90	90	90
	adp Mg		0.00931	0.018	0.0162
	adp Si		0.0619	0.045	0.0606
	adp O		0.0605	0.057	0.0564
	r_w		0.59	0.55	0.42
Antigorite Tb	Scale factor	1	0.849	0.793	0.865
	Delta1	0	1.047	1.141	1.058
	a	43.5	43.437	43.422	43.442
	b	9.23	9.455	9.401	9.395
	c	7.27	7.154	7.077	7.028
	α	90	90	90	90
	β	92	92	92	92
	γ	84.75	84.75	84.75	84.75
	adp Mg		0.0197	0.0312	0.0312
	adp Si		0.0144	0.00701	0.0081
	adp O		0.0244	0.0288	0.0269
	r_w		0.46	0.46	0.42
Antigorite M	Scale factor	1	0.769	0.546	
	Delta1	0	1.237	0	
	a	35.02	34.202	34.709	
	b	9.23	9.458	9.32	
	c	7.27	7.186	7.335	
	α	90	90	90	
	β	90	90	90	
	γ	90	90	90	
	adp Mg		0.0106	0.0274	
	adp Si		0.0352	0.0113	
	adp O		0.0441	0.0072	
	r_w		0.61	0.64	
Chrysotile	Scale factor	1	0.687	0.475	
	Delta1	0	1.535	0	
	a	5.34	5.339	5.468	
	b	9.241	9.497	9.196	
	c	14.689	15.067	14.823	
	α	90	90	90	
	β	93.66	93.66	93.66	
	γ	90	90	90	
	adp Mg		0.0049	0.025	
	adp Si		0.0355	0.0032	
	adp O		0.0915	0.0156	
	r_w		0.56	0.66	
Lizardite	Scale factor	1	0.123	0.128	
	Delta1	0	0.639	1.379	
	a	5.332	5.475	5.462	
	b	5.332	5.281	5.232	
	c	7.23	7.666	7.621	

α	90	90	90
β	90	90	90
γ	90	90	90
adp Si		0.0103	0.0079
adp Mg		0.00761	0.0196
adp O		0.0175	0.0195
adp H		0.000329	0.00033
r_w		0.69	0.68

Appendix D: ^{29}Si MAS NMR spectrum of the natural sepiolite detailed in chapter 3.2.

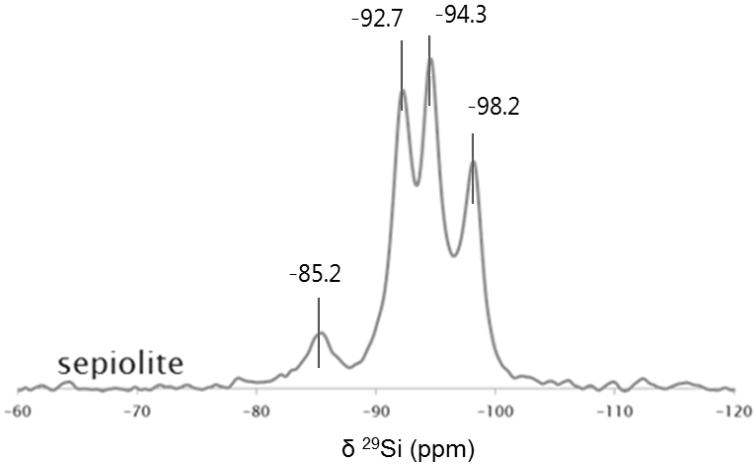

Appendix E: Presence of brucite and unreacted silica in the phase assemblage, Concentrations and pH of the solutions in equilibrium with the co-precipitated samples after 1 and 2 years at 20°C, and after 6 months and 1 year at 50°C. (bold samples correspond to the solid analysis parts), brucite content corresponds to the wt.% of brucite for 100g of dry mass.

		Ca/Si	time [years]	Brucite[a]	unreacted silica[b]	[OH][c]	[Ca]	[Mg]	[Si]	pH	log K_{s0}				
								mmol/l			$M_{0.78}SH_{1.48}$	$C_{0.8}SH_{1.94}$	$M_{0.68}C_{0.1}SH_{1.48}$	$M_{0.70}C_{0.08}SH_{1.48}$	$M_{1.2}C_{0.1}SH_{1.80}$
20°C	Ca/Si=0.8	references	*1*			0.14	1.04	---	2.19	10.3	-14.8	-11.74			
			2			0.24	0.86	---	1.62	10.5					
	Mg/Si=0.8		*1*		✓	0.00	---	0.330	1.36	8.5					
			2		✓	0.00	---	0.380	1.44	8.3					
50°C	Ca/Si=0.8	references	-			0.11	0.96	---	2.36	10.2	-13.90	-11.1			
			1			---	---	---	---	---					
	Mg/Si=0.8		*0.5*		✓	0.001	---	0.090	2.50	8.3					
			1		✓	0.001	---	0.100	2.57	8.3					
20°C		0.05	*1*	✓(4.9)	*n.d.*	0.01	0.16	0.006	1.47	9.2	-14.8		-14.6	-14.7	-22.5
			2		*n.d.*	0.01	0.15	0.004	0.62	8.9	-15.7		-15.5	-15.6	-23.8
		0.1	*1*	✓(2.2)	*n.d.*	0.06	0.30	0.009	1.00	10.0	-13.9		-13.7	-13.8	-20.8
			2	✓(2.0)	*n.d.*	0.01	0.29	0.000	1.02	9.3	-15.7		-15.4	-15.4	-23.8
		0.4	*1*	✓(10.7)	✓*	0.06	1.10	---	3.63	9.9	-15.8	-12.0	-15.3	-15.4	-24.0
			2	✓ (9.8)	✓*	0.05	1.14	---	3.44	9.9	-15.9	-12.1	-15.3	-15.4	-24.1

	0.5	*1*	✓(12.0)	✓*	0.07	1.16	---	3.96	10.0	-15.7	-11.9	-15.2	-15.3	-23.9
		2	✓(9.4)	✓*	0.06	1.07	---	3.48	9.9	-15.8	-12.1	-15.3	-15.4	-24.0
	0.7	*1*	✓(5.1)	*n.d.*	0.09	1.21	---	3.66	10.1	-15.7	-11.8	-15.1	-15.3	-23.7
		2	✓(5.8)	*n.d.*	0.08	1.19	0.000	3.21	10.1	-15.0	-11.9	-14.5	-14.6	-22.5
	0.75	*1*	✓(2.3)	*n.d.*	0.12	1.15	---	3.11	10.2	-15.7	-11.8	-15.1	-15.2	-23.5
		2	✓(3.6)	*n.d.*	0.12	1.08	0.000	2.61	10.2	-14.7	-11.9	-14.3	-14.4	-22.0
	0.05	*0.5*			0.00	0.26	0.006	1.55	8.3	-14.8		-14.6	-14.7	-22.6
		1			0.01	0.21	0.001	1.30	8.8	-14.4		-14.1	-14.2	-21.7
	0.1	*0.5*	✓(3.0)		0.03	0.43	---	1.83	9.1	-15.8		-15.3	-15.4	-23.9
		1	Tr(0.7)		0.06	0.46	0.001	1.53	9.3	-14.1		-13.9	-13.9	-21.3
	0.4	*0.5*	✓(8.1)	*n.d.*	0.03	1.21	---	4.12	9.1	-15.1	-11.3	-14.6	-14.7	-22.9
		1	✓(4.3)	✓*	0.06	1.10	0.001	3.47	9.3	-13.4	-11.1	-13.1	-13.2	-20.1
	0.5	*0.5*	✓ (8.5)	*n.d.*	0.04	1.25	---	4.25	9.2	-15.8	-12.0	-15.3	-15.4	-24.0
		1	✓(2.2)	*n.d.*	0.10	0.93	0.000	2.31	9.5	-14.5	-11.8	-14.1	-14.2	-21.9
	0.7	*0.5*	✓(3.1)		0.09	1.05	---	2.16	9.5	-15.5	-11.8	-15.0	-15.1	-23.4
		1	Tr(0.7)		0.18	0.88	0.001	1.82	9.7	-13.7	-11.7	-13.4	-13.5	-20.5
	0.75	*0.5*	Tr(0.7)		0.23	0.88	---	1.45	9.8	-15.3	-11.6	-14.8	-14.9	-22.8
		1			0.13	0.89	0.002	2.06	9.6	-13.5	-11.6	-13.2	-13.2	-20.1
50°C														

[a]from TGA, [b]from ^{29}Si MAS NMR, [c] Hydroxide concentrations calculated from the measured pH values

*amorphous silica detected by FTIR

Magnesium detection limit: 0. 01µmol/l

Appendix F: Concentrations of the cations sorbed on co-precipitated samples compared to M-S-H 0.8 and C-S-H 0.8 measured by cobalt hexamine method as a function of the initial Ca/Si. CEC measurements by colorimetry (black circles) have been added for comparison (samples synthetized at 50°C).

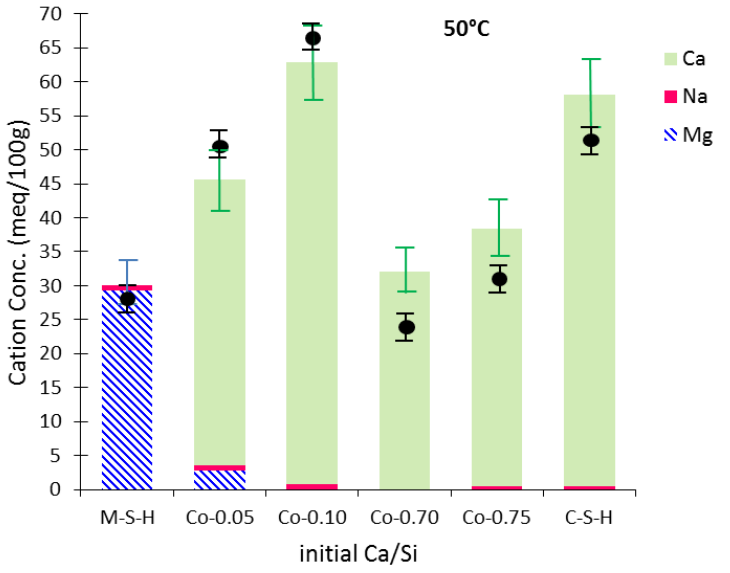

Appendix G: Exchangeable magnesium and calcium per silicon co-precipitated samples compared to M-S-H 0.8 and C-S-H 0.8 calculated from CEC (samples synthetized at 50°C)

sample	exchangeable Mg^{2+} per Si	exchangeable Ca^{2+} per Si	total
M-S-H	0.018	--	0.018
Co-0.05	0.002	0.025	0.027
Co-0.10	<0.001	0.038	0.038
Co-0.70	<0.001	0.022	0.022
Co-0.75	<0.001	0.027	0.027
C-S-H	<0.001	0.041	0.041

Appendix H: TEM images of Co-0.70 sample: a) magnesium rich particle and b) calcium rich particle.

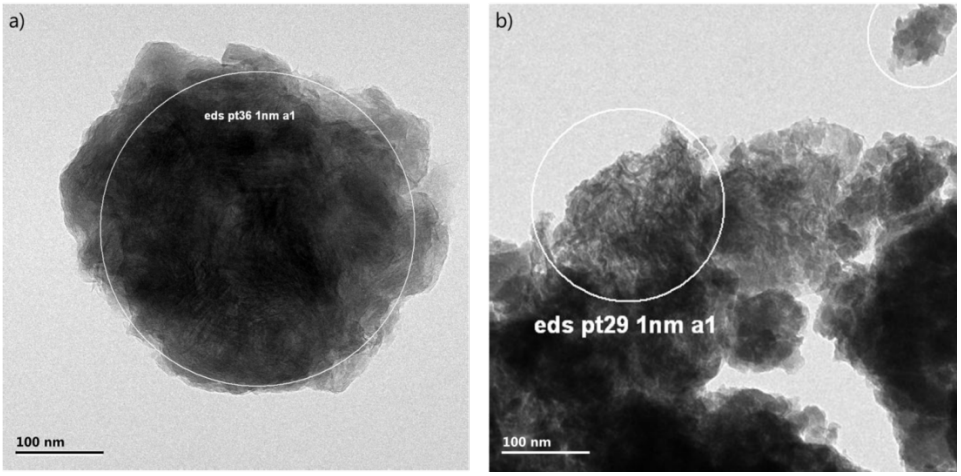

Appendix I: Modelling of the main phases' evolution with M-S-H and C-S-H phases only (suppressing M-(C)-S-H formation) a) after 3 months and b) 12 months of interaction at the C-S-H / M-S-H interface at 25°C.

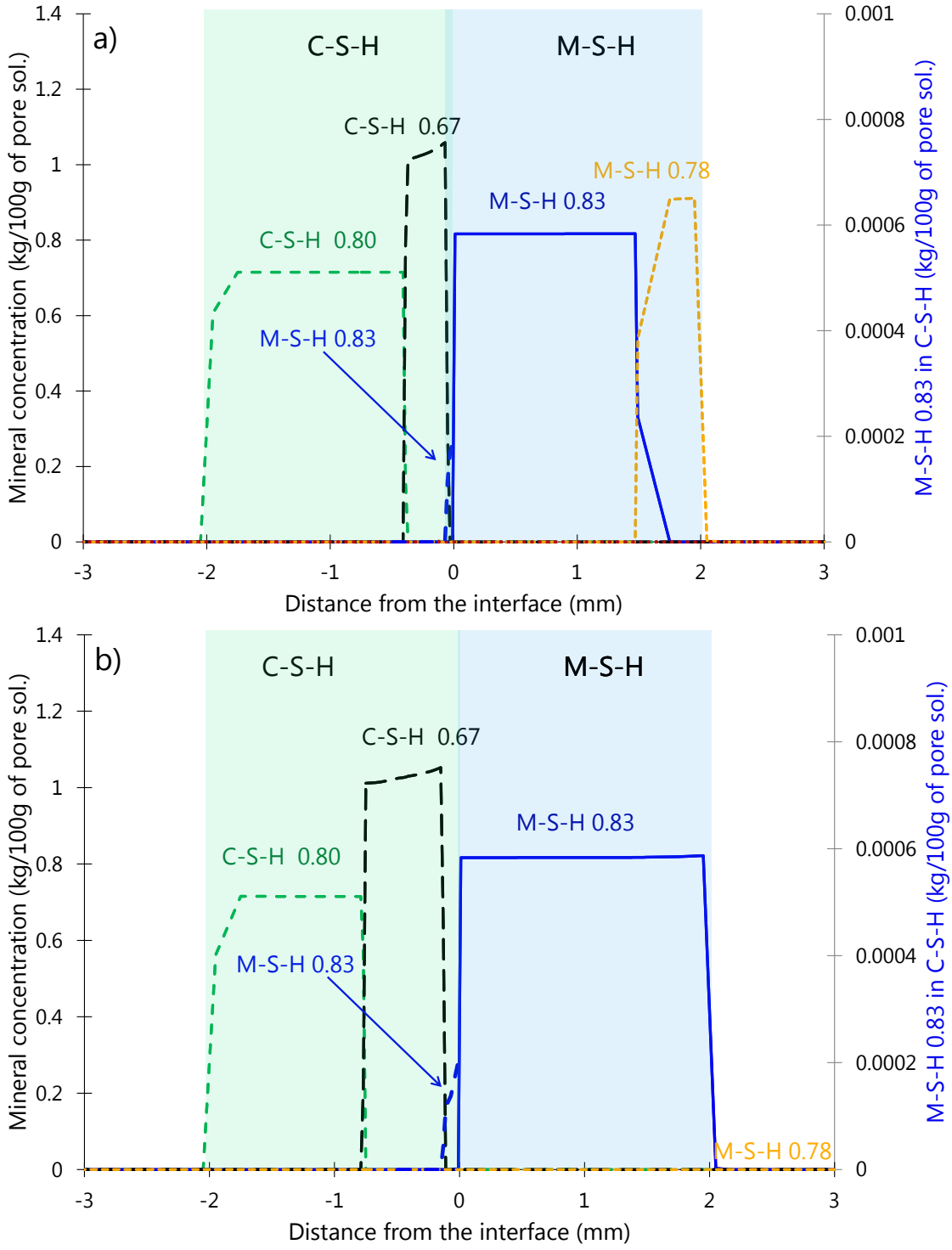

Appendix J: Thermogravimetric analysis of the M-S-H samples synthesized in the presence of sodium nitrate after 1 year of curing at 20°C compared to TGA of pure M-S-H 1.2 (*=trace of brucite).

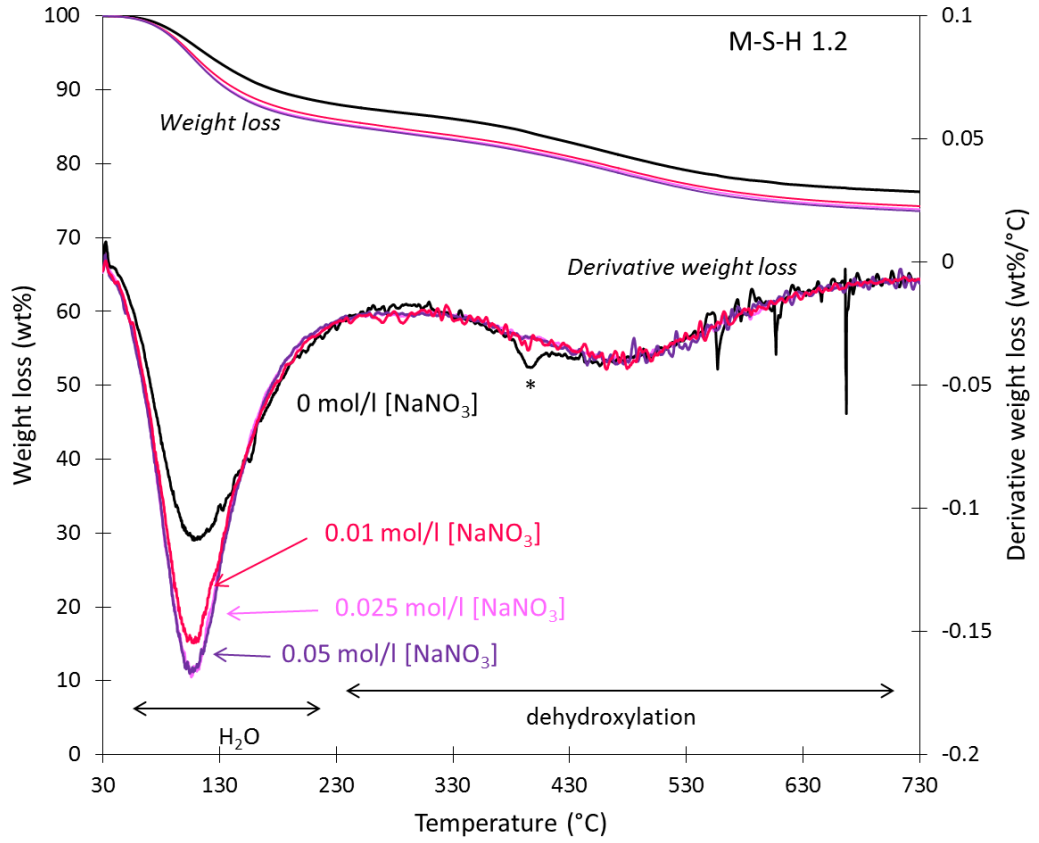

Appendix K: FTIR spectra of M-S-H samples synthesized in the presence of sodium nitrate after 1 year of curing at 70°C.

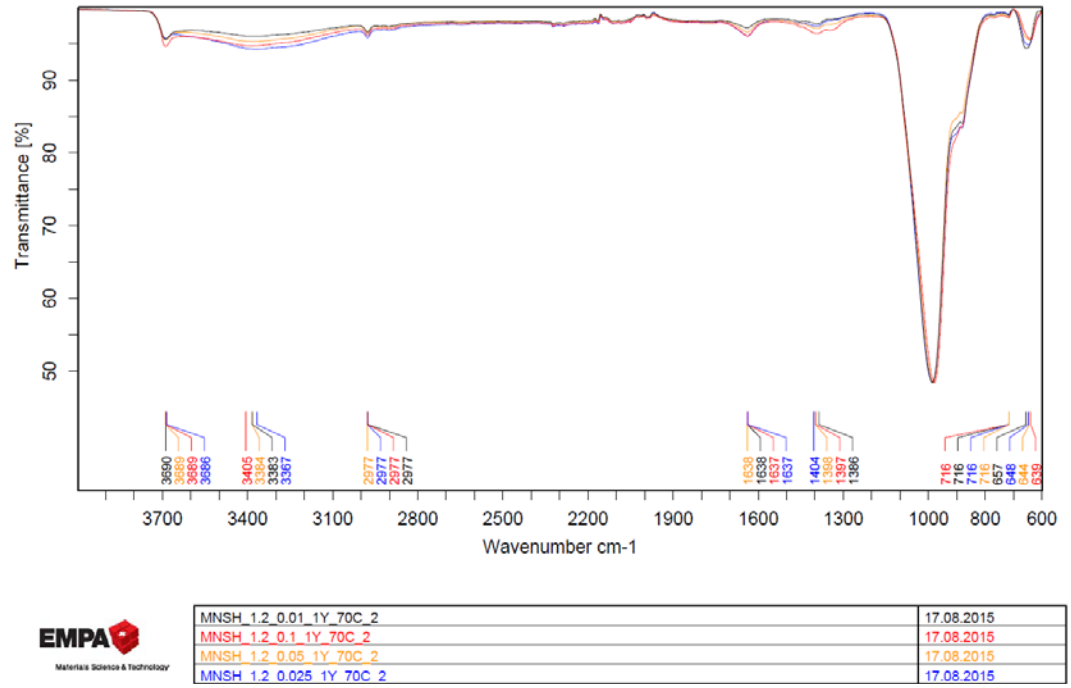

Appendix L: 29Si MAS NMR spectra with assignments of single sites of M-S-H samples synthesized in the presence of sodium hydroxide compared to pure M-S-H.

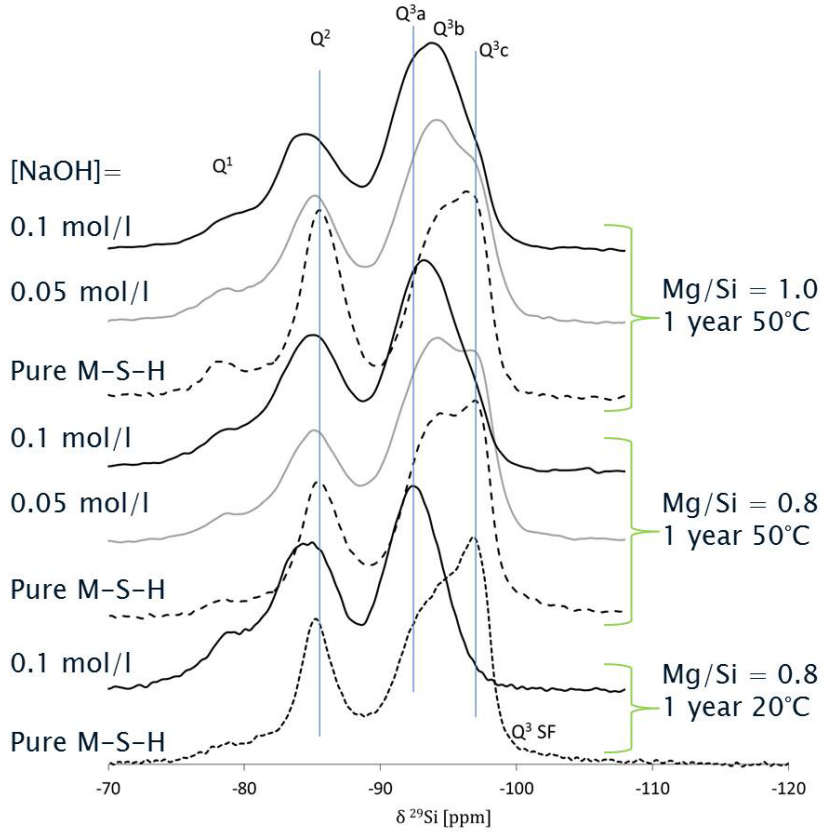

Appendix M: The effect of the measuring method on the alkali/Si in M-S-H at low concentrations.

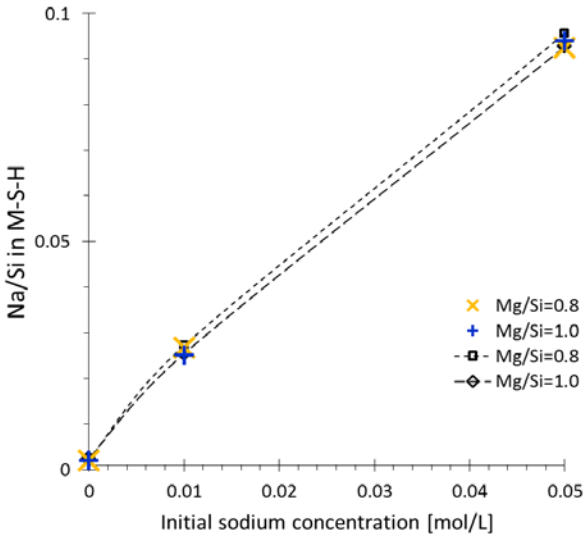

Appendix N: ^{29}Si MAS NMR spectrum measured for saponite, the saponite composition is described in (Gailhanou et al., 2013).

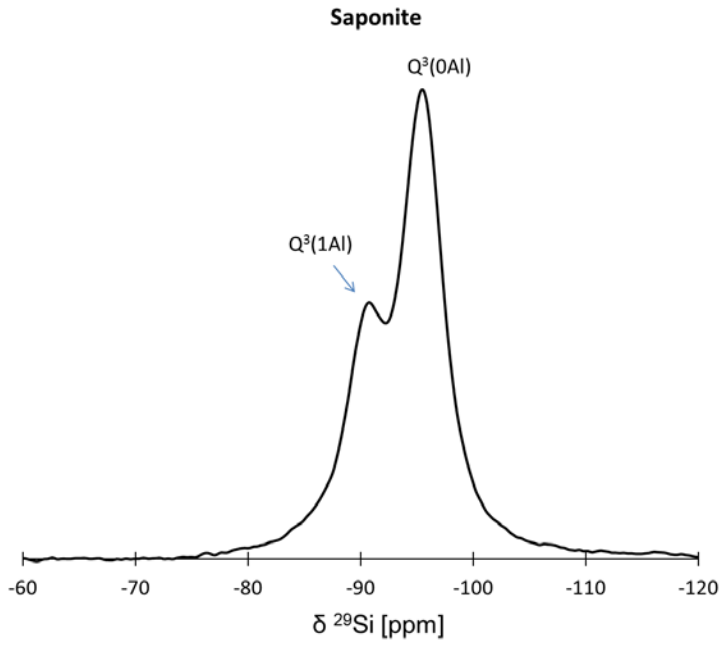

Appendix O: ^{27}Al MAS NMR spectrum measured for saponite. The saponite composition is described in (Gailhanou et al., 2013).

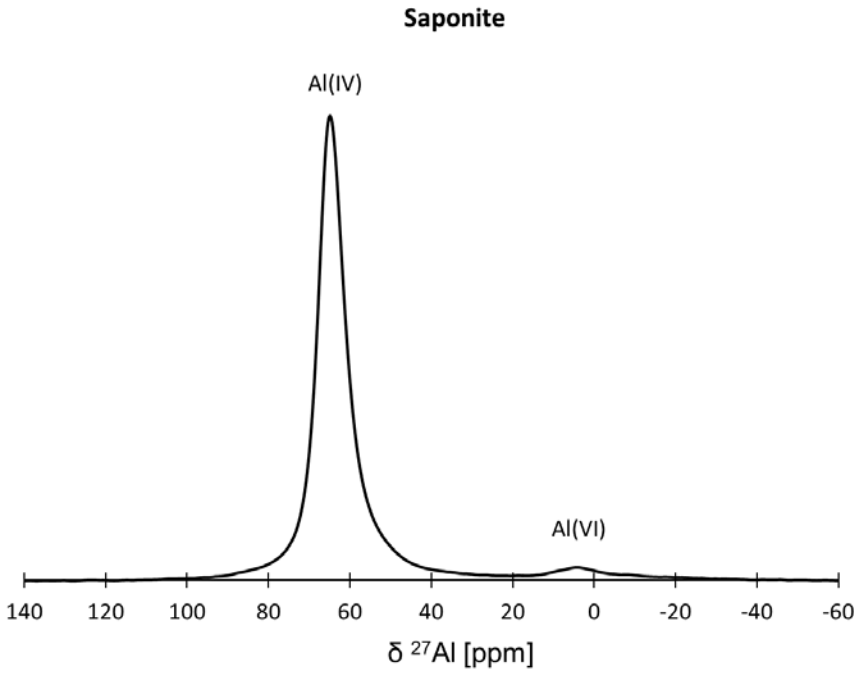

Appendix P: ^{27}Al MAS NMR spectra of synthesized hydrotalcite and poorly ordered $Al(OH)_3$.

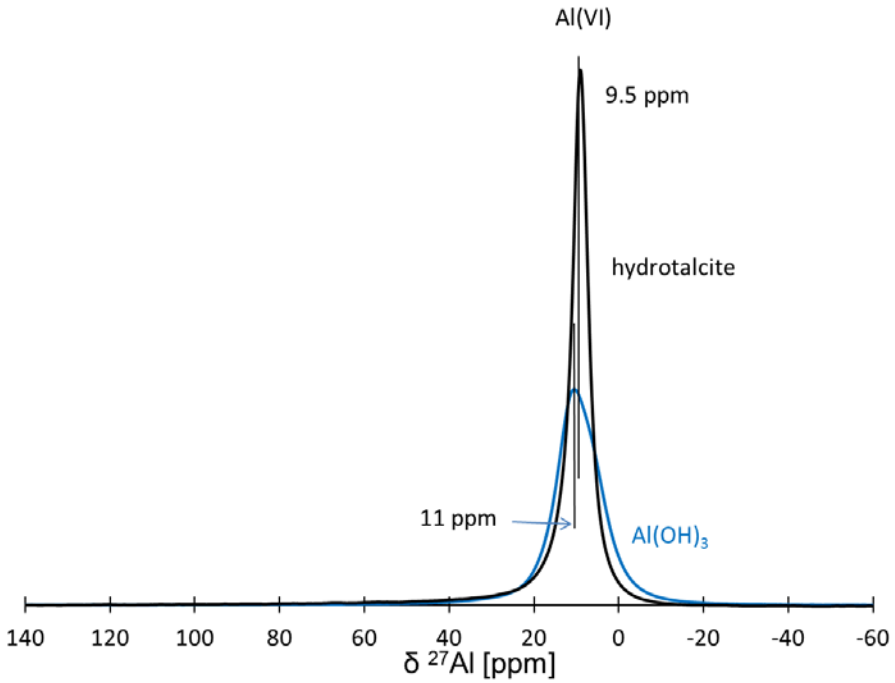

Abstract

The various options to store radioactive wastes in deep geological strata considered in France or Switzerland include the use of large volumes of cementitious materials for infrastructure in contact with argillaceous rocks. So-called low-pH binders were developed to minimize disruption to the surrounding rock by the alkaline plume. Studies conducted on the interaction zone between concrete and clay systematically highlighted the formation of magnesium silicate phases including magnesium silicate hydrate (M-S-H) at the interfaces, which can presently be modeled only partially due to incomplete thermodynamic data. The purpose of this study was to characterize these phases in temperature, aluminum, calcium, and alkali conditions in order to provide the thermodynamic data and improve the calculations on physicochemical evolutions of low-pH concretes and possibly Portland concretes.

M-S-H phases were synthesized from magnesium oxide and silica fume in batch experiments at different temperatures, for various times and varying Mg/Si. A large number of different techniques such as chemical solid characterizations coupled with suspension investi-gations and liquid analyses were used to characterize the phases synthesized. Initially a M-S-H phase with Mg/Si equal to 1 was precipitated in addition to amorphous silica and brucite whatever the total Mg/Si used for the synthesis. After long equilibration times, 2 to 3 years at 20°C or 1 year at 50 and 70°C, the Mg/Si in M-S-H ranged from ~0.8 to ~1.4. The temperature had little influence on the M-S-H formed even if the M-S-H formation occurred faster and M-S-H was thermodynamically slightly less stable when the temperature was increased. At or near to equilibrium, M-S-H phases were characterized with ill-defined structure comparable to nano-crystallite, hydrated phyllosilicates with a surface area greater than 200 m^2/g. A M-S-H solid-solution model was calculated and implemented in the thermodynamic database.

It was observed that M-S-H also form from calcium silicate hydrate (C-S-H) with a Ca/Si = 0.8 in the presence of additional magnesium. In batch experiments, a low pH of the suspensions (pH ≤ 10) destabilized C-S-H or prevented its formation and favored the precipitation of M-S-H. Detailed investigations showed that small amounts of calcium could be incorporated in M-S-H (Ca/Si ≤0.10), such that also calcium containing end-members were added to the M-S-H solid-solution. At pH ≥ 10-10.5, two separate silicate phases coexist: C-S-H and M-S-H. The interface between a simplified “low-pH” binder mimicked by C-S-H with Ca/Si = 0.8 and a magnesium-rich environment mimicked by M-S-H with Mg/Si = 0.8 confirmed these phenomena. SEM-EDS observa-tions and reactive transport modelling using the thermodynamic data derived in the batch experiments showed the fast deterioration of the C-S-H and the precipitation of C-S-H in the C-S-H disk at the interface and a homogeneous uptake of calcium in the M-S-H disk.

The increase of pH favors the sorption. M-S-H with a sodium uptake up to Na/Si ~ 0.20 and without brucite formation were observed at high pH (12.5). The sorption on M-S-H was favored in the order Na^+ < Mg^{2+} < Ca^{2+}. Finally, aluminum was incorporated into M-S-H to form magnesium alumino-silicate hydrate (M-A-S-H). An Al/Si ratio up to 0.2 was observed in presence of sodium aluminate or metakaolin. ^{27}Al MAS NMR data showed that aluminum was present in both tetrahedral and octahedral sites of M-(A-)S-H. The M-(A-)S-H formed had a similar structure as M-S-H with a comparable polymerization degree of the tetrahedral silicates and a similar surface charge.

Keywords: *Geological disposal, clays, low-pH cement, calcium silicate hydrate (C-S-H), magnesium silicate hydrate (M-S-H), magnesium (alumino-) silicate hydrate (M-(A-)S-H), alkali and calcium binding, chemical composition, thermodynamic modelling*

Résumé

Les différentes options envisagées par la France et la Suisse pour le stockage de déchets radioactifs en couches géologiques profondes argileuses prévoient l’utilisation d’importants volumes de matériaux cimentaires. Les liants dits bas-pH ont été développés afin de limiter la perturbation de la roche encaissante par le panache alcalin. Les études expérimentales menées sur les interfaces béton bas-pH-argile mettent systématiquement en évidence la formation de phases silico-magnésiennes, potentiellement de silicate de magnésium hydraté (M-S-H), mal modélisées à cause de données thermodynamiques limitées. Cette étude a pour objectif de caractériser ces phases en température, en présence d’aluminium, calcium et d’alcalins pour alimenter les bases de données thermodynamiques et améliorer les calculs sur les évolutions physico-chimiques des bétons bas pH et éventuellement des bétons de Portland.

Des suspensions de M-S-H ont été synthétisées à partir d'oxyde de magnésium et de fumée de silice à différentes températures, à différents temps de réaction et différents rapports Mg/Si. Un panel de techniques d’analyses de chimie du solide et des mesures en suspensions couplées à des analyses des phases liquides a été utilisé pour caractériser les phases synthétisées. Initialement, et quel que soit le Mg/Si total choisi pour la synthèse, un M-S-H avec un rapport Mg/Si ~1 précipite en présence de brucite et de silice amorphe. Lorsque l’équilibre du système est atteint, 2 à 3 ans à 20 °C ou 1 an à 50 et 70 °C, le Mg/Si varie de ~0,8 à ~1,4. La température a peu d'influence sur le M-S-H formé même si le M-S-H se forme plus rapidement et qu’il est légèrement moins stable thermodynamiquement lorsque la température augmente. A l'équilibre, sa structure mal définie est comparable à des nano-cristallites de phyllosilicates hydratés avec une surface spécifique supérieure à 200 m^2/g. Un modèle de solution solide pour le M-S-H a été calculé et ajouté à la base de données.

Dans un second temps, les travaux ont été focalisés sur la formation de M-S-H à partir de silicate de calcium hydraté (C-S-H) avec un faible Ca/Si (= 0,8) et de magnésium. Le C-S-H n’est pas stable à des pH avoisinant un pH = 10, ce qui favorise la précipitation de M-S-H. Des recherches détaillées montrent que du calcium peut être faiblement incorporé dans le M-S-H (Ca/Si ≤ 0,10), et des solutions solides contenant du calcium ont été ajoutés à la base de données. Pour des pH supérieurs à 10-10,5, les C-S-H et M-S-H coexistent. L’observation par MEB-EDS d’une interface en cellule de diffusion entre C-S-H (Ca/Si=0,8 représentant un liant bas pH) et M-S-H (Mg/Si=0,8), couplée à la modélisation de celle-ci en transport réactif, sur la base des nouvelles données thermodynamiques dérivées des expériences précédentes, montrent la détérioration rapide du C-S-H et la précipitation de M-S-H dans le disque C-S-H, ainsi qu’une absorption homogène du calcium dans le disque de M-S-H.

L’augmentation du pH en solution favorise la sorption de cations. Des M-S-H présentant une sorption de sodium jusqu'à Na/Si ~ 0,20 en absence de brucite ont été observés à des pH avoisinants 12,5. La sorption sur le M-S-H est favorisée dans l'ordre Na^+ < Mg^{2+} < Ca^{2+}. Enfin, l'aluminium s’incorpore dans le M-S-H pour former du M-A-S-H. Un rapport Al/Si jusqu’à 0,2 est observé dans des suspensions synthétisées en présence d’aluminate de sodium ou de métakaolin. Les données de RMN de l’aluminium ont montré que celui-ci est présent dans les sites tétraédriques et octaédriques du M-A-S-H. La phase formée a une structure similaire à celle du M-S-H avec un degré de polymérisation des silicates et une charge effective de surface comparables.

Mots-clés*: Stockage en couches profondes, argiles, pâtes de ciment bas-pH ; silicate de calcium hydraté (C-S-H) ; silicate de magnésium hydraté (M-S-H) ; alumino-silicate de magnésium hydraté (M-A-S-H) ; adsorption d’alcalins et de calcium ; composition chimique ; modélisations thermodynamiques*